The path towards the Giant Radio Array for Neutrino Detection

Olivier Martineau-Huynh

Mémoire d'habilitation à diriger des recherches

présenté le 6 juillet 2021 à Paris par

Olivier Martineau-Huynh
(Laboratoire de Physique Nucléaire et des Hautes Énergies, Sorbonne Université, CNRS/IN2P3)

The path towards the Giant Radio Array for Neutrino Detection

devant le jury composé de :

Marianne Lemoine-Goumard (Centre d'Études Nucléaires de Bordeaux-Gradignan) - Présidente
Melissa Ridel (Laboratoire de Physique Nucléaire et des Hautes Energies) - Examinatrice
Frank Schröder (University of Delaware) - Examinateur
Nick Van Eijndhoven (Vrije Universiteit Brussel) - Rapporteur
Stephanie Wissel (Pennsylvania State University) - Rapportrice
Enrique Zas (Universidad de Santiago de Compostela) - Rapporteur

Acknowledgements

Many people had major contributions to the work presented in this document. I tried to acknowledge these throughout the text, but I would also like to thank several people in these forewords. At first order, I must express all my gratitude to Wu XiangPing for his continous support since our first meeting in summer 2007. Nothing would have been possible without him and I will never be grateful enough for his efforts and friendship.

I would also like to express my recognition and friendship to Kumiko Kotera, the first GRANDer, whose enthousiasm has since been a major driver for the project, Valentin Niess, for our great collaboration and his key contributions since the very first days, and Charles Timmermans, in particular for the very nice moments during our quest for radio-detection sites throughout Western China. I enjoyed his unique expertise in experimental physics as much as his sense of humour. I also thank him for his carefull reading of the preliminar version of this manuscript.

I took a lot of pleasure working with Valentin Decoene, Simon Chiche, Sandra Le Coz, Thomas Saugrin, Zhang Jianli et Zhang Kewen. I wish they learnt from this collaborative work as much as I did, and I hope we can keep collaborating in the future. I must also thank Matias Tueros and Tanguy Pierog for the great contributions to the project and their friendship.

I send my warm regards to my friends in China, in particular Hu HongBo for his perfect welcome at IHEP, Gu JunHua for his key help in so many occasions, Huang Yan for her constant support and great expertise, Feng Yang and the Ulastai team for the great moments and valuable help in Western China, as well as Zhang Pengfei and Zhang Yi for their key contributions in the present (and future!) phases of the GRAND project. I extend these acknowledgements all GRANDers: seing people getting enthousiastic about the project and working with them at giving shape it to is a major source of pleasure and motivation for me!

My thanks also go to the electronics staff at LPNHE for their sucess in building GRANDProto35 electronics, and to Marco Zito for his support to GRAND.

I am very thankfull to Nick Van Eijndhoven, Stephanie Wissel and Enrique Zas for reviewing this document, and to Marianne Lemoine-Goumard, Melissa Ridel and Frank Schröder for taking part in this Habilitation jury.

This document was written between March 2020 and April 2021, a period tainted with the Covid pandemic and various phases of confinment in France. These have certainly been favorable for this type of solitary work, but my company was probably not the best possible during that period of time: I am therefore gratefull to Emilie, Elias and even more to Rita for her constant support and adaptability to my exotic working hours during this very peculiar period.

Contents

Introduction

It has become a common place to say that we are living privileged times for research in Physics and the progress of our understanding of the laws of Nature. Yet the present situation is indeed unique. Take for instance astroparticle physics —the field at the intersection of high energy physics and astrophysics— which aims, among other topics, at understanding violent phenomena in the Universe. For thousands of years, the sky could be observed only through naked eyes, and with telescopes after the 17^{th} century. Only in the last 100 years did our window to the Universe finally expand to other wavelengths —radio, infrared, GHz frequencies— and a new messenger type with the detection of cosmic rays by Victor Hess. In the last ten years, neutrinos and gravitational waves added to the list. The remarkable increase in the number and quality of observational tools notably fostered progress in our understanding of the mechanisms at play in violent phenomena in the Universe. We can now be (reasonably) hopeful that the source(s), nature and mechanism(s) of production of Ultra-High Energy Cosmic Rays (UHECRs) —the particles with the highest energy in the Universe, with values beyond 10^{20} eV, seven orders of magnitude beyond what is achieved in human-made accelerators— will be determined in the very next years.

Still missing in the list of messengers from the Universe are Ultra-High Energy neutrinos, with energies beyond 10^{16} eV typically. Particle physics shows that their production would be tightly coupled to that of UHECRs, while —unlike these particles— neutrinos travel unimpeded over cosmological distances, pointing back to their sources even if at cosmological distances. UHE neutrinos could therefore be the key to the UHECRs mystery. Yet their fluxes are expected to be very low at the highest energies —less than one per km^2 per century— and neutrinos are elusive particles by nature, with mean free path in dense targets of the order of the Earth diameter. Their detection thus requires gigantic detection areas and powerful methods of identification. Detection of the faint and brief electromagnetic pulse induced in the radio frequency range by the interaction of an UHE neutrino with the Earth target could prove to be a winning strategy: radio antennas are cheap, easy to deploy and maintain, robust and stable detectors and are thus very well adapted for the required gigantic detection areas. Besides, giant radio arrays can also be used for the direct observation of UHECRs or other transient radio phenomena like Fast Radio Burst, another booming field.

I embarked on the adventure of radio-detection of UHE neutrinos in a rather uncommon way. In 2007, I met Wu XiangPing, radio-astronomer at the National Astronomical Observatories of China, at a time I was considering living in this country. Familiar to the topic of UHE cosmic particles thanks to my participation in the Auger and H.E.S.S. experiments, I was charmed by the exciting challenge of trying to detect cosmic rays with 21CMA, the radio array XiangPing had built for the study of the Epoch of Reionization. I therefore moved to Beijing in 2008, and started a 12-year long journey in the field of autonomous radio-detection of cosmic particles. I present the results of this work in this document.

In chapter 5, I detail my work on TREND (Tianshan Radio Experiment for Neutrino Detection) the experiment of cosmic ray radio detection I conducted on the 21CMA setup. I then present its tentative upgrade GRANDProto35 in chapter 6, and the preparatory phases of GRANDProto300 in chapter 7. This experiment, about to be deployed in a remote desert area at the rim of the Tibetan plateau, is a pathfinder for the Giant Radio Array for Neutrino Detection. GRAND is a very ambitious proposal to build a network of radio antennas covering a total area of 200 000 km^2, the size of England. GRAND would aim at detecting and studying UHE cosmic particles and transient radio phenomena. I present my work on the GRAND project in chapter 3, and our first attempts to reconstruct cosmic particle properties from GRAND radio signals in chapter 4. The science case for GRAND and its detection principles are introduced in chapters 1 and 2.

Part I

The Giant Radio Array for Neutrino Detection

Chapter 1

Science with a giant radio array

In this chapter, we first expose the scientific case for the detection of ultra-high energy cosmic messengers. These particles are the main target for the giant radio detector —200 000 radio antennas deployed over a total area of 200 000 km^2— which constitutes the pillar of the work presented in this document. In section 1.3, we will show that such an instrument also offers exciting perspectives for radio-astronomy, and in particular the detection of Fast Radio Burst and other transient events, as well as for the study of the Epoch of Reionization.

This chapter is mostly based on the GRAND white paper [1] and two contributions [2, 3] written for the prospective work carried out in 2019 within the IN2P3 institute.

1.1 The case for Ultra-High Energy Cosmic Messengers

1.1.1 The puzzle of Ultra-High Energy Cosmic Rays

1.1.1.1 The quest for UHECRs

In 1991, a particle of cosmic origin was detected with the Fly's Eye experiment with an estimated energy of $3.2 \cdot 10^{20}$ eV [4]. This particle, now known under the name "Oh-my-God particle" remains the most energetic ever detected, and corresponds to the tremendous energy of few tens of Joules, enough to heat up a cup of coffee, or to propel a tennis ball at ∼100 km/h. This is also roughly eight orders of magnitude higher than the energy achievable in the most powerful human-made particle accelerators. This was of course an important milestone in the quest for Ultra-High Energy Cosmic Rays (UHECRs, often defined as cosmic particles with energies $E \geq 10^{18}$ eV), initiated by the pioneering work of Pierre Auger, who first intuited their existence in the late 1930's [5], and fostered by the first detection of UHECRs in the 1960's[6]. Another climax in this search was reached a decade after the Fly's Eye"Oh-my-God" event, when diverging results were obtained by the two major cosmic rays experiments at that time.

The AGASA array of scintillation detectors, covering an area of 111 km^2 in Japan, claimed [7] in 1998 that the Greisen-Zatsepin-Kuz'min (GZK) cut-off could not be observed in their data (see Fig. 1.1 left). This drop in the cosmic ray flux is a consequence of the interaction between photons from the cosmic microwave background and UHECRs of hadronic origin for energies above $10^{19.5}$ eV (see Eqs. 1.1 and 1.2). Its absence in the AGASA spectrum, combined with an isotropic distribution of the measured UHECRs directions of origin, was therefore suggesting that UHECRs could be elementary particles —photons or neutrinos for instance— produced through exotic, "top-down" scenarios associated with phenomena (super-heavy dark matter decay, topological defaults, magnetic monopoles, see [8] and reference therein for more details) taking place at energies unreachable with particle accelerators. With AGASA results, the exciting perspective that UHECRs could be used as a probe for New Physics was therefore taking shape!

Soon after however, the HiReS experiment [9] claimed that it observed the GZK cut-off in the data collected with its pair of telescopes. These were detecting the fluorescence light emitted by N_2 molecules excited by charged particles composing the air shower generated by UHECRs interactions in the atmosphere. However, HiReS's limited exposure and relative systematic offsets in the energy determination of AGASA and HiRes did not allow for a firm conclusion for a long period of time. Despite (or because of) this experimental tension, the situation at that time generated considerable excitement in the community (see Fig. 1.1 right).

It was incidentally a main driver for me to orientate my research towards this field by joining the Pierre Auger

collaboration in 2002 as a PostDoc in Karlsruhe. I indeed hoped, as many others, that the Auger hybrid detector —four fluorescence telescopes surrounding an array of 1600 Cerenkov tanks covering an area of 3000 km^2 which were being deployed at that time— could solve the mystery of UHECRs within a few years.

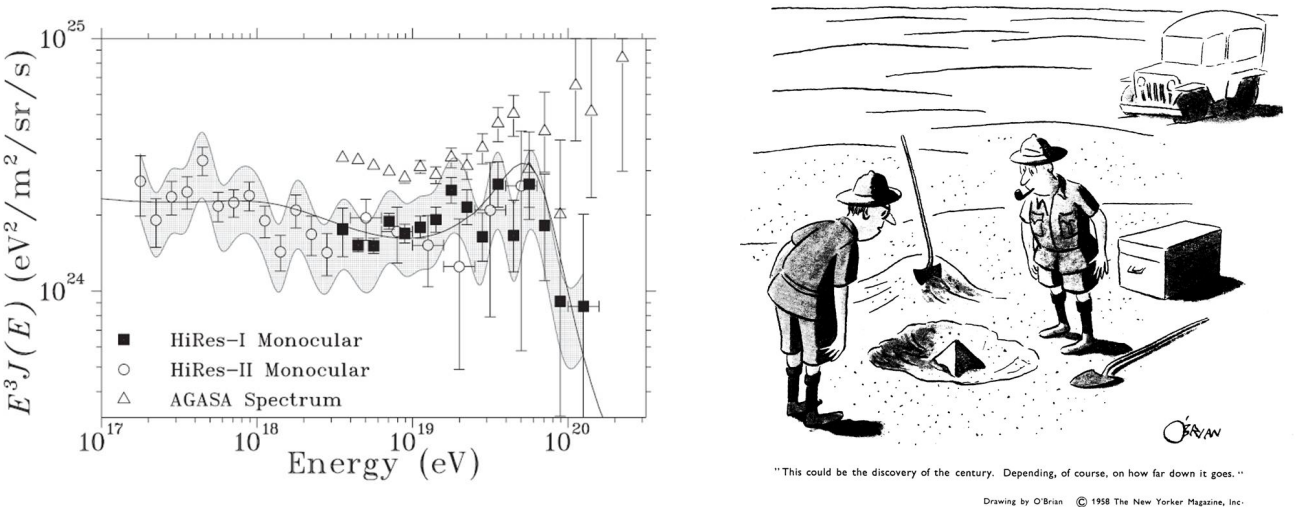

Figure 1.1: *Left: combined HiRes monocular spectrum. The squares and circles represent the HiRes-I and II differential flux J(E), multiplied by E^3. The error bars are statistical only, and the systematic uncertainties are indicated by the shaded region. The line is a fit to the data of a model of galactic and extra-galactic cosmic ray sources. The AGASA spectrum [10] is shown by triangles for comparison. Taken from [9]. Right: the exciting situation in the field of UHECRs in 2002, as presented by Murat Boratav in a seminar I attended that year.*

Fast forward to 2020: Auger did not find the answer to the origin of UHECRs, despite intense efforts. Important results were however achieved and the situation is now much clearer, though less exciting: it was in particular established that the spectrum of UHECRs drops sharply above $\sim 5 \times 10^{19}$ eV [11] (see Fig. 1.2) and that UHECRs are —at least in their vast majority— not photons [12] nor neutrinos [13], but nuclei. These results definitely discard top-down models to the benefit of bottom-up scenarios, where UHECRs are accelerated in cosmic sources, still to be identified. Recently it was established that these sources were extragalactic [14], with ∼10% of the events detected by Auger above 40 EeV pointing towards bright, close-by starburst galaxies [15].

The results of Telescope Array —the other major experiment in the field— on the spectrum, composition and directions of origin are in tension with Auger, but this could be explained by different systematic effects between the two experiments and the fact that they observe different fraction of the sky [11].

Another important Auger result in the last decade is that the average composition of UHECRs gets heavier for energies above $10^{18.3}$ eV (see Fig. 1.2). The distribution of X_{max} —maximum of shower development, see chapter 2 for details— measured with its Fluorescence Detector (FD) points towards a predominant fraction of nitrogen nuclei for energies above 10^{19} eV, with a negligible contribution of Fe [20]. The FD statistics at the highest energies are limited by its ∼10% duty cycle, but analysis of the much larger data from the Surface Detector (SD) leads to a similar conclusion [21]. Auger is upgrading its Surface Detector (SD) with plastic scintillators placed atop the Cerenkov tanks [22] in order to improve the determination of the primary nature of UHECRs, thanks to the different response of these two detectors to electrons and muons.

1.1.1.2 Challenges of UHECRs detection

We have seen in the previous section that the nature, origin and acceleration mechanisms of the most energetic particles in the Universe are very incompletely known. In view of the tremendous efforts put in the quest during the last 90

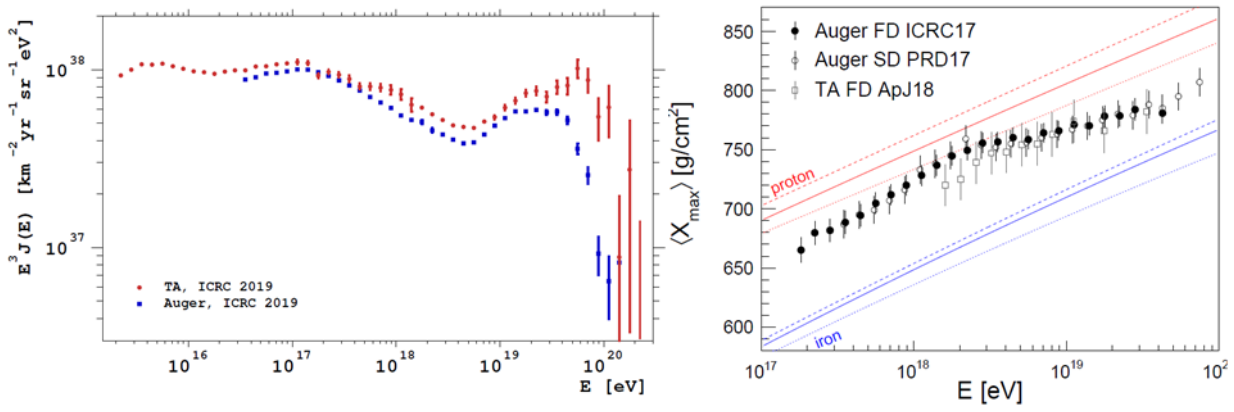

Figure 1.2: *Left: energy spectra of the Pierre Auger Observatory and the Telescope Array scaled by E^3, presented at the ICRC2019 conference. Taken from [11]. Scaling the TA points down by 5% in energy and the Auger points up by the same quantity —a value compatible with systematic errors of the two experiments— makes the TA flux compatible with Auger up to $10^{19.5}$ eV [16]. Right: measurement of the mean of the distribution of shower maximum X_{max} as a function of energy. Data points from the Pierre Auger Observatory are shown as published since they have been corrected for detector effects. Data from the Telescope Array have been approximately corrected for detector effects by shifting the mean by +5 g/cm^2 [17] and by subtracting an X_{max} resolution of 15 g/cm^2 [18] in quadrature. Furthermore, the TA data points were shifted down by 10.4% in energy to match the energy scale of the Pierre Auger Observatory. All error bars denote the quadratic sum of the quoted statistical and systematic uncertainties. The energy evolution of the mean of Xmax obtained from simulations [19] of proton- and iron-initiated air showers are shown as red and blue lines respectively. The line styles indicate the different hadronic interaction models used in the simulation. Taken from [20].*

years, knowing so little about such a fundamental question [1] is a very unsatisfying situation.

Several reasons may explain this: first, UHECRs are —at least in a vast majority of cases— charged particles. Hence they do not point back to their source because of the deflection by magnetic fields along their cosmic journey. Second, the flux of UHECRs is very low: only 1/km^2/century above $4 \cdot 10^{19}$ eV. This implies that they can be detected with reasonable probability only with setups covering very large areas (typically thousands of km^2), which can obviously be deployed on the Earth surface only. UHECRs are therefore detected indirectly only, through the so-called extensive air showers (EAS) produced by their interaction in the atmosphere. These air showers consist of a plasma of electrons, positrons, muons, photons and hadrons propagating at relativistic speed towards ground (see chapter 2 for details). In the first stages of the shower development, these particles interact at energies too large to be reproduced in accelerators. Relevant parameters of shower development —cross-sections, particle multiplicity, etc— can therefore only be extrapolated from measurements carried out at energies 10 or 100 times smaller. This very indirect process and associated uncertainties induce a sizable challenge in the reconstruction of the nature and energy of the primary UHECRs, an additional difficulty for their study. Third, while the reactions allowing to accelerate elementary particles to EeV energies are very well known from theory and experiments carried out at accelerator facilities, our knowledge about the possible sites where such phenomena could actually take place is incomplete: data are scarce, affected by large uncertainties due to the complex environment of these sources, while propagation effects affect the signals *en route* to the detector. The resulting loose constraints allow for a copious number of scenarios —all equally consistent with observations— explaining violent phenomena in the Universe.

It is therefore likely that the Auger Upgrade and its counterpart TAx4 [24] in the Northern hemisphere will not be able to give a definite answer to the mystery of the UHECRs sources. They will in particular most likely fail to collect enough statistics at energies above $5 \cdot 10^{19}$ eV and determine if the flux drop at the end of the UHECRs spectrum is due to the GZK cut-off during propagation or sources running out of steam. The fact that a significant fraction of UHECRs have intermediate mass (with Z>5) also imply that their trajectories are significantly deflected during propagation, making the identification of the individual sources nearly impossible. Finally, the limited field of view of

[1] Finding the source of UHECRs was selected as one of the eleven most fundamental Science questions of the XXIst century by the US National Research Council [23]

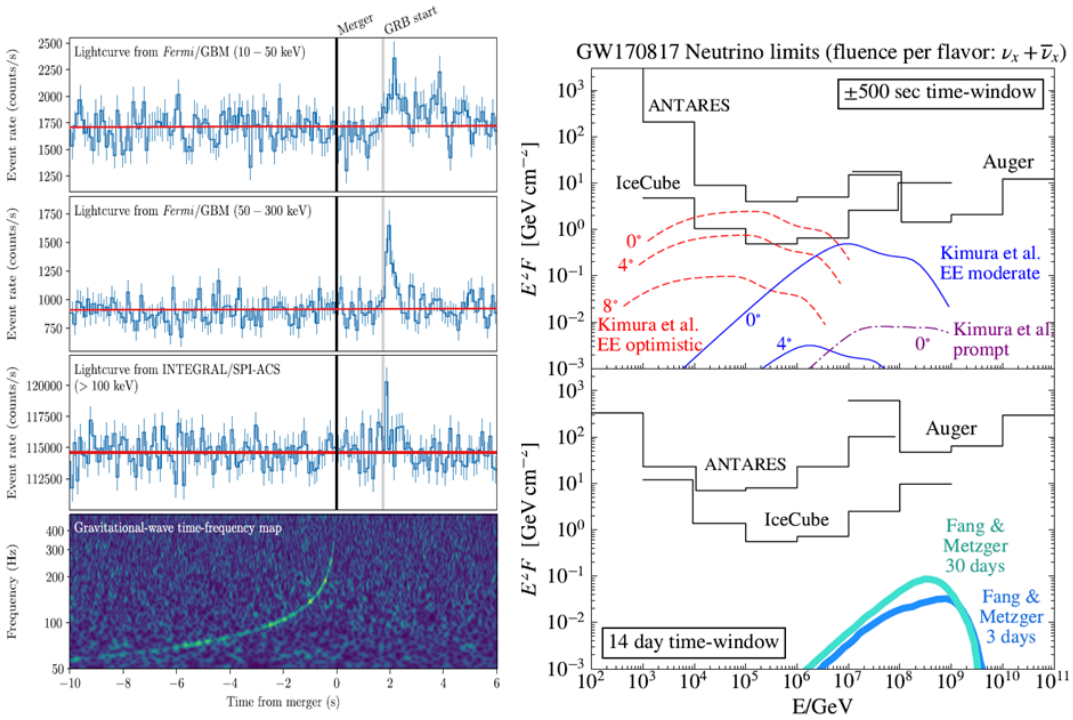

Figure 1.3: *Left: joint, multi-messenger detection of GW170817 and GRB0170817A. Top: the summed GBM light curve for sodium iodide(NaI) detectors 1, 2, and 5 for GRB0170817A between 10 and 50 keV, matching the 100 ms time bins of the SPI-ACS data. Second: the same as the top panel but in the 50-300 keV energy range. Third: the SPI-ACS light curve with the energy range starting approximately at 100 keV and with a high energy limit of least 80 MeV. Bottom: the time-frequency map of GW170817 was obtained by coherently combining LIGO-Hanford and LIGO-Livingston data. All times here are referenced to the GW170817 trigger time. Taken from [25]. Right: Upper limits (at 90% confidence level) on the neutrino spectral fluence from GW170817 during a ±500s window centered on the GW trigger time (top panel), and a 14-day window following the GW trigger (bottom panel). In the upper plot, models from [26] for both extended emission(EE) and prompt emission are scaled to a distance of 40 Mpc, and shown for the case of on-axis viewing angle and selected off-axis angles to indicate the dependence on this parameter. In the lower plot, models from [27] are scaled to a distance of 40 Mpc. All fluences are shown as the per flavor sum of neutrino and anti-neutrino fluence, assuming equal fluence in all flavors, as expected for standard neutrino oscillation parameters. Taken from [28].*

Auger and TA (which share only a small fraction of the sky, see Fig. 3.18) will also be prejudicial.

It appears clearly from the above that relying solely on UHECRs data makes it very difficult to find the sources of the highest elementary energies in the Universe, but multi-messenger observations could be a key to remove the degeneracy between models of the origin of UHECRs. This is detailed in the next section.

1.1.2 The birth of multi-messenger astronomy

Understanding the nature and origin of UHECRs is extremely difficult. Yet, an important asset in this quest comes from the fact that the production of highly energetic nuclei is tightly bound to that of other particles —γ-rays or neutrinos— through well-known particle interactions happening in the source environment (p-p or pγ processes for instance [29]) or during propagation through the GZK process. Study of other cosmic messengers thus provides an indirect but important source of information on UHECRs, allowing to constrain models.

In this perspective, significant progresses accomplished recently in fields related to UHECRs feed optimism in the community: γ-ray astronomy in particular has entered a precision era up to the highest energies with experiments such as Fermi, H.E.S.S. or MAGIC. Combination of data from these experiments together with radio and optical

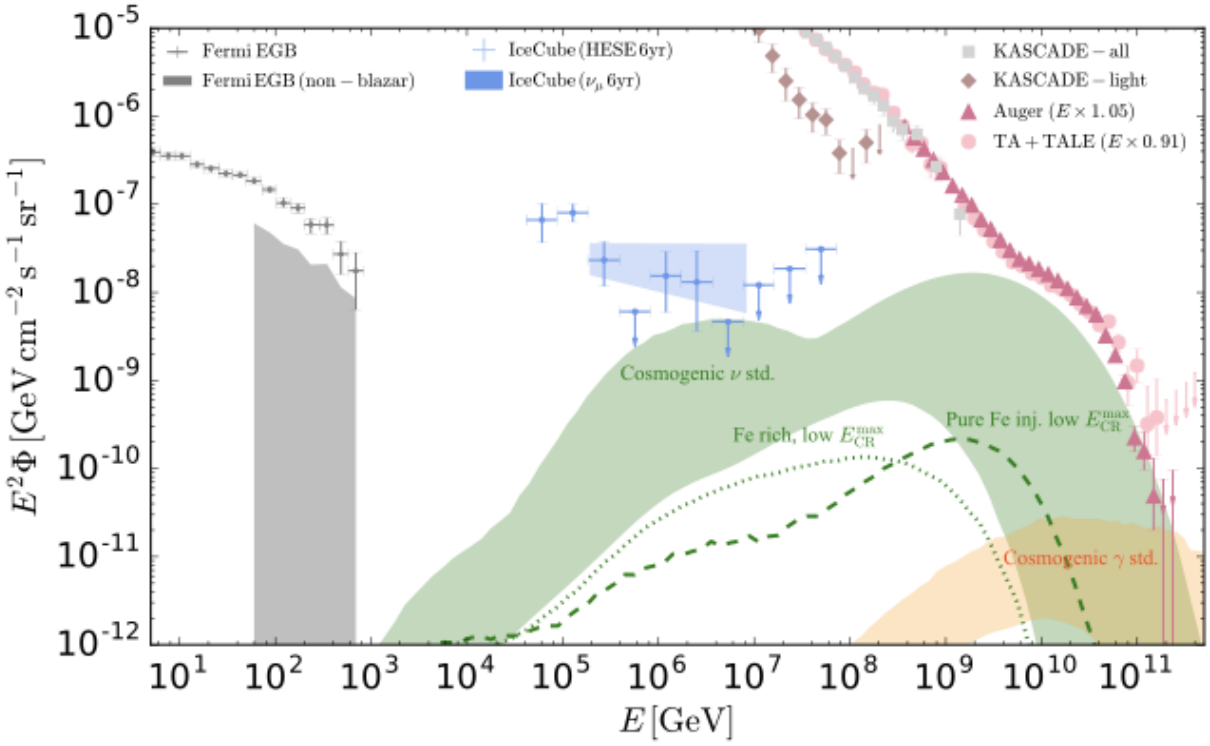

Figure 1.4: *Energy density spectra of cosmic messengers. For γ rays, we show the extragalactic gamma-ray background measured by Fermi-LAT [38, 39] and, shaded, the contribution due to unresolved, non-blazar sources. For neutrinos, we show the all-flavor 6-year measurements by IceCube [40, 41]. For cosmic rays, we show measurements by KASCADE-Grande [42], Auger [43], and Telescope Array [44]. We show the predicted ranges of cosmogenic neutrino flux from [45] and of cosmogenic γ-rays from [38]. Adapted from [1].*

observations for various Supernovae Remnants (SNRs) has for example shown unambiguously that these objects are acceleration sites for hadronic particles [30, 31]. The soft γ-rays spectra observed by these experiments however challenge the standard paradigm where SNRs are PeVatrons (i.e. sources of galactic cosmic rays up to PeV energies). They incidentally illustrate the power of combining different probes with excellent precision to eventually draw firm conclusions on complex and numerous hypotheses. Even more remarkable, two milestones in the field of astronomy were reached in the last decade, with the detection of neutrinos of astrophysical origin [32] and gravitational waves [33]. The power of combining cosmic probes is illustrated at best through the beautiful example of the gravitational wave GW170817 detected jointly by the Virgo and Ligo interferometers, and its associated GRB observed 1.7 s later by Fermi, Integral and many other instruments [34] (see Fig. 1.3). This remarkable result allowed for a giant leap in our understanding of the production of short GRBs [34, 35], the production of heavy elements [36], and more generally, violent phenomena in the Universe or cosmology [37]. No neutrinos were detected in this event [28], yet, as visible in Fig. 1.3, this negative result actually contributed to constrain GRB models and the geometry of the source [26, 27].

Experimental progress also made it possible to build a precise combined spectrum of the diffuse emission by electromagnetic radiations, neutrinos and cosmic particles (see Fig.1.4). The similar range observed for energy densities of these three messengers again highlights the strong connection of their emission process. Another striking feature of this plot is the lack of measurements at the high-energy end of the neutrino spectrum, which obviously calls for a dedicated effort: UHE neutrino detection is uncharted territory, and it is the essence of fundamental research to go for the unknown. This is one of the most basic —yet essential— motivation for the GRAND project. More elaborate reasons for the detection of UHE neutrinos are detailed in the next section.

1.1.3 Search for UHE Neutrinos

Among all cosmic messengers, neutrinos are often presented as the cleanest probe of the Universe: due to their low cross section, they can escape dense astrophysical environments opaque to photons and travel unimpeded over cosmological distances, allowing direct observation of sources at high redshifts. Unlike cosmic rays, they are not deflected by magnetic fields and can be observed in spatial and temporal coincidence with photons and gravitational waves.

Neutrinos of energies above 10^{17}eV —called Ultra-High Energy neutrinos in the following— present additional attractive features for the understanding of violent phenomena in the Universe, whether they are produced by UHECRs during their propagation through the GZK effect or directly at the source.

1.1.3.1 Cosmogenic neutrinos

A diffuse flux of cosmogenic neutrinos is guaranteed to exist, produced through the GZK effect already mentioned in section 1.1.1.1. If the UHECRs are protons, the GZK reactions are:

$$\gamma + p \longrightarrow \Delta^+ \longrightarrow p + \pi^0 \tag{1.1}$$

or

$$\gamma + p \longrightarrow \Delta^+ \longrightarrow n + \pi^+ \tag{1.2}$$

where the target photon can be associated to CMB or extragalactic background light (EBL). So-called *cosmogenic* neutrinos are produced by the subsequent decay of the charged pions

$$\pi^+ \longrightarrow \mu^+ + \nu_\mu \text{ followed by } \mu^+ \longrightarrow e^+ + \nu_e + \bar{\nu}_\mu \tag{1.3}$$

The relative number of $\nu = \bar{\nu}$ of different flavors is therefore $(N_{\nu_e} : N_{\nu_\mu} : N_{\nu_\tau}) = 1 : 2 : 0$. This could be different in the case of nuclei of atomic number $A > 1$, for which various competing processes have to be considered for interaction with the CMB photons [46]. Yet photodisintegration of these highly energetic nuclei yields neutrino production, but at much lower rate than protons for a same energye [47], and possibly with a different flavor ratio. However neutrino oscillations redistribute the flavors, so that at Earth the relative number of all flavors should be about the same, i.e., $1 : 1 : 1$. Even if oscillation parameters are allowed to vary within standard model uncertainties, ν_τ make up no less than 15% of the flux [48].

The neutrino energy is $E_\nu \simeq 0.05 \times E/A$ for an UHECR of energy E. Cosmogenic neutrinos with energies above 10^{17}eV are thus directly linked to the end of the cosmic ray spectrum, the prominent bump observed around 10^{17} eV in Fig. 1.5 being due to photohadronic interactions of the most energetic UHECRs with the peak of the CMB spectrum. Moreover, their flux highly depends on properties of UHECRs and their sources, and thus provides a powerful handle on key parameters such as the distribution of sources with redshift, the neutrino source emissivity, the injected UHECR spectrum and the mass composition of the injected cosmic rays. Because these parameters are uncertainly known, there is a large spread in the predictions of the cosmogenic neutrino flux. The left panel of figure 1.5 shows the range of cosmogenic neutrino flux predictions at 90% confidence level as a gray area. These predictions are determined in [45] from fitting the UHECR spectrum and mass composition simulated with CRPropa [49] to those measured by the Pierre Auger Observatory [50, 51]. The predictions assume that the sources are uniformly distributed up to redshift $z = 6$ and that they emit UHECRs with the same luminosity and spectra. The conservative range in Fig. 1.5 is obtained using a generic form for the evolution of the source emissivity $\alpha(1+z)^m$; the fit favors negative source evolution, i.e., $m < 0$ [52]. The standard range in Fig. 1.5 is spanned by the fluxes generated with all other choices of source emissivity: star formation rate, gamma-ray bursts (GRB), and active galactic nuclei (AGN). The simulations neglect the effect of extragalactic magnetic fields and inhomogeneities in the source distribution, which, in reality, would increase the flux past the standard range.

Other treatments yield more pessimistic [53] or optimistic [54] predictions, but a common conclusion to these various studies is that an integrated sensitivity in the range 10^{-9} - 10^{-10} GeV/cm^2/s/sr would allow to probe deeply in the models parameter space, and at the same time significantly constrain the fraction of light nuclei in the UHECRs population [55].

1.1.3.2 Neutrinos from sources

EeV neutrinos are not only produced when UHECRs interact with background photons during propagation from their sources to the Earth, but also when UHECRs interact with photons and hadrons inside the sources themselves.

Because different classes of astrophysical sources would produce UHE neutrinos on-site on different time scales and under different production conditions, the integrated neutrino fluxes from different source classes may have different spectra. The diffuse neutrino spectrum thus contains important information about the dominant source class. The right panel of figure 1.5 summarizes predictions of the diffuse fluxes of EeV neutrinos from astrophysical sources, including AGNs [56], GRBs [57], galaxy clusters [58, 59], pulsars and magnetars [60]. An upper-bound on the expected neurino-flux was directly derived from the observed cosmic-ray flux [61] with a minimal set of hypothesis on the production mecanisms of neutrinos at source. Though debated [62, 63], the so-called Waxmann-Bahcall bound, given by $E^2dN/dE = 0.3 \cdot 10^{-8}\mathrm{GeV}^2/\mathrm{cm/s/sr}$, is often used a reference. In any case, an experimental sensitivity in the range 10^{-9} - 10^{-10} GeV/cm^2/s/sr would allow to probe a large number of models.

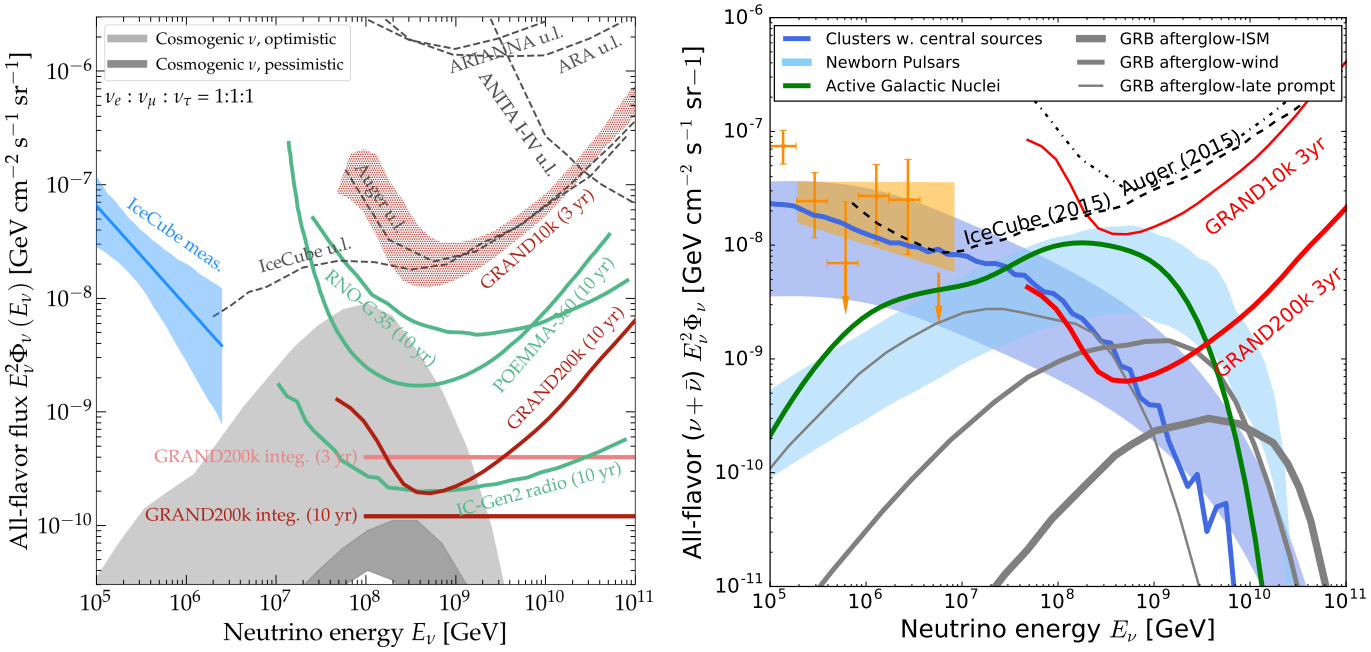

Figure 1.5: *Left: predicted cosmogenic neutrino flux, compared to experimental upper limits and sensitivities. Gray-shaded regions are generated by fitting UHECR simulations to Auger spectral and mass-composition data [45]. See the main text for details. The astrophysical neutrino signal below 3 PeV was reported by IceCube [64]. We also show the upper limit (90% C.L.), from IceCube [65], Auger [66], ANITA [67], ARA,[68] and ARIANNA [69]. Projected 3-year sensitivities of the 10 000-antenna array GRAND10k, and the full 200 000-antenna array GRAND200k are shown together with other planned instruments such as POEMMA[70] (assuming full-sky coverage), RNO-G [71] and IceCube-Gen2 [72]. As detailed in section 3.2.2, the GRAND10k band is spanned by the choice of antenna detection voltage threshold, from a conservative threshold at the top of the band to an aggressive one at the bottom of it. Plot by Mauricio Bustamante. Right: Predicted neutrino flux from different classes of astrophysical sources, compared to upper limits on UHE neutrinos from IceCube [73] and Auger [66], and projected 3-year sensitivity of GRAND10k and GRAND200k (see section 3.2.2). Expected neutrino fluxes for several source classes accounting for the observed UHECR spectrum are plotted: galaxy clusters with central sources [58, 59], fast-spinning newborn pulsars [60], active galactic nuclei [56], and afterglows of gamma-ray bursts [57]. Taken from [1].*

Recent results in the detection of prompt, highly energetic phenomena mentioned in section 1.1.2 illustrate the rise of transient astronomy, with timescales ranging from few seconds to a few days in the high energy range. To contribute to this field, it is obviously of key importance that a detector maximizes its field of view and achieves an angular resolution at a fraction of a degree.

Finally, it should be stressed that the tight link between UHECR and UHE neutrino production implies that if

neutrinos with energies larger than 10^{17} eV are detected from a given point source, then this is also a source of UHECRs. Such a smoking-gun event would be a gigantic step towards solving the mystery of UHECR origin.

1.1.4 Detection of UHE cosmic rays

The limitations of present UHECR experiments have been outlined in section 1.1.1.2. Among them, event statistics at the highest energy remains a key issue. In its 15 years of operation, Auger collected less than 300 events above $5 \cdot 10^{19}$ eV (and only 15 above 10^{20} eV [74]). To learn more by direct detection of UHECRs, the next-generation experiments must therefore collect a much larger number of events —an exposure 10 times larger than Auger appearing like an attractive target— through a much larger portion of the sky, ideally covering both Northern and Southern hemisphere in order to disentangle the discrepancies between Auger and TA mentioned in section 1.1.1.1.

Finally, the mass composition of the UHECRs is of utmost importance to understand the mechanism which accelerate UHECRs. Performances comparable to the $20\,\mathrm{g/cm^2}$ resolution on X_{max} of the Auger fluorescence telescope should be achieved.

1.1.5 Search for UHE photons

Like cosmogenic neutrinos, cosmogenic UHE γ-rays are a guaranteed by-product of photo-pion interactions of UHECRs with the CMB, through the subsequent decay of π^0 produced through the reaction given in equation 1.1. Cosmogenic γ-rays can also be generated through inverse-Compton scattering of CMB photons by electrons or positrons produced by UHECRs scattering off the CMB. Like for neutrinos, higher fluxes are expected if UHECRs are dominated by protons than if they are dominated by heavy nuclei or have a mixed mass composition. To date, UHE gamma rays have not been detected, and by constraining the photon fraction to be <0.1% of their total event rate [12], Auger rules out some of the region of photon fluxes predicted in astrophysical scenarios for a proton-dominated mass composition [75].

In addition, because gamma rays produced inside astrophysical sources point back at them, a next generation experiment for the detection of UHE cosmic messengers could detect nearby sources of UHE gamma rays, i.e., sources that lie within the mean free path of EeV gamma rays on the CMB, $\sim$10 Mpc. This is particularly attractive for searches of transient multi-messenger sources. The detection of UHE gamma rays would also probe the little-known diffuse cosmic radio background (CRB) [76], for which the energy range from 10^{19} to 10^{20} eV is optimal to constrain the impact of the CRB on UHE photon propagation.

1.2 Fundamental physics with a giant radio array

Cosmic neutrinos of ultra-high energies (E> 10^{17} eV) are unique probes of fundamental physics in an uncharted and otherwise unreachable energy and distance regime. Provided they can be detected in sufficient number, they would allow us to explore the cosmic and energy frontiers of particle physics, complementing current and future colliders. We list below various topics for which detection of UHE neutrinos would be useful.

1.2.1 Neutrino cross-section

The neutrino-nucleon cross section was measured using astrophysical and atmospheric neutrinos detected with IceCube [77, 78]. These results agree with Standard Model predictions within statistical errors (see Fig. 1.6 left). Detection of neutrinos in the EeV range would probe the cross section at center-of-momentum energies of 100 TeV, where Beyond-Standard Models (BSM) may induce significant deviation from Standard-Model predictions [79].

1.2.2 Neutrino flavor ratio

The detection of tau neutrinos by IceCube [80] is a direct confirmation that high-energy cosmic neutrinos oscillate during their cosmic journey. The predicted allowed region of the ratios of each flavor to the total flux is small according to the Standard Model, even after accounting for uncertainties in the parameters that drive the oscillations and in the neutrino production process [48]. However, mixing is untested at ultra-high energies and over cosmological propagation baselines, while BSM effects could affect oscillations, vastly expanding the allowed region of flavor ratios and making them sensitive probes of BSM [48], as illustrated in Fig. 1.6 right. It should also be stressed that measurements of

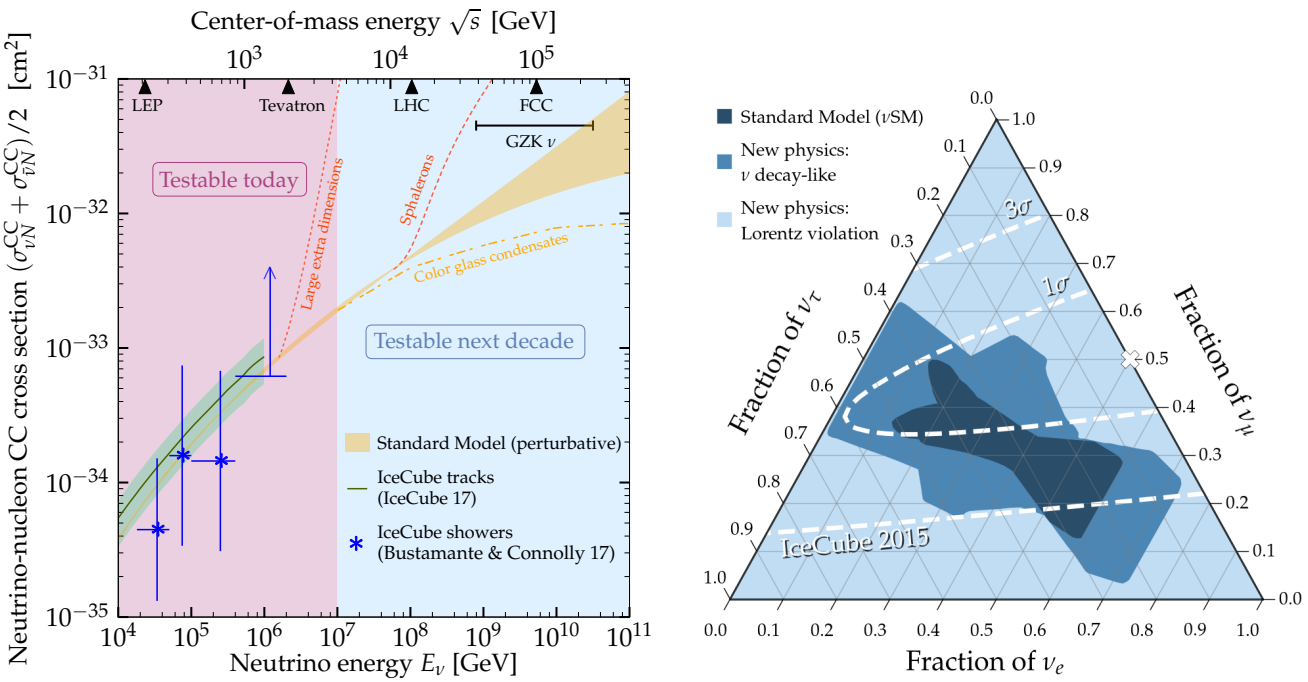

Figure 1.6: *Left: Measurements and predictions of the high-energy neutrino-nucleon cross section using IceCube data [78]. Right: Flavor composition at Earth of high-energy cosmic neutrinos, indicating the "theoretically palatable" [48] regions accessible with the Standard Model with massive neutrinos (νSM), with new physics similar to neutrino decay, and with new physics similar to Lorentz-invariance violation. The neutrino mixing parameters are generously varied within their uncertainties at 3σ. The tilt of the tick marks indicates the orientation along which to read the flavor content. Figures extracted from [81].*

the flavor ratio are free from uncertainties on the flux normalization. UHE cosmic neutrinos would therefore provide a powerful test for the nature of neutrinos and new physics.

1.2.3 Search for new physics

Numerous new-physics models have effects whose intensities are proportional to some power of the neutrino energy E_ν and to the source-detector baseline L, i.e., $\alpha\kappa_n E_\nu^n L$, where the energy dependence coefficient n and the proportionality constant κ_n are model-dependent (see details in [1]). For instance, for CPT-odd Lorentz violation or coupling to a torsion field, $n=0$; and for CPT-even Lorentz Invariance Violation (LIV) or violation of the equivalence principle, $n=1$. If neutrinos of energy E_ν coming from sources located at a distance L would be detected, then, nominally, new physics could be probed with exquisite sensitivities of $\kappa_n \sim 4 \cdot 10^{-50} (E_\nu/EeV)^n (L/Gpc)^{-1} EeV^{1-n}$. This is an enormous improvement over current limits of $\kappa_0 \leq 10^{-32}$ EeV and $\kappa_1 \leq 10^{-33}$, obtained with atmospheric and solar neutrinos [82, 83]. This holds even if the diffuse neutrino flux is used instead, since most of the contributing sources are expected to be at distances of Gpc.

UHE photons could also be used to probe open questions in fundamental physics, such as the existence of axion-like particles [84] and LIV [85]. Since models of LIV predict energy-dependent delays in photon arrival times that are linear or quadratic in the photon energy, LIV studies would benefit significantly from the detection of UHE γ-rays.

Finally, BSM could not only affect flavor or cross section as mentioned before, but also the spectral shape of detected neutrinos. Indeed neutrino energy spectra are expected to be power laws, while new physics could introduce additional spectral features, like peaks, troughs, and varying slopes. New physics models include neutrino decay [86], secret neutrino interactions [87], and scattering of dark matter [88].

1.2.4 Search for dark matter

The distribution of the direction of arrivals of measured neutrinos allows to measure the cross-section, following for instance the method detailed in [78]. It is also a way to test the presence of dark matter: interactions of neutrinos with high-density regions of dark matter would indeed modify the distribution of neutrinos' directions of arrival: a DM clump around the Galactic Center may for instance imply a deficit of neutrinos in this direction [89].

1.3 Astronomy with a giant radio array

We have seen that there is a strong scientific case for the detection of ultra-high energy cosmic messengers. We will explain in the next chapter how this could be achieved with a giant radio array working in the 50-200 MHz frequency band. Before that, we will detail how such an array could also be an attractive tool for two specific topics of radio-astronomy. As I did not take part in the associated studies, expected performances for radio astronomy of a giant radio array are only briefly presented here for the sake of completeness, while the evaluation of its potential for the detection of UHE cosmic particles is the central topic of chapter 3.

1.3.1 Detection of transient radio events

1.3.1.1 Fast Radio Bursts

Fast radio bursts (FRBs) are a recently discovered class of astrophysical transient events. They are short radio pulses, typically lasting a few ms, emitted in a broad frequency band, mostly measured between 400 MHz and 2 GHz, even though a FRB detection was also reported at 111MHz [90]. When received on Earth, the bursts are however heavily dispersed in arrival times (see Fig. 1.7) because of interactions with the free electrons along the line of sight. The delay in arrival time is $\delta t \alpha DM \times f^{-2}$, where f is the observing frequency, and the dispersion measure DM $\sim \int n_e dl$ is the column depth of free electrons. The large dispersion of DM values and the brevity of the pulses —ms scale after de-dispersion— suggests that FRBs are produced by extragalactic compact sources with sizes of a few thousand kilometers.

The first FRB was reported in 2007 [91]. Since then, many more were detected [2], especially after the CHIME [92] instrument came into operation. A few of them have been found to repeat [93, 94]. Extrapolations from present-day small-number statistics suggest that a few thousand FRBs occur every day. Their origin remains unexplained, though several possible explanations have been proposed [95, 96, 97].

The standard method to detect FRBs [98] consists in searching for prompt variation in the frequency spectrum measured over the sky with a phased radio array. As finite time synchronization performances prevent phasing of the antenna signals on a giant radio array, incoherent summing of the Fourier transforms of all antennas is the only possibility for detection. One of the advantages of this method is its very large field of view, equivalent to that of one single antenna. If in addition FRB searches can be performed with a 100% observation cycle, unmatched observation statistics could be achieved. With potentially orders of magnitude more FRBs detected than the currently available sample, a giant radio array could discover different categories of FRB-like events, with unique, repeating, chaotic, or regular signatures, nearby or at cosmological distances. The large statistics will help to answer key questions, providing insight on the space density of FRBs in the local Universe, the shape of the radio spectra at low frequencies with the possible existence of a cut-off, the dispersion of the radio signal at low frequencies or the number of FRB repeaters.

Incoherent summing allows to infer the dispersion measure, but does not locate the FRB. It also comes at a cost of a reduced sensitivity compared to an equivalent phased array, signal-to-noise ratio being then proportional to the square root of the number of antenna versus a linear scaling in the coherent case. A dedicated study of a 200 000 antennas array potential for FRB detection was performed by Valentin Decoene, a PhD student I co-advised together with Kumiko Kotera between 2017 and 2020, and Philippe Zarka, also member of the GRAND collaboration. Using single-polarization antennas and assuming that frequency measurements can be performed with 25 kHz steps in the 100-200 MHz band every 10 ms, the study shows that a 30 Jy source with a DM = 500 pc·cm^{-3} could be detected with a 10σ significance (see Fig. 1.7), assuming a flat frequency spectrum for the FRB and a noise corresponding to the galactic background (see section 2.3.1.3 for details). This translates into an event rate between 100 and 1000 day^{-1} (see [1, 99] for details).

[2] See http://frbcat.org/ for an updated list.

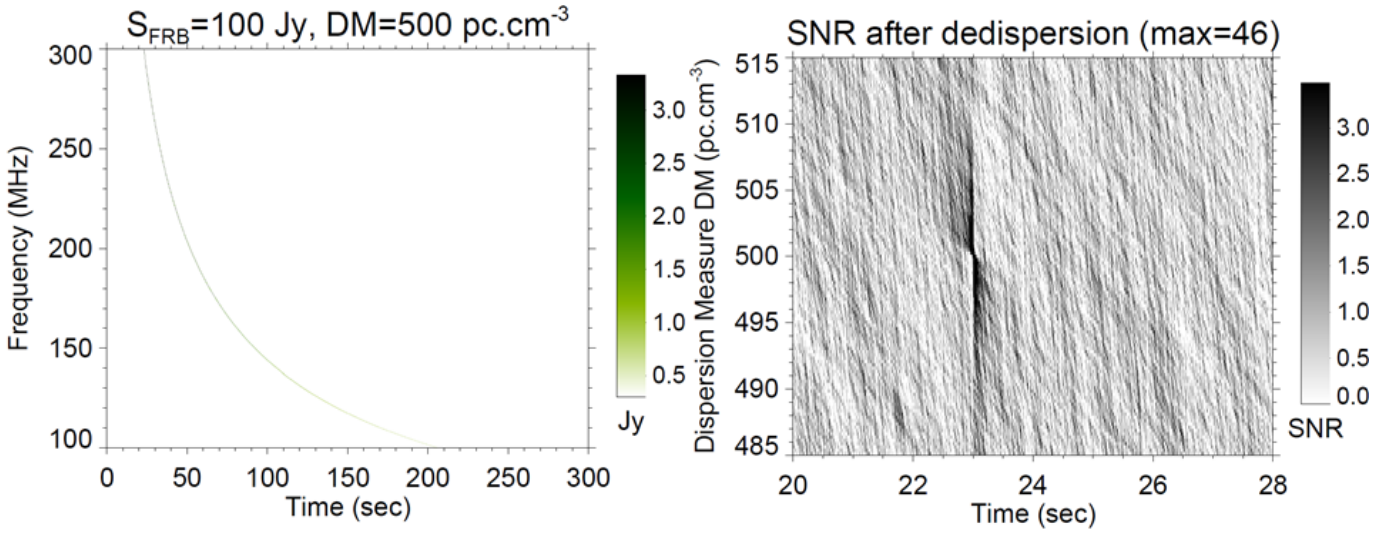

Figure 1.7: *Left: simulated FRB with a flat spectrum of 100 Jy, intrinsic duration of 5 ms, and dispersion measure of 500 pc·cm^{-3}, after being dispersed and scattered by propagation and detected with a resolution of 10 ms and 25 kHz. The dominant Galactic background noise is not shown. The dispersive drift starts at time t = 23 s in our simulation. Right: Result of a blind search for FRBs using GRAND. For each trial DM value, the dynamic spectrum is de-dispersed and integrated in frequency, and the resulting intensity profile is normalized by its standard deviation after subtracting its mean, i.e., it is displayed as a signal-to-noise ratio (SNR). The SNR is small except near t = 23 s, where it increases to reach a maximum value of ∼46 at 500 pc·cm^{-3}. Taken from [1].*

1.3.1.2 Giant Pulses

Like FRBs, giant radio pulses (GP) are transient astrophysical events: coherent, ms-long, intense, intermittent radio pulses associated to Galactic pulsars, like the Crab [100]. They are 1000 times shorter and brighter than FRBs, and have smaller dispersion measures. They are seen at frequencies from tens of MHz to a few GHz, with fluxes up to 500 kJy. Their rate is high: from the Crab, they are detected on the scale of minutes. The origin of GP is however poorly known. It has for instance been proposed that giant pulses could result from radio emission that is Compton-scattered by the electron-positron plasma of the pulsar [101], or that FRBs could be super-giant pulses in galaxies at cosmological distances [102].

GPs could be detected with a giant radio array through incoherent summing of the antenna signals, just like for FRBs. Observation in the 100-200 MHz would improve low-frequency statistics in this range, which is presently poor, and thus help improve our understanding. Similarly continuous coverage of half or more of the sky by a giant radio array —vs. a few square degrees for radio-telescopes— could discover new classes of sources of GPs that have not yet been identified because their rate is too low to be detected by pulsar surveys, e.g., < 1 hr^{-1} or < 1 day^{-1}. Simulations similar to those carried out for FRBs yield a SNR = 42 for a GP of fluence equal to 1 Jy·s and DM = 57 pc·cm^{-3} corresponding to the Crab dispersion measure. See [1] for details.

1.3.2 Study of the Epoch of Reionization

The Universe remains largely unknown between redshifts $z = 1100$, corresponding to the surface of last scattering, and $z = 6$, the end of the Epoch of Reionization (EoR). At redshifts $z > 20$ —the Dark Ages— the only radiation in the Universe was from CMB photons and those emitted by the hyperfine transition of the 21-cm spin state of neutral hydrogen. At $z = 20$ —the beginning of the EoR, also dubbed the Cosmic Dawn— the first generation of stars appeared. Through $z = 6$, stars ionized neutral hydrogen. The 21-cm line from the Cosmic Dawn imprinted itself onto the cosmic radiation background as a line-like absorption feature, redshifted today to frequencies between 10 and 200 MHz, depending on the moment when reionization occurred.

Thus, measuring the 21-cm signal would reveal how the Universe transitioned from a dark phase to a bright phase, how the growth of large-scale structure changed from the linear to the non-linear regime, and how baryonic matter

became preeminent in the formation and evolution of cosmic structures [103]. Direct imaging of ionized regions [104] and statistical studies of brightness fluctuations in the 21-cm spectrum using interferometry [105] could measure the 21-cm cosmic signal with high sensitivity, though they are regarded as challenging observations.

Radio-interferometers such as 21CMA (see chapter 5 and [106]) or LOFAR [107] are perfectly adequate to perform such measurement and SKA [108] will also do so with unprecedented sensitivity, but a giant radio array will offer an alternative and more direct method to detect EoR. By measuring the temperature of the sky with mK precision as a function of frequency, it will reconstruct the global EoR signature and identify the absorption feature due to reionization below 100 MHz. Unlike other observables, the global EoR signature can reveal the cosmic history of neutral hydrogen. With this method, using one single-polarization antenna, EDGES [109] recently found a 500 mK-deep absorption feature centered at 78 MHz, the first claimed observation of the Cosmic Dawn. However, the depth and shape of the feature –a relatively flat plateau— differ from theoretical predictions, which has prompted possible explanations involving charged dark matter [110]. Improved measurements with a radio array will help decide between competing hypotheses. A computation carried out by Wu XiangPing, co-spokesperson of the GRAND project, and presented in [1], shows that a resolution down to 1 mK could be achieved using 30 antennas only. This however requires that each antenna is calibrated down to this level of precision, and that this calibration is monitored over long period of times. This could prove to be a challenging task.

1.4 Detector wish list

We will conclude this chapter by summarizing the features of a next-generation detector required to contribute to the science case presented in this chapter:
• As UHE neutrinos have been identified as a key tool to determine the origin of the most energetic particles in the Universe, the detector should in priority reach a sensitivity in the range 10^{-9} - 10^{-10} GeV/cm^2/s/sr. This is a necessary condition to probe most models of neutrinos production, and probably a sufficient one to detect cosmogenic neutrinos within a few years.
• This sensitivity should be reached for neutrinos energies down to 10^{17} eV in order to probe models for source emission in particular. Bringing the threshold below this value would however be extremely valuable, as it would significantly increase the number of detected events (neutrinos spectra are expected to be steep, typically $\propto E^{-2}$), allow to probe other models of UHE emission and fill the energy gap with experiments such as IceCube or KM3Net.
• The detector should obviously cover the largest instantaneous field of view, which would in particular be decisive for the search of transient events.
• An angular resolution below 0.1° on the direction of origin of the detected neutrinos would additionally allow for neutrino astronomy, a key feature in the context of multi-messenger astronomy.
• The measurement of the neutrino energy would eventually allow to determine its spectrum, a key ingredient to disentangle the various hypothesis for their sources.
• The detection of the three neutrino flavor is obviously necessary to study flavor ratio at the highest energies, which could open a window on physics beyond the Standard Model.

In addition to neutrinos, the detector should also search for UHECRs and UHE γ-rays, as a strong science case exists for these messengers as well. These require:
• An extremely large exposure, typically ten times that of Auger. It is yet foreseen that this will be redundant with the above-mentioned request on the neutrino sensitivity, which will also require gigantic detection areas.
• An excellent determination of the nature of the primary particle, at the level of $\sim$20 g·cm^2 on X_{max}. This should allow a deep insight on the composition of UHECRs at the highest energies, as well as a good identification of γ-rays and neutrinos.

We will see in the next chapters that radio detection in the 50-200 MHz complies with (most of) these constraints, provided that the array of antennas is deployed on sufficiently large areas. This thus opens the door to radio-astronomy, if additional constraints can be latched. We think in particular about:
• Search for Fast Radio Burst and Giant Pulses, provided that frequency spectra can be computed at a 10 ms pace with 25 kHz frequency step.
• Study of the Epoch of Reionization, if the calibration of the individual antennas can be performed and monitored over time with a $\sim$mK precision.

Chapter 2

Detection of UHE cosmic particles

We have detailed in chapter 1 the appealing science that would be accessible through the detection of ultra-high energy cosmic particles. In this chapter, we will present some of the experimental methods envisioned in order to achieve this goal, focusing in particular on the most elusive cosmic messenger, the neutrino. We will briefly see how dense targets (ice in section 2.1 and rock in section 2.2) and very large detectors led to very competitive solutions to solve the double challenge of very low cross section and flux, and eventually allowed the detection of the first neutrinos of astrophysical origin less than a decade ago. We will then detail in section 2.3 how radio antennas deployed on Earth surface may also allow us to detect neutrinos, thus opening the door for giant radio arrays dedicated to the search of UHE cosmic messengers, as will be detailed in the following chapter.

2.1 In-ice detection of UHE neutrinos

2.1.1 Detection methods

A neutrino interacting in ice initiates a shower of secondary particles (electrons, positrons, muons, hadrons, as will be detailed in section 2.2.1.3) which develops over a few meters —with a lateral extension in the centimeter range— before it is eventually absorbed.

The charged particles from the shower propagate at relativistic speeds in the dielectric ice medium and thus emit a broadband electromagnetic radiation through the Cerenkov effect. This radiation adds up coherently around a cone which opening angle with respect to the propagation direction is given by $\cos\theta_C = 1/n$ ($\theta_C \sim 55^\circ$ at $\sim$200 MHz in ice). Thanks to the surprisingly [111] good optical properties of deep ice, the faint Cerenkov flashes can be seen by photo-multipliers at distances up to hundreds of meters. With photo-multipliers deployed along strings composed of hundreds of optical modules, reconstruction of the shower geometry becomes possible through triangulation, eventually allowing an estimation of the neutrino direction of origin as well as its energy. This is illustrated in the left panel of figure 2.1 with one of the first neutrino events detected above PeV energies. The dominant background of the targeted cosmic neutrinos are high energy muons and neutrinos produced by cosmic rays in the atmosphere. The former can be efficiently rejected by selecting events starting inside the detector volume (so-called **High Energy Starting Events** or HESE in IceCube), while the latter correspond to a spectrum softer than what is expected from astrophysical sources (see Fig. 2.2).

Similar methods are implemented by the ANTARES [112] and KM3Net [113, 114] projects using the water of the Mediterranean sea as the target volume.

A related method for in-ice neutrino detection relies on the so-called Askaryan effect: as atomic electrons in the ice are dragged in the shower through Compton, Bhabha or Moller scattering while some positrons annihilate, a $\sim$20% excess of negative charges builds up in the shower. This time-varying net charge leads to an electromagnetic emission [115], coherent along the Cerenkov cone for wavelengths larger than the shower size ((larger than $\sim$10 cm, corresponding to frequencies below $\sim$3 GHz). This radiation is detectable thanks to radio antennas operating in the hundreds to thousand of MHz because of the $\sim$1 km attenuation length, forming an economic alternative to photo-multipliers (see right panel of figure 2.1). The Askaryan effect was observed thanks to dedicated experiments at the SLAC particle accelerator at the beginning of the century [116].

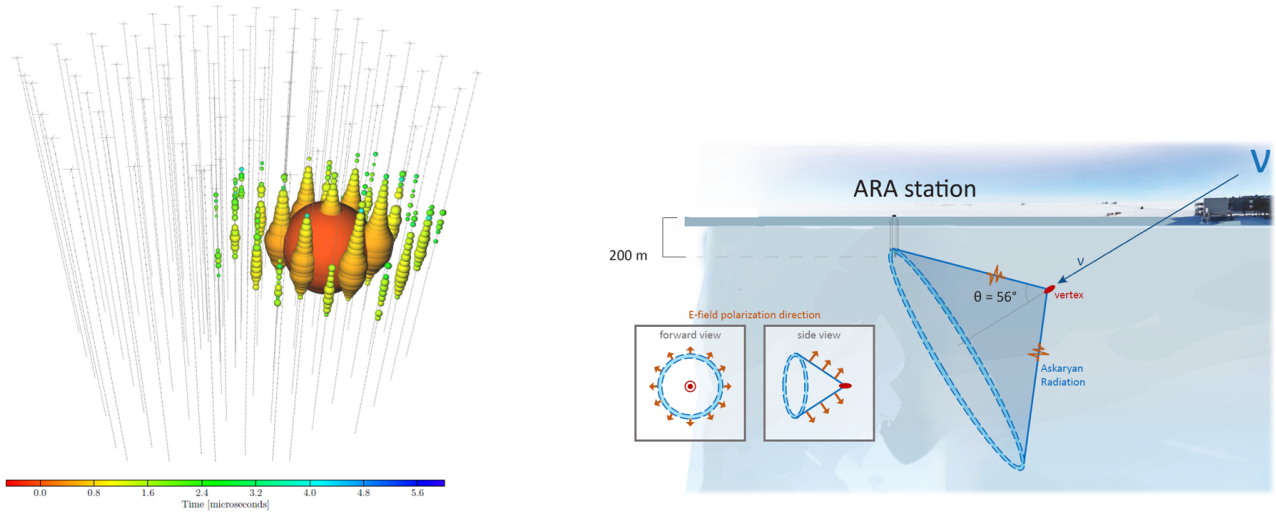

Figure 2.1: *Left: display of an event detected by the IceCube detector. The volume of each sphere is proportional to the light received by the corresponding optical module, while the color indicates its relative timing. The initial energy deposit obviously takes place inside the detector volume, allowing to tag it as a neutrino candidate. The deposited energy was estimated to 1.1 PeV, making this event, dubbed Ernie, one of the most energetic neutrino detected by IceCube. Taken from [32]. Right: principle of in-ice radio-detection of UHE neutrinos, illustrated with the example of the ARA project (see section 2.1.2 for details). The insets show how the Askaryan emission and its polarization would be observed if seen along, and perpendicular to, the shower axis. Taken from [68].*

2.1.2 Experimental status

In 2013, the IceCube collaboration announced the discovery of neutrinos of astrophysical origin [32] in its cubic-kilometer detector composed of 86 strings of optical detectors deployed at depth between 1450 and 2450 m below the South Pole. This claim relied on the detection of 28 High Energy Starting Events with energy deposits larger than 30 TeV between May 2010 and May 2012. The number of events expected from atmospheric backgrounds in that period of time was $10.6^{+5}_{-3.6}$ events according to simulations. This initial result was confirmed by later observations (see Fig. 2.2), bringing the number of HESE events to a total of 102 after 7.5 years of observations [117].

As already mentioned in section 1.1.2, this result surely represents a major milestone in the history of astronomy, opening a third window on the Universe, after electromagnetic radiation centuries ago, and cosmic rays decades ago, and few years before gravitational waves were detected [118]. IceCube has already provided a wealth of information on high energy phenomena in the Universe and the nature of neutrinos (see [119] and [120] for two examples among others) and will surely continue to do so in the coming years. Yet, it should be pointed that only three events were detected with energies in excess of 1 PeV in its 7.5 years of operation. The IceCube analysis yields the best limit on the diffuse flux of neutrinos at energies beyond PeV energies (see Fig. 2.2 right), while the Gen2 upgrade [72] of the IceCube detector is foreseen to increase its acceptance at the highest energies. Still, it is probably fair to say that an optical detector is not best suited to instrument the gigantic volumes requested for the observation of the high energy tail of the neutrino spectrum.

The radio-detection technique has been proposed to tackle this instrumental issue. The ARA (Askaryan Radio Array) and ARIANNA (Antarctic Ross Ice shelf ANtenna Neutrino Array) projects proposed, after the pionnering work by RICE [121] to deploy detection units composed of several antennas each, for a total area of a few hundred square-kilometers and several kilometers between two units. Few years of data taking with a pair of ARA [68] and several ARIANNA [69] stations have already achieved respectable sensitivities to neutrinos with energies higher than 10^{16} eV (see Fig. 2.2 right).

These results, and the scalability of the in-ice radio technique to larger size, clearly establish it as the most mature alternative for future detectors of UHE neutrinos, such as the IceCube-Gen2 radio array [72] or the Radio Neutrino

Observatory in Greenland [71].

Yet if the beautiful IceCube results indicate that the extreme polar environment could be manageable for giant radio arrays, two obstacles might however handicap this approach in my opinion:

• First, some experimental results suggest that inhomogeneities or defaults of the ice structure result in a complex or unforeseen propagation path for the radio signal, which would then affect the reconstruction of the radio signal propagation [122] back to the neutrino interaction point. It is also suggested in [123] that substructures in the ice volume could explain the detection by the balloon-borne experiment ANITA of two events with clean neutrino signatures [124, 125] with energies too high to be consistent with their large emerging angles for standard hypothesis on the neutrino nature and cross-section.

• Second, a precise reconstruction of the direction of origin of a detected neutrino is challenging. Because the radio wave is highly beamed around the Cerenkov cone (see Fig. 2.1), in most cases only a single detection unit is hit, and the limited distance —few tens of meters at most— between antennas in that unit result in a poor angular resolution. The achievable resolution strongly depends on the total number of antennas with signal, the distance to the vertex or on the chance probability that a reflected signal is also detected, but values significantly below 1° seem to be out of reach with present reconstruction algorithms and detector designs [126, 72, 127]. This level of performances would impede the possibility to point towards individual astrophysical sources, hence limiting the potential of the technique for neutrino astronomy.

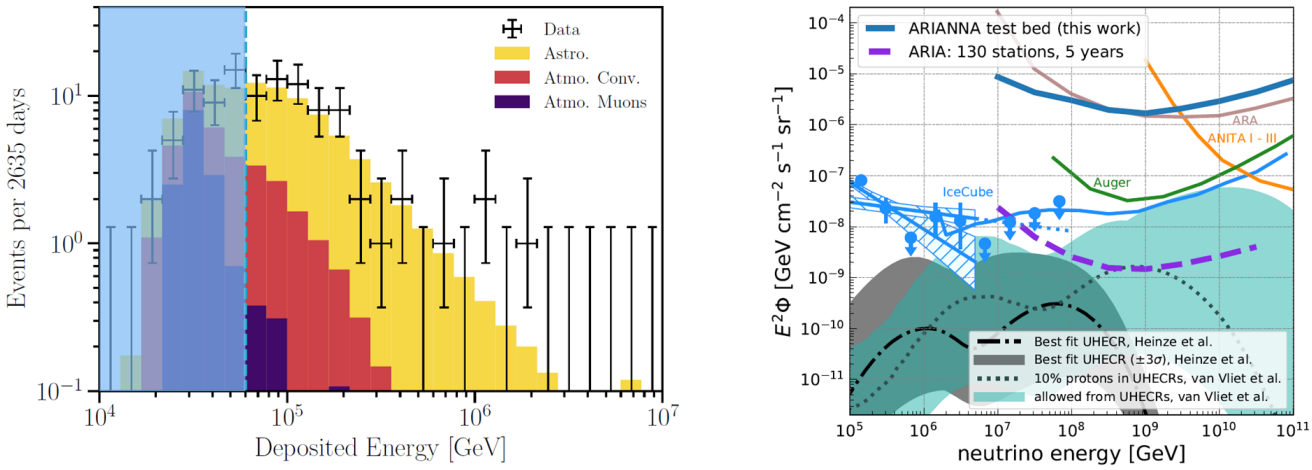

Figure 2.2: *Left: distributions of HESE events (crosses) and expected event counts for atmospheric muons (purple) and neutrino (orange) backgrounds, and best fit for a single power law for neutrinos of astrophysical origin (yellow). Taken from [117]. Right: model independent limit on a diffuse neutrino flux obtained by ARIANNA [69] (blue) and ARA [68] (brown) with 4.5 and 4 years of data taking respectively. Also shown in light blue are the IceCube observed flux [128] and limits at energies larger than* 10^{15} *eV for IceCube [129] and Auger [66]. Taken from [69].*

2.2 Detection of neutrino-induced air showers

A natural alternative to in-ice detection consists in using the atmosphere as the target for neutrinos and detect the induced air showers. As detailed below, the interaction cross-section of neutrinos with matter is however too low to induce a significant event rate, except for energies larger than 10^{19} eV typically [66]. Below this value, a denser target is needed. In a 3-pages conference proceeding, Fargion *et al.* [130] suggested in the late 1990's that tau neutrinos with energies higher than 10^{17} eV could undergo charged current interactions with rock atoms in the volume of mountains, and that the daughter tau leptons could eventually emerge in the atmosphere (above "canyons or deep valleys"), where their decay would induce inclined air showers which could be detected thanks to fluorescence light emitted by N_2 atoms from the atmosphere excited by the shower development. We will detail below this detection principle and its

experimental status.

2.2.1 Principle

2.2.1.1 UHE neutrino interaction in Earth

Reference [78] provides a synthetic and comprehensive introduction on the topic of neutrino interaction with matter at high energy: "above a few GeV, neutrino-nucleon interactions are typically deep in-elastic scatterings (DIS), where the neutrino scatters off one of the constituent partons of the nucleon - a quark or a gluon. In both the charged-current (CC, $\nu_l + N \to l^{\pm} + X$) and neutral-current (NC, $\nu_l + N \to \nu_l + X$) forms of this interaction, the nucleon N is broken up into partons that hadronize into a final state X. The final-state hadrons carry a fraction y —the inelasticity— of the initial neutrino energy, while the final-state lepton carries the remaining fraction $1 - y$. Calculation of the cross section $\sigma_{N\nu}$ requires knowing the parton distribution functions (PDFs) in the nucleon." This is the case with satisfying previsions only for neutrino energies up to ∼PeV energies. Beyond this value, calculations rely on extrapolations, and even assuming that only standard physics processes are at play, different assumptions in the computations result in factors-of-a-few differences in the cross-sections at energies of 10^{20} eV (see Fig. 1.6). All agree however that at ultra-high energies, the CC and NC cross-sections vary as a power of neutrino energy:

$$\sigma_{\nu N} = \sigma_0 \left(\frac{E_\nu}{1\,GeV} \right)^{\alpha} \tag{2.1}$$

and that there is no difference between neutrinos and antineutrinos. Reference [131] quotes values $\sigma_0 = 5.53 \times 10^{-36}\,\mathrm{cm}^2$ for CC, $\sigma_0 = 2.31 \times 10^{-36}\,\mathrm{cm}^2$ for NC and in both cases $\alpha = 0.363$. These cross-sections translate into interaction lengths in rock of 6 000 km at PeV to a few hundred km at EeV. This means that the Earth is opaque to UHE neutrinos, a characteristic which will have significant experimental implications, as we will see below.

As the hadron shower induced by a NC interaction is absorbed in a meter-thin layer of rock, only CC interactions are of direct interest in the case we are concerned with. However, the daughter neutrino of a NC interaction could later undergo CC interaction and thus contribute to the detectable signal. Because of this neutrino beam regeneration process, NC interactions should not be ignored when simulating neutrino detection.

Computation of CC interactions inelasticity results in broad distributions which shape varies marginally with energy (see left panel of figure 2.3), and an average value $< y >$ in the 0.1-0.3 range, again depending on the calculation hypothesis [132, 133]. Again, no significant difference between neutrinos and anti-neutrinos is expected at these energies.

2.2.1.2 Lepton propagation and decay

Once the associated lepton is produced through neutrino CC interaction, it loses energy in matter, a process usually described by the following equation:

$$\frac{dE}{dX} = \alpha + \beta E \tag{2.2}$$

where X is the column depth of the material in which the charged lepton propagates, E its energy, α a coefficient associated to ionization processes and β to Bremsstrahlung, pair production and photo-nuclear interactions. At the highest energies of interest here, ionization is negligible for all leptons. For electrons, the large value of β^{brem} leads to a range —the average distance traveled by the particle of a given initial energy before being stopped— smaller than one meter. Hence the probability that an electron neutrino converted in rock induces a detectable signal in the atmosphere can be neglected.

As β^{brem} varies like the squared inverse of the lepton mass (inverse of the mass for β^{nuc} and β^{pair}), muons — and even more taus, with a mass ∼4000 times larger than electrons— are much more penetrating. Bremsstrahlung, pair production and photo-nuclear interactions contribute similarly to the muon energy loss at energies above PeV, while for taus, Bremsstrahlung is always negligible and photo-nuclear interactions dominate for energies larger than 10^{17} eV [133]. Typical range values of few kilometers are computed for energies of 10^{17} eV or more (see right panel of figure 2.3), which means that taus have to be produced within a few kilometers from the Earth surface in order to reach it. As the mean free path of UHE neutrinos ranges between few hundred to few thousands of kms (see previous section), this implies that only Earth-skimming trajectories allow for a tau lepton emerging in the atmosphere. If we

consider a flat topography (i.e. no mountains), these correspond to upward-going trajectories at the emergence point. We will see in chapter 3 however that mountains should also be considered as a significant target (see Fig. 3.17 in particular).

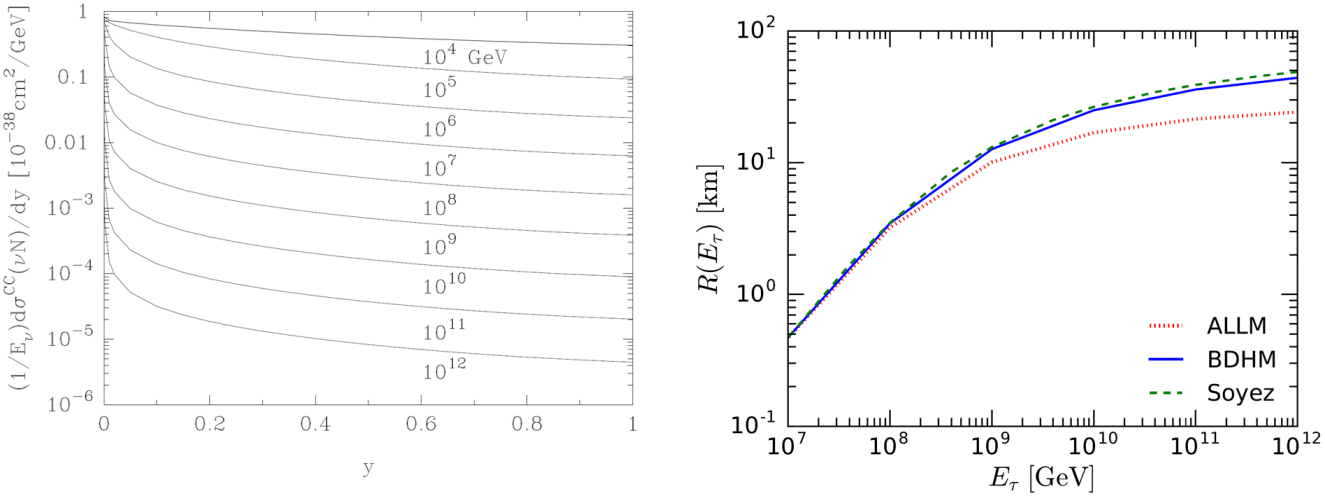

Figure 2.3: *Left: differential cross section $d\sigma/dy$ of the neutrino-nucleon CC interaction as a function of inelasticity y for various neutrino energies E_ν. $d\sigma/dy$ is normalized by a factor ${E_\nu}^{-1}$ here for convenience. Taken from [132]. Right: tau range in rock, computed with different transport MC codes for phonically interactions. Taken from [133].*

If the charged lepton eventually emerges in the atmosphere, it must decay close to the Earth surface to generate a detectable signal (see below for details). For ultra-relativistic particles, the decay length is given by $L_{\rm decay} = \gamma\beta c\tau$, where γ is the particle Lorentz factor and τ its rest frame lifetime. With $\tau_\mu = 2.2$ μs, it is very unlikely that muons decay close to the ground at the energies of interest. Hence these cannot be detected with the scenario proposed in [130], and we are left with the possibility to observe tau leptons only, for which the decay length $\gamma c\tau \sim 50 E_\tau$ km (E_τ being the tau energy in EeV) is ideally suited for detection.

With a mass $m_\tau = 2.2\,$GeV, a large number of decay channels exist for tau leptons. Hadronic modes represent in total a 0.66 branching ratio, while leptonic channels $\tau^- \to e^-\nu_e\bar{\nu}_\tau$ and $\tau^- \to \mu^-\nu_\mu\bar{\nu}_\tau$ represent a 0.174 branching ratio each. The latter represents a "ghost channel", as none of these decay products is likely to induce a detectable signal. In all other cases, the daughter particles are bound to interact with atoms in the atmosphere and induce an extensive air shower. This is detailed in the next section.

2.2.1.3 Extensive air showers

The physics of air showers being detailed in numerous references —such as [134] for an up-to-date and detailed one or [135] for a synthetic overview— we will simply outline here their most remarkable features, with a specific emphasis on elements related to their electromagnetic emission, a topic of direct interest to us (see section 2.3.1).

When a highly energetic particle collides with an atom in the atmosphere, a significant fraction of its initial energy is transferred to the products of this interaction, which in turn collide, and generate more relativistic particles. This cascade effect forms a so-called **extensive air shower** (EAS), which features significantly depend on the nature of the primary cosmic particle. The two generic cases —electromagnetic and hadronic primaries— are presented separately in the next paragraphs.

2.2.1.3.1 Electromagnetic primaries If the primary particle is an electron of energy $E_0 \gg m_e c^2$, it predominantly dissipates energy in the atmosphere by Bremsstrahlung, characterized by a typical radiation length $X_0 \sim 37\,\mathrm{g{\cdot}cm^{-2}}$, corresponding to distances of $\sim$1 km at 10 000 m altitude ($\sim$300 m at 1 000 m). At high energies, each produced photon generates in turn a $e^{\pm}$ pair. The process repeats as illustrated in figure 2.5, feeding the growth of the shower.

This holds until the mean energy of the electrons drops below a critical value $E_c = 86\,\mathrm{MeV}$. Ionization then becomes the dominant process over Bremsstrahlung. The ionized electrons being non-relativistic, they don't participate in the shower, which therefore decreases in size and eventually fades.

A simple analytical description of electromagnetic EAS development was proposed by Heitler [136]. This toy model considers that at each stage of development characterized by a length λ_e, the number of particles doubles and the energy is equally shared among all produced particles. The maximum of shower development X_{max} being reached when the particles individual energy reaches the value E_c, the corresponding number of particles is simply:

$$N_{\max} = \frac{E_0}{E_c} \text{ reached at a depth } X_{\max} \sim X_0 \ln \frac{E_0}{E_c} \tag{2.3}$$

if we take $\lambda_e = X_0$. Values $X_{\max} \sim 1000\,\mathrm{g{\cdot}cm^{-2}}$ and $N_{\max} \sim 10^{11}$ particles are found for $E_0 = 10^{19}\,\mathrm{eV}$ with equations 2.3. A vertical shower induced by a 10^{19} eV γ-ray therefore requires the full atmosphere thickness to reach its maximum: the "extensive" term often associated with air shower is obviously not overused.

It may also be pointed at this stage that 90% of the total kinetic energy of its 100 billion particles is then contained within a 100 m radius. The short mean free path of photons and electrons indeed implies that the particle density drops rapidly when moving away from the shower axis (see left panel of figure 2.4). Let us be exhaustive on the dimensions of the shower by mentioning that its thickness is a few meters only, hence the name **shower pancake** to describe its shape at a given instant.

The Heitler model is of course approximate: it ignores for instance photo-hadronic interactions with atmosphere atoms, but detailed simulations with CORSIKA, AIRES or other Monte-Carlo codes show that Eq. 2.3 provides a reliable parametrization of electromagnetic showers. The logarithmic dependence of X_{max} with energy obtained with the Heitler model is in particular confirmed at first order for hadronic primaries, as illustrated in figure 1.2.

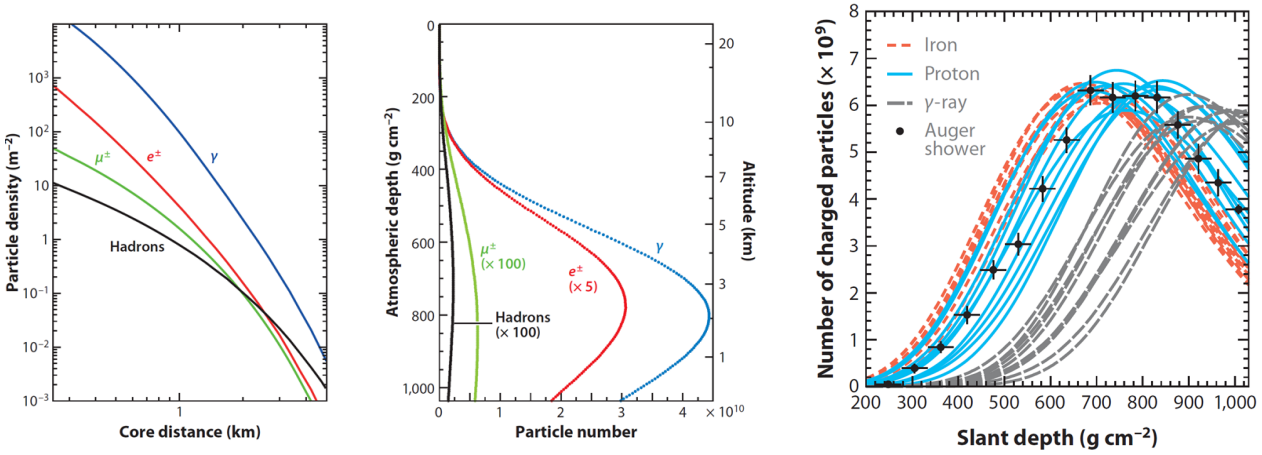

Figure 2.4: *Left and center: Average lateral and longitudinal shower profiles for vertical, proton-induced showers at 10^{19} eV. The lateral distribution of the particles at ground is calculated for 870 g·cm^2, the depth of the Pierre Auger Observatory. The energy thresholds of the simulation were 0.25 MeV for γ and $e^{\pm}$ and 0.1 GeV for muons and hadrons. Right: Longitudinal shower profiles of 10 proton, iron, and photon-induced showers of 10^{19} eV, simulated with SIBYLL. The data points correspond to one shower of approximately the same energy measured by the Pierre Auger Observatory [137]. All figures are taken from [135].*

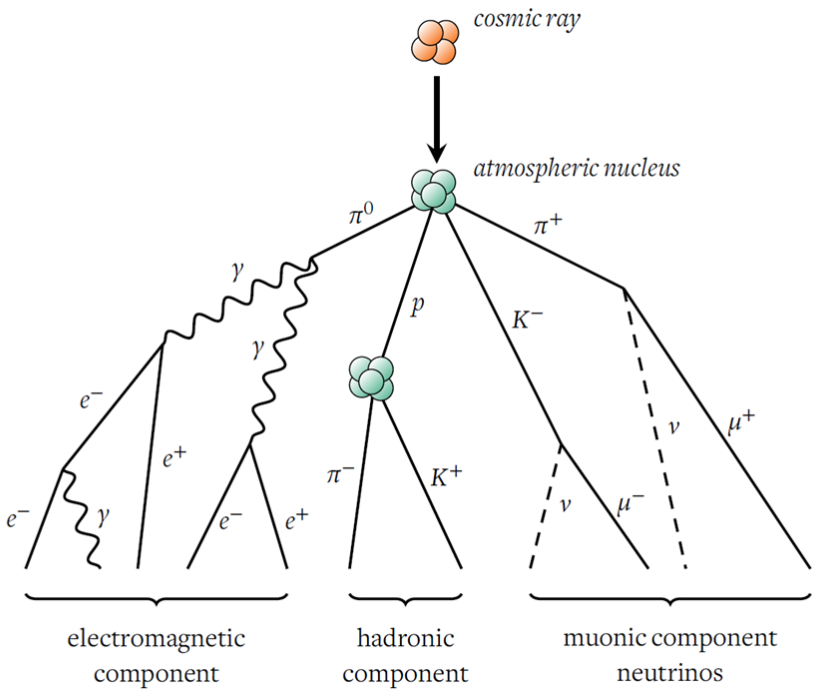

Figure 2.5: *Schematic representation of the development of an extensive air shower induced by a cosmic nucleus in the atmosphere. Note that only photons, electrons and positrons are tagged as electromagnetic particles, because muons, in a way similar to neutrinos, are not likely to interact and participate further in the shower development. Taken from [138].*

2.2.1.3.2 Hadronic primaries Things are somewhat more complicated for hadronic primaries. When a UHE proton enters the atmosphere for instance, it interacts with a nitrogen or oxygen nucleus through hadronic processes inducing nuclei fragmentation an multiparticle production. The details of the very first interactions drive the subsequent development of the shower, and their probabilistic nature thus induce significant shower-to-shower fluctuations. Cascading hadronic interactions follow, with massive production of hadrons. The high multiplicity of hadronic reactions implies that the maximum of shower development is reached at smaller depth than for electromagnetic showers (see Fig. 2.4 right). Another remarkable difference is the presence of muons (see the right panel of figure 2.5): these are produced by the decay of mesons (e.g. $\pi^{\pm} \to \mu^{\pm} + \nu_{\mu}/\bar{\nu}_{\mu}$), a phenomenon in competition with particle interaction. Relativistic time dilution implies that the former phenomenon is more frequent later in the shower development, when the mean particle energy decreases. Muons usually do not decay before reaching ground and thus propagate further away from the shower axis than electrons (see Fig. 2.4 left).

A UHE nucleus of atomic number A can be considered in a first approximation as a collection of A nucleons with individual energies E_0/A because the nucleon binding energy ($\sim$5 MeV) is negligible with respect to the energies at play in the first interactions of a cosmic primary. This implies that showers induced by iron nuclei are characterized by shallower maxima of development and smaller shower-to-shower fluctuations compared to proton showers (see Fig. 2.4 right). This also explains why heavier primaries lead to a larger fraction of muons for a same initial energy E_0, as illustrated in figure 2.6: in a sub-shower induced by an individual nucleon of energy E_0/A, light mesons indeed reach the critical energy where decay becomes more likely than interaction sooner than for a proton shower of initial energy E_0.

Unlike EAS associated with electromagnetic primaries, those induced by nuclei require the use of dedicated models based on QCD —QGSJet, SYBILL or EPOS to mention some of the most popular— to describe the hadronic interactions at the core of the shower development. A major challenge in this process lies in the fact that the energies at play in interactions initiated by UHECRs exceed those achievable in particle colliders by one order of magnitude or

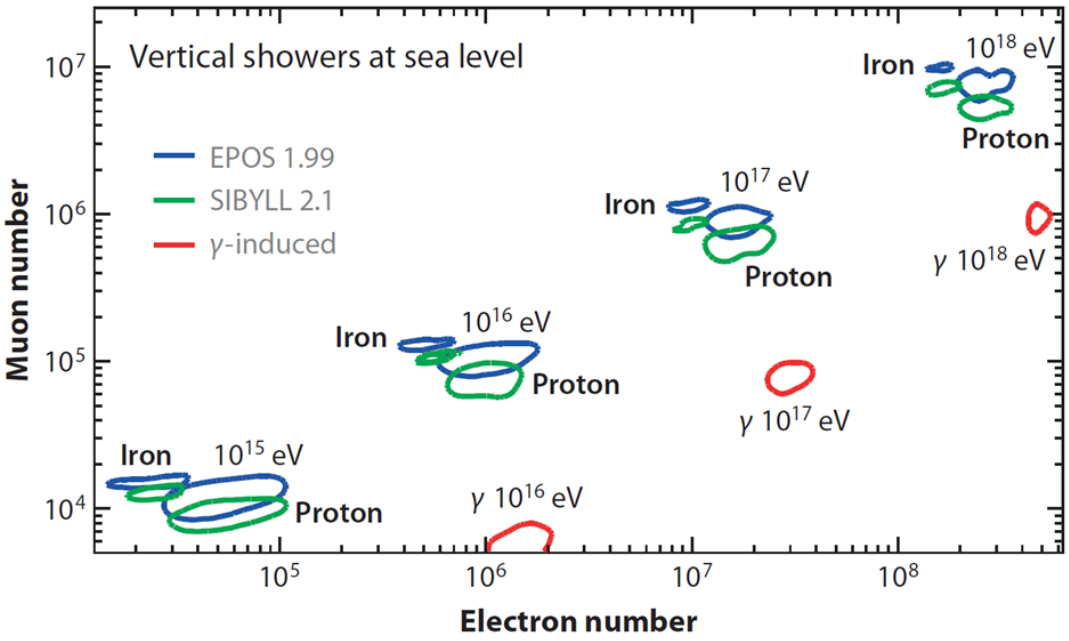

Figure 2.6: *Predictions for the correlation between the number of electrons and the number of muons at sea level for showers of different energies. The simulations were performed with CORSIKA using the same energy thresholds for secondary particles as in figure 2.4. In the case of photon primaries, muons are produced through hadronic interactions with atmosphere nuclei. Taken from [135].*

more: LHC collisions provide for instance ∼14 TeV in the center of mass, equivalent to a 10^{17} eV particle hitting a fixed target. Hadronic models may therefore be tested against experimental data at LHC energies and parameterized to adjust accelerator data at best [139], but they have to rely on orders-of-magnitudes extrapolations to model UHECR shower development. In addition, processes in the forward regions of the interaction —those relevant to describe shower development— are only marginally accessible, and only for a few dedicated experiments such as TOTEM at CERN [140]. Consequently, significant discrepancies exist on several quantities between MC simulations and these experimental measurements, the most striking being a systematic deficit of muons on the simulations [141]. This points towards a certain level of misunderstanding —or imperfect modeling— of hadronic processes.

Because of these various reasons, there are, in the case of hadronic primaries, significant systematic uncertainties in the determination of the characteristics of the cosmic particles from EAS data recorded with detectors deployed at ground. As already discussed in section 1.1.1.2, this is probably one of the major handicaps to interpret results of experiments like Auger or Telescope Array.

The decay products of a tau lepton produced by a neutrino interaction underground will generate an EAS very similar to the ones above described. A noticeable difference resides however in the fact that neutrino-induced EAS would develop in the dense atmosphere existing at low heights above ground, as only Earth-skimming, nearly-horizontal trajectories allow for a sizable probability of tau emergence in the atmosphere, as explained in section 2.2.1.2.

We have now described the full physical process going from the neutrino reaching the Earth target down to the full development of the associated EAS. We will now give a brief overview of the experimental status of the search of such neutrino-induced EAS.

2.2.2 Experimental status

The Auger experiment has pioneered the search of neutrino-induced EAS [142] with a detection principle similar to the one presented in [130]. Neutrino-induced air showers should in principle be singled out from standard ones thanks in

particular to their muon content. For very inclined trajectories targeted for neutrino searches, air showers induced by cosmic rays have gone through a layer of atmosphere thick enough so that a large fraction of electrons and photons have been absorbed in the atmosphere before reaching ground level (see e.g. Fig 7.2), so that their relative muon content is high. Neutrino-induced showers are much younger, hence their relative muon content is comparatively significantly smaller.

More than a decade of data taking yields a sensitivity limit very close to the IceCube one in the 10^{17}-10^{19} eV energy range [66] (see Fig 2.2). The Auger neutrino search however suffers from its poor detection efficiency for neutrino-induced showers: their upward-going trajectories, combined with their reduced width and strong attenuation in the atmosphere ($\sim$1000 g·cm^2 at 10^{19} eV, see previous section) indeed imply that only a small fraction of the shower has a chance to reach the Auger Surface Detector tanks. As fluorescence emission is isotropic, the upward-going showers would be detected with excellent efficiency by the Auger Fluorescence Detector. Its $\sim$10% duty cycle however severely affects its sensitivity, as I showed in a study carried out during my post-doc on Auger [143].

Alternative projects based on the fluorescence detection of neutrino-induced EAS have thus been proposed on scales much larger than Auger: NTA [144] or Trinity [145] are conceptual proposals for optical telescopes observing huge volumes of atmosphere forming a gigantic calorimeter for neutrino-induced air showers, while JEM-EUSO [146] or POEMMA[147] are proposals for space-based telescopes overlooking hundreds of thousands km^2 of Earth surface.

A third path may be considered for neutrino-induced EAS search: radio detection. Radio antennas are affordable, robust, stable detectors which are easy to deploy and maintain. They thus represent a credible option to achieve the very large detector areas requested for neutrino detection, fostering various concept studies [148] or experimental projects such as GRAND. We detail in the following the process of coherent electromagnetic emission EAS, and how radio antennas can detect it.

2.3 Radio-detection of air showers

2.3.1 Radio emission by air showers

2.3.1.1 Principles

As for in-ice showers (see section 2.1.1), a negative charge excess builds up in EAS, mainly because atmospheric electrons are picked up by the shower through Compton scattering. However the low density of the atmosphere does not allow for the negative charge ratio C_x to grow above $\sim$10% [149].

If radio emission due to charge excess is thus comparatively not as significant as for the in-ice case, other phenomena, specific to showers developing in the atmosphere, contribute to its electromagnetic radiation. These are related in particular to the Earth magnetic field, noted $\vec{B}$ throughout this document. Positrons and electrons drift in opposite directions under its influence thanks to the Lorentz force $\vec{F_L} = \pm e\vec{v} \times \vec{B}$. The Larmor radius of the corresponding trajectories is given by [150]:

$$R_L = \frac{\beta\gamma m_e c \sin\alpha}{eB} \tag{2.4}$$

We find $R_L \sim 2000$ m for typical values $\beta = 1$, $\gamma = 50$ and a geomagnetic angle $\alpha = (\vec{v}, \vec{B}) = 90°$. For a typical mean free path L of few hundred meters (see section 2.2.1.3), this corresponds to an angular deviation $\theta = L/R_L \lesssim 10°$ and an average drift velocity $< v_d >= c\theta/2 \sim 0.05c$ [150]. The effect can be neglected for muons and hadrons, because it leads to a broader Larmor radius. Radio emission is thus related to the electromagnetic part of the shower only. This can be seen as an asset, given the issues related to modeling of hadronic showers exposed in section 2.2.1.3.

The geomagnetic field thus induces a drift of elementary charges (i.e. an electric current) flowing through the dense plasma of billions of relativistic particles composing the $\sim$meter-thick shower pancake. This induces an electromagnetic radiation often referred as the **geomagnetic effect**. Calculations detailed in [150] show that it dominates by order of magnitudes both synchrotron radiation by the $e^{\pm}$ pairs and the dipole radiation due to the position offset between barycenters of the positive and negative charges. Besides, experimental results [151] indicate that the geomagnetic effect is even larger than emission by charge excess by a factor 10 typically. This ratio however varies with distance to the shower axis (see section 4.3), $X_{\max}$ height and of course the geomagnetic angle α: if the direction of propagation

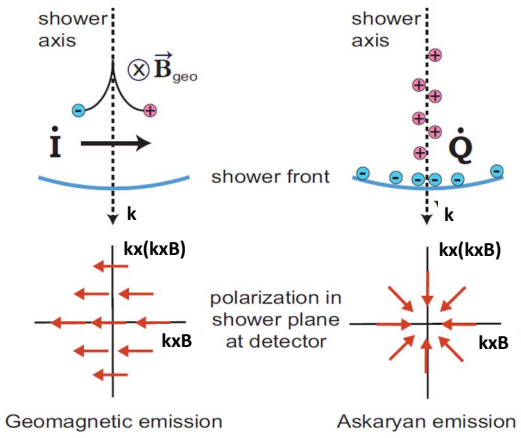

Figure 2.7: *Dominant mechanisms for electromagnetic emission by air showers. Polarization vectors are conveniently represented in the* $(\vec{k}\times\vec{B},\vec{k}\times\vec{k}\times\vec{B})$ *referential often used in this document. Adapted from [153].*

of the shower is close to the geomagnetic field orientation then the Lorentz force $\vec{F_L} \propto \vec{v}\times\vec{B}$ —hence the geomagnetic effect— is obviously negligible.

Classical electrodynamics allow to give an analytical expression for the shower's electromagnetic radiation:

$$\vec{E} = \vec{\nabla}A^0 - \frac{\partial\vec{A}}{\partial t} \tag{2.5}$$

where $(A^0, \vec{A})$ is the four-vector Liénard-Wiechert potential field. Following [150] and [152], one finds that charge excess is the dominant contribution to the first term of equation 2.5, and geomagnetic to the second. In addition, these two terms can be explicited as:

$$A^0 \sim A^{ce} = -\frac{eN_{\max}}{4\pi\epsilon_0}C_x\int_0^\infty dh\frac{f_1(t_r)f_p(h)}{R} \tag{2.6}$$

and

$$\vec{A} \sim \vec{A}^{geo} = \frac{eN_{\max}}{4\pi\epsilon_0}\frac{<v_d>}{c}\int_0^\infty dh\frac{f_1(t_r)f_p(h)}{R}\vec{u}_{v\times B} \tag{2.7}$$

where $N_{\max}$ is the number of particles at shower maximum, C_x the charge excess ratio, R the distance to the observer, $f_1(t_r)$ the longitudinal distribution function of the shower as a function of emission (or retarded) time, and $f_p(h)$ the lateral distribution as a function of height h.

Both contributions induce an electric field polarized linearly in a plane perpendicular to the direction of propagation of the shower, a result confirmed at the 1% level by simulations. However the geomagnetic contribution is polarized along the $\vec{k}\times\vec{B}$ direction, as one would expect from its Lorentz origin, while it derives from equation 2.5 that charge-excess contribution points towards the shower axis, as illustrated in figure 2.7. The two contributions will therefore interfere constructively for positive values along the $\vec{k}\times\vec{B}$ axis, and destructively for negative ones, thus generating an asymmetry in the amplitude profile with respect to the perpendicular axis $\vec{k}\times\vec{k}\times\vec{B}$. It is worth noting that for horizontal showers of interest for us, the signal polarization will be mostly horizontal because the Earth magnetic field has a predominant vertical orientation in most locations around the world (e.g. around 30° from zenith at the TREND site).

One should finally note that the emitted electric field expressed in equation 2.5 reaches macroscopic magnitudes only if the electromagnetic emission by the $e^\pm$ pairs in the shower is coherent. IF we put aside teh specific case of directiosn near the Cerenkov angle, this is the case for radiation wavelengths significantly larger than the typical dimension of the shower pancake, hence frequencies $f \ll c/d = 300\,\text{MHz}$ for shower thickness of $d \sim 1$ meter typically, as seen on the right panel of figure 2.8. Electromagnetic emissions by the above-mentioned mechanisms thus takes place in the tens of MHz frequencies range, hence the name of air showers radio emission.

2.3.1.2 Propagation through the atmosphere

The Earth atmosphere is transparent to radio waves to an excellent approximation, one of the reasons the radio technique was developed so largely. When considering emission from a point source, dilution effects only should therefore be taken into account. Energy conservation arguments lead to an amplitude of the electric field varying as the inverse of the distance to the observer, as could already be seen in equations 2.6 and 2.7.

However, when considering emission from an extended zone —as is the case for EAS— more complex effects have to be taken into account to correctly describe the signal at observer's position. It should in particular be pointed out that the emitted radiation propagates through the atmosphere at a speed $v = c/n$ where the refractive index n is a function of temperature, pressure and humidity, and thus varies with altitude h. The relation:

$$n(h) = 1 + 3.25 \cdot 10^{-4} \exp(-0.1218h) \tag{2.8}$$

fits the data at the 1% level up to 10 000 m a.s.l. [154], with h expressed in km.

The value $n > 1$ of the air refractive index has a significant effect on the radio signal received by an observed at ground level: radiations emitted at different heights along the shower —which propagates at a speed $\sim c > c/n$— will arrive at different times, thus leading to a stretch —or a compression— of the received signal, depending on the shower geometry and the relative position of the observer with respect to the shower axis (see Fig. 2.8 left).

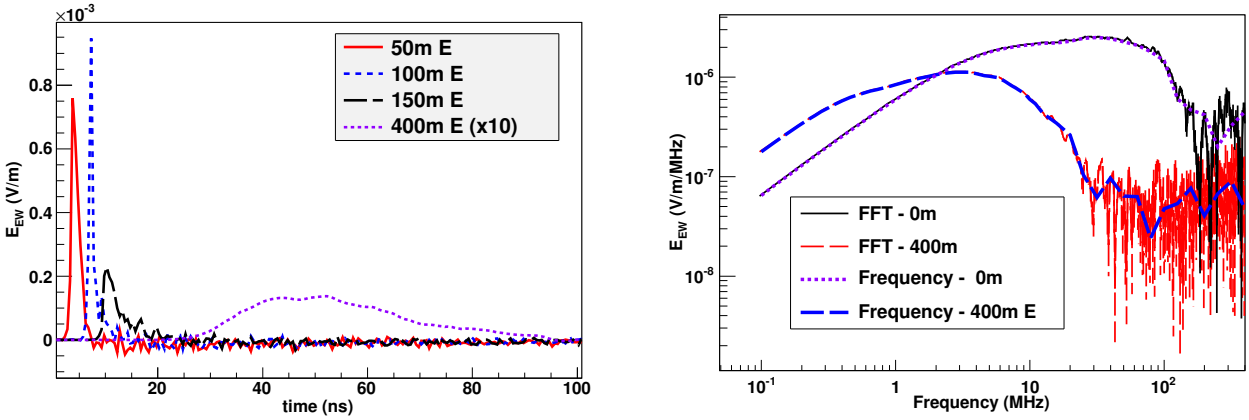

Figure 2.8: *Left: time traces of the East-West component of the electric field at distances of 50, 100, 150 and 400 m eastwards of the shower core as obtained in ZHAireS simulations of a 10^{17} eV proton-induced vertical atmospheric shower. Right: emission spectra calculated by ZHAireS in the frequency domain for the same shower at core position and 400 m East of it. Also shown in red are the analytical FFTs of the time traces. Taken from [154].*

These effects are studied in detail in [155] and [156]. Here we will simply stress that the direction of emission defined by the Cerenkov angle corresponds to a specific case where all paths lead to simultaneous arrival times. The observed pulse is then very brief and of very high amplitude, which translates into the frequency domain in a flatter spectrum, extending to higher frequencies. This enhancement of the signal along the Cerenkov cone increasing with frequency is illustrated in figure 2.9. It can be seen as a very specific signature for EAS radio emissions.

For emission angles larger than the Cerenkov value, the signal drops very quickly because of relativistic effects. The radio emission is therefore strongly beamed in a cone of angle around 0.8° at 10 000 m altitude, opening to slightly larger values for showers developing closer to the ground (see left panel of figure 2.9). The nearly horizontal trajectories of neutrino-induced showers presented in section 2.2 thus produce very elongated radio footprints at ground, as visible on the right panel of Figure 3.15. This, together with the mild $1/R$ decrease of the signal amplitude of the radio signals implies that a sparse radio array is enough to detect neutrino-induced air showers. We will see in the next chapter that 1 km^{-2} is a very good compromise. This possibility to detect showers with such a sparse array is a major asset for the radio detection of neutrinos-induced EAS, and a necessary condition for the existence of such projects, given the required detector areas.

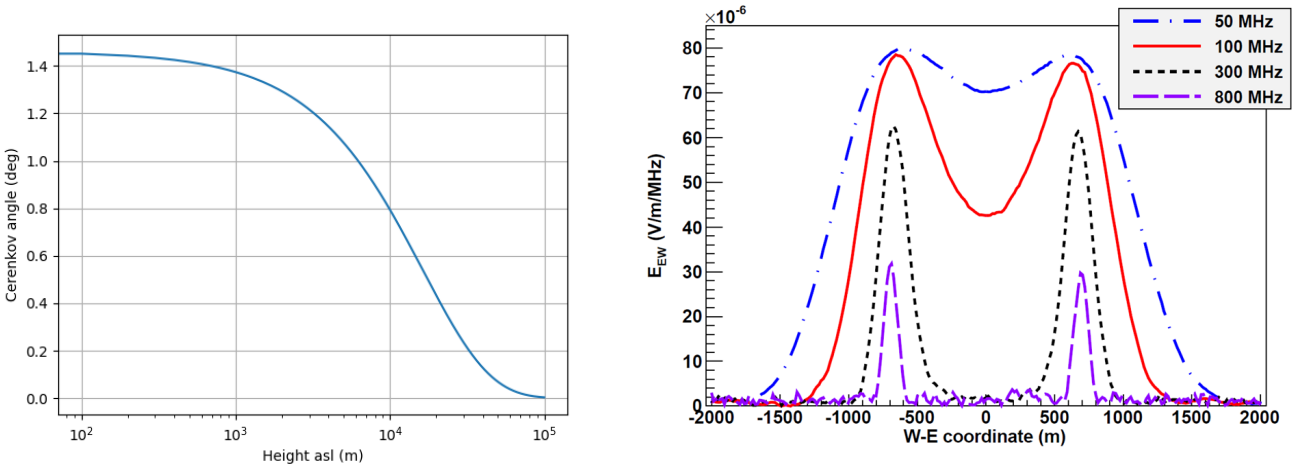

Figure 2.9: *Left: value of the Cerenkov angle calculated as* $\theta_C = \cos^{-1}\left(\frac{1}{n}\right)$ *at the average* X_{max} *height as a function of altitude. The refractive index* n *is computed here with equation 2.8. Right: Fourier components of the electric field at 50, 100, 300, 800 MHz as a function of the distance to the shower core for a* 10^{19} *eV shower coming from the North with zenith angle* $\theta = 80°$*. Antennas are placed along the perpendicular East-West axis. The enhanced amplitude density around the Cerenkov angle is increasingly visible with frequency. Taken from [155].*

The mechanisms of electromagnetic emission by air showers exposed in this paragraph are now very well understood. This allowed for the development of very reliable simulation codes, which compute the field radiated by air showers individual particles produced with Monte-Carlo simulations from electrodynamics first principles at positions defined by the user. CoREAS [157] and ZHAirES [154] for example provide radio extensions of CORSIKA and AireS respectively, and reach equivalent results [158, 159]. They are however CPU-intensive: simulating the electric-field traces of 200 radio antennas for one air-shower of primary energy 10^{17} eV and a thinning level of 10^{-4} with the ZHAireS simulation code costs about 2 hours on one node [160]. Codes using a **macroscopic** approach, such as MGMR [152, 161], basically solve equation 2.5 to determine the electric field at the observer position. They are thus much faster and achieve equivalent results [162] in most cases, but rely on simplifying hypothesis or modelisation which, for now, make them not as trusted as the **microscopic** approaches above mentioned.

2.3.1.3 Radio background sources

We briefly list here the stationary background sources to be considered for EAS radio observation.

The dominant emission in the frequency range of interest comes from diffuse synchrotron radiation by the Galaxy. The strength of this unpolarized emission varies significantly with the observed direction, with a dominant contribution coming from the Galactic plane (see Fig. 5.20). Its brightness falls steeply with increasing frequency: $B_\nu \propto \nu^{-2.55}$ [163], with full-sky-averaged temperatures varying from $T_{sky} \sim 5000\,\mathrm{K}$ at 50 MHz to $T_{sky} \sim 100\,\mathrm{K}$ at 200 MHz. Sky temperature is defined here from the Rayleigh-Jeans approximation of its brightness:

$$T_{sky} = \frac{B_\nu c^2}{2k_B \nu^2} \tag{2.9}$$

with brightness B_ν given in $\mathrm{W/m^2/sr/Hz}$ by:

$$B_\nu(\theta, \phi, \nu) = \frac{dP}{(\cos\theta d\sigma) d\nu d\Omega} \tag{2.10}$$

where dP is the power emitted in solid angle $d\Omega$ and frequency range $d\nu$, and received through the instrument collection area at ground $d\sigma$; The factor $\cos\theta$ arises from the projection into the plane perpendicular to the radiation direction

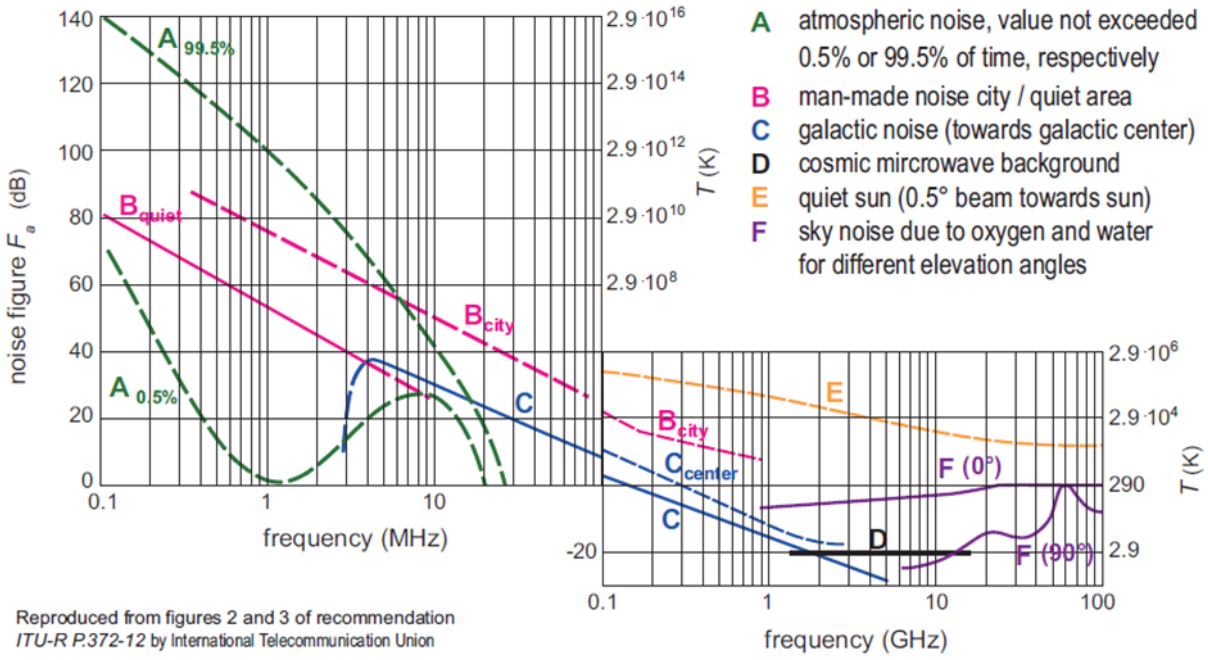

Figure 2.10: *Sources of stationary electromagnetic noise as a function of frequency, expressed as temperature T or noise figure $F = 10\log_{10}(1 + T/T_{amb})$. Taken from [1].*

of propagation. The corresponding rms value of the electromagnetic field integrated over a frequency range $[\nu_0, \nu_1]$ is then given by:

$$E_{\rm rms}{}^2 = \frac{Z_0}{2}\int_{\nu_0}^{\nu_1}\int_{2\pi} B_\nu(\theta,\phi,\nu)\sin\theta d\theta d\phi d\nu \tag{2.11}$$

where $Z_0 = 376.7\,\Omega$ is the impedance of free space and the factor $1/2$ arises from the projection of the (unpolarized) Galactic radiation along the antenna axis. We found $E_{\rm rms} = 22\,\mu$V/m for $[\nu_0, \nu_1] = [50\,\text{MHz}, 200\,\text{MHz}]$ [164], computing B_ν with the Global Sky Model code [165]. This stationary noise level sets a hard limit around $10^{16.5}$ eV [166] on the energy threshold for radio-detection of air showers using an array of unphased antennas. Advanced methods for triggering or signal extraction may however radically change the situation in the future. This is discussed in more details in section 7.5.1.

In addition to Galactic noise, continuous wave emissions also represent a major issue for the radio-detection of air showers. Short-waves are in particular present below 30 MHz (see section 5.3 and Fig. 5.5 for more details) and set a lower-bound value for the experimental frequency range exploitable for EAS detection, an unfortunate situation given the significant fraction of the total emitted power below this frequency (see Fig. 2.8 right). Black-body radiation from the atmosphere (with an equivalent temperature usually taken equal to T=290 K) should not be neglected above 150 MHz (see Fig. 2.10)

2.3.2 The basics of antenna detection

We will present in this section the few concepts of antenna theory relevant to EAS radio-detection. The reader willing for a complete introduction to the topic may adequately refer to [167] among numerous valuable textbooks.

Finally, various man-made noise sources may affect the radio background in addition to short waves. Their intensity and rate strongly depend on the observer location (see Fig. 2.10). This is further discussed in part II of this document.

2.3.2.1 Antennas for air shower detection

A widely used type of antenna is a **dipole**. These are simply formed by two aligned conducting rods (the antenna arms), with their closest ends connected to a resistive load in reception mode, or a generator in emission mode, which justifies the name —feed point— of this central part of the dipole. Its working principle in reception mode is extremely simple: when an electromagnetic wave $\vec{E}$ sweeps through the antenna arms, the electric force $\vec{F_e} = e\vec{E}$ puts charges in motion. This induces at the macroscopic level an electric current I which is measured as a difference of potential at the output of the load. The extreme simplicity of the physical processes at play in radio-detection explains to a large extend why antennas are robust, stable and cheap detectors, thus making them excellent candidates to constitute very large arrays. Quantitative predictions of the antenna response yet require a bit more modeling, briefly introduced below. It relies on decades of extensive theoretical and experimental developments on radio communication, which makes antennas extremely well understood and controlled detectors, another strong asset for EAS radio-detection.

The length l of a dipole antenna is usually chosen to match a specific wavelength λ_0 of the radiation to be detected (or emitted). For half-wavelength dipole for instance, $l = \lambda_0/2$. When exposed to a stationary radiation of frequency $\nu_0 = c/2l$, a standing electric wave establishes through the resonant antenna, with null current at the ends of the antenna arms, and a maximal current amplitude at feed-point, thus allowing for the best detection sensitivity.

Half-wavelength dipoles offer a good starting point to build antennas for EAS radio-detection because they are not very directional, as analytical computations show [167]. This is an important point as cosmic particles obviously come from a broad range of directions. Yet the resonant aspect of dipole antennas also implies that their performances degrade at frequencies $\nu \neq \nu_0$. This is problematic because EAS emission is broadband, with a power density maximal in a wide range between few to ∼100 MHz (see Fig. 2.8). As mentioned in the previous section, short waves push the lower bound up to 30 MHz, but on the other hand raising the upper bound above 100 MHz allows for a better detection of the Cerenkov cone, a distinct feature of EAS (see Fig. 2.9). As will be detailed in section 3.2.1.4, the 50-200 MHz frequency range was chosen for GRAND, and most experiments performing cosmic-ray radio-detection similarly operate in a frequency range of several tens of MHz.

I will briefly present here two solutions used by EAS radio experiments to circumvent this issue:
• Log-Periodic Dipole Antennas (LPDA) (see Fig. 5.5) consist of a collection of i half-wavelength dipoles of distinct length l_i chosen following a logarithmic law —hence their name— so that their combined resonances at frequencies ν_i given by:

$$\nu_i = \frac{c}{2l^i} \tag{2.12}$$

offers a flat response by the LPDA over a large frequency range. Resonance at a frequency $\nu = 50$ MHz requires that the dipole of the LPDA should be 3 m long with several other dipoles down to 75 cm for the shortest one. This solution would be a huge mechanical challenge given the very large number of antennas needed for a radio detector of neutrinos.
• Butterfly —or bow-tie— antennas offer an alternative. They consist of dipoles with antenna arms of triangular shape, which allow more resonant modes to fit in the structure, hence significantly enlarging the antenna resonance for a size much smaller than an LPDA. This is the design chosen for the GRAND antenna (see section 3.2.1.4).

We will briefly present in the next sections how the antenna response is computed.

2.3.2.2 Antenna electric model

In the so-called receiving mode where it is used to measure an electromagnetic radiation, the antenna can be conveniently modeled by a complex impedance $Z_A = R_A + jX_A$, where R_A and X_A are the antenna's radiative resistance and reactance respectively, combined to a voltage source V_A, the voltage generated by the electric field. This is shown in the left panel of Figure 2.11.

When a load Z_L is plugged at the antenna output, a current I flows through the circuit and a voltage V_L appears at the output of Z_L. It is this information precisely that is recorded and eventually treated in the analysis of a EAS radio detector to determine the physical characteristics of the primary cosmic particle. It is worth noting at this stage that R_A has nothing to do with the —usually negligible— electric resistance of the material composing the antenna. It is instead related to the power P_{rad} re-radiated (or scattered) by the antenna:

$$P_{rad} = R_A I_{\text{rms}}^2 = \frac{1}{2} R_A |I|^2 \tag{2.13}$$

assuming that the electric current is a sine wave of amplitude $|I|$. The power P_L measured at the load can for its part be written as:

$$P_L = R_L I_{\rm rms}^2 = \frac{1}{2} R_L |I|^2 = \frac{1}{2} \frac{R_L}{|Z_A + Z_L|^2} |V_A|^2 \tag{2.14}$$

One of the goals of the electronic chain design will consist in maximizing P_L. Equation 2.14 shows that is achieved under the conjugate matching conditions defined by $Z_L = Z_A^*$, i.e. $R_L = R_A$ and $X_L = -X_A$, in which case equation 2.14 re-writes as:

$$P_L = \frac{|V_A|^2}{8 R_A} \tag{2.15}$$

It is obvious from equations 2.13 and 2.14 that for conjugate matching conditions the power transferred to the load is equal to the power re-radiated by the antenna. Only half of the total power captured by the antenna $P_{in} = P_L + P_{rad}$ is then actually accessible to the user, and this corresponds to an ideal —and almost impossible— case! Achieving conjugate matching is indeed extremely hard in practice because the antenna impedance is a function of frequency, as illustrated in the right panel of figure 2.11.

To conclude, one may note that the resonant condition above mentioned corresponds to a maximal electric current I for a given radiation amplitude, and hence a given voltage V_A. Resonance therefore translates in a minimal value of antenna impedance $|Z_A| = |V_A/I - Z_L|$.

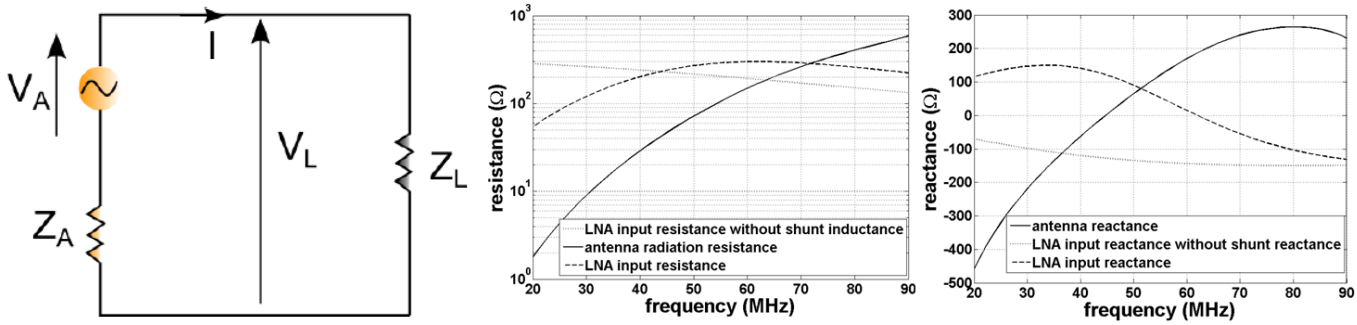

Figure 2.11: *Left: electric model of an antenna in receiving mode: voltage source V_A and radiative impedance Z_A. Right: simulated resistance and reactance of the antenna developed by D. Charrier (dotted line) for the CODALEMA experiment [168], then used in AERA [169] (solid line) and of the input impedance of the Low Noise Amplifier connected to it. Taken from [168].*

2.3.2.3 Antenna directivity

The amplitude of the antenna response obviously depends on the direction of propagation of the wave with respect to the dipole axis $\vec{l}$, the current being maximal if $\vec{E} \parallel \vec{l}$. The quantity often used to characterize the directivity of the antenna response is its gain, a dimensionless quantity defined in emission mode as:

$$G(\theta, \phi) = 4\pi \frac{U(\theta, \phi)}{P_{out}} \tag{2.16}$$

where $U(\theta, \phi)$ is the intensity radiated in the direction (θ, ϕ) (in W/sr), and P_{out} is the total power accepted by the antenna from the generator and fully radiated for an antenna with null electrical resistivity. We thus understand from equation 2.16 that $G(\theta, \phi) = 1$ for an isotropic antenna.

Another relevant quantity to characterize antenna directivity in receiving mode is its effective area A_e (in $\rm m^2$). It is defined as the ratio between the power P_L collected at the antenna load to the radiation flux density (in $\rm W/m^2$) to which the antenna is exposed. In the case where the source is a plane wave with sinusoidal electric field $\vec{E_0}$ polarized

linearly, for which the average flux density is given by:

$$< E_e >= \frac{|\vec{E_0}|^2}{2Z_0} \tag{2.17}$$

the power measured at the load is thus:

$$P_L = A_e \times < E_e > \tag{2.18}$$

if $\vec{E} \parallel \vec{l}$, while $P_L = 0$ if $\vec{E} \perp \vec{l}$. In the case of an unpolarized radiation of spectral radiance B_ν emitted in the frequency range $[\nu_0, \nu_1]$, then the total power available at antenna output is equal to:

$$P_{in} = \frac{1}{2} \int_{\nu_0}^{\nu_1} \int_{4\pi} A_e(\theta, \phi, \nu) B_\nu(\theta, \phi, \nu) \sin\theta d\theta d\phi d\nu \tag{2.19}$$

where the factor 1/2 arises from the projection of the unpolarized radiation along the antenna axis.

The reciprocity principle —a cornerstone of antenna theory— states that antennas work identically in reception and emission modes. It allows to relate gain and effective area through the following equation:

$$G(\theta, \phi) = \frac{U(\theta, \phi)}{U^{iso}} = \frac{A_{eff}(\theta, \phi)}{A_{eff}^{iso}} \tag{2.20}$$

with $U^{iso} = P_{out}/4\pi$ the intensity radiated by an isotropic antenna accepting the same power P_{out} from a generator, and A_{eff}^{iso} its effective area.

In addition, a beautiful thermodynamic argument[1] leads to

$$A_{eff}^{iso} = \frac{\lambda^2}{4\pi} \tag{2.21}$$

from which we can easily derive:

$$A_{eff}(\theta, \phi) = \frac{c^2}{4\pi\nu^2} G(\theta, \phi) \tag{2.22}$$

2.3.2.4 Antenna effective length

Effective area is the relevant quantity to compute received radiation power, but voltage is more adequately computed at antenna output from the antenna effective length (in m), defined by:

$$V_A = \vec{l}_{eff} \cdot \vec{E} \tag{2.23}$$

Similar to the effective area, effective length is a function of the direction of origin of the wave (θ, ϕ) and its frequency ν. It is a complex quantity —meaning that the voltage signal is not necessarily in phase with the electric field $\vec{E}(t)$— and a vectorial one, usually decomposed on the spherical base: $\vec{l}_{eff} = l_{eff}^{\theta} \vec{e_\theta} + l_{eff}^{\phi} \vec{e_\phi}$.

Equating equations 2.14 and 2.18, and also using equations 2.17 and 2.23, it is possible to write for a plane wave with $\vec{E} \parallel \vec{l}$:

$$|\vec{l}_{eff}| = \sqrt{\frac{|Z_A + Z_L|^2}{R_L} \frac{A_{eff}}{Z_0}} \tag{2.24}$$

which, under conjugated matching conditions, and with equation 2.16, simplifies as:

$$|\vec{l}_{eff}| = \sqrt{\frac{R_A}{Z_0} \frac{c^2}{\pi\nu^2} G} \tag{2.25}$$

In practice however, the so-called equivalent length $\vec{l}_{eq}$ defined as:

$$V_L = \vec{l}_{eq} \cdot \vec{E} \tag{2.26}$$

is computed by including the load Z_L in numerical electromagnetic simulation of the antenna response with codes such as NEC4 [170]. It is preferred over the effective length as it allows to compute directly the voltage V_L at load output, the variable of interest for the data analysis.

[1] Presented for example here: `https://www.cv.nrao.edu/~sransom/web/Ch3.html#S1.SS4`

2.4 Summary

We have seen in this chapter that radio antennas may detect air showers induced by the interaction of neutrinos with the Earth target, if their initial energy is around 10^{17} eV or above. Moreover, specific features of EAS radio emission —detectability at far distances and large footprints of the horizontal showers associated with neutrinos— and characteristics of radio detection —very basic design and robustness of the antennas— imply that radio detection units could be deployed at a gigantic scale, and thus form a competitive instrument for the quest of UHE neutrinos. This will be evaluated quantitatively in the next chapter.

Chapter 3

Sensitivity study of the GRAND detector

Figure 3.1: *View over the Tianshan mountains from the Tiger Mouth pass.*

In this chapter, we compute the sensitivity to UHE neutrinos of a giant radio array and optimize its design for this purpose, leading to the formulation of the GRAND proposal. This effort finds its origin in the first days of 2011, when I stopped at the *Hu Kou* —the "Tiger Mouth", a 4 200 m high pass in the Tianshan mountains— on my way back from maintenance operations on the TREND detector presented in chapter 5. Enjoying the view from the pass, I started thinking that it might be possible to deploy a radio array all over these mountains and far beyond, provided the antennas were autonomous and basic enough so that an array of several tens of thousand units remained achievable.

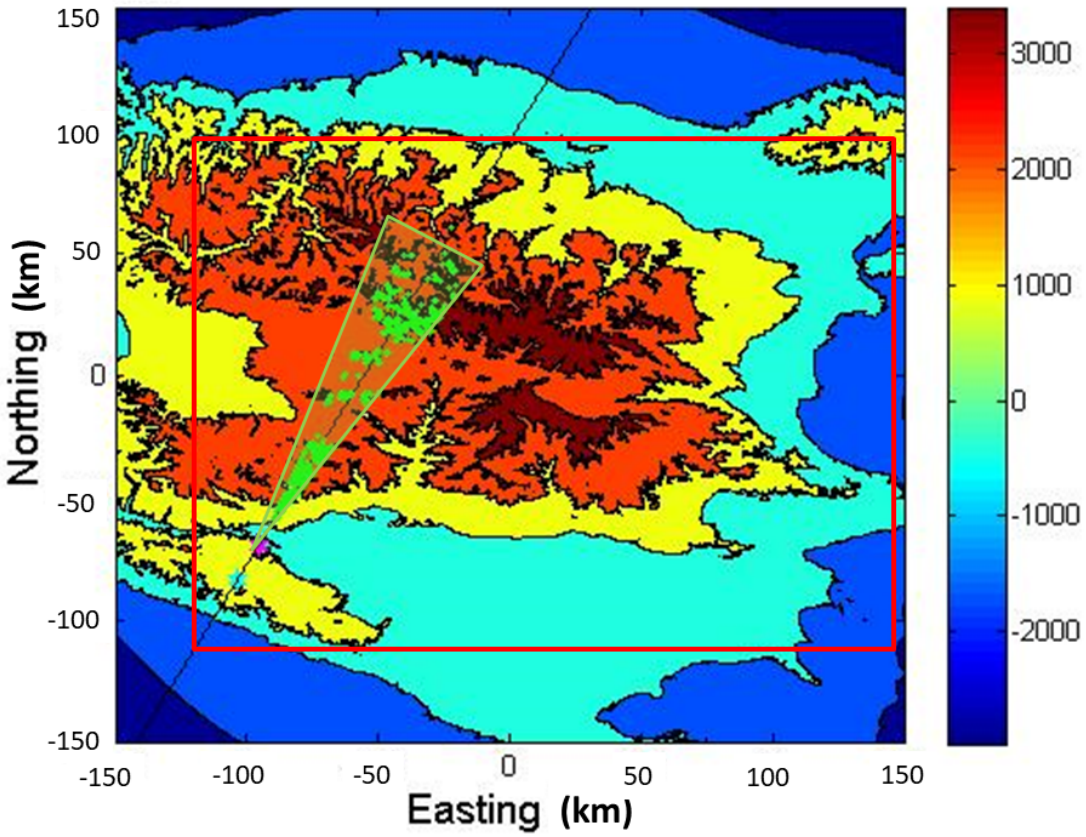

Figure 3.2: *The area considered for the Tianshan neutrino sensitivity study: a 300×300 km^2 square centered on the TREND site in the Tianshan mountain range. The z value is given in km with respect to a horizontal plane set at sea level at the map central location. The 60'000 km^2 antenna array considered in this study is shown as a red square. An event is displayed, with the ν_τ underground interaction point shown as a cyan star and the τ decay point in magenta. The cone computed from this specific shower (see section 3.1.2.2) is shown in green, and the triggered antennas as green crosses. The antenna layout chosen for this study is a 400 m square grid, and mountain shadowing effects are taken into account.*

Later that month, I attended a workshop in Clermont-Ferrand where Pascal Lautridou, one of the pioneers in the field of EAS radio-detection, suggested that a radio detection unit could be produced for less 800€, which convinced me further in this direction. Soon after that, we started with Valentin Niess, my long-time friend from the *Laboratoire de Physique Corspusculaire* in Clermont-Ferrand, a simulation to evaluate the potential for neutrino detection of a radio array deployed over the full area of the Tianshan mountains. This so-called **Tianshan study** is the starting point of the GRAND proposal. It is detailed in the next section.

3.1 Initial neutrino sensitivity studies for a giant radio array: the Tianshan study

3.1.1 Computation principle

The area considered for the simulations is a rectangle of $300 \times 300\,\mathrm{km}^2$ centered on the TREND site (86°44' E, 42°57' N). The topography of the site is interpolated from a 400 m-step elevation map derived from public NASA satellite data[1] (see Fig. 3.2). Energies ranging between 10^{17} and $10^{20.5}$ eV with a half-decade step are considered for the incoming tau neutrinos. Zenith angles θ range between 86 and 93° with a one-degree step. The θ values are measured with

[1] https://earthdata.nasa.gov

respect to the z axis, and thus differ from the true angular value at the τ emerging position. 18 values are considered over the whole azimuthal range with a 20° step.

For each of the resulting 1152 sets (E, θ, ϕ), the simulation area is projected in the plane perpendicular to the (θ, ϕ) direction, noted $\mathcal{A}^{\theta,\phi}$. A trajectory is defined by randomly choosing the track intersection point with this surface. The neutrino interaction process is then simulated for this trajectory following an algorithm detailed in section 3.1.2.1. If it results in a τ decaying above the simulation area, with a corresponding shower of initial energy $E_{sh} \geq 10^{16}$ eV, then this track is tagged as valid and relevant information is logged. The process is repeated n_{Gen} times for each (E, θ, ϕ) set, until $n_{Comp} = 100$ valid tracks are produced.

In a further step, we use an analytical parametrization of τ-induced showers radio emission to determine which of the n_{Comp} recorded tracks would be detected by a radio array deployed over the simulation area. This is detailed in section 3.1.2.2. If n_{Det} showers are found to be detected for the (E, θ, ϕ) set, then the corresponding differential effective area of the detector is computed as:

$$\mathcal{A}_{eff}^{E,\theta,\phi} = \mathcal{A}^{\theta,\phi} \times \frac{n_{Det}}{n_{Gen}} \tag{3.1}$$

Assuming an isotropic neutrino flux, we can then write the detector integrated effective area (in $\mathrm{cm}^2{\cdot}\mathrm{sr}$):

$$\mathcal{A}_{eff}(E) = \int_{86}^{93}\int_{0}^{360} \mathcal{A}_{eff}^{E,\theta,\phi} d\phi \sin\theta d\theta \tag{3.2}$$

For an all-flavor differential neutrino flux $\Phi(E)$ given in units of $\mathrm{GeV}^{-1}{\cdot}\mathrm{cm}{\cdot}^{-2}{\cdot}\mathrm{s}^{-1}{\cdot}\mathrm{sr}^{-1}$, the number of events expected in the detector for a live exposure time Δt is then equal to:

$$N = \int \Phi(E)\mathcal{A}_{eff}(E)dE \times \Delta t \tag{3.3}$$

Furthermore assuming an E^{-2} power law for the neutrino flux

$$\Phi = \Phi_0 \times E^{-2} \tag{3.4}$$

we determine a limit on the value Φ_0 for null detection over the period Δt. We do this by considering that the 90% confidence level limit for 0 events is equal to 2.44 for a Poisson distribution of low-stat events [171] :

$$\Phi_0 \leq \frac{2.44 \times 3}{\int \mathcal{A}_{eff} \frac{d\log E}{E} \times \Delta t} \tag{3.5}$$

where the factor 3 arises from the fact that the radio array is sensitive to tau neutrinos only (see section 2.2), and assuming as well an equal flux for the three neutrino flavors at Earth, a reasonable hypothesis (see section 1.1.3). A differential limit can also be derived. It is defined in this study as the 90% confidence level limit on Φ_0 for 0 event detected per decade of energy. This evaluates to :

$$\frac{dN}{d\log E} \leq \frac{7.32}{\log 10} \tag{3.6}$$

With equations 3.3 and 3.4, this yields :

$$\Phi_0 \leq \frac{7.32 \times E}{\log 10 \times \mathcal{A}_{eff} \times \Delta t} \tag{3.7}$$

Results of this treatment are presented in section 3.1.3. Before that, we detail the implementation of the simulation pipeline leading to the computation of the number of detected showers n_{Det}.

3.1.2 Implementation

3.1.2.1 From the neutrino to the shower

The processes leading to the production of an air shower from of a UHE neutrino interacting with the Earth target were described in section 2.2. They were implemented in C++ by Valentin Niess for the Tianshan simulation. I simply give here a brief summary of it for the sake of completeness.

A simplified 1D tracking was performed for the n_{Gen} trajectories generated in the (E, θ, ϕ) set. Given the energies considered, transverse transportation can indeed be safely neglected down to the τ decay. The simulation medium is filled with dry air above the $z(x, y)$ topographic values and with Standard Rock [172] of density 2.65 g/cm^3 below. For each track, a dedicated geometry package allows to map any air $\leftrightarrow$ rock medium change along the trajectory.

In the atmosphere, any stochastic interaction or energy loss is neglected. Therefore density variations in the air are not modeled, and simulation starts only when the incoming ν_τ penetrates below the Earth surface. If this happens outside the simulation area, the track length is extended to its entry below the Earth surface (assumed for simplicity to be at the same altitude as the track entry point in the simulation area) and an equivalent grammage in Standard Rock is computed according to the Preliminary Earth Model [173].

In rock, deep-inelastic scattering (DIS) neutrino interaction lengths are taken from [131]. The energy dependent interaction depths for Neutral Current (NC) or Charged Current (CC) events are sampled accordingly and located along the trajectory. The kinematics of the neutrino DIS event is delegated to Pythia6.4, using CTEQ5d probability distribution functions. The simulation is stopped if the neutrino escapes the simulation volume before a CC interaction occurs. Otherwise, a τ simulation starts, while the neutrino simulation could later go on for the secondary ν_τ produced by a possible τ decay.

The τ energy loss and proper time distributions have been previously simulated with GEANT4.9 for various primary energies and depths in Standard Rock. A simple parametrization was derived for the almost 100 % correlated distributions with only 2 parameters per primary energy and depth, making it easy and light to tabulate. Photo-nuclear interactions are of prime importance for UHE leptons (see section 2.2.1.2). They have been extended in GEANT4.9 above PeV energies following [174]. If a decay in flight occurs within the simulation volume it is simulated with the TAUOLA package [175]. If the induced shower energy E_{sh} (computed as the τ final energy minus the energy of neutrinos and muons secondaries) is above 10^{16} eV, then the τ decay data are recorded to be used as input for the shower simulation (see section 3.1.2.2) and the n_{Comp} variable is incremented.

3.1.2.2 Parametrization of the shower radio emission: the Cone Model

Simulating the radio emission by air showers with standard microscopic codes is extremely CPU-demanding, as already mentioned in section 2.3.1. This is particularly true in the case of neutrino-induced showers, whose nearly horizontal trajectories imply that several hundred antennas lie in their tens-of-kilometers-long footprints. It was therefore chosen to parameterize the radio emission by air showers rather than simulating it.

I initiated this work together with Valentin Niess and Washington Carvalho, a colleague then based in Santiago de Compostela with ties to the GRAND project. The task was later taken over and finalized by Valentin Decoene, the PhD candidate I supervised together with Kumiko Kotera between September 2018 and September 2020. Very clearly, the proposed treatment does not intend at being a precise and reliable tool to compute the radio signal. It is rather a simple, analytical and approximate parametrization which produces results nearly instantaneously and requires only minimal disk space and no specific simulation software, an attractive feature when it comes to perform simulation for thousands of detection units covering vast detection areas.

The treatment is based on a geometric modeling of the volume inside which the electromagnetic field amplitude is large enough to trigger an antenna, hence called **trigger volume** in the following. We give to this volume the shape of a cone, oriented along the shower axis, with its apex placed at the $X_{\max}$ position, half-angle Ω and height H. Values of Ω and H depend on shower energy, and are adjusted from ZHAireS [154] simulations. Different adjustments were used throughout the development of this so-called **Cone Model**. We briefly present here the one detailed in [164].

As illustrated in figure 3.3, the strength of the electromagnetic emission by an air shower first increases along its propagation axis, as the number of particles in the shower. After reaching a maximum at a location close to X_{max}, the signal then decreases and once the shower vanishes, the radio signal amplitude simply drops as $1/R$ —the observer's distance to X_{max}— simply because of signal dilution effects, as already established in section 2.3.1.2. It follows that the cone height H should scale linearly with shower energy, a result confirmed through simulations [164]. A detailed study presented in in the same article shows that a conical parametrization of the trigger volume is valid, with a logarithmic dependency of its opening angle Ω with energy (see Fig. 3.3). For a radio signal filtered in a frequency range 50-200 MHz, the optimal cone parametrization was found to be:

$$H|_{50-200\mathrm{MHz}} = \quad a \; + \; b \left(\frac{E_{\mathrm{sh}} - 10^{17}\mathrm{eV}}{10^{17}\mathrm{eV}} \right), \tag{3.8}$$

$$\Omega|_{50-200\mathrm{MHz}} = \quad c \; + \; d \log \left(\frac{E_{\mathrm{sh}}}{10^{17}\mathrm{eV}} \right). \tag{3.9}$$

with $E_{\rm sh}$ expressed in eV in the formulas. Numerical values of a, b, c, d are given in table 3.1 for two threshold values of 66μV/m and 110μV/m, corresponding to 3 and 5 times the average sky radiation (see Eq. 2.11). The 66 μV/m threshold represents an aggressive hypothesis, where advanced methods for signal treatment allow triggering on smaller signals. The 110μV/m value is a more conservative one, already achievable today. In the Tianshan study, the cone parametrization differs, and the threshold values considered were 30 and 100 μV/m, partly because a 30-80 MHz frequency range was then assumed for the parametrization. It was found that these discrepancies had an impact smaller than 50% on the simulation results.

Shadowing effects by mountains were also included in the treatment (see Fig. 3.2), as only antennas in direct view of the τ decay point can trigger. This is illustrated with one example event in figure 3.2.

Finally a shower is tagged as detected —and the value of n_{Det} incremented accordingly— only if it is associated with clusters of 8 or more neighboring antennas. This is an arbitrary value, considered realistic when taking into account reconstruction and background rejection considerations.

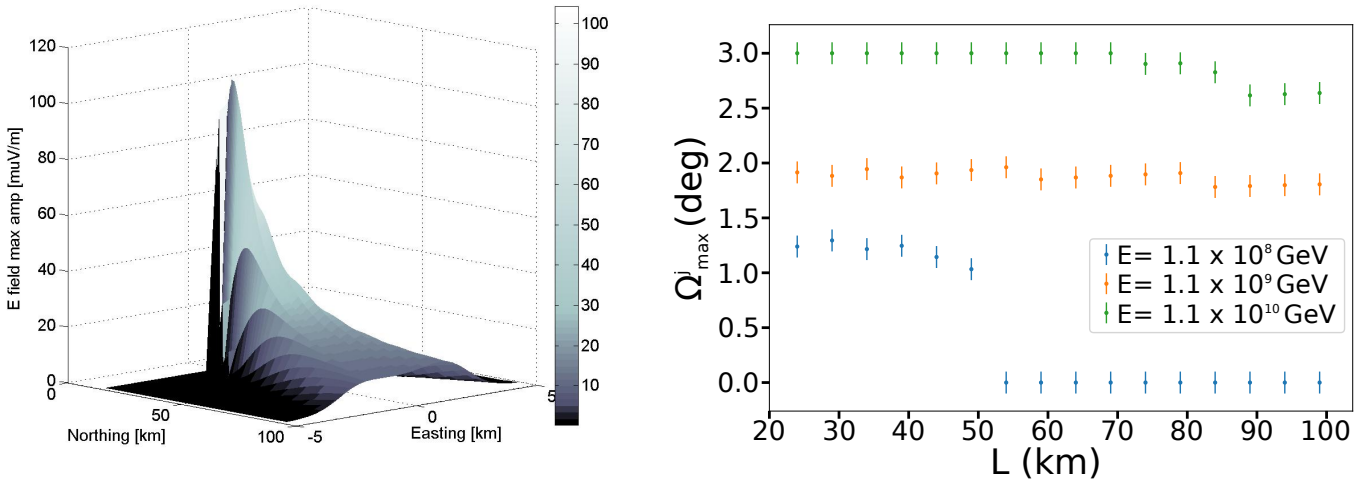

Figure 3.3: *Left: Expected distribution of the E-field peak value in the 30-80MHz frequency range at ground level for a ZHAireS simulation of a $E_{sh} = 9.6 \cdot 10^{16}$ eV, shower induced by a 10^{17} eV τ decaying at position (0,0,50 m) and propagating horizontally towards North. E-field amplitude is given in μV/m. Right: angle Ω as a function of longitudinal distance for various shower energies. The angle Ω measures the maximum opening angle of the cone describing the trigger volume inside which the electric signal amplitude is larger than a threshold value, taken here equal to 110 μV/m. A filtering in the 50-200 MHz frequency range is applied to simulated signals in this treatment. For the shower of energy $E = 1.1 \times 10^8$ GeV, Ω drops to 0 for $L > 50$ km because the cone height H does not extend beyond this value at this energy. Taken from [164].*

threshold	a	b	c	d
aggressive	109 ± 15	116 ± 3	1.3 ± 0.2	1.00 ± 0.02
conservative	42 ± 7	48 ± 1	1.0 ± 0.3	0.80 ± 0.03

Table 3.1: Parameters for the fitting functions given in Equations 3.8 and 3.9 for aggressive and conservative thresholds. Parameters a and b are in km, c and d in degrees. Taken from [164].

3.1.3 Results

The simulation process detailed in the previous section was applied to a 92812-antennas detector covering a total area of $220 \times 270 = 59\,400$ km^2, with a 800 m-step square grid. The detector area is shown as a red square in figure 3.2. Its differential effective area, computed with equation 3.1, is presented in the left panel of figure 3.4, and its integrated value in figure 3.14 as a function of neutrino energy. Assuming no neutrino candidate is detected within 3 years of live observations, it yields in the aggressive scenario an integrated limit equal to 2.0×10^{-9} GeV·cm^{-2} s^{-1} on the parameter Φ_0 defined in equation flux for an all-flavor, isotropic, $\propto E^{-2}$ neutrino flux. The limit is 7.2×10^{-9} GeV·cm^{-2} s^{-1} for the conservative threshold value.

In June 2014, I presented a preliminary version of this analysis to Kumiko Kotera, a researcher from the *Institut d'Astrophysique de Paris* who I had met few months before at the MACROS workshop she had organized. Much more aware than me about the science potential of such an instrument, she enthusiastically suggested that we organize a dedicated workshop to present and further discuss this study with experts from the theory and experimental sides of the field of UHE phenomena in the Universe. This was the beginning of a solid friendship and very fruitful collaboration, and incidentally the birth of the GRAND project. The results of the Tianshan study were also the base of the first presentations of the GRAND project at the ICRC conferences in 2015 and 2017 [176, 177]

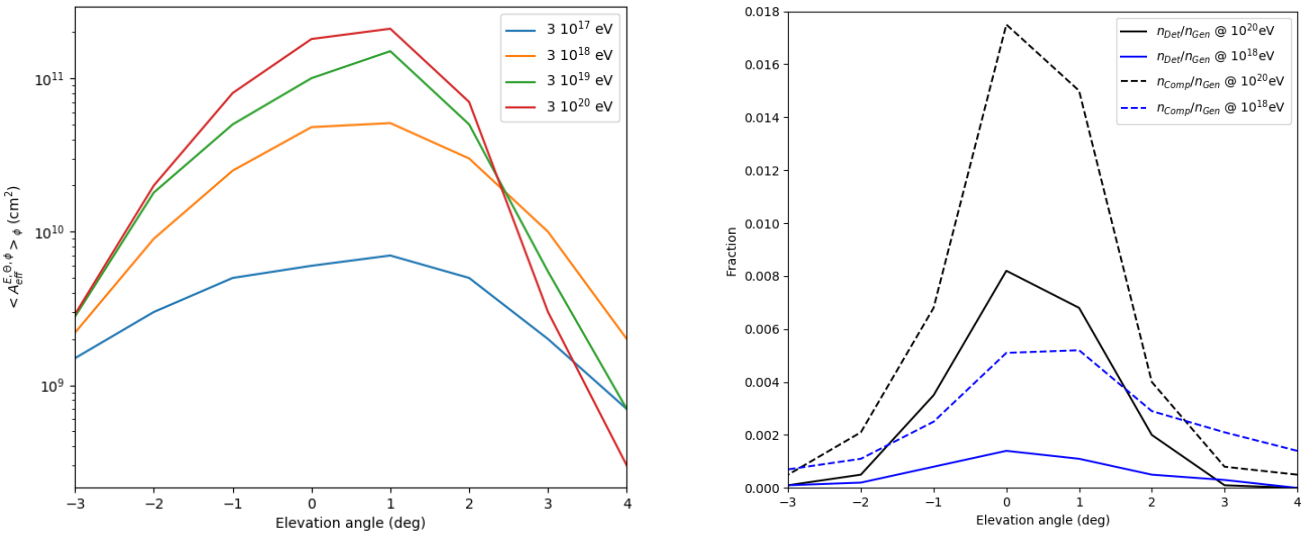

Figure 3.4: *Left: differential effective area $A_{eff}^{E,\theta,\phi}$ as a function of the elevation angle (counted positively from horizon for upward trajectories) for various ν_τ energies for the ∼60 000 km^2 simulated array used in the Tianshan study. An aggressive threshold is assumed here and the curves are averaged over azimuth angles. Right: fraction n_{Det}/n_{Gen} of showers detected in this study (plain line) for ν_τ energies of 10^{18} and 10^{20} eV. Also shown are the fractions n_{Comp}/n_{Gen} of simulated trajectories inducing detectable showers (dotted line). These plots confirm that only trajectories very close to the horizontal can be associated with non-negligible probabilities for the detection of neutrino-induced showers, and these remain very low, with typical values around a few ‰ in the best cases.*

3.1.4 The GRAND proposal

3.1.4.1 Role of topography

The seminal GRAND workshop took place in February 2015 at LPNHE (see Fig. 3.5). One of its most important outcomes certainly was that the 60 000 km^2 detector considered in the Tianshan study was simply too small in regards of

the science at stake: in the very optimistic case of a neutrino flux equal to the so-called Waxman-Bahcall limit [61] —an absolute upper bound determined from cosmic ray measurements— about 8 events would be detected every year. This would be hardly sufficient to perform a complete statistical analysis allowing to answer relevant questions such as: "what is (are) the source(s) of the detected neutrinos?" or "what is their spectrum?" for instance. A $\sim 10^{-10}$ GeV·cm^{-2} s^{-1} integral limit for three live years—about ten times better than the one obtained in the study— appeared to be the appropriate target to treat such issues.

Figure 3.5: *Picture taken during the seminal GRAND workshop at LPNHE in February 2015.*

However a 10-fold increase in detector size seemed out of question for practical reasons. Yet the Tianshan study had shown that the detection rate strongly depended on topography, with much larger detection rates by antennas deployed on the Southern rim of the Tianshan mountains. Together with Valentin Decoene and other GRAND colleagues, we studied in more details the role of the topography on the detection of neutrino-induced air showers in [164]. We did so using a toy setup composed of a radio array deployed on a plane area tilted by an angle α with respect to the horizontal. The detector is illuminated by air showers initiated by neutrino-induced taus emerging from a spherical Earth and decaying at a distance D from the detector, as sketched in the top panel of figure 3.6).

This toy setup study showed that even mild slopes of a few degrees inclination induce an increase by a factor up to 3 in the detection rate compared to a flat detector (see bottom panel of figure 3.6). The low detection efficiency for a flat detector is clearly a consequence of the strong beaming of the radio emission combined with the upward-going trajectories of neutrino-induced showers, while denivelation inside the detection area largely increases the chances to intercept the radio beam. For gentle slopes, this may happen at distances D as large as several tens of kilometers, but the mild decrease of the radio signal strength with distance, combined with the excellent transparency of the atmosphere to radio waves, still allows radio-detection at such large distances, as confirmed experimentally [178]. Hence there is not a significant advantage for steep slopes, as far as detection efficiency is concerned. Besides, distances $D > 20\,\mathrm{km}$ allow for showers to fully emit their electromagnetic radiation (see left panel of figure 3.3) and correspond to larger footprints at ground, thus allowing detection with sparser arrays. In conclusion, the study presented in [164] confirms the indications of the Tianshan study that wide valleys or large basins offer topographies better suited than high mountain areas for the detection of neutrino-induced air showers. A site corresponding to these considerations was selected for the GRAND study (see section 3.2.2.2).

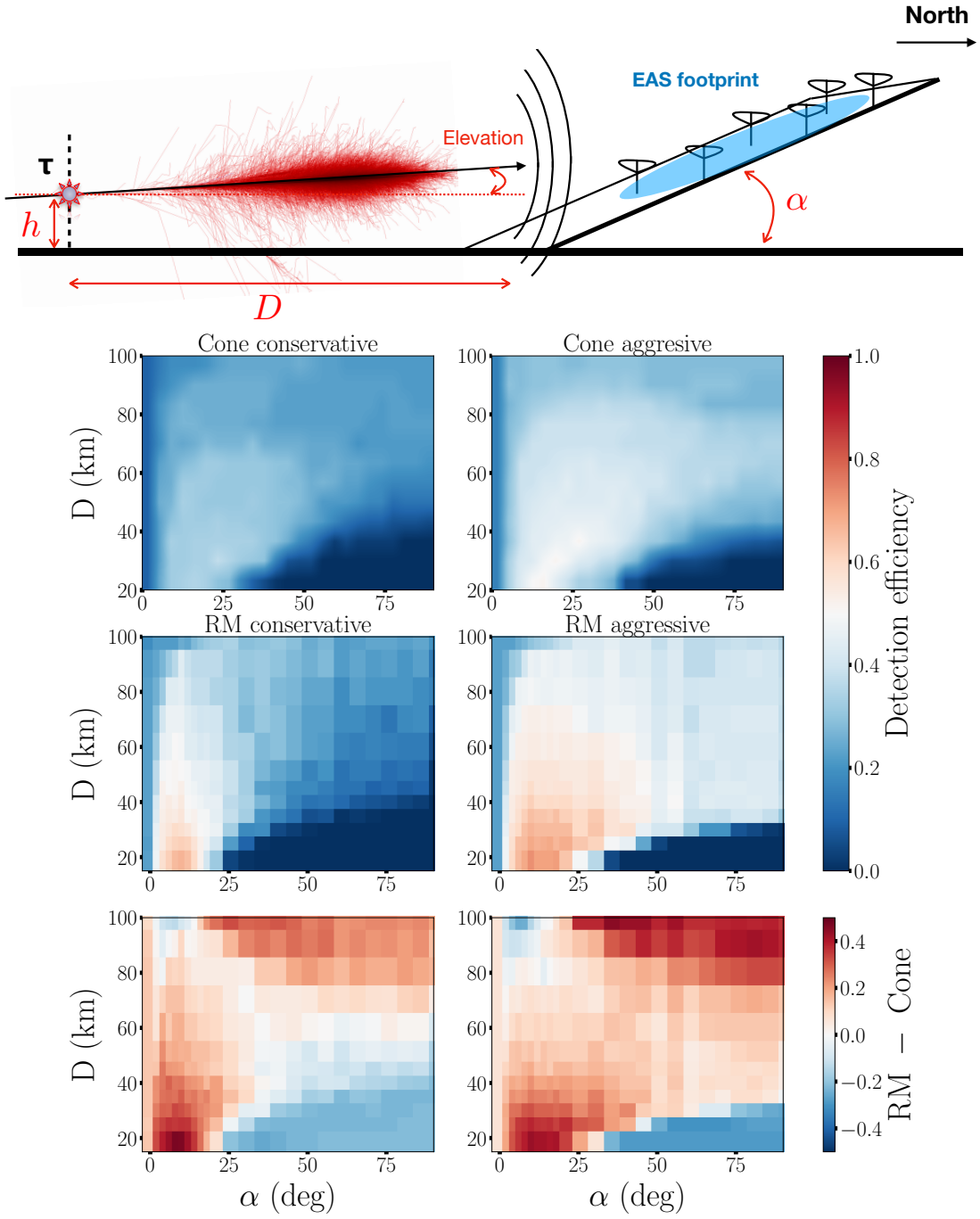

Figure 3.6: *Top: Layout of the toy-setup considered in the topography study. A tau particle decays at a location represented as a star, producing an air shower. The radio signal emitted by the shower impinges the detector plane, tilted by an angle α from the horizontal. The intersection between the detector plane and the horizontal plane is set at a horizontal distance D from the decay point. The parameter D is therefore a measurement of the amount of free space in front of the detector. Bottom: Detection efficiency as a function of distance D and slope α for the simulation set with a primary neutrino energy of* 10^9 *GeV. Efficiency is defined here as the ratio of the number of triggered showers —5 antennas above threshold— to the number of simulated showers. Results are plotted for the Cone Model (top) and Radio Morphing (middle). The difference (Radio-Morphing - Cone Model) is plotted in the bottom panel. Conservative (left) and aggressive (right) threshold hypothesis correspond here to threshold values of 110 and 66* $\mu V/m$ *respectively. See section 3.2.1.2 for details on Radio Morphing. Both figures are taken from [164].*

3.1.4.2 The GRAND detector network

Considering the key role of topography on the detection rate of neutrino-induced air showers, it was projected that an increase of a factor ∼3 in size of the total detector area —hence reaching ∼200 000 km^2— may translate into a factor 10 gain in neutrino sensitivity compared to the TianShan study, provided that the detector is deployed at locations with favorable topography. It was also suggested that the detector could be divided into independent sub-arrays of typical side dimension of 100 km without significantly affecting its sensitivity, as the sub-detector area would remain significantly larger than the typical radio footprint of a neutrino-induced shower.

Dividing the detection areas in several sub-arrays deployed at various locations around the world present several advantages: first, it allows to select sites with optimal topologies only, which could hardly be the case for a 200 000 km^2 continuous area. Second, it allows to split the load of detector operation in maintenance between several sites and countries. From a physics point of view, deploying a detector at various longitudes maximizes the instantaneous field of view of the detector, a key parameter in the perspective of transient events. Detection of FRBs with sub-arrays distant by several thousands kilometers may also allow to triangulate the position of the source and thus indicate the direction where the FRB was emitted, thus circumventing one of the drawbacks of incoherent summing of the radio signals mentioned in section 2.3.1.2.

The **Giant Radio Array for Neutrino Detection** was therefore defined as a proposal to deploy ∼20 sub-arrays of ∼10 000 km^2 each, placed at optimal locations around the world. This network of detectors forms the GRAND array, the largest detector in the world, with the clear aim not only to set limits on the neutrino flux, but actually detect them with sufficient statistic to achieve the physics goals discussed in chapter 1. After this proposal was formulated, it was decided to set up a full scale, reliable, end-to-end simulation to compute its sensitivity to neutrinos. This is presented in the next section.

3.2 GRAND neutrino sensitivity computation

3.2.1 Simulation chain

The GRAND neutrino sensitivity computation was my main research activity between February 2015 and August 2018. I was in particular involved in setting the basis of the method used to compute the electromagnetic field (detailed in section 3.2.1.2), computing the antenna response (see section 3.2.1.4) and analyzing the results of the simulation in order to optimize the detector design. However a major part of my time was devoted to coordinate the work of the small team involved in this study: Valentin Niess, Anne Zilles (post-doc at IAP between April 2017 and December 2019), Sandra Le Coz (post-doc on TREND and GRAND in NAOC between 2015 and 2017) and Didier Charrier (engineer at the SUBATECH lab). I detail below the components of the simulation pipeline we set up before presenting their results in section 3.2.2.

3.2.1.1 DANTON

A dedicated code was developed to simulate the processes of neutrino interaction and lepton transport detailed in section 2.2, assuming in particular stochastic energy losses in a 3D framework. This code, named DANTON [179], was solely developed by Valentin Niess, and I will therefore not detail it here. Two features are however worth stressing, which make it a significant upgrade compared to the code presented in section 3.1.2.1:

• DANTON can be operated in both Forward (classical) or Backward Monte-Carlo mode. The latter consists of back-tracking the particles from tau decay up to ν_τ trajectory, applying appropriate weighting factors. As no particles are lost in the simulation process, backward mode is much more efficient than the standard mode (in particular at low energies), and thus represents a huge gain in terms of computing time (see Fig. 3.7).

• DANTON incorporates detailed 3D topographies over the very large areas needed for the GRAND simulations. Elevation data are retrieved along a 200 m-step mesh with a $\sigma z \sim 10$ m resolution from Digital Elevation Models (DEM) such as ASTER [180] or SRTMGL1 [181]. The points at the interface between ground and air along the trajectory are then computed thanks to an iterative algorithm based on a dichotomic search. This method, implemented by Valentin Niess in a dedicated library called TURTLE [182], requires much less memory than the standard ones based on triangular tessellations of the topography, which are not applicable to problems involving $\mathcal{O}(10^9)$ nodes such as this one.

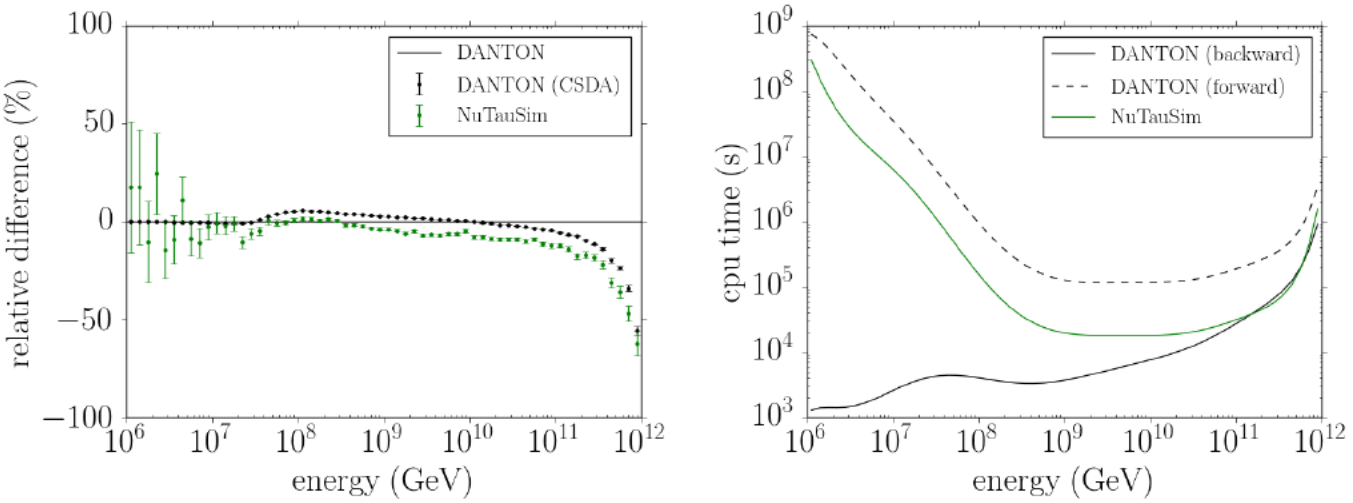

Figure 3.7: *Comparison between DANTON and NuTauSim [183], a simulation code with similar objectives as DANTON, of the τ energy for a flux emerging from the Earth with an elevation angle of 1° and a $1/E^2$ primary ν_τ flux. Left: relative difference to DANTON for the differential flux. CSDA stands for Continuous Slowing Down Approximation, a regime where stochastic energy losses are replaced by their average value, an approximation used by NuTauSim and usually considered valid in the ionization regime. Right: CPU time needed for reaching a 1% Monte-Carlo accuracy. Results of both codes are consistent, while the Danton backward mode allows for significant computation time gains, especially at low energies. Taken from [179].*

3.2.1.2 Radio Morphing

The Cone Model used for the Tianshan study to evaluate radio emission is not reliable enough for the GRAND study, while CPU constraints prevent the use of microscopic code. I therefore proposed a semi-analytical solution to tackle this issue, which was implemented by Anne Zilles. This method, called Radio Morphing, is detailed in [160]. I summarize below its main features.

Radio Morphing mainly consists of re-scaling radio signals from a single **reference shower** via a series of simple mathematical operations to determine the signal expected for a **target shower**. If the target shower B and reference shower A have a same direction of propagation ($\vec{v}_A = \vec{v}_B$), then the signal at a position $\vec{x} - \vec{x}_{X^B_{max}}$ will for instance be deduced from the signal of shower A at a position $\vec{x} - \vec{x}_{X^A_{max}}$ by applying a scalar factor E_B/E_A, where $\vec{x}_{X^Z_{max}}$ is the position of maximum of development for shower Z. A coefficient $\sin\left(\vec{v}_B, \vec{B}\right)/\sin\left(\vec{v}_A, \vec{B}\right)$ applied to the $\vec{v}\times\vec{B}$ component of the electric field corrects for its part for different directions of propagation. Different X_{max} heights —caused by different zenith angles or different heights for the shower injection points— require a slightly more subtle treatment: first a lower altitude translates in a denser atmosphere, hence a weaker charge drift current within the shower pancake and eventually a smaller geomagnetic emission (see Eq. 2.7), while it also induces a larger refractive index (see Eq. 2.8) and thus a wider radio beam. The former effect can be adequately accounted for with a factor $\sqrt{\rho(X^B_{max})/\rho(X^A_{max})}$ applied to the $\vec{v}\times\vec{B}$ component of the electric field, and the latter through an homothetic transformation of the antenna positions from the reference shower's antenna positions $\vec{x}_B = k\vec{x}_A$ with:

$$k = \frac{\arccos n(X^B_{max})}{\arccos n(X^A_{max})} \tag{3.10}$$

The underlying concept of Radio Morphing is shower universality, i.e. the fact that the distribution of electrons and positrons in extensive air-showers —and consequently, their electromagnetic emission— depends on a very limited set of parameters, mainly the depth of the shower maximum X_{max} and the number of particles in the cascade at that position [184, 185]. In practice RadioMorphing is implemented as follows:

(i) First a reference shower A is simulated (using ZHAireS for this specific study). The simulated positions follow a 3D mesh composed of planes perpendicular to the propagation axis. For each of these so-called **shower planes**, antenna positions $\vec{x}_A$ are set along a star-shape pattern, the optimal layout to describe the radio emission by air showers.

(ii) Then for any given target shower B, the above-mentioned scaling coefficients are computed and applied to the signals at positions $\vec{x}_A$.

(iii) Following, the morphed shower is rotated along the same propagation axis $\vec{v}_B$ and translated so that $X^A_{max} = X^B_{max}$. The homothetic transformation given in equation 3.10 is also applied. The resulting antenna positions of the morphed shower are noted $\vec{x}_A$' in the following.

(iv) The final step of RadioMorphing consists in computing the radio signal at the requested antenna positions $\vec{x}_B$. This is done by interpolation on the closest $\vec{x}_A$' positions.

The whole process thus allows in principle to compute in a fraction of a second the radio signal generated at any position by any shower from one single simulated reference shower. The signals obtained with the RadioMorphing method were compared with those obtained through ZHAireS simulations (see Fig. 3.8). After a filtering of the signals in the 50-200 MHz band, the total signal amplitude was found to be larger than those computed with ZHaireS by 8.5% on average with a 25% rms dispersion [160], with largest differences observed close to the Cerenkov cone. The timing information obtained with RadioMorphing was however found not to be valid. Finally, RadioMorphing was tested with very inclined trajectories only. These issues have a limited impact on the computation of the chance probability that a shower is detected by a radio array and RadioMorphing could thus be included in the GRAND neutrino sensitivity simulation chain.

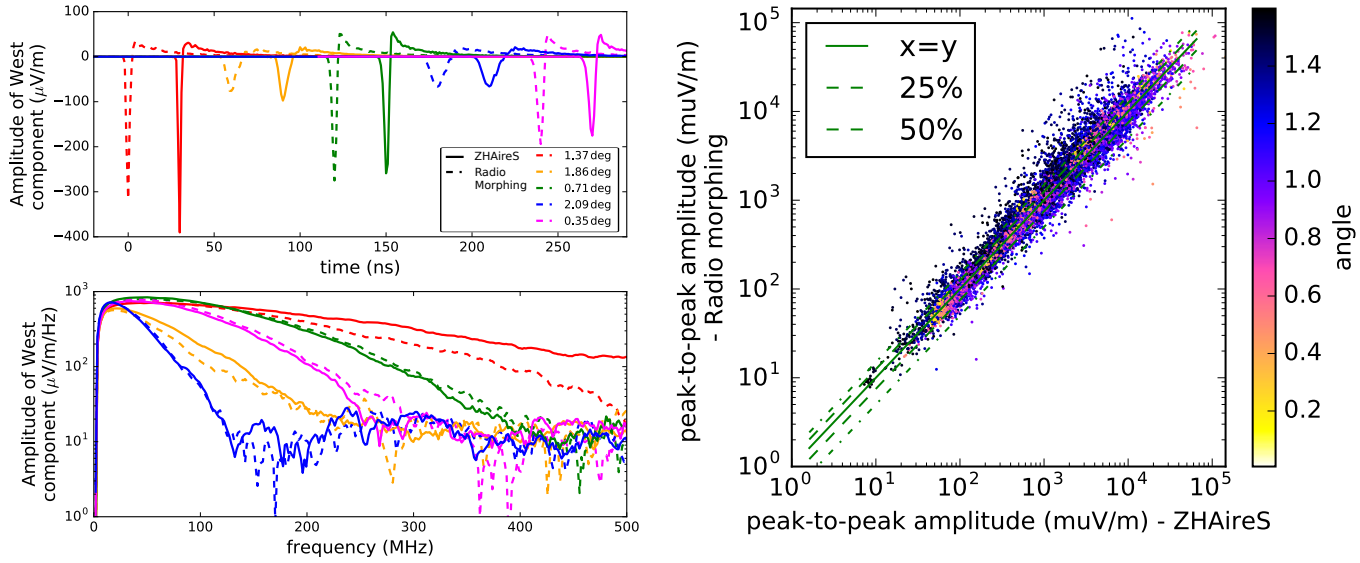

Figure 3.8: *Left: Example signal traces for an air shower induced by an electron with an energy of 1.05 EeV, an azimuth angle of 50° and a zenith angle of 89.5° (i.e. slightly up-going shower) using Radio Morphing (solid) and ZHAireS (dashed lines) for comparison. The antenna positions are at a 75 km distance along the shower axis from the shower maximum while the Cerenkov ring is expected to be at an off-axis angle of ∼1.4°. Top: Time-traces of the West-East component of the electric field for antenna positions in different distances to the shower axis, given as off-axis angle, in the time domain. The time-traces are shifted in time for a better visibility. Bottom: corresponding frequency spectra. Right: Comparison of the peak-to-peak amplitude in the East-West component of the signal detected by each antenna in a set of ∼300 inclined showers, calculated with Radio Morphing and simulated with ZHAireS. The color code represents the off-axis angle of the observer position with respect to the shower axis. The green solid line marks equivalent amplitudes, the dashed (dashed-dotted) line a 25% (50%) difference. Both plots are taken from [160].*

3.2.1.3 Radio signal propagation

If atmosphere is nearly transparent at radio frequencies, interactions with ground cannot be neglected for waves propagating along the horizon. The dominant effect is diffraction [186], which may induce a significant attenuation of the signal. A rigorous treatment would require that a complete ray-tracing is performed from the transmitter (i.e. the shower) down to the receiver (i.e. the antenna), taking into account all possible reflections on ground and also possible variation of refractive index. Software's performing such computation exist (see [187] for instance), but are too slow for our needs, and according to colleagues who tested in the framework of the BEACON project [148], results lack reciprocity.

Yet, it is in practice observed [186] that diffraction phenomena are negligible if there is no obstacle within the first Fresnel ellipsoid (see Fig. 3.9) and defined by an ellipsoid radius R:

$$R = 550\sqrt{\frac{d_1 d_2}{(d_1 + d_2)\nu}} \tag{3.11}$$

where ν is the frequency in MHz, d_1 and d_2 the respective distances in km from transmitter and receiver to the point where the ellipsoid radius R is calculated in meters.

For 79% of the trajectories simulated in the GRAND study and presented in section 3.2.2, the Fresnel ellipsoid intercepts ground only in the last 5 km (or less) for at least five antennas receiving the signal. Hence, ground effects during propagation can be considered as a second-order effect and solely included in the antenna response. This is discussed in the next section.

To be exhaustive on the treatment of signal propagation in this study, we may mention that antennas which are not in direct view of the point of maximum of shower development are excluded in a way similar to what is done in the Tianshan study.

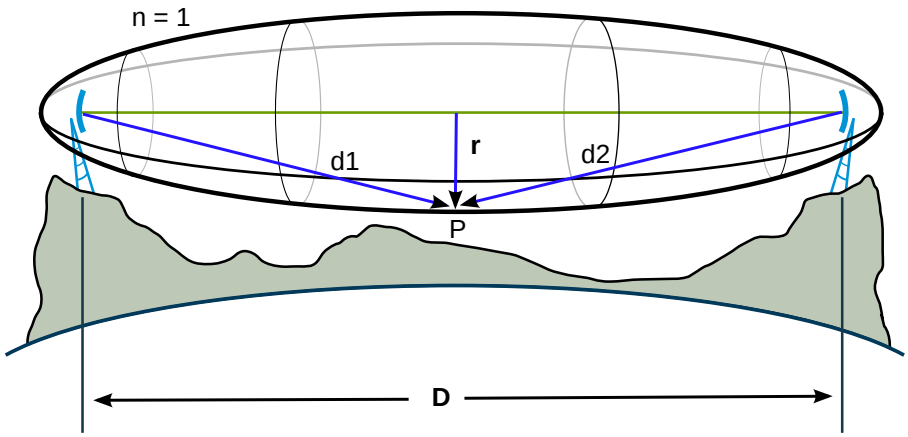

Figure 3.9: *Schematic of the Fresnel ellipsoid. Taken from Wikipedia.*

3.2.1.4 Antenna response

The next step in the simulation chain consists in computing the voltage induced at antenna output by the received electromagnetic radiation. From a technical point of view, this can be done by calculating the scalar product between the electric field time-trace at antenna location $\vec{E}(t)$ with the equivalent length $\vec{l}_{eq}$ of the loaded antenna (see Eq. 2.26). In practice though, the scalar product is calculated in the frequency domain because the antenna equivalent length is determined for fixed frequencies only. The voltage is eventually obtained by inverse Fourier transform:

$$V(t) = \int \vec{l}_{eq}(\theta^*, \phi^*, \nu) \cdot \vec{E}(\nu) e^{2i\pi\nu t} d\nu \tag{3.12}$$

where (θ^*, ϕ^*) is the *effective* direction of origin of the wave, computed in the local ground referential (see below).

3.2.1.4.1 Frequency range Maximizing the antenna effective length is an important aspect of the work at this stage of the simulation chain. This can be done in particular by selecting the operating frequency range corresponding to the best signal-to-noise ratio. A dedicated study was carried out on this specific issue by Sandra Le Coz, Anne Zilles and Aswathi Balagopal, then a PhD student at the Karlsruhe Institute of Technology, when she visited IAP in January 2018. They adapted to the specific case of GRAND a study Aswathi had led for the radio extension of the IceTop experiment [188]. Taking into account the typical environmental noise (see section 2.3.1.3) and the specific features of the electromagnetic field time-traces induced by horizontal showers, the study concluded that the 50-200 MHz range is appropriate for GRAND (see Fig. 3.10). This is somewhat higher than the typical frequency used in AERA [169] or TREND (see chapter 5), and is a consequence of the strong Galactic background at lower frequencies.

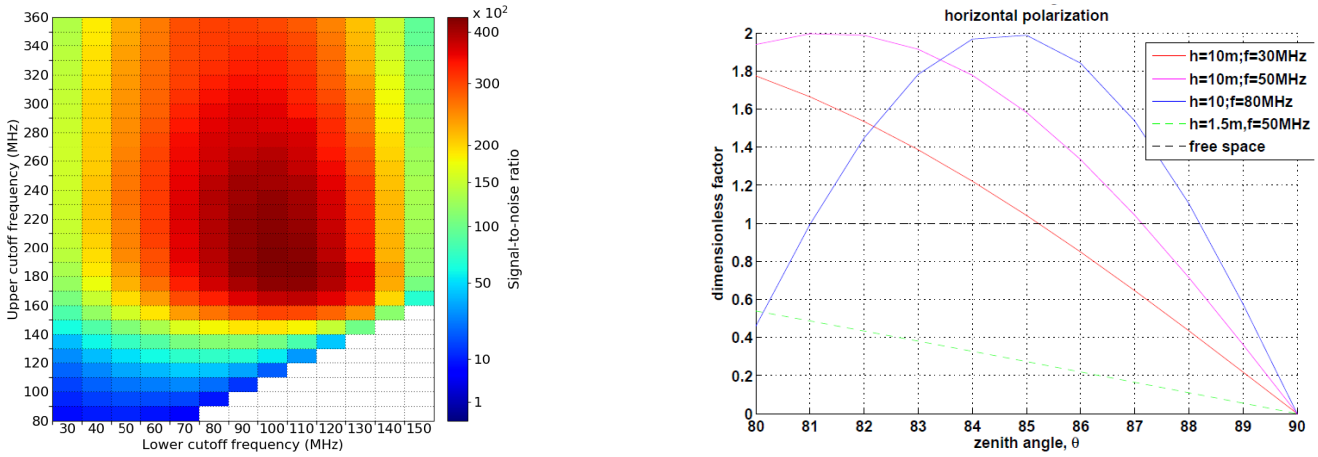

Figure 3.10: *Left: Simulation of the signal-to-noise (SNR) ratio seen in an antenna located on the Cerenkov ring made by a slightly up-going neutrino-initiated air shower of energy 0.5 EeV. The lower and upper cut-off in frequency were varied to maximize the SNR and optimize the frequency band. For an antenna position inside the Cerenkov ring, the optimal frequency range is somewhat lower. Figure taken from [1]. Right: signal amplitude at receiver location normalized by the amplitude at emission as a function of zenith angle for different frequencies and antenna heights. The computation was performed by Didier Charrier for an infinitely flat, conductive ground.*

Higher frequencies also imply smaller dimensions for resonant antennas (see e.g. Eq. 2.12). The design proposed by Didier Charrier for the GRAND simulation and latter optimized by Zhang PengFei, from Xi'An Xidian University, called the HorizonAntenna, is thus only 90 cm long, which has obvious mechanical advantages. It is a bow-tie antenna (see section 2.3.2.1) to improve its broad-band response, with 3 perpendicular arms, oriented along the East-West, North-South and vertical directions. It is represented in the left panel of figure 3.11.

3.2.1.4.2 Ground effects Ground has a significant effect on the antenna response, in particular for horizontally-polarized waves, i.e. those of concern for GRAND (see section 2.3.1.1 for details). These undergo a phase inversion when reflecting on the ground, which result in destructive interference with the incident one for path differences equal to multiples of the radiation wavelength λ. The corresponding zenith angles θ_n are given by:

$$\cos\theta_n = \frac{h}{n\lambda} \tag{3.13}$$

with h the antenna height above ground. For a perfectly reflective ground, this results in a null signal for zenith angles θ_n. This is true in particular for $\theta_\infty = 90°$ as clearly visible in the right panel of figure 3.10. This figure also shows that the ratio h/λ should be maximized to optimize the antenna response for incoming wave directions just a few degrees above horizon. The height of the HorizonAntenna was therefore set to 5 m above ground in the simulation.

In practice, the HorizonAntenna response is computed with the dedicated NEC software, assuming a flat ground of finite conductivity $\sigma = 1/\rho = 10\,\Omega^{-1}\mathrm{m}^{-1}$ and effective relative permittivity $\epsilon_r = 10$. These values correspond to a so-called *sandy dry ground*, conditions which describe at best those observed in remote desert-like areas of West China were the first GRAND sub-array is likely to be deployed (see section 7.5).

As expected from equation 3.13, this NEC computation results in a complex lobe pattern due to the constructive and destructive interactions of the reflected wave with the incident one, which are more frequent for an antenna high above ground. This effect certainly averages out when considering the full frequency range of the radio signal, but may raise serious challenges when it will come to a precise calibration of the antenna response. This will be investigated experimentally in the prototype phase of GRAND, called GRANDProto300 and presented in chapter 7).

NEC computations also indicate that the ground slope further impacts the lobe shape, as it rotates with the ground orientation (see right panel of figure 3.11). This effect was taken into account in the simulation by computing the effective direction of origin of the wave (θ^*, ϕ^*) in the ground referential, i.e. correcting the true direction of origin of the signal (θ, ϕ) by the ground slope, determined by averaging DEM data available in a radius of 200 m around the antenna position.

The strong effect of ground on the antenna response revealed by this computation raises serious concerns on the reliability and precision of the antenna response computation. This is especially critical for the GRAND neutrino sensitivity studied here, as the antenna gain varies by several dB over a few degrees only for directions close to the horizon. Determining and monitoring the actual ground effect will be a critical task in GRAND, which will also be initiated with GRANDProto300.

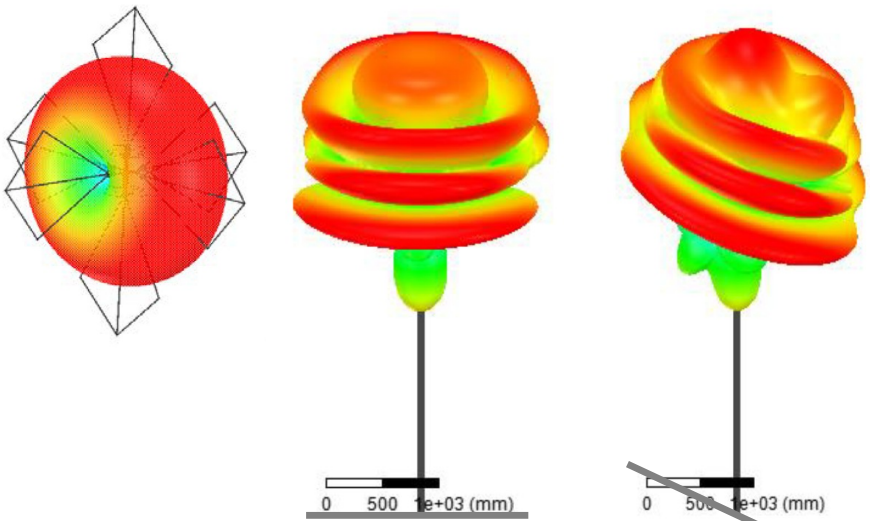

Figure 3.11: *Gain of an horizontal arm of the HorizonAntenna computed by Zhang Pengfei (Xidian University) with the HFSS program at a frequency of 125 MHz as a function of wave direction of origin in free space (left), for a flat ground (center) and for a 20° slope (right). The color code stands for the gain value in dB: red is +5 dB, blue is -5 dB. The HorizonAntenna is drawn on the left plot. The ground is indicated in the middle and right plots by a thick gray line. Antenna equivalent lengths are eventually determined from gain values through formula 2.25.*

3.2.1.4.3 Free space computation For the purpose of the GRAND study, it therefore appeared necessary to perform a cross-check of the simulation based on the HorizonAntenna response with ground by an independent calculation, where antenna response is determined in free space, in which case the lobe exhibits much smoother variations, as can be seen on the left panel of figure 3.11. The ground effect is then calculated analytically following the empirical treatment presented in [186] and summarized below.

The diffraction field strength E, relative to the free-space field strength E_0, can be computed as:

$$20 \log \frac{E}{E_0} = F(X) + G(Y_1) + G(Y_2) \tag{3.14}$$

with X the normalized length of the path considered:

$$X = 2.188\nu^{1/3}R_{\oplus}^{-2/3}d \tag{3.15}$$

and Y_1 and Y_2 the normalized heights of the wave at the emitter and receiver positions respectively:

$$Y_{1,2} = 9.575 \cdot 10^{-3}\nu^{2/3}R_{\oplus}^{-1/3}h_{1,2} \tag{3.16}$$

Then

$$\begin{cases} F(X) & = 11 + 10\log(X) - 17.6X \text{ for } X \geq 1.6 \\ F(X) & = -20\log(X) - 5.6488X^{1.425} \text{ otherwise} \end{cases}$$

and

$$\begin{cases} G(Y) & = 17.6\sqrt{(Y-1.1} - 5\log(Y-1.1) - 8 \text{ for } Y > 2 \\ G(Y) & = 20\log\left(Y + 0.1Y^3\right) \text{ otherwise} \end{cases}$$

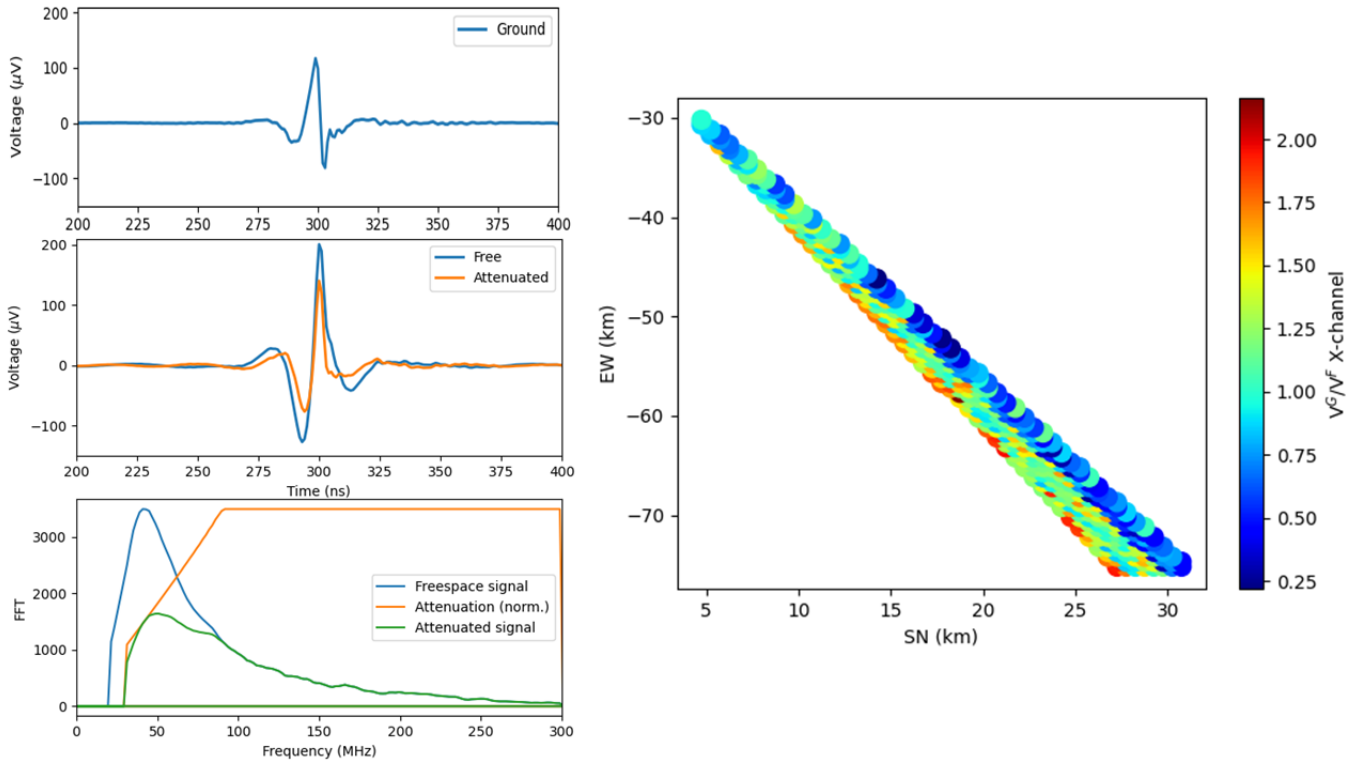

Figure 3.12: *Left: free space treatment for an antenna illuminated by a wave of zenith angle $\theta = 85°$ (middle panel). The blue curve is the antenna voltage computed in free space, orange after analytical treament from Equation 3.14. The corresponding FFTs are shown in the bottom panel. For this example there is no attenuation by ground for frequencies $\nu > 100$ MHz. The top panel is the voltage computed with the standard treatment (i.e. ground effect included in the antenna response). Right: ratio of the peak-to-peak voltage amplitudes in the 50-200 MHz range computed with free space and ground treatments for East-West arms of antennas deployed over a flat ground and illuminated by a $\theta = 87°$, $E = 9 \cdot 10^{17}$ eV shower. The mean ratio value is 1.10 and maximal amplitude value is 815 μV for this simulation.*

This treatment is applied to the section of the propagation path extending from the first point of the shower trajectory for which the Fresnel ellipsoid intersects ground —which we will call Fresnel point in the following— down to the antenna. Consequently the parameter d in equation 3.15 corresponds to the geometrical path length between these two points (in km), h_1 is the height of the signal path at the Fresnel point (in m) and h_2 the antenna height (in m). Following standard notations $R_{\oplus}$ is the Earth radius (in km) and ν the signal frequency in MHz.

The attenuation coefficient $\frac{E}{E_0}$ is computed from equation 3.14 for all frequencies in the 50-200 MHz range and the electric field at antenna location is then determined by inverse Fourier transform of the free-space field $\vec{E_0}(\nu)$. The treatment is then repeated for all antennas in a simulated event.

The treatment was first tested in the case of a detector deployed over a flat ground (see right panel of figure 3.12) for a set of ∼10000 simulations with inclined down-going trajectories $85° < \theta < 90°$. The ratio of the signal amplitudes determined with the standard treatment (i.e. ground effect included in the antenna response) to the analytical one was on average 1.0, 0.9, 0.8 for North-South, East-West and Vertical arms respectivelly, with standard deviations of 0.4, 0.3 and 0.5. Despite its large dispersion —not fully understood, but could be linked to the complex lobe structure of the antenna and abrupt gain variation close to the horizon—, we estimate that this result validates this independent approach, with could therefore be applied to the GRAND simulations.

3.2.1.5 Acquisition chain

The last element of the simulation chain consists of simulating the acquisition chain and the trigger. As there are very limited firm decisions taken on the technical details of the GRAND detector, only very basic assumptions are made for this simulation. They are detailed below.

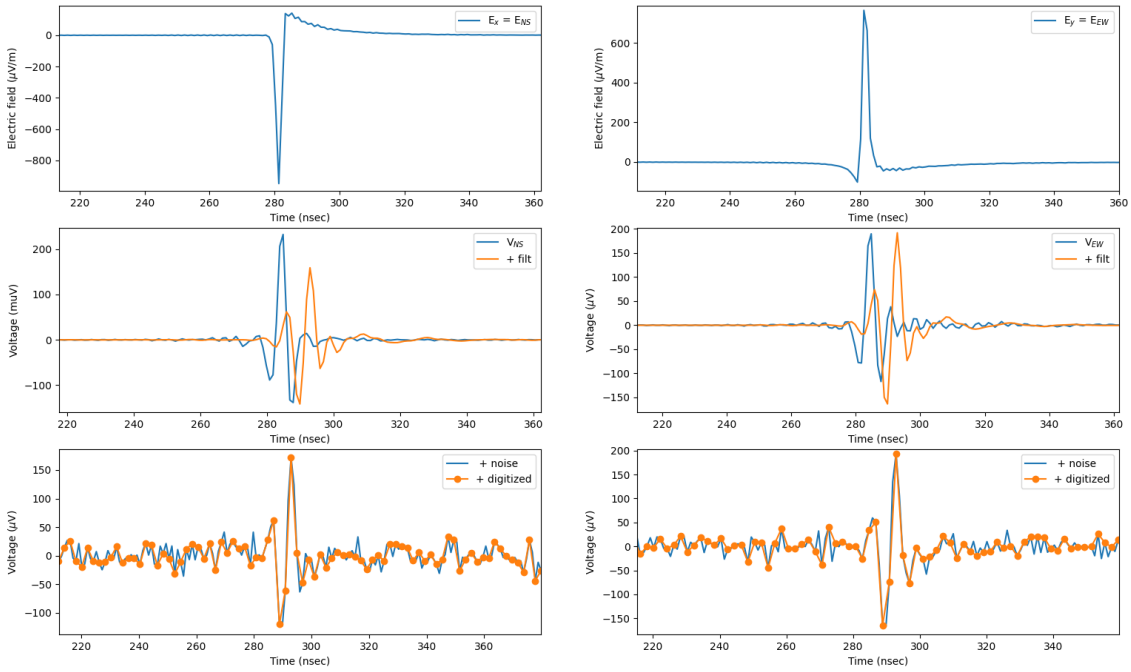

Figure 3.13: *Top: Horizontal components (left: North-South, right: East-West) of the electric field time-trace $\vec{E}(t)$ induced at one GRAND antenna position by a $E = 10^{19}$ eV, $\theta = 88°$ simulated shower. Middle: voltages computed with equations 3.12 at the HorizonAntenna output before (blue) and (after) the 50-200 MHz filtering. Bottom: signal after applying a Gaussian noise realization with $\sigma = 15\mu V$ (blue) and a 500MS/s sampling (orange).*

3.2.1.5.1 Front-end electronics The first stage of the GRAND electronic chain will most certainly consist of a signal amplification, so that latter noise contributions do not further alter the signal-to-noise ratio. Low-noise amplifiers (LNA) with equivalent temperatures as low as few tens of K —a value to be compared to the few thousands of degrees from the Galactic background (see e.g. figure 2.10)— are commercially available (see section 5.4.2.1).

Imperfect impedance matching at the antenna output (see Eq. 2.14) is likely to mitigate this statement and increase this contribution to a 20 to 50% fraction of the total noise, as computed by Didier Charrier in early studies for the HorizonAntenna. Nonetheless, LNA noise remains a minor contribution, and for the sake of simplicity, only the Galactic contribution (see section 2.3.1.3) was considered here. Its value varies with time because of the transit of the Galactic plane in the antenna field of view (see section 5.5.2.2 for details) but an average rms value of 15 μV was calculated for the HorizonAntenna in the 50-200 MHz range, using equation 2.19.

A Gaussian noise of standard deviation $\sigma_{\text{noise}} = 15\,\mu$V was correspondingly added to the simulated signal at antenna output. Prior to that, a filtering in the 50-200 MHz bandwidth applied to the trigger signal, a frequency range which might be later adjusted in a future study in order to optimize the trigger sensitivity. A 5^{th} order Butterworth filter was selected in the simulation, as this band-pass filter exhibits sharp edges, limited phase dispersion and can be easily implemented in practice.

The final stage of the simulated Front-End electronic treatment consists of digitizing the signal. A sampling rate of 500 MSamples/s was applied, a safe choice considering the 200 MHz upper bound of the GRAND frequency range. The different phases of the treatments are illustrated in figure 3.13.

3.2.1.5.2 Trigger A trigger decision is then made on the digitized signals. Again, very limited information is already defined on the trigger that will be implemented in the GRAND experiment. Consequently, only basic trigger schemes are considered in this simulation. It was in particular decided that the trigger decision would be divided in two levels: the first based on the digitized signal at the individual unit level, the second gathering information from units with first-level triggers.

Similarly to the Tianshan study, two options were considered for the first-level trigger. In the conservative one, antennas trigger if their peak-peak amplitude is larger than $5\sigma_{\text{noise}} = 75\,\mu$V. This threshold value corresponds to what is presently achievable. In an aggressive scenario a $2\sigma_{\text{noise}} = 30\,\mu$V threshold value is considered. It would be achievable only if innovative signal treatments were implemented online. This is further discussed in section 7.5.1.

For the second-level trigger, it is requested in this study that at least 5 antennas in a 9-unit square cell have first level triggers, a condition which would in practice limit the chance for random spurious coincidence between first-level triggers.

Background transient events are not considered here. As will be detailed in section 3.2.3, this will be taken into account in a further implementation of this study.

3.2.2 Results

3.2.2.1 Validation on Tianshan detector

The GRAND simulation chain presented in the previous section was first used to compute the response of the Tianshan detector for a set of 20 000 neutrinos. The result was compared on an event-by-event basis to the one obtained with the treatment presented in section 3.1.2 applied to the same input data set.

Figure 3.14 shows that both results are comparable, but the number of triggered antennas per event is on average smaller with the GRAND pipeline, and 11832 showers are detected versus 14306 with the initial simulation chain. The resulting exposure is consequently smaller, yielding an integral limit on a diffuse all-flavor flux of $3.7{\cdot}10^{-9}$GeV cm^{-2} s^{-1}, a factor $\sim$2 larger than the results of the Tianshan study presented in section 3.1.3.

The thinner stepping of the Digital Elevation Models used in the new analysis (200 m vs 400 m for the Tianshan study) partly explains this discrepancy. Switching back to a 400 m step indeed results in a larger effective area and a $2.7 \cdot 10^{-9}$cm^{-2} s^{-1} integral limit. Our understanding is that a denser DEM naturally leads to more obstacles, hence a larger shadowing effect and eventually a smaller number of showers detected. The significant influence of the DEM on the effective area raises concerns on the robustness of this treatment and urges us to plan for a more rigorous treatment of obstacles in future implementations of this study (see section 3.2.3 for more details). The second-level trigger —5 antennas in a square cell of 9 neighboring antennas, see previous section— also significantly affects the detection potential of the array: alleviating this constraint results in a $1.6 \cdot 10^{-9}$GeV cm^{-2} s^{-1} limit —41% better— while applying the same condition results in a 5% effect only on the limit in the initial treatment. Differences in particles transportation are likely to account for the remaining differences.

We can conclude that the factor 2 difference in the results of the two treatments is understood and remains acceptable, given that they correspond to two independent implementation of a complex process. This discrepancy however shows that important systematic effects affect the treatment, and should be included in the study.

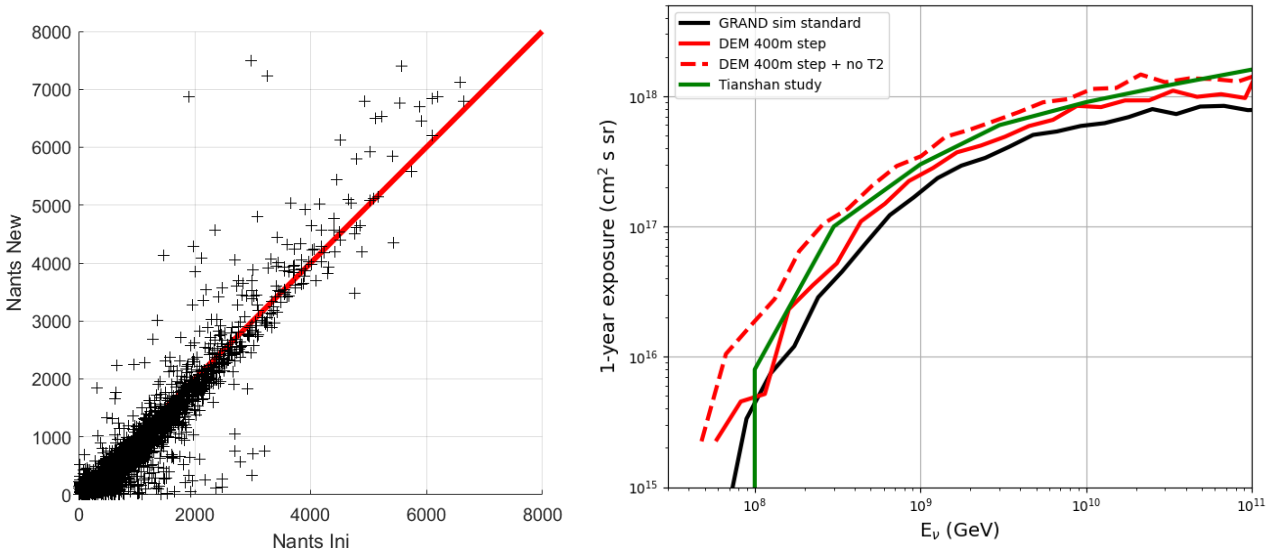

Figure 3.14: *Left: comparison between the numbers of triggered antennas in an event simulated with the GRAND and initial pipelines (y and x axis respectively) . The input to both treatments is an identical set of 20 000 neutrinos generating a tau decay. Right: one year exposure for the same detector. The green curve is obtained with the initial treatment, and the plain black one with the standard GRAND one. The red curves were computed with a 400 m step in the Digital Elevation Model data (200 m in the standard one), and without the 2nd level trigger for the dotted one.*

3.2.2.2 HotSpot 1

The neutrino sensitivity was then computed with the GRAND standard simulation chain for a radio array with 1 km-step square grid deployed over a $150\times67\,\mathrm{km}^2$ area on the Southern rim of the Tianshan mountains, centered on coordinates (42.1°N, 86.3°E), (see Fig. 3.15). This site, referenced as **HotSpot 1** (or HS1 for short) in the following, was selected because it is associated with enhanced events rates in the Tianshan study, and its topography —a ∼80 km wide basin— complies with the optimal configuration identified in [164].

We simulated 20 000 air showers initiated by ν_τ interactions underground, with the condition that the shower trajectories cross HS1. Neutrino energies range from $3\cdot10^{16}$ to $3\cdot10^{19}$ eV with 10 values per decade. Directions of origin are isotropic, but only a $\sim\pm4°$ range around the horizon is considered. For the wave propagation, we use separately the standard treatment —NEC antenna response computed with ground— and the alternative treatment —analytical computation of ground attenuation and antenna response computed in free space. We consider the aggressive and conservative detection thresholds separately. The DANTON simulations were run on the farm hosted at the IN2P3 Computing Center while electric field and voltage traces were mostly computed at the ForHLR cluster hosted by the Karlsruhe Institute of Technology. The resulting data —a list of peak-to-peak amplitudes for each triggered antenna— was small enough to finalize the treatment on personal computers. Figure 3.15 shows, for illustration, the result of one simulated neutrino-initiated shower.

Figure 3.16 shows the results of our simulation in terms of the exposure of the detector. The effect of the choice of treatment of wave propagation is small, and compatible with statistical fluctuations. Using the aggressive threshold instead of the conservative threshold increases the effective area roughly by a factor of 2.5. Hence the achieved detection threshold will be key to improve the statistics of detected events. The event rate is roughly four times smaller for a flat topography than for HS1: mountains do play an important role for the detection of neutrino-induced showers. This is confirmed when looking at the distribution of the events directions of origin in figure 3.17.The zenith distribution (top left) in particular peaks in a narrow window around the horizon, with about 40% of events having downward-going trajectories, initiated in the mountains volume. The azimuth distribution (bottom left) shows a clear excess for

ϕ_τ around 0 and 180°, corresponding to showers propagating along the South-North axis and detected by antennas deployed on the Southern slopes of the Tianshan mountain range or on the mountain ridge closing the basin to its South.

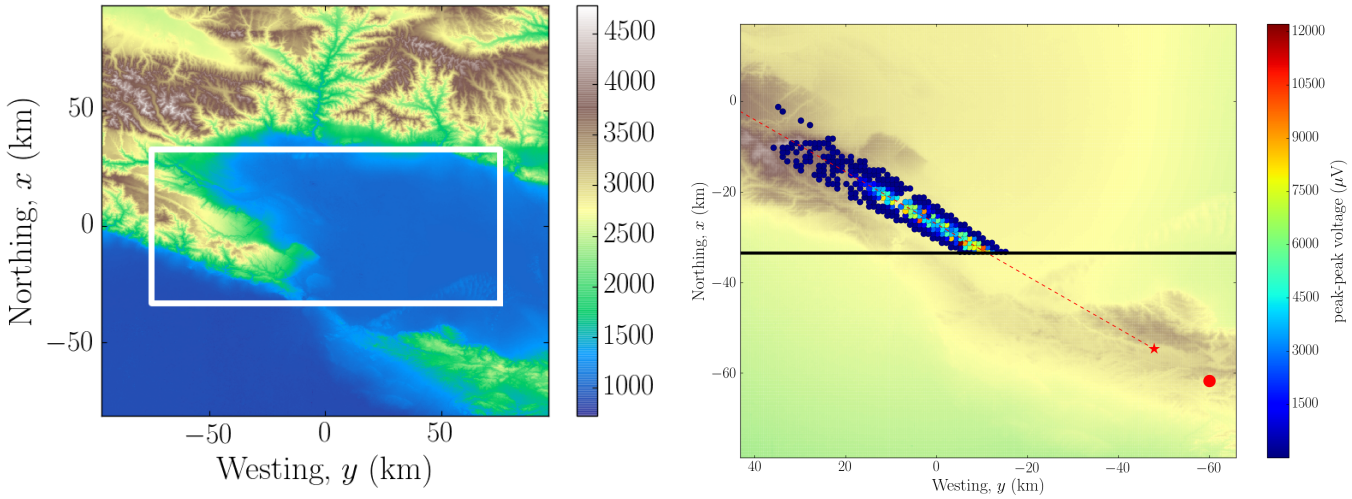

Figure 3.15: *Left: the HotSpot 1 detector (white rectangle) deployed around a large basin on the Southern rim of the Tianshan mountains. The color code stands for the altitude above sea level in meters. Right: One simulated neutrino event displayed over the ground topography of HotSpot1. The red circle shows the position of the tau production and the red star, its decay. The dotted line indicates the shower trajectory. Circles mark the positions of triggered antennas. The color code represents the peak-to-peak voltage amplitude of the antennas. The Southern border of HotSpot1 is indicated with a black line. Taken from [1].*

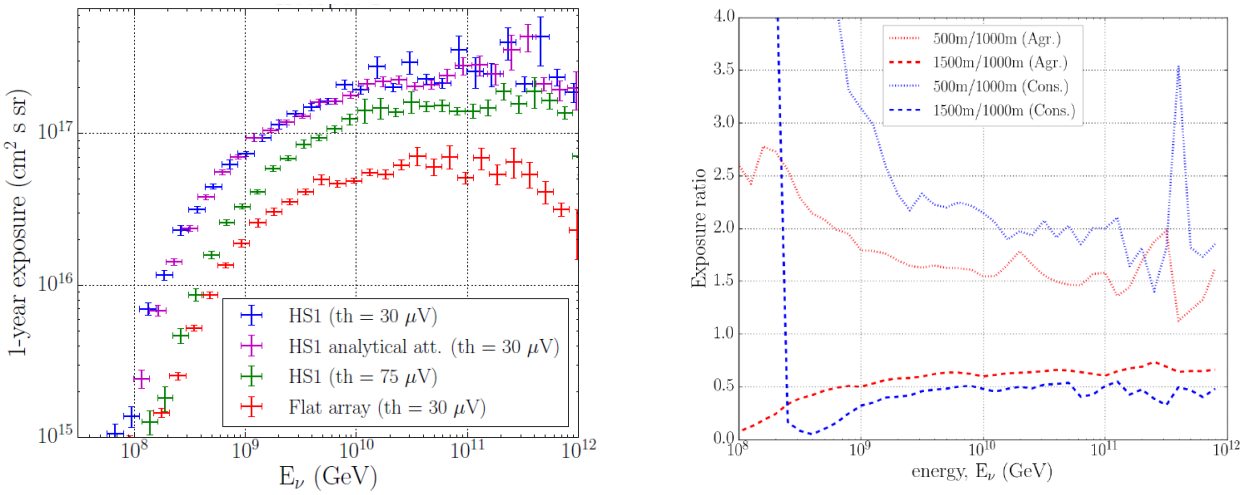

Figure 3.16: *Left: effective area for HotSpot1 for aggressive (purple) and conservative (green) trigger thresholds. Also shown are the effective areas for the analytical treatment of the ground attenuation (purple) and a flat site of same size (red). Taken from [1]. Right: exposures for arrays with spacing between antennas of 500 and 1500 m relative to the value obtained with the standard 1000 m spacing. The conservative 1500 m/1000 m curve (blue dashed) should be ignored for energies below $10^{8.5}$ GeV.*

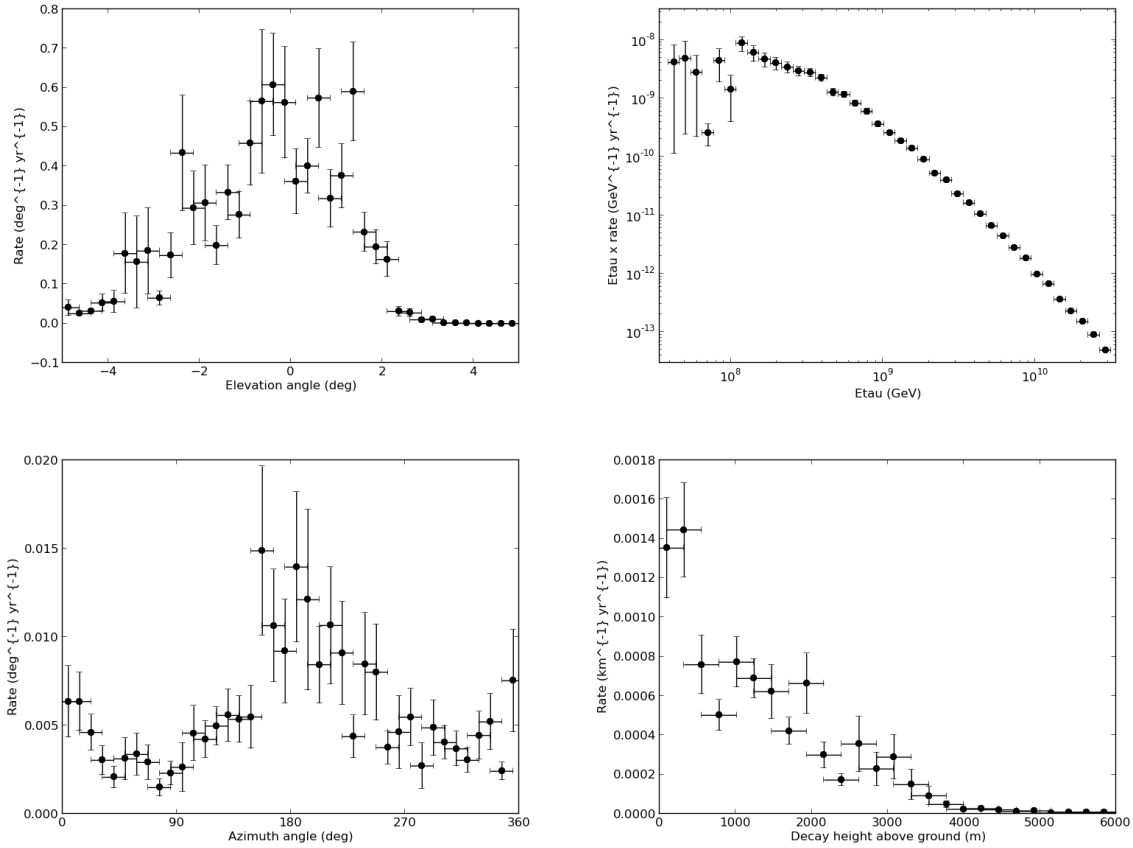

Figure 3.17: *Differential event distributions computed with the aggressive scenario for a Waxmann-Bahcall neutrino flux [61]. Elevation is defined as the angle counted positively when moving upward from the horizon and is measured here at the tau decay point.*

The effect of antenna density was also studied, with simulations run for antenna spacings of 500 m and 1500 m. It was found that a 4 times larger antenna density yields a factor ∼2 in exposure on average (more at low energies), while a factor 1.5^2=2.25 sparser array corresponds to an exposure twice lower, with a $10^{17.5}$ eV threshold for the conservative scenario (see Fig. 3.16). The 1 km step thus appears like a good compromise. However this statement may be adjusted in due time, depending on the targeted science case. This is further discussed in the next section.

From the effective area computation a $8.1 \cdot 10^{-9}$GeV cm^{-2} s^{-1} 3-years limit can be derived on an all-flavor diffuse neutrino flux in the aggressive scenario using equation 3.5. The limit is $2.0 \cdot 10^{-8}$GeV cm^{-2} s^{-1} for the conservative hypothesis. The corresponding differential sensitivity limits are plotted in figure 1.5.

As the simulation process was performed on HS1 only, the sensitivity of the full GRAND array could only be derived by scaling the present results to the full 200 000 km^2 area. Hence it is assumed that a sensitivity 20 times better may be achieved with GRAND200k, corresponding in the aggressive scenario to a integral limit of $4 \cdot 10^{-10}$ GeV cm^{-2} s^{-1} for 3 years of observation if no neutrino candidates are observed.

3.2.3 Next steps

The HS1 study is only a first step in the study of the GRAND sensitivity to neutrinos. Several additional tasks need to be achieved before this work can be considered complete.

First, the simulation chain should be improved. In particular:

• Radio Morphing should be upgraded. Matias Tueros, an active GRAND member from the *Instituto de Fisica* at La Plata and based at IAP since 2018, has solved the timing issue mentioned in section 3.2.1.2 and greatly improved the quality of interpolation [189]. We believe that this, combined with a refined morphing algorithm, could lead to a RadioMorphing treatment providing radio time-traces very similar to those obtained with microscopic codes, for any range of directions of origin. Given the huge gain in computing time that Radio Morphing represents, this would incidentally open the way to an extensive use of the method inside the GRAND collaboration, and beyond, for other radio projects. Work in this direction was recently initiated by Simon Chiche, the PhD student I advise together with Kumiko Kotera since October 2020.
• a proper ray-tracing of the electromagnetic radiation from source to observer should be implemented, taking into account interaction with ground, modeled for instance through a tessellation of DEM data. Systematic uncertainties associated to this specific issue should also be estimated and adequately propagated through the treatment.
• a precise determination of the antenna lobe computation should be performed, taking into account the influence of ground conditions, slope, and any relevant experimental parameter. This task will be initiated on GRANDProto300 (see chapter 7), using as a work base previous calibration work carried out on AERA [190]. Here again, systematic uncertainties should be evaluated and included in the calculation.
• realistic elements of the DAQ chain should be included in the simulation. These could be based on the GRAND-Proto300 detector. Similarly, trigger strategies presently being investigated within GRAND —in particular by the very active GRAND group in Rio de Janeiro— could be included. The very crude second level trigger algorithm applied in the simulation should also be refined.
• a more refined model should be used for the noise. Here again, GRANDProto300 could be instrumental as measurement of the background radio environment could provide appropriate input to the GRAND simulation.
• finally the square grid should be replaced by an hexagonal one. It has been shown [191] that this may improve the detection efficiency by ∼10%, while it will most likely improve event reconstruction performances because of the reduced number of peculiar directions compared to a square grid.

Second, background events should be injected in the simulation in order to determine how neutrino events could be discriminated from them. This would be extremely challenging —if possible— for events of anthropic origin, as there is no actual model for those, neither data on scales instrumental to GRAND. This should however not be a critical issue, as there are a number of ways to identify these transient radio noises, as will be discussed in part II.

Another source of background may however be more problematic: cosmic rays. For very inclined trajectories, some of them could indeed be wrongly reconstructed as coming from below the horizon. Since the corresponding showers would induce similar features to neutrino-induced ones, there is a high risk that they would be tagged as neutrino candidates. Selecting events with incoming direction significantly below the horizon —a few times the angular resolution $\delta\psi$ for instance— could be a way to reject them, because it would require an unlikely large error on the direction of origin for a cosmic ray event to pass this cut. In the meantime, this cut would only mildly affect the neutrino detection efficiency for $\delta\psi$ small enough and in the case of a mountain site: as the rejected angular range just below the horizon line probably represents a negligible target for neutrinos to induce showers. Position of the shower maximum —much deeper for neutrino-induced showers— provides another tool to identify cosmic-rays. Yet, since the cosmic rays flux exceeds that of neutrinos by order of magnitudes, such qualitative arguments are not enough, and a careful study should obviously be carried out.

Third, this simulation chain should be applied over a significant fraction of the Earth surface —targeting remote mountain areas in Asia or America for instance— in order to identify the 20 sub-arrays composing the full GRAND detector. This is technically possible, in particular because DANTON was designed to run over continent-size areas. Only once this simulation has been performed will we be able to predict reliably the GRAND sensitivity to neutrinos.

Achieving these various tasks would however not be the end of the road: it would then be worth evaluating quantitatively the answers GRAND could provide to the questions raised in chapter 1. We could for example try to infer from the distribution of directions of origin and energy spectrum of a given set of neutrino candidates the constraints implied on their sources, one of the first question being: "are the neutrinos cosmogenic or do they correspond to one source or several sources from a same type, or different populations?". On this specific issue a study [192] has shown that an excellent angular resolution is key. This naturally drives us to the topic of the reconstruction of the primary particle reconstruction, detailed in the next chapter.

Before that, we will conclude this chapter by briefly discussing GRAND's potential for the detection of UHECRs

and UHE γ-rays. As mentioned just above, a complete study of the GRAND detector's response to these cosmic messengers remains to be done, but a very preliminary study was carried out by Nicolas Renault-Tinacci, post-doc at IAP between March 2017 and December 2018, for the GRAND white paper [1] under my supervision. I summarize it below.

3.3 Detection of Ultra High Energy Cosmic Rays with a giant radio array

Given the sparse layout of the GRAND detector, UHECRs with very inclined trajectories only are likely to induce footprints on ground large enough to include five antennas or more, the minimal number for trigger and reconstruction, as clearly visible on the left panel of figure 3.18.

Large zenith angle values correspond to a thicker layer of atmosphere, hence showers developing further away from the detector (see Fig. 3.19). Dilution of the radio signal implies that the detection threshold will be higher than neutrino-induced showers, which will develop closer to the detector. Preliminary simulations, carried out for proton primaries with energies between 10^{17} and 10^{19} eV however indicate that an excellent detection efficiency is achieved for θ >65° and E> $5 \cdot 10^{18}$ eV in the case of the GRAND detector, thus yielding an aperture around 25 times larger than the 4500 km^{2}sr averaged value obtained by Auger over its 14 years of operation above this energy.

For a detector deployed at moderate latitudes, sensitivity at large zenith angles also translates into a much larger field of view. Assuming for instance that 20 arrays with acceptance identical to HS1 are uniformely distributed between latitudes of 60° North and 40° South, Figure 3.18 shows that the GRAND exposure would cover a declination range which encompasses both Auger and TA ones.

As γ-rays are more penetrating, similar exposure are expected for them at energies above $5 \cdot 10^{18}$ eV, opening very attractive prospects for the search of cosmogenic γ-rays (see section 1.1.5). The level of performances needed for γ-ray identification —and how to achieve them— have not been studied yet.

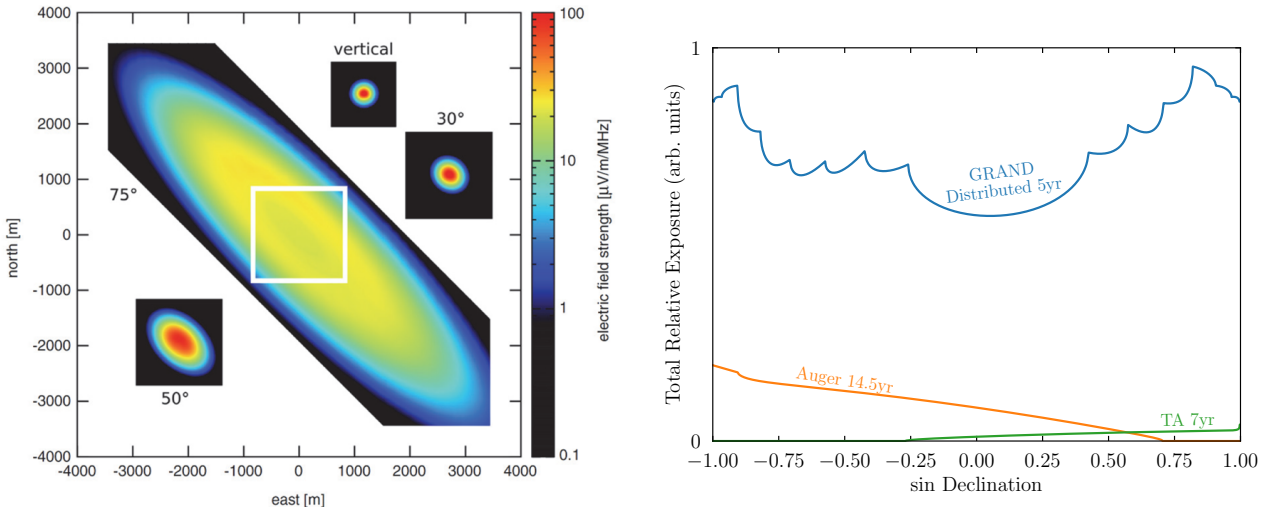

Figure 3.18: *Left: Simulated EAS radio footprints with various zenith angles in the 30-80 MHz frequency band for an energy of* $5 \cdot 10^{18}$ *eV. The detection threshold corresponds here to ∼1-2 V/m/MHz. The white rectangle denotes the size of the 50° inset. Taken from [193]. Right: The relative annual geometric exposure to UHECRs of Auger, TA and GRAND. The GRAND exposure is computed assuming that 20 arrays with acceptance identical to HS1 are uniformely distributed between 60°N and 40°S. At high energies these detectors are fully efficient so the geometric exposure approximates well the true exposure. Plot by Peter Denton.*

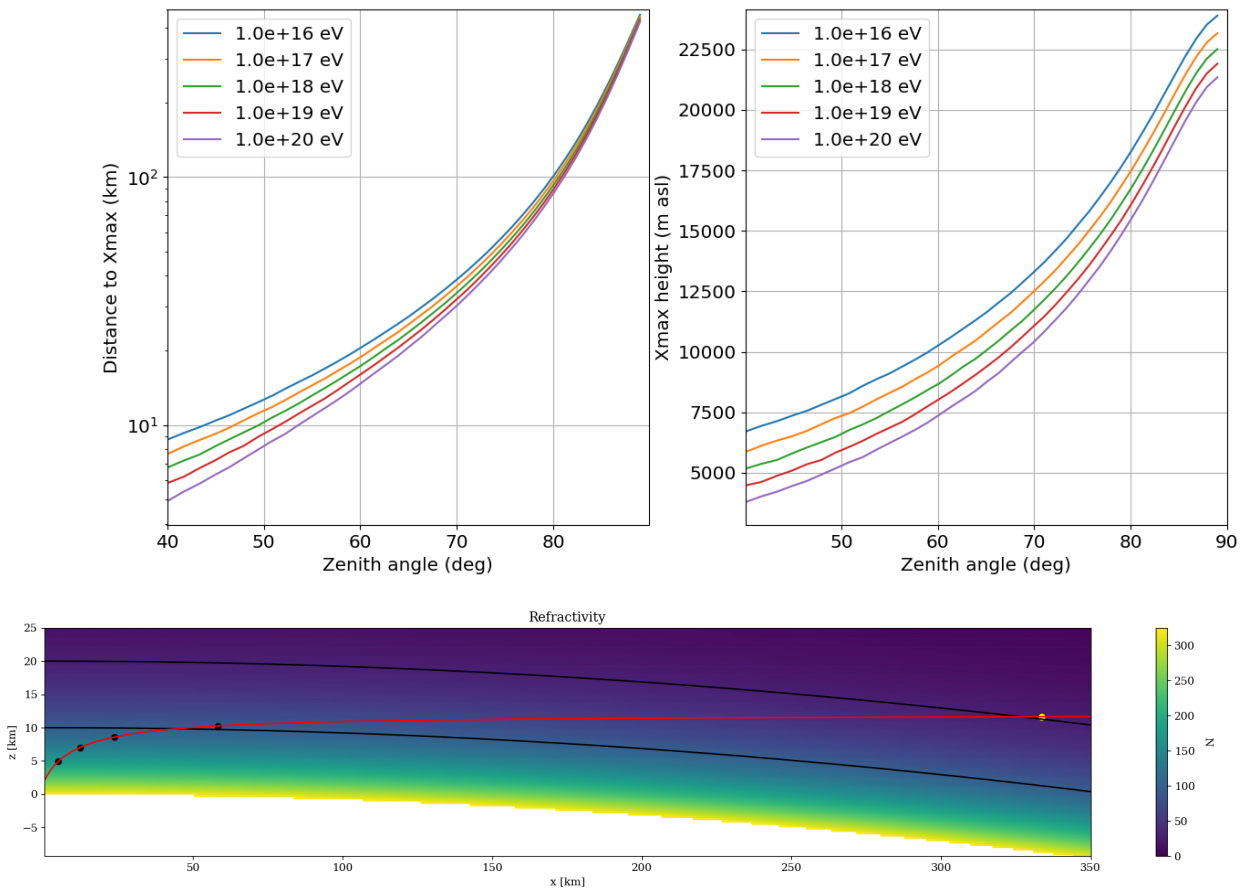

Figure 3.19: *Top: Distance to ground (left) and height a.s.l. (right) for the average X_{max} position of a proton at various energies. Bottom: refractivity $N = (n-1) \times 10^6$ as a function of height (vertical axis). The white zone corresponds to the Earth volume. Also shown as dots are the average positions of shower maximum as a function of ground distance to core (horizontal axis) and height for zenith values θ = 45, 60, 70, 80 (black) and 88° (yellow). Plot by Matias Tueros.*

Chapter 4

Reconstruction of cosmic particle properties with GRAND

The quality of the reconstruction of the characteristics of cosmic particles —direction of origin, energy, and nature of the primary— detected with the GRAND detector will be key to achieve the science goals defined in chapter 1. Impressive progress in the analysis of the EAS radio data has been achieved over the last years, thanks in particular to the AERA [194], LOFAR [195] and Tunka-Rex [196] experiments, reaching performances comparable to those of other techniques (array of particle detectors, fluorescence telescopes or Cerenkov detectors). This was possible thanks to sophisticated reconstruction algorithms building on a precise understanding of the signal characteristics of radio emission from extensive air showers and their successful implementation in dedicated Monte-Carlo codes (see section 2.3.1 for details).

Yet, most of these analyses have been been carried out on showers with zenith angles $\theta < 60°$ and data recorded in the 30-80 MHz frequency band. Dedicated reconstruction procedures therefore have to be developed for the specific case of GRAND radio signals, i.e. recorded in the 50-200 MHz from nearly horizontal showers.

I have devoted a sizable fraction of my time to this task over the last two years, through the supervision of the work of two young researchers on issues directly related to this topic: Valentin Decoene, graduate student at IAP between 2017 and 2020, studied in his PhD the time and amplitude information of radio signal from inclined EAS in order to reconstruct the characteristics of the cosmic primaries, while Simon Chiche, Master student between March and July 2020 and now PhD student at IAP, investigated the polarization information of EAS radio signals. Both Valentin and Simon implemented and led these analyses with large autonomy, but I took an active part in defining the research goals and methods of these studies, adjusting the work plan throughout the process and interpreting the results together with them. I give a summary of these two analyses in this chapter using material taken from [99, 197] and [198] respectively.

4.1 Wavefront of inclined showers

We focus in this first section on the the description of the shape of the radio wavefront. While the shower wavefront is loosely defined —in particular because of different arrival times for muons and electrons— simulations show that the radio wave is very compact, with a signal concentrated within few nanoseconds at the Cerenkov angle. This provides favorable conditions for its analysis.

After a brief summary of previous work, we will show how the work carried out by Valentin led to the conclusion that a spherical approximation was suficient to describe the radio wavefront of inclined showers.

4.1.1 Modelisation

4.1.1.1 An evolving wavefront

4.1.1.1.1 Previous works Various studies (e.g. LOPES and LOFAR experiments [199, 200]) have proposed different models to describe the EAS radio wavefront. The wave arrival times on LOFAR antennas were in particular

found to be best fitted by an hyperbolic function of the lateral distance to the shower [200] (see Fig. 4.1):

$$ct_i - n\,\vec{k}\cdot(\vec{x}_i - \vec{x}_0) = \sqrt{a^2 + b^2 r_i^2} - a\ , \tag{4.1}$$

where c is the light velocity, n the air refractive index and $\vec{x}_0$ the position of the shower core at origin. Antenna positions are noted $\vec{x}_i$, and correspond to distances r_i from the shower axis defined by $\vec{k}$. The term on the left of equation 4.1 thus corresponds to the time delay of the antenna trigger instant t_i to a plane wavefront, modeled by an hyperbolic function (right term of the equation), characterized by two (empirical) parameters a and b adjusted through a fit.

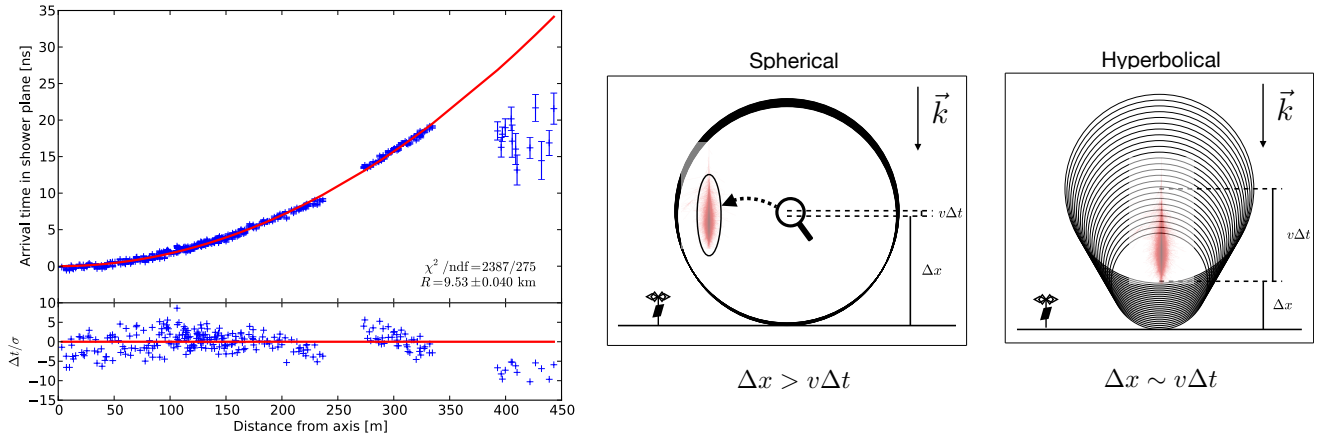

Figure 4.1: *Left: arrival time differences from a plane wave as a function of distance to the shower axis with a hyperbolic fit (top panel) and deviations from the best fit scaled to the uncertainty for each data point (bottom panel). Center and right: toy model describing a point source moving vertically at a velocity $v > c/n$ and emitting for a limited amount of time Δt. The solid horizontal line represents the ground plane. Observers at large (intermediate) distances Δx from the source see a spherical (hyperbolic) wavefront shape. Taken from [200].*

4.1.1.1.2 Inclined showers Valentin Decoene focused in his PhD thesis on the description of the wavefront of very inclined showers. The material used in this study consists of cosmic ray simulations with zenith angles θ between 80 and 88°, performed with the ZHAireS code. The detector layout is composed of antenna planes placed perpendicularly to the shower axis at longitudinal distances L_j from X_{max} ranging from 5 to 200 km. This work showed that the radio wavefront indeed follows an hyperbolic shape on each of these antenna planes (see left panel of figure 4.2). However, the sets of values of the hyperbola parameters (a_j, b_j) defined in equation 4.1 where found to differ significantly when adjusted independently for each antenna plane j, thus indicating that the radio wavefront shape evolves as the signal propagates.

A similar result was found for neutrino-induced horizontal showers illuminating a large array of antennas deployed on the ground, indicating that GRAND-type detectors should be sensitive to the longitudinal development of air showers. This is major difference with most types of EAS detectors, which take an snapshot of the nearly vertical showers at the instant when the particles or electromagnetic radiation reach ground.

The analysis further showed that the ratio b^2/a drops as the inverse of the longitudinal distance to X_{max}: $\left(b^2/a\right) \propto (n/L_i) \ll 1$ (see right panel of figure. 4.2). Eq. 4.1 then reduces to:

$$ct_i - n\vec{k}\cdot(\vec{x}_i - \vec{x}_0) \approx \frac{n}{2L_i} r_i^2 \tag{4.2}$$

Choosing additionally $\vec{x}_0 = \vec{X}_{max}$, we have $\vec{k}\cdot(\vec{x}_i - \vec{x}_0) = L_i$, longitudinal distance between X_{max} and antenna i, and eventually:

$$ct_i \approx nL_i + \frac{n}{2L_i} r_i^2 \tag{4.3}$$

an expression which also corresponds to a first order development of the spherical equation $ct_i = nR_i$, with R_i the total distance of antenna i to X_{max}, which can be written as the quadratic sum of lateral and longitudinal distances r_i and L_i. This development is valid for inclined showers, as then $r_i \ll L_i$.

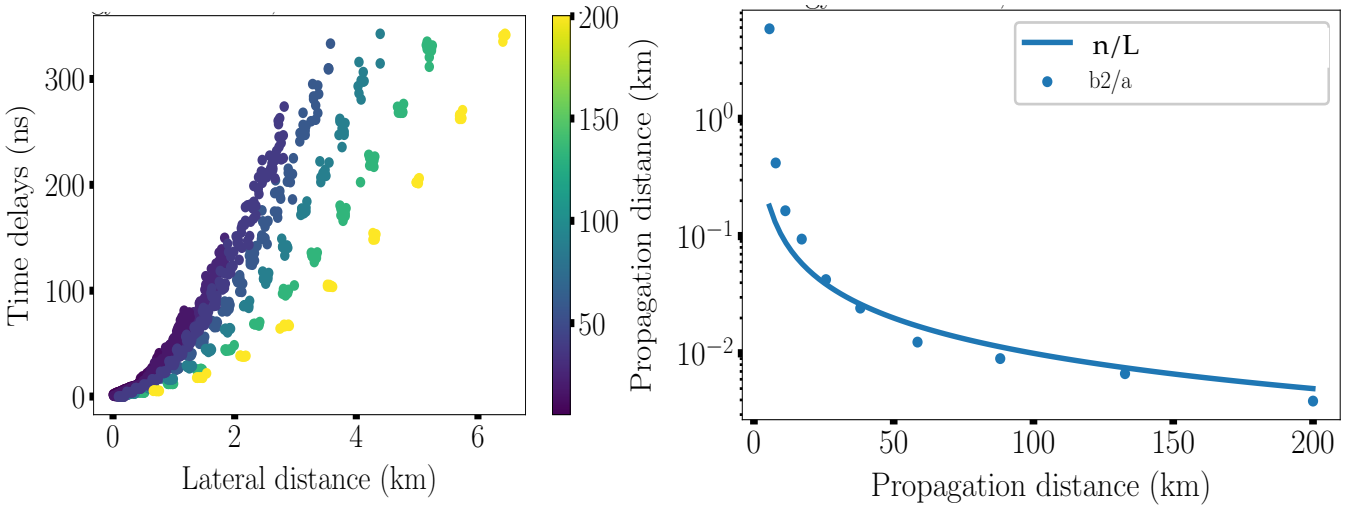

Figure 4.2: *Left: arrival time differences from a plane wave as a function of lateral distance for antennas placed at fixed longitudinal distances L_j = 17.5, 25.8, 35.8, 58.5, 88.1, 132.7 and 200 km from X_{max}. Time delays from each antenna plane j can be adjusted satisfyingly with a hyperbolic wavefront (with $\sigma_{residuals}$ <2 ns for each plane), but data from all planes together cannot, as the wavefront shape clearly flattens with increasing longitudinal distance. Right: ratio (b^2/a) as a function of L_j, with a and b parameters of the hyperbola as in equation 4.1. The function n/L is also plotted. Figures by Valentin Decoene.*

4.1.1.2 Spherical approximation

Equation 4.3 is the analytical form of a sphere inflating at a speed c/n, which indicates that the wavefront of inclined showers is approximately spherical, i.e. its source of radiation can be considered as point-like and static. This corresponds, in the model detailed in [200], to the case where the extension of the emission zone of the radiation is much smaller than its mean distance to the observer (see the sketch at the center of figure 4.1). This condition is indeed fulfilled for inclined showers: coherence arguments indicate that the strength of the electromagnetic radiation is directly proportional to the number of particles (see Eq. 2.7), hence peaking sharply —ie over a few kilometers at most— around X_{max}, while the shower maximum is distant by several tens of kilometers for showers induced by neutrinos, and hundreds in the case of cosmic rays (see left panel of figure 3.19).

Adjustments with a spherical fit of the simulated trigger times yielded residuals comparable to those of a hyperbolic fit for $L_i \gtrsim$80 km [99], hence confirming that the approximation of a point-like, static source for the electromagnetic radiation by EAS was valid for inclined showers.

4.1.2 Reconstruction

A spherical fit was applied to cosmic-ray-induced showers simulated over the GRANDProto300 detector (see chapter 7), a small-scale version of the GRAND HS1 array studied in section 3.2.2.2. To make this treatment realistic, the antenna trigger times were smeared with a σ=5 ns Gaussian jitter mimicking the experimental timing resolution while only antennas with peak-to-peak amplitudes larger than 110 μV were included in the analysis. Proton, iron and gamma primaries were considered, with energies ranging from 10^{17} to $3.98 \cdot 10^{18}$ eV and zenith angles between 63 and 87°.

The treatment yielded a lateral distance —i.e. in the direction perpendicular to the shower axis— between the reconstructed source position X_{radio} and the shower maximum X_{max} of 90 m on average, with a standard deviation of

150 m. No significant dependency on energy or primary nature was observed, but the distance was found to increase with zenith, which is certainly due to the larger distance to X_{max}, hence sphere radius [99]. This impressive lateral resolution —we are talking here of errors below 100 m for a source distant by ∼100 km at least– is achieved thanks the large extension of the detector array, which provides a powerful lever arm to constrain this parameter.

As one could expect, the longitudinal resolution is however not as good, with a distance to X_{max} equal to $-3 \pm 20\%$ for the full statistics considered. This negative average value means that the source is systematically reconstructed further away than the shower maximum, an effect presently under investigation [197].

The reconstructed source position X_{radio} may potentially be used as a proxy to determine the nature of the primary cosmic ray, in a way similar to X_{max}. Systematic differences between different primaries have been observed, but the resolution of this method is still under investigation in a study led by Valentin, together with Matias Tueros and myself [197].

To conclude on this section, we may point that a spherical treatment of the wavefront has the advantage of simplicity, and may also provide a handle for the determination of the nature of the primary, as just mentioned. There is however a downside: the propagation of the radiation being then considered isotropic, information of the direction of origin of the particle cannot be determined from a spherical wavefront shape. To determine it, additional information is needed. The possibility to use the amplitude pattern of the radio signal was investigated. This is detailed in the next section.

4.2 Amplitude pattern of EAS radio signals

4.2.1 Methods and tools

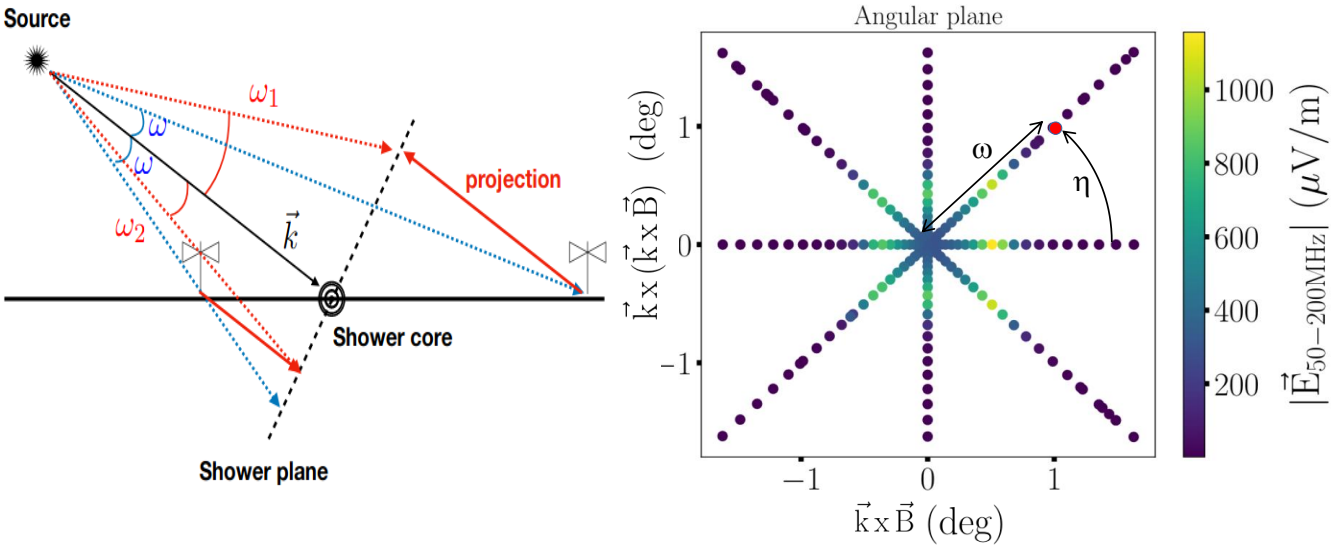

Figure 4.3: *Left: representation of the angular distance ω between antenna and shower axis, with the X_{radio} position (see section 4.1.2) used as the origin. Also shown on the plot is the so-called shower plane, perpendicular to the shower propagation direction $\vec{k}$ and placed at the intersection of the shower axis and ground. Right: representation in the angular plane of a simulated event over the star-shape antenna layout. Positions are represented in the angular plane with polar coordinates ω and η which is measured counter-clockwise from the $\vec{k} \times \vec{B}$ axis. The Cerenkov ring appears as a circle in the angular plane. Taken from [99].*

The amplitude pattern was studied in the so-called **angular plane** (ω,η) represented in figure 4.3. The angle ω defines the angular distance of the antenna to the shower axis measured from the radiation point source X_{radio} defined in section 4.1.2), while η measures the antenna angular position with respect to the $\vec{k} \times \vec{B}$ axis. We found this representation

to be best adapted to the conical symmetries of the EAS radio emission already pointed in section 3.1.2.2. We note in particular that the Cerenkov ring is in the angular plane a circle of radius $\omega = \omega_C$, with $\omega_C = \arccos(1/n)$ the Cerenkov angle, while it is an ellipse when projected on ground or in the shower plane.

The antenna layout used in this study follows a star-shape pattern on a flat ground, with constant step in ω values. A star-shape layout allows to sample at best the features of the radio amplitude pattern.

ZHAireS simulations were used in this study with gamma, proton and iron primaries for energies ranging between $2.5 \cdot 10^{16}$ and $3.94 \cdot 10^{18}$ eV and zenith angles between 38 and 88°.

4.2.2 (A)symmetries in the amplitude pattern

The goal of the study presented in [99] is to adjust the 2D amplitude pattern in the (ω, η) plane with an analytical formula depending on the shower propagation direction $\vec{k}$. To build this fit function, the various contributions to the amplitude pattern must first be explicated.

4.2.2.1 Geomagnetic effect

The interplay between the charge excess and geomagnetic emission processes, already presented in section 2.3.1.1, induces an asymmetry along the $\vec{k} \times \vec{B}$ axis. It was described analytically by Simon Chiche through the development detailed hereafter.

Given the respective symmetries of the charge excess and geomagnetic contributions $\vec{E}_{ce}$ and $\vec{E}_{geo}$ (respectively radial and parallel to $-\vec{e}_{k\times B}$, see figure 2.7), the components of the total electric field $\vec{E}$ in the angular plane write as:

$$\vec{E}_{k\times B} = -(E_{geo} + E_{ce}\cos\eta)\vec{e}_{k\times B} \tag{4.4}$$

and

$$\vec{E}_{k\times(k\times B)} = -E_{ce}\sin\eta\vec{e}_{k\times(k\times B)} \tag{4.5}$$

As $E_{ce} \ll E_{geo}$ fro inclined showers (see section 4.3 for more details on the topic), the full radio signal can be approximated by

$$|\vec{E}| = \sqrt{(E_{k\times B})^2 + (E_{k\times(k\times B)})^2} = \sqrt{(E_{geo})^2 + (E_{ce})^2 + 2E_{geo}E_{ce}\cos\eta)} \tag{4.6}$$

$$\approx E_{geo} + E_{ce}\cos\eta \tag{4.7}$$

At this stage we may introduce the ratio $a = \sin\alpha(E_{ce}/E_{geo})$ which accounts for the $\propto \sin\alpha$ dependency of E_{geo} where $\alpha = (\vec{k}, \vec{B}_{\text{geo}})$ is the geomagnetic angle. Hence equation 4.6 re-writes as:

$$|\vec{E}| \approx E_{geo}\left(1 + a\frac{\cos\eta}{\sin\alpha}\right) \tag{4.8}$$

Equation 4.8 reproduces the amplitude asymmetry expected along the $\vec{k} \times \vec{B}$ axis, with a constructive interaction between the two effects for positive values along $\vec{k} \times \vec{B}$ corresponding to $\cos\eta > 0$, and conversely.

4.2.2.2 Early-late effect

As seen in section 2.3.1.2, the electric radiation by EAS dilutes as the inverse of the distance between source and observer. The effect increases with shower inclination, when the distance to X_{max} becomes significantly shorter for the antennas triggered first (so-called **early antennas**) than last (**late antennas**), as illustrated in the left panel of figure 4.4.

4.2.2.3 Cerenkov effect

It was mentioned at several occasions already that all optical paths are equivalent in time for directions defined by the Cerenkov angle $\cos\omega_C = (1/n)$, an effect resulting in a narrow radio pulse of high amplitude along the direction $\omega = \omega_C$, the so-called Cerenkov compression.

This symmetry is however rigorously true for vertical showers only: for different shower trajectories —and in particular for the most inclined ones, where observer positions within the radio footprint can be far apart— the different optical paths, and different refractive indexes along them, will result in different Cerenkov angle values. This is also observed in simulations, where the average refractive index along the optical path —used to simulate the radio signal propagation— is computed as:

$$< n >= \frac{\int n(h) dl}{\int dl} \tag{4.9}$$

and therefore explicitly depends on the actual optical path l from the source down to the observer. The average value of the refractive index $< n >$ thus varies with the azimuthal angle η defined in section 4.2.1, and so does the Cerenkov ring $\omega_C = f(\eta)$, with a largest offset for values $\eta = \pm\pi/2$ corresponding to early and late antennas. This incidentally means that the circular shape of the Cerenkov ring in the angular plane is only a first-order approximation.

An analytical modelisation of this effect was performed in [99], using a very basic toy model, where only two emission points along the shower track are considered (see Fig. 4.4). The equation $\omega_C = f(\eta)$ established with this toy model is solved numerically by defining the Cerenkov angle as the direction for which the optical paths from these two points to ground are equivalent in time. The resulting values of ω_C are found to match the simulated position of the Cerenkov ring in the angular plane (see right panel of figure 4.4).

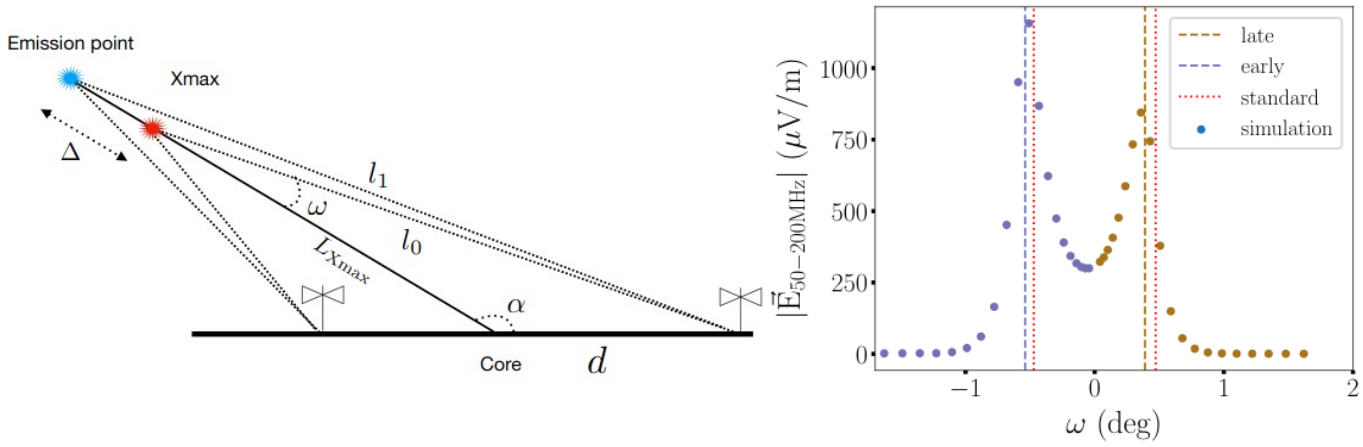

Figure 4.4: *Left: schematic of the toy model used to study the Cerenkov asymmetry, where two emission points separated by a distance Δ are considered. One early and one late antenna are also represented. Right: distribution of the amplitude for antennas placed along the $k \times (k \times B)$ axis (i.e. $\eta = \pm\pi/2$, with blue (brown) points for early (late) antennas. The standard Cerenkov angle $\omega_C = \arccos(1/n)$ is shown as a dotted line, and the ones computed with the toy model for early and late antennas as dashed lines. The latter better match the positions of the amplitude peaks. Taken from [99].*

4.2.3 The Angular Lateral Distribution fit

It is possible to establish an analytic function describing the angular distribution of the radio signal strength in the 50-200 MHz by taking into account the various effects detailed in the previous sections. This so-called Angular Distribution Function (ADF) writes as follows:

$$f^{ADF}(\omega_i, \eta_i, R_i, \alpha) = \frac{\mathcal{A}}{R_i} f^{\text{Geom}} f^{\text{Ch}} \tag{4.10}$$

where α is the shower geomagnetic angle, (ω_i, η_i) the position of antenna i in the angular plane and R_i its distance to the radio emission source. The term f^{Geom}, derived from equation 4.8, describes the Geomagnetic-Charge Excess interplay:

$$f^{\text{Geom}}(\eta_i, \alpha) = 1 + \mathcal{B}\frac{\cos\eta_i}{\sin\alpha} \tag{4.11}$$

(with $\mathcal{B}$ a scalar parameter), while $f^{\rm Ch}$ is an empirical function adjusting the Cerenkov peak:

$$f^{\rm Ch}(\omega_i, \eta_i) = \frac{1}{\left[1 + 4\frac{(\tan\omega_i/\tan\omega_C(\eta_i))^2 - 1}{\delta\omega}\right]^2} \tag{4.12}$$

The peak position ω_C of the $f^{\rm Ch}$ distribution is determined through the treatment presented in the previous section, while its width $\delta\omega$ is adjusted from the distribution of amplitudes with different values for early ($\omega < 0$) and late ($\omega > 0$) antennas. The scalar term $\mathcal{A}$ is a parameter of the ADF function adjusted to the set of antennas i triggered by the shower, together with $\mathcal{B}$ and $\delta\omega$.

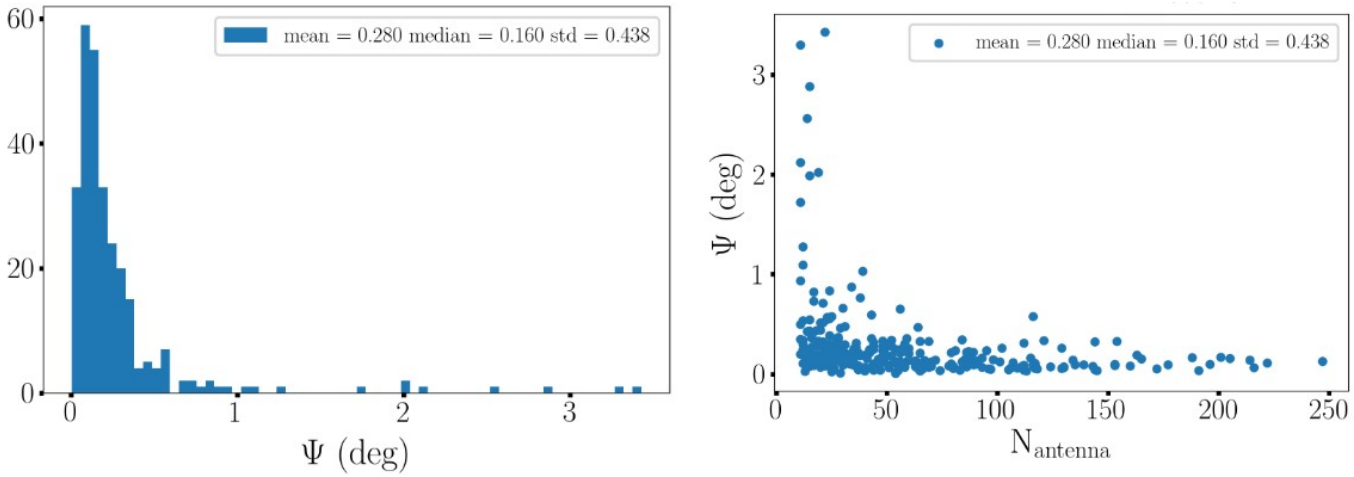

Figure 4.5: *Left: angular error $\delta\psi$ on the reconstruction direction of origin of neutrino showers simulated over HS1. Right: angular error as a function of the number of antennas in the events for the same data set. Plots by Valentin Decoene.*

It should yet be stressed that the set of 4 variables of the ADF functions $\{\omega_i, \eta_i, R_i, \alpha\}$ are not fixed in the reconstruction process, as they directly depend on the direction of propagation of the shower $\vec{k}$ through the following equations:

$$\omega_i = (\vec{k}, \widehat{\vec{x_i} - \vec{X}_{radio}}) \tag{4.13}$$

$$\eta_i = \arctan\left(\frac{y_i^{SP}}{x_i^{SP}}\right) \tag{4.14}$$

$$\alpha = \arccos\left(\vec{k}, \vec{B}\right) \tag{4.15}$$

$$L_i = \vec{k} \cdot (\vec{x_i} - \vec{X}_{radio}) \tag{4.16}$$

where x_i^{SP} and y_i^{SP} are the coordinates of antenna i in the shower plane (see left panel of figure 4.3) while $\vec{X}_{radio}$ is the position of the emission point reconstructed from the spherical fit of the wavefront (see section 4.1.2).

During the fitting procedure of the ADF function to the amplitude distribution in the angular plane, the vector $\vec{k}$ is also adjusted together with the parameters ($\mathcal{A}$, $\mathcal{B}$, $\delta\omega$) in a χ^2 minimization procedure, and the set of variables $\{\omega_i, \eta_i, R_i, \alpha\}$ recalculated accordingly at each iteration. The shower direction $\vec{k}$ obtained through the fit yields the reconstructed direction of origin of the cosmic particle (θ, ϕ).

It is interesting to point at this stage that there is no hypothesis made on the trajectory of the shower in this procedure. In particular it is not assumed that the trajectory crosses ground. Hence this treatment can equivalently be applied to downward or upward-going trajectories, such as those associated with neutrinos interacting underground. Resolution achieved for the reconstruction of the direction of origin of neutrino-induced showers are discussed in the next section, together with the performances for cosmic rays on GRANDProto300.

4.2.4 Angular reconstruction of the direction of origin

A fit with an implementation close to that given in equation 4.10 was applied to the GP300 simulated data set already presented in section 4.1.2, after a 10% Gaussian smearing was applied to the antenna amplitudes to mimic the calibration uncertainties. The treatment resulted in a median error on the reconstructed direction of origin of the cosmic ray equal to 0.07° [99], with a rms value of 0.06° on this average resolution.

The same treatment was applied to neutrino-induced showers triggered on HS1. The median error on the reconstructed direction is then 0.16°, and probably even better if events with more than 30 antennas were selected (see Fig. 4.5). Such a resolution, if achieved experimentally, would be an extremely appealing result.

It should be noted however that the fit converges for 60% of the simulated events only. As this ratio depends marginally on the antenna layout or noise level added, it is most likely that this mediocre result is a consequence of the complex fit procedure (in particular re-calculation of antenna positions in the angular plane), for which the algorithm implementation has not been optimized yet.

4.3 Polarization of the EAS radio signal

As a result of the complex interplay between the charge excess and geomagnetic processes (see Fig. 2.7), polarization of the EAS radio signals —defined here as the instantaneous direction of the electric field vector— is a rich source of information on the characteristics of the air shower. It has however not been investigated extensively so far (see e.g. [151, 201] for some rare analysis). Kumiko Kotera and myself therefore proposed to Simon Chiche, our Master student, a dedicated study in Spring 2020 to evaluate the potential of EAS polarization for the identification and reconstruction of air showers. I summarize below his work, which we supervised together with Kumiko in Covid times. The text of this section is mostly extracted from [198].

4.3.1 Reconstruction of the polarization

Following standard procedures detailed in [151] for instance, the polarization of radio signals is reconstructed as follows. First, the signal intensity is computed as $I(t) = |\vec{E(t)}|^2 = \sqrt{(E_x(t))^2 + (E_y(t))^2 + (E_z(t))^2}$, where $E_{i=x,y,z}(t)$ are the time-traces of the simulated electric field along the South-North, East-West and vertical directions respectively. The time window Δt where the instantaneous intensity $I(t)$ is larger than half its maximal value (see Fig. 4.6) is then used to compute the three remaining Stokes parameters of the radiation:

$$Q = \frac{1}{n}\sum_{i=1}^{n} x_i^2 + \widehat{x}_i^2 - y_i^2 - \widehat{y}_i^2 \tag{4.17}$$

$$U = \frac{2}{n}\sum_{i=1}^{n} x_i y_i + \widehat{x}_i \widehat{y}_i \tag{4.18}$$

$$V = \frac{2}{n}\sum_{i=1}^{n} \widehat{x}_i y_i - x_i \widehat{y}_i \ , \tag{4.19}$$

where n corresponds to the number of samples in the time window Δt, x_i and y_i correspond to the values of the traces $E_{k\times B}(t)$, $E_{k\times k\times B}(t)$ after the electric field vector has been projected in the shower plane ($\vec{k}\times\vec{B}$, $\vec{k}\times(\vec{k}\times\vec{B})$) (see Fig. 4.3). The functions $\widehat{x}_i$ and $\widehat{y}_i$ are the imaginary part of the traces obtained by extending the traces in the complex domain using a Hilbert transform.

From the Stokes parameters we can then derive the so-called **polarization angle** $\phi_p = (\vec{k}\times\vec{B}, \vec{E})$:

$$\phi_p = \frac{1}{2}\arctan\frac{U}{Q} \tag{4.20}$$

and eventually the two components of the polarization in the shower plane, scalar values not to be confused with the projections in the shower plane of the time-dependent total electric field $E_{k\times B}(t)$ and $E_{k\times k\times B}(t)$:

$$\mathcal{E}_{k\times B} = \sqrt{I}\cos\phi_{\rm p} \ , \tag{4.21}$$

$$\mathcal{E}_{k\times k\times B} = \sqrt{I}\sin\phi_{\rm p} \ . \tag{4.22}$$

An illustration of this treatment is plotted in the right panel of figure 4.6. It is then possible to determine the contributions of the geomagnetic and charge excess emission processes E_{geo} and E_{ce} using their respective symmetries:

$$E_{ce} = \frac{|\mathcal{E}_{k\times k\times B}|}{|\sin\eta|} , \tag{4.23}$$

$$E_{geo} = |\mathcal{E}_{k\times B}| - |\mathcal{E}_{k\times k\times B}|\frac{\cos\eta}{|\sin\eta|} , \tag{4.24}$$

where η is the angle between the antenna position and the $\vec{k}\times\vec{B}$ axis as defined in section 4.2.1. One may however note that these equations are not applicable for the horizontal baseline of antennas (i.e. along the $\vec{k}\times\vec{B}$ axis) as the charge excess then has no component along $\vec{k}\times(\vec{k}\times\vec{B})$.

We Finally define the a**-ratio** as:

$$a = \sin\alpha\frac{E_{ce}}{E_{geo}} \tag{4.25}$$

We will evaluate in the following how this parameter —and more specifically, its dependency with the angle ω— can be used to characterize and reconstruct air showers.

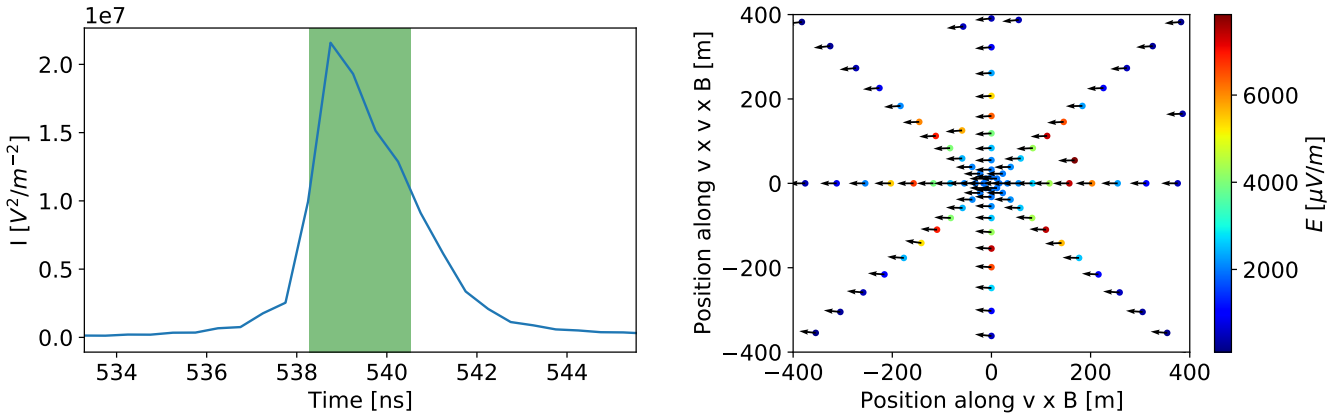

Figure 4.6: *Left: instantaneous intensity $I(t) = |\vec{E(t)}|^2$ of a simulated electric-field time-trace used in this study. The window Δt used to compute the Stokes parameters is shown in green. Right: polarization vectors for a $E = 6.8\cdot10^{17}$ eV, $\theta = 53°$ simulated shower at antenna positions represented in the shower plane. Taken from [198].*

4.3.2 Theoretical expectations for the a-ratio

As already discussed in section 2.3.1.1, the analytical expressions of the charge excess and geomagnetic contributions to the shower electromagnetic radiation can be approximated as:

$$E_{geo} \approx \frac{dA^{geo}}{dt} , \tag{4.26}$$

$$E_{ce} \approx \frac{dA^{ce}}{dx} . \tag{4.27}$$

where x measures the distance along $\vec{k}\times\vec{B}$. Following [150], we then introduce the retarded time t_r (defined as observer time - propagation time):

$$E_{geo} \approx \frac{dt_r}{dt}\frac{dA^{geo}}{dt_r} , \tag{4.28}$$

$$E_{ce} \approx \frac{dt_r}{dx}\frac{dA^{ce}}{dt_r} . \tag{4.29}$$

which, together with equations 2.6 and 2.7, allows to write the a-ratio as:

$$a \equiv \sin\alpha \frac{E_{ce}}{E_{geo}} \approx \sin\alpha \frac{C_x}{\langle v_d \rangle} \frac{dt_r}{dx} \left(\frac{dt_r}{dt} \right)^{-1} \tag{4.30}$$

with C_x the fraction of particles contributing to the charge excess with respect to the total number of positrons and electrons, $\langle v_d \rangle$ the mean drift velocity of the electrons in the air-shower plasma (in units of c) and α the geomagnetic angle. Equation 4.30 then simplifies as [150]:

$$a \approx \sin\alpha \frac{C_x}{\langle v_d \rangle} \sin\omega \tag{4.31}$$

As radio signals are sizable only for $\omega \lesssim \omega_C \approx 1°$ (see right panel of figure 4.4 for instance), we can approximate the a-ratio by:

$$a \approx \sin\alpha \frac{C_x}{\langle v_d \rangle} \omega \ , \tag{4.32}$$

This linear dependency with ω indicates that for the radio emission of a given air-shower, the a-ratio will not be uniform in the radio footprint. It may also be noted that the fraction of particles that contributes to the charge excess C_x is expected to increase with air density, while the drift velocity $\langle v_d \rangle$ should follow the inverse trend. Assuming that the emission is concentrated in a limited region around X_{max} —an hypothesis supported by the point-source approximation of the emission validated in section 4.1—, this implies that the a-ratio should decrease significantly with higher X_{max} positions.

4.3.3 Simulation results

4.3.3.1 Cosmic rays

The distribution of the a-ratio was then studied with simulations performed withhe ZHAireS code over a star-shape layout. 5000 showers with proton and iron primaries were considered, with energies ranging between $2 \cdot 10^{16}$ and $4 \cdot 10^{18}$ eV and 38° to 87.1°. As expected from equation 4.32, the a-ratio was found to decrease with zenith angle (see Fig. 4.7), dropping below 5% for zenith angles θ >70°. For such showers, the amplitude of the charge excess contribution was found to be too small to be used for the reconstruction of the core position of the shower, one of the initial motivations of this study.

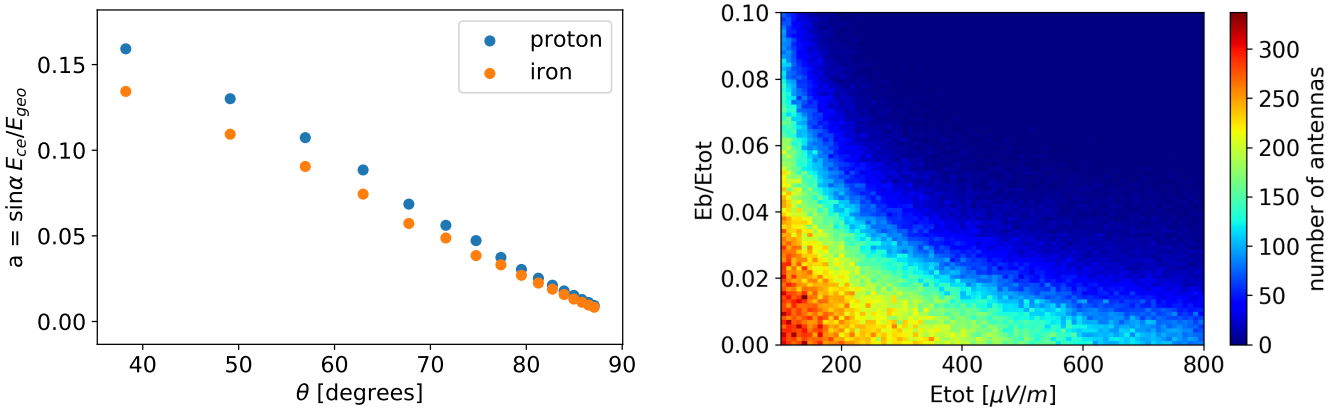

Figure 4.7: *Left: median of the a-ratio computed for 5 000 iron and proton primaries averaged over various energies. Right: ratio E_B/E_{tot} as a function of signal amplitude E measured on each antenna of a star-shape layout for a set of 11 000 simulations with peak amplitudes above 100μV/m. Taken from [198].*

However, the nearly pure geomagnetic origin of inclined showers' electromagnetic emission can be instrumental for shower identification, as the electric field should in this case lead to a very small component E_B along the $\vec{B}$ direction.

The distribution of the ratio E_B/E_{tot}, shown in figure 4.7 for the full simulation set, confirms this hypothesis, with a E_B/E_{tot} ratio value lower than 0.07 for 95% of the signals.

Assuming on the other hand a random polarization for background radio signals, it was computed in [198] that only a $1.23{\cdot}10^{-3}$ fraction of noise events would pass this cut. The E_B/E_{tot} parameter may thus provide a very efficient tool for background rejection. This however requires the direction of origin of the signal to be known, because the electric field information can be built from the voltage only be deconvoluating the antenna response, which is highly dependant on the direction of origin of the signal (see e.g. Fig. 3.11). This cut can thus be applied at DAQ level only, where the combined information of triggered units allows to perform direction reconstruction. Yet the quantity V_B/V_{tot} can be built from the voltage information already available at the antenna level, and selecting values below 0.28 only allows to reject 98% of the background and select 90% of the EAS signals. The possibility to include these two treatments in the online trigger respectively at the DAQ and unit levels of an autonomous radio detector of EAS will be investigated in the GRANDProto300 experiment.

4.3.3.2 Neutrinos

The ratio E_B/E_{tot} was also computed for neutrino-induced air showers from the HS1 study (see section 4.2.4). Because of a deeper position in the atmosphere of the radio emission source compared to cosmic-ray showers (see Figs. 3.17 and 3.19), the values of the a-ratio are significantly higher for neutrinos than for cosmic-rays (see Fig. 4.8). However, further studies will be carried out to optimize the use of the polarization information in the identification of neutrino-induced air showers.

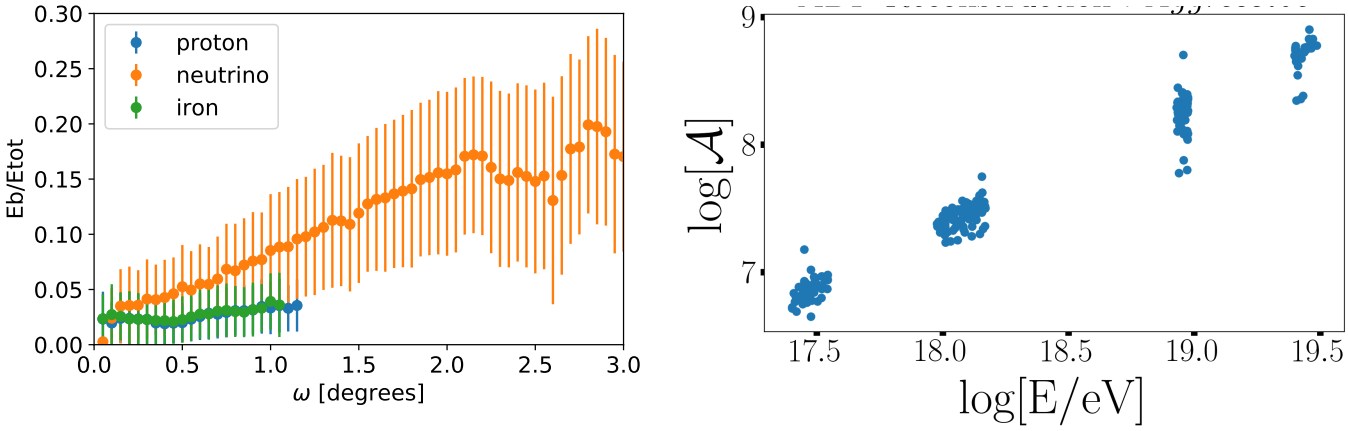

Figure 4.8: *Left: E_B/E_{tot} ratio as a function of angle ω for radio signals associated with proton (blue), iron (green) and neutrino (orange) induced showers and peak amplitudes above 100μV/m. Taken from [198]. Right: Value of parameter $\mathcal{A}$ obtained by the ADF fit (see Eq. 4.10) as a function of shower energy for a set of simulated cosmic-ray showers over a star-shape layout, with a 5 ns Gaussian jitter on antenna trigger times and a 10% jitter on signal amplitudes. The obvious correlation indicates that the ADF fit could also be used to perform energy reconstruction. Plot by Valentin Decoene.*

4.4 Next steps

The analyses presented in this chapter are not optimized yet. The Toy Model of the Cerenkov asymmetry could for instance be refined in order to provide an analytical computation of the Cerenkov peak width δw, and its implementation modified to improve speed and convergence. Beyond angular reconstruction, the method is also being investigated for the determination of the nature of the primary as well as the shower energy reconstruction (see Fig. 4.8). The parameter E_B/E_{tot} could also be further studied in the perspective of the identification of neutrino-induced showers, possibly to be included in the trigger algorithm.

On a broader perspective, these two studies clearly prove that inclined showers have very specific features which, if properly used in dedicated analyses, should allow for excellent performances in the reconstruction of shower properties and associated cosmic particles characteristics. I will stress in particular the fact that the detection of inclined showers with large arrays gives access to their longitudinal development, a very rich information unreachable with standard showers. One axis of work I find particularly appealing in the context of GRAND reconstruction would consist of combining the full radio information —time, amplitude and polarization at each antenna position— in a single reconstruction procedure which output would be shower geometry, energy and primary nature. Achieving such a global fit is at the core of Simon Chiche's PhD work initiated last October under the co-supervision of Kumiko Kotera and myself. A key ingredient to it would be a simulation fast enough to perform the computation of the electric field time-traces on the fly and embed it in the fit procedure. Simon is presently evaluating if the RadioMorphing tool presented in section 3.2.1.2 fulfills the corresponding requirements for speed and precision.

To conclude Part I of this document, I will come back to the wish-list detailed at the end of chapter 1 and see how they are matched by the GRAND performances presented in the last two chapters:
• **Sensitivity to UHE neutrinos:** GRAND is specifically designed to achieve a sensitivity better by one or two orders of magnitude than present best for energies larger than 10^{17} eV, hence falling in the range of expected fluxes for cosmogenic neutrinos. In light of the recent AUGER analyses on composition and spectrum of UHECRs [50], latest computations [45, 53] however indicate that GRAND could detect only a few cosmogenic neutrinos. Yet GRAND remains an extremely competitive instrument, and will in particular allow to probe very efficiently the fraction of protons in UHECRs [55]. Besides a lower detection threshold —still to be investigated— would significantly improve prospects.
• **Point and transient sources:** GRAND instantaneous field of view is a few degrees only, in directions very close to the horizon. Yet deploying sub-arrays at different locations in the world could significantly improve this situation. Besides, the detector full azimuthal range allows for a nearly full sky coverage within 24 hours at a single site. Finally the expected exquisite angular resolution of the GRAND detector makes point source detection and neutrino astronomy possible. However the detection principle of GRAND only allows for a lower bound on the neutrino energy. Reconstruction of the neutrino spectrum is thus impossible, even though large statistics may allow for an insight on this specific issue, a topic remains to be studied.
• **UHECRs and γ-rays:** the detector acceptance and field of view make GRAND a very appealing detector for the study of the tail of the UHECR spectrum. This statement would be reinforced if the nature of the primary particle could be determined with a precision comparable to standard detectors, a performance still to be established. Excellent primary determination would also allow for the study of γ-rays at the highest energies.
• **Fundamental physics:** the prospects for fundamental physics output with GRAND are quite uncertain in practice as they will depend very much on the statistics achieved. The study of the nature of the neutrino would additionally require that different neutrino flavors can be detected. As only taus can be observed through Earth-skimming trajectories, detecting several flavors is possible only for neutrinos directly interacting in the atmosphere, a phenomenon which cross-section is non-negligible at the highest energies only, making physics case could be reachable only if neutrinos fluxes are higher than presently expected.

In conclusion, GRAND is certainly an appealing proposal for the study of UHE cosmic particles. A threshold lower than 10^{17} eV and a precise determination of the primary nature would make the instrument even more appealing, but this has not been studied in details yet. Now that we have established that the GRAND concept is valid, we will study in Part II of this document the path to implement it.

Part II

Autonomous radiodetection of air showers

Introductory comments: the case for autonomous radio arrays

We have seen in chapter 1 that the low flux of Ultra-High Energy neutrinos implies that only gigantic instruments can achieve sensitivities allowing for their detection. We presented in chapter 2 the arguments in favor of using a radio array to detect air showers induced by these elusive particles. We stressed in particular that the ease of deployment of radio antennas, their robustness, the stability of their response, and their very affordable price make the radio technique particularly well suited for deployment over the required gigantic large areas. We confirmed in chapter 3, through a dedicated end-to-end simulation, that the 200'000 km^2 GRAND detector would reach the targeted neutrino sensitivity, and presented in chapter 4 encouraging results on the reconstruction of the characteristics of cosmic particle primaries from GRAND data associated to neutrino-induced inclined air showers.

Quite obviously, areas in the range of hundred thousands square kilometers imply that radio detection should be performed in a **standalone mode**[1]: a trigger should be based on radio signals only and primary particle information should be reconstructed from radio data only. This requires in particular that GRAND should achieve at the same time a very good **detection efficiency** for air showers and an excellent **detection purity** by rejecting a very large fraction of spurious events. If we want to be more quantitative, we may first note that the neutrino sensitivity of the GRAND experiment —shown in figure 1.5 for instance— varies linearly with the EAS detection efficiency. A neutrino detection efficiency below 80% would therefore severely impede the performances of the GRAND detector, and can be considered as a viable target. It is much harder to put a specific figure on expected performances for background rejection, and probably even artificial, as the rejection ratio depends on the electromagnetic environment of the site, or the number of units chosen to define an event for instance. Let us simply state at this stage that the rate of background events wrongly identified as air showers should be reduced by several orders of magnitude to reach a value much smaller than cosmic particles.

There are substantial reasons to believe that such performance can be achieved in principle. We have seen in the first part of this document that simulated radio signals associated to EAS exhibit specific characteristics —wavefront shape, amplitude or polarization pattern for instance, see e.g. figures 2.9, 3.15, 4.2, or 4.6— providing extremely strong signatures which cannot be faked by background events. If it is confirmed experimentally that identification of EAS is possible from radio data only based on these features, the issue of self-radio-detection is then reduced to organizing trigger and data collection so that this identification can be performed in the most efficient and economic way.

Over the last twelve years, I devoted most of my research time to the two issues above-mentioned: the Physics one —identification of air showers from radio data— and the technical one —trigger and collection of these radio data. I initiated this endeavor through the TREND experiment, a basic setup of 50 self-triggered radio antennas running at a time when autonomous radio detection was mostly seen as an impossible task; GRANDProto35, an attempt to upgrade the TREND setup to reach the above mentioned performances; and GRANDProto300, a pathfinder for the GRAND detector which should demonstrate that autonomous radio-detection and identification of very inclined air showers is possible. Before this, I should pay here a tribute to the H.E.S.S. experiment, which very certainly shaped my strong conviction that autonomous radio-detection of air showers was possible.

[1] GRAND being a standalone radio-detector does not necessarily mean that sub-arrays could not run synchronously with other types of detectors deployed at a same site.

I was recruited in September 2004 as an assistant professor at the *Université Pierre et Marie Curie* to work on the H.E.S.S. experiment in the LPNHE laboratory. Fifty years after the first detection of Cerenkov light in the atmosphere [202], and fifteen years after the first observation of a γ-ray source at TeV energies [203], Imaging Air Cerenkov Telescopes and the associated analysis methods were finally reaching maturity, and this was a very exciting period for H.E.S.S., with literally a γ-ray source discovery for every new observation period. I must admit I felt somewhat a stranger to the excitement of my colleagues in the collaboration —probably by lack of maturity— and soon became attracted by the exciting prospect of starting a radio-detection project in China. Still, I admired the performance of the H.E.S.S. detector, and in particular its trigger system, to which the LPNHE team contributed largely [204]. I was startled by the fact that γ-rays could be detected with such high efficiency and purity, while their rate —few events per minute for the Crab nebula— is lower by orders of magnitudes than the individual trigger rate of the PMTs composing the camera. This result was made possible thanks to an excellent understanding of the background noise and a tailor-made trigger system, adjusted to the specific features of noise and signal and their respective rates. The H.E.S.S. trigger system was in that respect a strong inspiration for my work on radio-detection.

Chapter 5

The Tianshan Radio Array for Neutrino Detection

Figure 5.1: a TREND detection unit in front of the Tianshan mountains.

5.1 Genesis

The topic of cosmic ray detection was familiar to me since my post doctorate on the Auger experiment between November 2002 and July 2004 at the Karlsruhe Institute of Technology, where I developed a Graphical User Interface for the Fluorescence Detector and also performed a study on the FD sensitivity to neutrinos [143]. Around that time, I also got interested in radio-detection of air showers, as I was offered a position of assistant professor in SUBATECH Nantes to work on CODALEMA, one of the pioneering experiments in the field. As mentioned already, I eventually chose to join the H.E.S.S. group at LPNHE, but I kept on following with great interest the progress of CODALEMA and other experiments in the field.

In 2007, at a time when I was starting considering the possibility to settle down in China for a long period of time and perform my research there, I was introduced by Charling Tao to Wu XiangPing, professor at the National Astronomical Observatories of China (NAOC). He had built two years before a radio interferometer in a remote valley of the Tianshan mountains in the XinJiang Autonomous Province (western China). The aim of this detector, called the 21 CM Array [106] (21CMA) was to use the 21 cm transition line of neutral hydrogen atoms as a tracer for the study of the Epoch of Reionization [205]. Because of the expansion of the Universe, the radiation emitted when the first stars lit up —the so-called Epoch of Reionization— stretches at present in the tens to hundreds MHz frequency range. The 10 287 log periodic antennas composing the 21CMA therefore operate in the 50-200 MHz frequency range, and a scan in frequency over the sky images produced by the interferometric treatment of the 21CMA data thus corresponds to a scan in time during the Epoch of Reionization.

Together with Pascal Lautridou, leader of CODALEMA experiment, and with inputs from François Le Diberder and Stavros Katsanevas, then members of the IN2P3 scientific management team, I started evaluating the possibility to perform autonomous air shower radio detection using the 21CMA setup. The idea was to make limited adjustment on an existing radio detector working in the frequency range of radio emission from air showers, in order to build swiftly, and at a moderate cost, a setup detecting transient radio pulses from air showers.

Figure 5.2: Left: Daniel Ardouin, Didier Charrier, Pascal Lautridou, Wu XiangPing and Zhao Meng (from left to right) discussing during the seminal TREND meeting in April 2008 at SUBATECH Nantes. Right: Thomas Saugrin, post-doctorate on TREND between 2009 and 2011, and Valentin Niess doing tests for TRENDproto in front of a 21CMA pod in an early phase of the TREND project.

Thanks to the support of FCPPL[1] and its dynamic director Lydia Roos, I went to Beijing in summer 2007 and presented this idea to Wu XiangPing, who reacted very positively to it. FCPPL support then allowed to organize a workshop in the SUBATECH laboratory in April 2008, where we could elaborate on the possibility to develop an experiment of radio-detection of air showers based on the 21CMA infrastructure. Wu XiangPing and Zhao Meng (computing engineer on the 21CMA experiment) came to Nantes and participated, together with Cristina Carloganu (member of the Antares collaboration) and myself in the meeting hosted by Pascal Lautridou, Daniel Ardouin and

[1]The France China Particle Physics Laboratory is a CNRS Associate International Laboratory built to foster and structure scientific collaboration between researchers in High Energy Physics and related fields. The Chinese Academy of Science —to which NAOC belongs— and IN2P3 are FCPPL's driving institutions.

Didier Charrier, members of CODALEMA (see Fig. 5.2). A visit to the 21CMA site in June 2008 then allowed to validate the proposal, and IN2P3 finally gave its approval to my departure to China to start this project, on the condition that I get involved in the management of FCPPL, a responsibility I gladly undertook until 2017. I therefore moved to Beijing together with my family in September 2008 at the invitation of Wu XiangPing and Hu HongBo, professor at the Institute of High Energy Physics (IHEP) who I had also met during my visit to Beijing in summer 2007. The Tianshan Radio Experiment for Neutrino Detection (TREND) was born.

Arriving in a completely unknown country, I had the responsibility to build and run an experiment in a field I barely knew. This endeavor took most of my time and energy during the five years I spent in China, from September 2008 to September 2013. These efforts payed off in the end, and I am very proud to say that we succeeded in detecting cosmic rays [206] with the autonomous radio array built with very limited resources by our small team, composed of Zhao Meng, Valentin Niess and the three post-doctorates who worked on the TREND project at NAOC (Thomas Saugrin, Zhang Jianli and Sandra Le Coz). We also benefited throughout these years from the constant and vital support of Wu XiangPing, as well as the help of the staff on site. Twelve years after this adventure started, I now realize how much this successful outcome, and even more the path which led to it, helped me gain knowledge and confidence, and to a significant extent made me the physicist and person I am today.

5.2 TREND objective and design

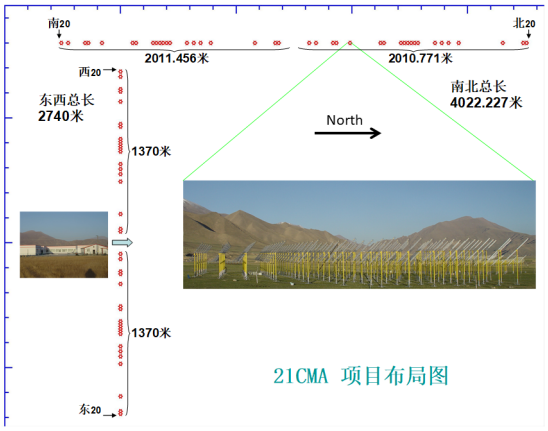

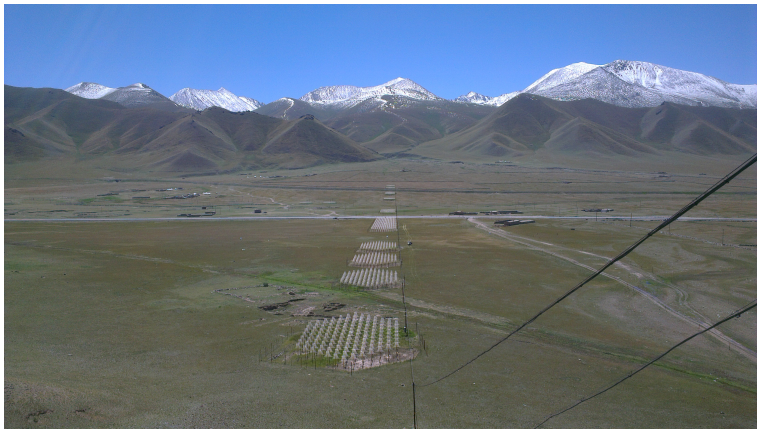

Figure 5.3: *Left: layout of the 21CMA experiment, composed of two baselines formed of 40 pods aligned along the East-West and North-South directions. The East-West baseline extends on 2740 m, the North-South on 4022 m, thus corresponding to equal lengths when projected in the plane tangent to the Earth at the North Pole. The pods are labeled 101 to 120 for the East arm, 121 to 140 for the West arm, 141 to 160 for the South arm, 161 to 180 for the North arm. Pictures of a pod and the Ulastai Observatory buildings are shown in the insets. The Ulastai Observatory buildings, located between the East and West arms of the 21CMA, host the DAQ rooms for the 21CMA and TREND experiments, a mechanical & electronics workshop and leaving quarters. Right: picture of several pods comprising the South arm of the 21CMA. Pods are group of 127 antennas forming an hexagon of 30 m length. Also visible at the bottom right corner of the picture is the cable bundle formed by the optical fibers and power supply for the pods.*

The TREND experiment relies heavily on the 21CMA infrastructure. This experiment is composed of 80 *pods* of 127 log periodic antennas each. These pods form two perpendicular baselines orientated along the North-South and East-West directions and extend for 4.0 and 2.7 km respectively (see Fig. 5.3). A 320 V power line and a pair of optical fibers connect each pod to an acquisition room placed at the center of the East-West arm. On each pod, the sum of the analog signals from the 127 antennas is continuously fed into an optical transmitter connected to one of the fibers. In the DAQ room, the signals from the 80 fibers are then digitized in parallel by 8-bits ADCs at a sampling rate of 200 MSamples/s. The data of each pod are finally buffered on 200 MB disks, where the signal processing is performed. A new DAQ room was put in operation for 21CMA early 2008, leaving this DAQ system —with its optical receivers, ADCs and computers— fully available for TREND.

The original TREND proposal, presented to the FCPPL scientific committee in November 2007, was based on the idea that one of the 127 antennas composing each pod could be isolated, their signal fed into the fiber not used by 21CMA and the recording of digitized time-traces would trigger each time a transient signal would reach an amplitude significantly larger than the baseline level. Offline analysis would then allow to select coincidences among the recorded pulses, perform background rejection and eventually study the selected sample of EAS events. Even though the design of the detector evolved with time and eventually departed somewhat from this original plan (see details in section 5.4), a very simple DAQ system —allowing to keep it fast— combined with a massive offline reduction of the data always remained at the core of the TREND philosophy. Such a basic DAQ design leaves us with limited possibility to control the trigger rate (the trigger threshold is the only free parameter of the DAQ), and thus absolutely requires that the rate of transients existing on site should be low enough to allow for online data trigger and waveform selection with very limited dead-time. This is the reason why the location of the TREND detector was chosen only after a careful in-field selection process carried out in Autumn 2008. As we will see, it eventually turned out to be a winning strategy, except during the last period of data taking, which confirmed how critical a parameter DAQ live-time is.

If the experimental aspects of the initial proposal —"building a self-triggered radio array of size $\sim$1 km^2"— were indeed implemented, the initial scientific ambitions of TREND —studying the cosmic rays and neutrinos of astrophysical origin— however had to be lowered down: AERA, powered by the efforts of the much larger and more powerful AUGER collaboration, dwarfed TREND by a factor 10 in size by the time TREND reached its final form in 2011, making cosmic ray studies in TREND somewhat irrelevant. But even before that, simulations had also shown that much larger instrumental areas —and more distant mountains— were required for neutrino detection, as already detailed in chapter 3.2.2.

Still, thanks in particular to our wise choices for experiment design and excellent conditions on site, our efforts to build a self triggered array were eventually rewarded, and TREND success paved the way for GRAND. The following section details the work carried out on radio-detection of air shower at TREND. For most parts, the materials presented here are extracted from [207] and [206].

5.3 The TREND site

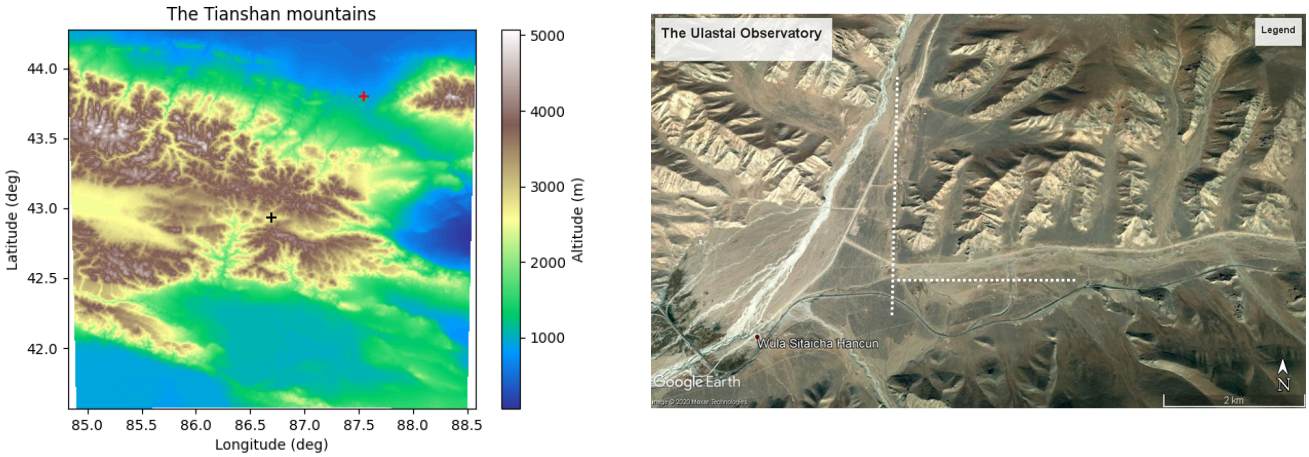

Figure 5.4: *Left: topography of the Tianshan mountains around the Ulastai Observatory, displayed here with a black cross. Urumqi, the capital city of the XinJiang province and 150 km North-East of Ulastai, is shown with a red cross. Right: Google Earth view of the Ulastai Observatory. The dotted lines indicate the approximate location of the 21CMA interferometer. Also visible on this satellite view are the train line running South of the array, Ulastai village in the South-West corner of the picture (labeled 'WuLaSiTai ChaHanCun', the phonetic transcription in Chinese of the Mongol name Ulastai), the road going from Ulastai to the North towards Urumqi and another road going to the East. The small white dot South of the East-West arm is the Observatory building.*

The Ulastai Observatory (42°56'N, 86°41'E) was built in a 2650 m-high valley surrounded by 4000 m-high mountains from the TianShan (*"mountains of Heaven"*). These efficiently screen the site from electromagnetic emissions from Urumqi, the capital city of the XinJiang province, 150 km —and 4 hours drive— to the North-East, and other urban centers (see Fig. 5.4). The excellent electromagnetic environment of the site was confirmed through a dedicated measurement I conducted at the time TREND was being deployed. It was performed using one of the 21CMA log periodic dipole array (see Fig. 5.5), composed of 18 half-wave dipoles with lengths varying from 0.48 to 1.66 m. As detailed in section 2.3.2.1, the response of the individual dipoles in the array exhibit a resonance around a frequency ν_i simply given by

$$\nu^i_{res} = \frac{c}{2l^i} \tag{5.1}$$

where l^i is the length of the i^{th} dipole and c the speed of light, ensuring a rather constant sensitivity of the antenna over a wide range of frequencies. The signal at antenna output was then amplified with two low-noise amplifiers of 24 dB gain each, and eventually plugged into a spectrum analyzer through a 10 m long coaxial cable.

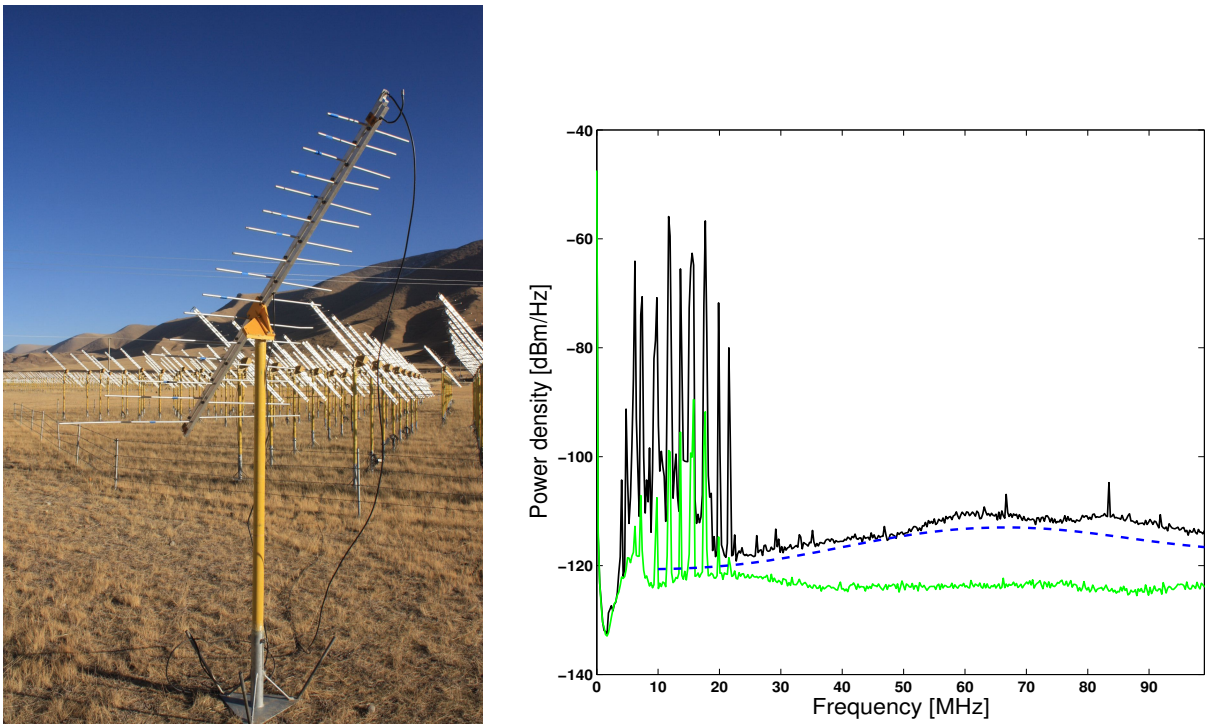

Figure 5.5: *Left: a log-period antenna from the TRENDproto setup (see section 5.4.2) standing in front of a 21CMA pod. An antenna similar to this one was used for the measurement of the electromagnetic environment (see section 5.3). Right: Power density spectrum of the sky at the Ulastai site, measured in the 0-100 MHz frequency range with a 21CMA antenna and a 48 dB low noise amplification (in black). The power density is given here in dBm/Hz, where* $\mathcal{P}_{[dBm]} = 10\log_{10}\frac{\mathcal{P}_{[W]}}{1\,mW}$. *The green curve shows the spectrum recorded when the input cable is disconnected from the antenna. The dashed blue curve is the simulated response of an ideal system to the sky background only. Few contributions beyond the sky emission are found above 25 MHz. Taken from [207].*

The resulting curve, displayed in Fig. 5.5, shows the power received by the antenna per unit frequency. The series of strong and narrow peaks at frequencies between 5 and 25 MHz are induced by so-called **short waves**, radio signals bouncing off the ionosphere, the ionized layer of atmosphere 60 km from ground and above [208]. The full reflectivity of ionosphere at these frequencies allowed pioneering intercontinental radio-communications in the early XX$^{\text{th}}$ century, and is still used by radio-amateurs to communicate over distances of thousands of kilometers. Short waves being

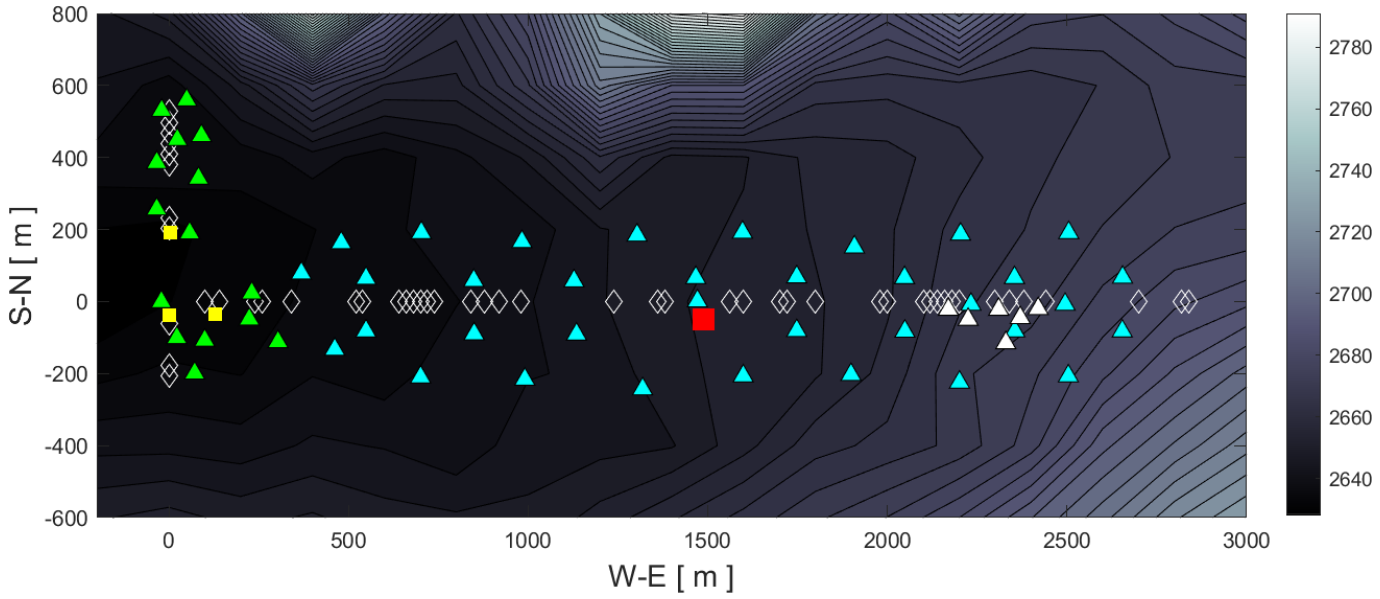

Figure 5.6: *Layout of the TREND detector. White triangle represent the TRENDproto setup, green the TREND15 setup, later extended to TREND50, shown in cyan. The three scintillators running in coincidence with the TREND15 array are depicted with yellow squares. Note that TRENDproto antennas were removed when TREND15 was deployed, and scintillators when TREND15 was extended to TREND50. Also displayed with a red square is the DAQ room. Positions are given in the TREND referential, with x-axis and y-axis corresponding to the the 21CMA West-East and South-North arms respectively, and an origin set at their cross-point. The color-bar on the right represents the altitude above sea level in meters. For better readability, antenna IDs are not shown on this plot, but on Fig. 5.23.*

measured at any location on Earth, they are however in our case a source of nuisance, which impedes detection of the faint radio signals induced by air showers for frequencies below 30 MHz. Above 30 MHz however, no significant peak emission is measured in Ulastai. FM —defined by frequencies from 87 to 108 MHz— is in particular absent, allowing to extend the TREND measurement up to 100 MHz, while most experiments stop at 80 MHz [166, 169]. Moreover, it can be seen on figure 5.5 that the measured noise level (in black) exceeds the minimal expected signal (dashed blue curve) by less than 3 dB/Hz. This minimal noise level was computed as the response of the setup to the background sky radiation following the method presented in section 5.5.2, also assuming assuming an ideal transmission line and neglecting other sources of noise. The limited difference to the measured level —corresponding to a 40% difference in terms of standard deviation of the voltage baseline— therefore signs Ulastai as a site with an excellent electromagnetic environment.

It should however be stressed at this stage that this statement applies for the power spectrum only, and while a clean spectrum is a necessary condition to allow for the (tiny) radio pulses induced by air showers to emerge from the ambient stationary noise, this parameter does not provide a complete characterization of the electromagnetic environment in regard to this type of detection. To illustrate this subtlety, let us imagine a quiet electromagnetic environment, polluted only by transient pulses repeating at a rate of 1 kHz, with pulse duration in the 100 ns range and amplitudes 10 times larger than the stationary radiation rms. The contribution of the transient pulses to the total power of the signal would be around $10^3 \times 100 \cdot 10^{-9} \times (10)^2 = 1\%$ only, and the power spectrum of such environment would therefore appear as excellent. However, these transient signals would obviously induce a 1 kHz trigger rate in an experiment designed to detect transient radio pulses. As will be seen in section 5.4.3, such a rate would exceed by far the maximal value allowed by the TREND DAQ, and would therefore disqualify this site.

5.4 The TREND detector

The TREND experiment underwent three different phases: in January 2009, a reduced setup composed of 6 units was used for a proof of concept for TREND and develop the reconstruction tools, as well as the background rejection

procedure. It is referred as TRENDproto in the following. Then a 15-antennas setup —surprisingly named TREND15— was deployed in March 2010 around the cross-point of the 21CMA arms. TREND15 was complemented with a basic setup of 3 scintillators, in order to demonstrate that air showers were indeed detected with the radio setup. In January 2011, TREND15 was extended to 50 units along the East-West arm of the 21CMA (see Fig. 5.6). TREND50 then ran until January 2014, when TREND data taking was terminated.

In the following we detail the elements composing the TREND detector for these three distinct stages, starting from the antenna down to the data recording.

5.4.1 The TREND antenna

21CMA log-periodic antennas were used for the TRENDproto and TREND15 phases, because they were the only available at that time. The general characteristics of these log-periodic antennas were detailed in section 2.3.2.1. We will simply add here that the antennas were oriented towards North, thus polarized along the East-West axis. An inclination of 47° with respect to ground —set in 21CMA so that antennas point towards the Polar Star— corresponds to a maximum of the gain pattern in the 40-60° zenith range over the 50-200 MHz frequency band.

Several parameters make these antennas not optimal for radio detection of air showers. First, their gain is too low in the lowest part of the TREND frequency range ($\nu_i = 90\,\mathrm{MHz}$ for $l_i = 1.66\,\mathrm{m}$ following equation 5.1). Also the antenna gain has a directional response, and as any log-periodic antennas, it most likely exhibits a degraded response in the time domain by construction (see right panel of figure 5.7).

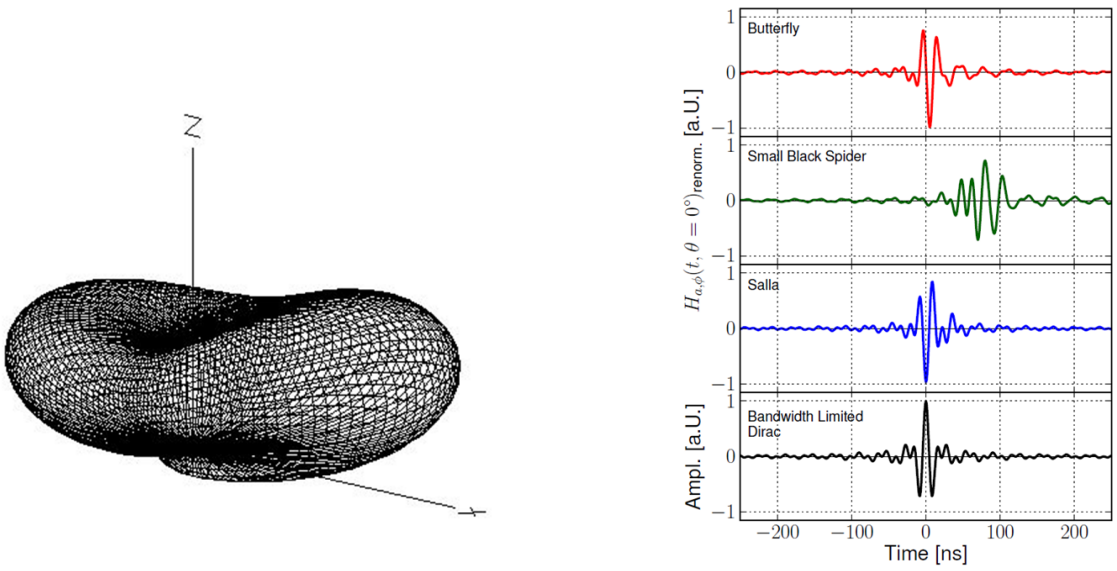

Figure 5.7: *Left: Gain at 100 MHz of a 21CMA log-periodic antenna oriented horizontally at a 1.5 m height above ground. The plotted surface corresponds to the antenna gain modulus for each incoming wave direction. It is significantly larger along the (x-axis) direction the antenna points to. Right: simulated impulse responses of various antennas considered for AERA. The response of the Small Black Spider, a log-periodic antenna, is noticeably smaller in amplitude, delayed and with a larger spread in time compared to the Butterfly antenna. Taken from [169].*

It was therefore decided to upgrade the TREND antennas to a new version, optimized for the detection of air showers, for the TREND50 phase. Following successful experience in AERA [169], bow-tie antennas were chosen. Their robust design, broad-band and relatively isotropic response, excellent behavior in time domain make them very well suited for our purpose. A RF transformer —also called a ballun— of primary/secondary impedance ratio equal to 1.5 was installed at the feed-point of the antenna, with primary on the antenna side, which optimizes impedance matching between the antenna and the load circuit of input impedance 75Ω (see Eq. 2.14). The TREND50 detection

unit was designed so that its equivalent length (defined in equation 2.26) is maximal in the 50-100 MHz frequency range, as illustrated in figure 5.8.

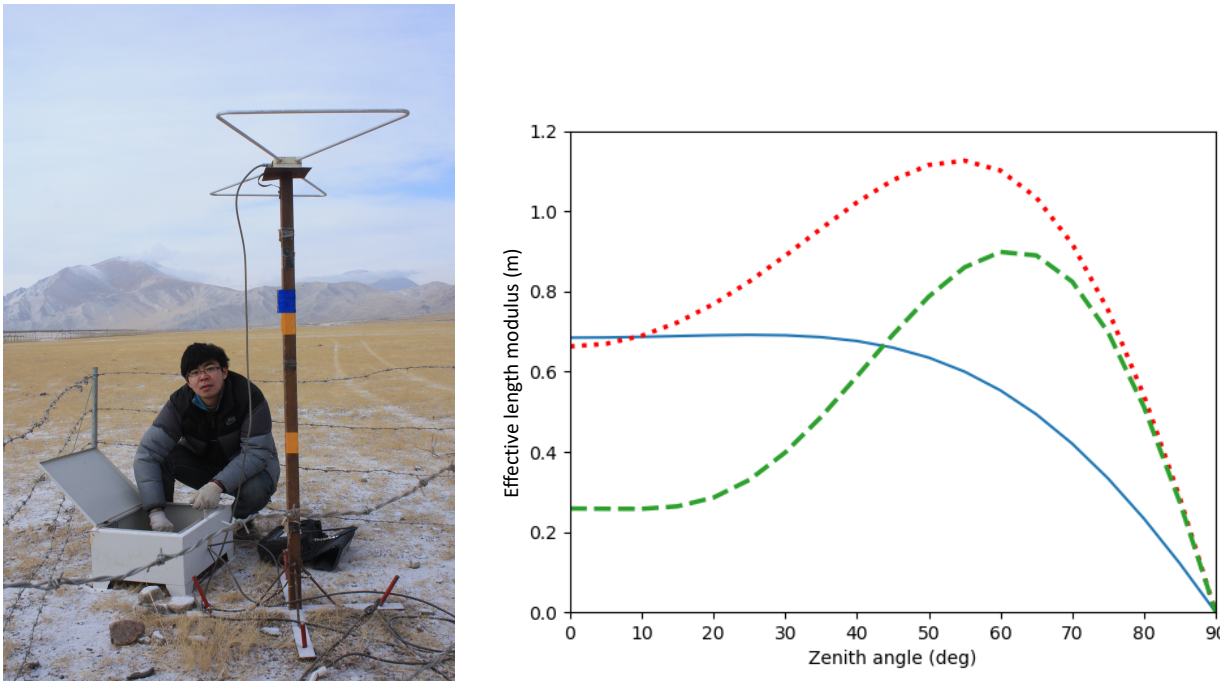

Figure 5.8: *Left: Zeng Lei, intern on TREND in 2011 and 2012, connecting a TREND50 detection unit —composed of a bow-tie antenna and a RF transformer placed inside a waterproof box at the antenna feed-point— to the front-end electronics installed in a box placed at the antenna foot. Right: magnitude of the effective length for the TREND50 detection unit as a function of zenith angle, for an incoming monochromatic plane wave with polarization in a plane parallel to the antenna main axis, of frequency 50 (solid blue), 80 (dashed green) and 100 MHz (dotted red). In this NEC2 simulation, the detection unit is connected to a 75 Ω load, and an infinite flat ground is assumed, with relative dielectric constant* $\epsilon_r = 10$ *and conductivity* $\sigma = 10^{-3}\,\Omega^{-1}\mathrm{m}^{-1}$. *Taken from [206].*

5.4.2 The TREND layout

5.4.2.1 TRENDproto

The 6 antennas composing the TRENDproto array were deployed in January 2009 between pods 110 and 117, on the East arm of the 21CMA interferometer and at walking distance from the the Ulastai Observatory. This site was also selected because preliminary tests carried out in Autumn 2008 together with Zhao Meng showed that the rate of transient signals was much lower there than at the location envisioned originally for TRENDproto, along the North arm (pods 169 to 175). The TRENDproto layout roughly formed a triangle of base 250 m and height 100 m, with an average ∼50 m separation distance between antennas (see Fig 5.6).

The absence of a power source outside of the pods imposed the electronic treatment of the antenna signals to be performed inside them, through an electronic chain composed of a 24 dB low-noise pre-amplification (equivalent temperature of 28 K), two additional 20 dB amplification stages and two 50-100 MHz filters (see Fig. 5.9). All of these were commercial components matched to an impedance of 75 Ω , and initially purchased for the 21CMA experiment. This incidentally imposed the 50-100 MHz frequency range to be used in TREND, while an extension to lower frequencies would have certainly improved the signal to noise ratio for air shower detection (see Fig. 2.8). The connection between antennas and electronic board was realized with coaxial cables, which attenuation (5.5 dB/100 m at 55 MHz, 9.4 dB/100 m at 211 MHz), combined with the impossibility to perform amplification at the antenna foot, required the antennas to be placed less than 200 m away from the pods. After shaping through the electronic chain, the analog signal was fed into an optical transmitter and transferred through optical fibers to the DAQ room.

5.4.2.2 TREND15

A year of operation of TRENDproto allowed uto validate the TREND concept and develop the reconstruction and selection tools, as detailed in section 5.7. TRENDproto was thus dismantled in January 2010 and replaced by TREND15, deployed at the cross-point of the 21CMA arms. This allowed for a larger and somewhat more regular layout, even though the road crossing the array just north of the EW baseline, and the persistent necessity to deploy antennas at close distance from the pods to avoid signal attenuation were severe constraints. The electronic chain was identical to TRENDproto.

An array composed of three scintillating detectors was also installed in March 2010 at the cross-point of the 21CMA arms, with a ∼200 m distance between detectors. Each of them was composed of a 0.5 m×0.5 m×2 cm standard plastic scintillator in direct view of a Photonis XP2020 photo-multiplier tube (PMT) (see Fig. 5.9). Due to the largest power content of the PMT signal at low frequencies compared to antenna signals, an optical transmitter working in the 20-200 MHz frequency range had to be used rather than 50-200 MHz for antenna signals. Scintillator signals were then digitized in the DAQ room with the same ADCs as for the radio data.

Figure 5.9: *Left: a TREND15 front-end electronic board, composed of a Low Noise Amplifier (left), two 50-100MHz filters, two additional 20 dB amplification stages and an optical transmitter. The two fibers connected to the DAQ room lie atop the board. Right: TREND15 scintillators about to be deployed. Picture taken with Thomas Saugrin, Zhao Meng and Chen ShiFu, a key member of the Ulastai staff. The scintillation plate is fixed atop a pyramidal structure which guides the light to the PMT fixed at its apex. The building in the back of the picture is the TREND DAQ room.*

5.4.2.3 TREND50

In October 2010, TREND15 was extended to 50 radio detection units separated by a distance of 175 m on average, thus covering a total ground surface of 1.5 km^2 (see Fig. 5.6). Cables carrying 12 V power supply were pulled down to the antenna positions, thus allowing signal amplification and filtering to be performed at the antenna foot. For antennas placed at distances larger than 250 m from their pod, an additional 20 dB amplification was performed in the front-end treatment. Then, as for earlier TREND setups, a coaxial cable routed the resulting voltage to the closest 21 CMA pod where it was transduced and sent to the DAQ room —distant by 2 km at most— through an optical fiber.

5.4.3 The TREND DAQ system

In the DAQ room, the signal of each antenna is first transformed back to an electric form through dedicated optical receivers. It is then filtered again in the 50-200 MHz band to erase a strong 65 kHz signal picked-up in the optical receiver and finally passed to a dedicated processing unit (PU), where the signal is continuously digitized by a dedicated 8-bits ADCs integrated in the PU. The ADC dynamic range is 2 V, corresponding to a voltage conversion factor K = 0.0076

V/ADC count. The baseline level of each channel is set around 5 ADC units ($\sim 40\,\mathrm{mV}$) by manually adjusting the gain of the optical receiver. The resulting voltage gain of the complete DAQ chain ranges between 10^4 to 10^6, as will be confirmed by a detailed calibration procedure (see Fig. 5.21). This allows for a proper measurement of the Galactic transit (see section 5.5.2) from the signal baseline, at the cost of saturated signals for large transient pulses.

The ADCs digitize the data at a 200 MSamples/s rate distributed by one single master clock (see Fig. 5.11) to all ADCs through cables of identical length, allowing synchronization of all ADCs at a level better than 1 ns. Digitized samples are buffered in one of the two 200 MBytes **time frames** —corresponding to 2^{28} samples— present in each PU. Given the 5 ns ADC sampling period, a time frame is filled in 1.342 s and the data is then automatically routed to the other buffer. When this happens, the PU processes the data from the buffer which has just been filled. The process repeats until data acquisition is stopped. The various recording modes defined are detailed in the following sections.

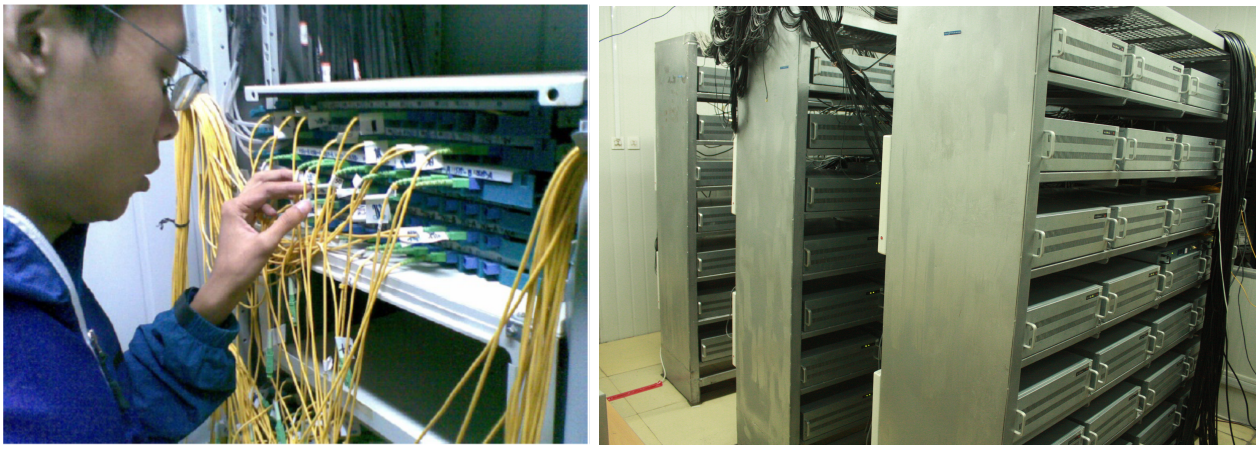

Figure 5.10: *Left: Zhang Jianli, post-doc on TREND between 2012 and 2014, checking the optical panel dispatching the fibers from each pod to the optical receivers. Right: the TREND processing units in the TREND DAQ room.*

5.4.3.1 Standard acquisition

In standard acquisition mode, the data are analyzed on the fly by the PU, which generates local triggers (T0) when a transient pulse is observed. The T0 algorithm proceeds as follows:

(i) For each **time frame** we compute the mean, μ, and standard deviation, σ, of the samples.

(ii) The time frame is then divided in 262 144 **sub-frames** of 1024 samples, noted S, each corresponding to a waveform duration of $\sim 5.1\,\mu$s.

(iii) For each sub-frame the maximum deviation, $d_{\max} = \max(|S_i - \mu|)_{i\in[0,1023]}$, and its corresponding time, $t_{\max}$, are computed.

(iv) If $d_{\max} \geq N\sigma$ a T0 trigger is issued.

N is a scalar adjusted by the user between 6 or 8, depending on the electromagnetic background conditions at the start of the run. In TRENDproto and TREND15, each T0 would result in a 1024-points time-trace (initially 2048 points) centered on the trigger time being written to disk in a dedicated data file. The ADC sampling index of $t_{\max}$ is written in a separate file gathering all trigger time information.

This rather basic software, written in 2008 by Zhao Meng, was eventually upgraded for TREND50, with major contributions from Valentin Niess. An additional stage was added, where the T0 triggers generated within one 1.342 s sub-frame are collected by a master unit MU. If at least four T0 triggers are causally coincident, then the MU sends a T1 signal back to the corresponding PUs, triggering the recording of the L waveforms participating in the coincidence to a local disk. The set of waveforms associated to a T1 trigger compose a so-called **event** of multiplicity L.

Formally, the T1 coincidence condition is defined as following:

$$|t_i - t_j| \leq \frac{d_{ij}}{c} \times T \tag{5.2}$$

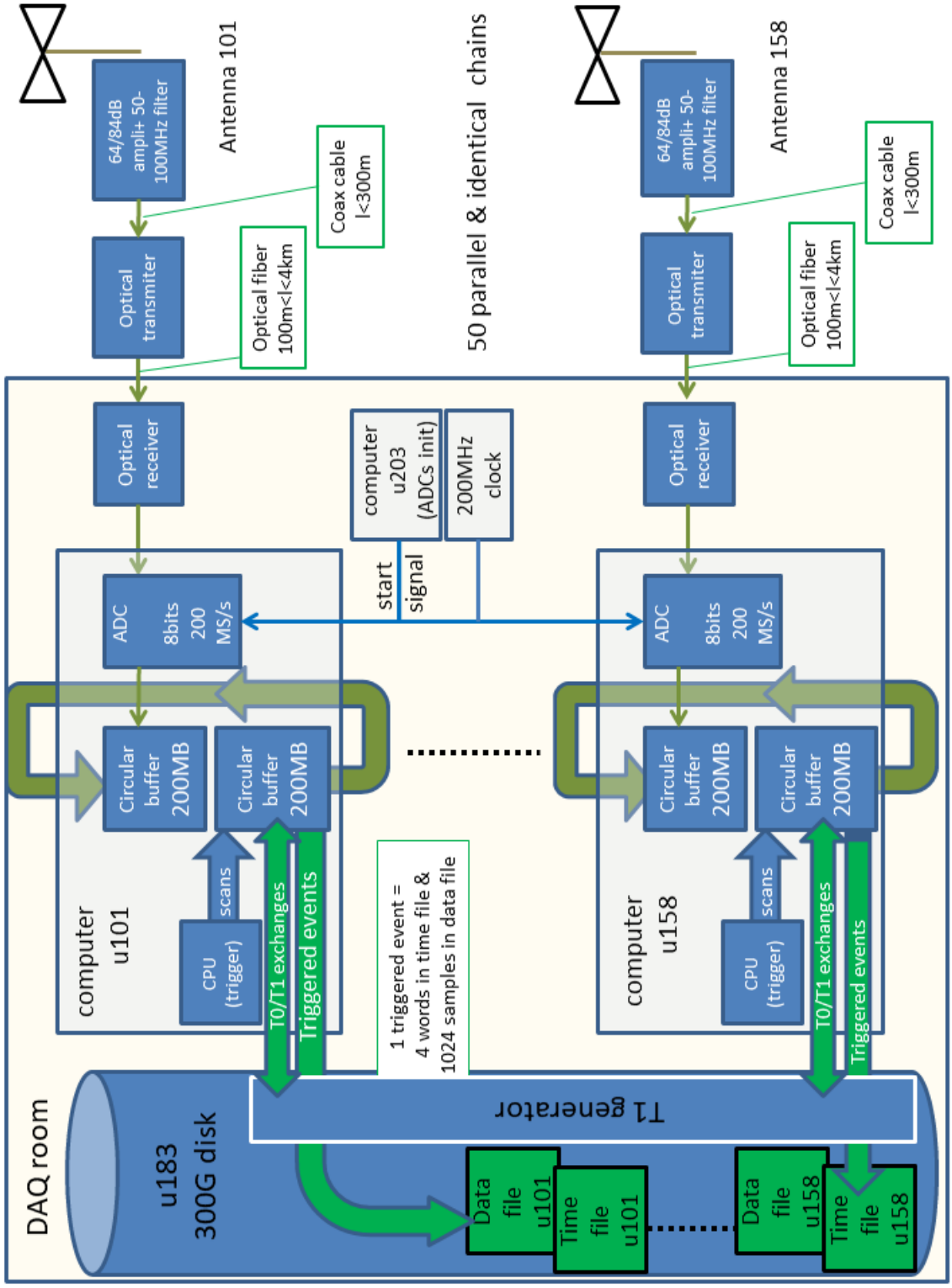

Figure 5.11: *DAQ system for the TREND50 radio array in standard acquisition mode. Only two chains are represented here (for antennas 101 and 158). The others are identical.*

where t_i and t_j are the T0 time values for two antennas i and j (after correction for their respective signal propagation delay, see section 5.5.1), d_{ij} the ground distance between the two antennas, c the velocity of light and T a factor introduced to allow for possible discrepancies between T0 and the "true" trigger time (that is, the actual time at which the electromagnetic wave reaches antenna i). A value $T = 1.1$ is chosen in the data acquisition, which is a safe factor considering the TREND timing resolution (see section 5.5.1).

Including this T1 trigger in the online stage allowed to reduce the data volume by a factor ∼10, and consequently simplifies greatly the offline analysis. However, it should be noted that if one time frame is processed in more than 1.342 s (i.e. if the T1 search is slower than the data flow), then it is lost, together with the following one. In order to avoid such situation, the number of T0s recorded by a PU was limited to a maximum of 256 per sub-frame (∼190 Hz). Subsequent T0s from this PU are lost. A continuous monitoring of such occurrences, and more generally, of the DAQ status, was implemented in the upgraded acquisition program in April 2012 by Fabio Hernandez, computing scientist at the IN2P3 computing center based in Beijing from 2010 to 2014.

5.4.3.2 Power Spectrum Density runs

After a software upgrade in January 2012, the Power Spectrum Density (PSD) at DAQ output was regularly estimated during standard acquisition for all detection units of TREND50, over calibration time frames of duration $\Delta t_{\rm cal}$ typically set to 20 minutes. To this end, time-traces of $N_s = 512$ samples are randomly selected with a stationary probability, p. This probability, p, is set such that on average 10,000 traces are selected in every calibration time frame. This random sampling procedure was used because it provides a non-periodic sampling over the whole calibration time frame while not disturbing the main DAQ task. Selecting all traces during $\Delta t_{\rm cal}$ would have blocked the DAQ, since it is too CPU consuming for our system.

Subsequently, the Fourier transforms of the traces are computed with a Fast Fourier Transform (FFT) algorithm and a Hann windowing using the IPPS library. Averaging the squared amplitudes yields the PSD estimate for the time frame, in units of V^2/Hz:

$$PSD(\nu) = \frac{2N_s K^2}{F_s f_{Hann}} \frac{1}{M} \sum_{i=1}^{M} |FFT_i|^2(\nu) \tag{5.3}$$

where the factor 2 counts for the fact that the IPPS FFT is computed for positive values of frequencies only. The coefficient N_s at the numerator arises from the forward normalization convention used for IPPS FFT. In addition, $K = 0.0076$ is the TREND's ADC conversion coefficient in V/ADC count, M∼10,000 is the actual number of selected traces, F_s=200 MHz is the ADC sampling frequency and $f_{Hann} = 0.3743$ is a normalization factor accounting for the Hann windowing. A PSD measurement is shown in figure 5.12 for illustration. PSD runs are used for amplitude calibration in particular (see section 5.5.2), or more generally, to assess data quality.

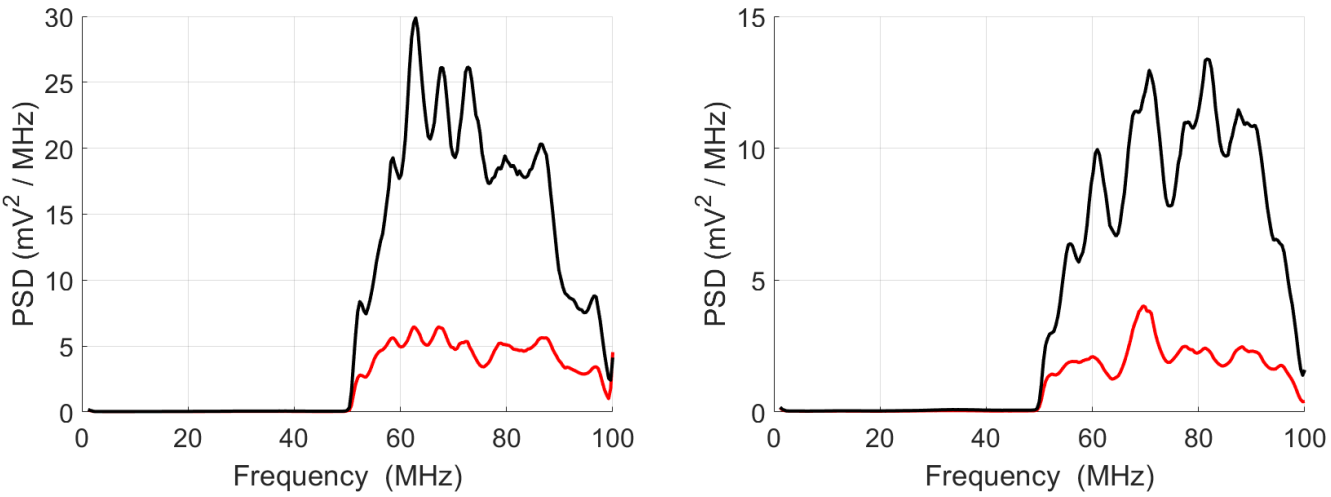

Figure 5.12: *PSD measurements for antennas 101 (left) and 114 (right) during run R3130 (black) and R3129 (red). In the latter the detection unit was replaced by an end plug at the input of the DAQ chain.*

5.4.3.3 Background runs

It is possible to continuously acquire time-traces for limited periods of time without any trigger conditions. The maximal run duration depends on the number of antennas involved, but it does not exceed a fraction of a second due to DAQ limitations. These so-called **background runs** are used, for instance, when a calibration signal is sent from an emitter (see section 5.5.1.3).

5.4.3.4 Scintillator data

Data from the three scintillators were recorded following the standard acquisition mode, except that the trigger level was set to a fixed value (typically 40 ADC units), given the fact that the noise level was very low and stable (see Fig. 5.35). Acquisition of the scintillator data was run fully independently from the radio array.

5.5 Detector Calibration

5.5.1 Time calibration

In the case of TREND, time calibration consists in determining the relative time delays induced by the DAQ chain on the signals detected by the units composing the detector. The quality of this calibration determines in particular the resolution achievable for the reconstruction of the origin of the electromagnetic pulses triggering events in TREND. Appendix A of [207] indeed establishes the analytical relation between a given timing precision Δt and the angular error ($\Delta\theta$, $\Delta\phi$) in the case of a plane wave, and shows that an uncertainty $\Delta t \lesssim 10\,\text{ns}$ on the relative time calibration results in an angular error below 3° —sufficient for TREND needs— for most trajectories and events with multiplicity of six units (see Fig. 8 of [207]). This timing resolution is therefore our target.

5.5.1.1 The PairDifference method

We detailed in section 5.4.3 how data from the TREND detection units are transferred in analog form to the DAQ room, where they are digitized through ADCs running synchronously. Time calibration in TREND is therefore reduced to measuring the differences in propagation times through optical fibers and coaxial cables. This was measured for the three phases of TREND together with Zhao Meng, Valentin Niess, Thomas Saugrin and the staff on site in the following way :

(i) Generate a 10 Hz, 500 mV amplitude square signal with a generator installed in the field, powered by a 12 V battery through a DC/AC converter.

(ii) Split the signal and feed it into the coaxial cables of two neighboring units at the level of the electronic boards' outputs for TREND50, or directly at the antenna output for TRENDproto and TREND15. In the latter case, the electronic boards are bypassed to avoid saturation and possible damage of the amplifiers.

(iii) Start an acquisition on these 2 units (without T1 condition) after the 50-100 MHz filters placed at the ADC input (see section 5.4.3) are replaced by 20 MHz high-pass filters. The square signal at input corresponds to a series of peaks at DAQ level, the optical system acting here as a high-pass filter. The peaks amplitudes are large enough to trigger the DAQ (see Fig. 5.13).

(iv) The mean value of the delay between the peaks associated to a same pulse can then be directly computed from the positions of the peaks in the time traces (see Fig. 5.13) and is considered as a reliable masurement of the relative time delay between these two units.

(v) Repeat the process step by step until all pair delays have been measured. Then all delays are re-computed with respect to A101, taken as the reference.

The very prompt rise of the recorded signal (see Fig. 5.13) allows for a determination of the time delay between the pulses of the antenna pair at the level of a single sample (i.e. 5 ns) typically. The main drawback of the PairDifference method, besides the burden of the measurement itself, is the fact that a given error in an antenna delay measurement will propagate through the following computations.

The precision on the detection units positions also affects the quality of the reconstruction. Antenna positions were measured for the three phases of TREND using a theodolite. Redundant measurements showed that a mean accuracy $\Delta x \sim$3 m could be typically achieved, a value confirmed with GPS measurements carried out in 2014. As $\Delta x \sim c\Delta t$, the errors on the antenna positions have a comparable contribution to TREND's angular resolution and the global timing error is therefore taken equal to 10 ns.

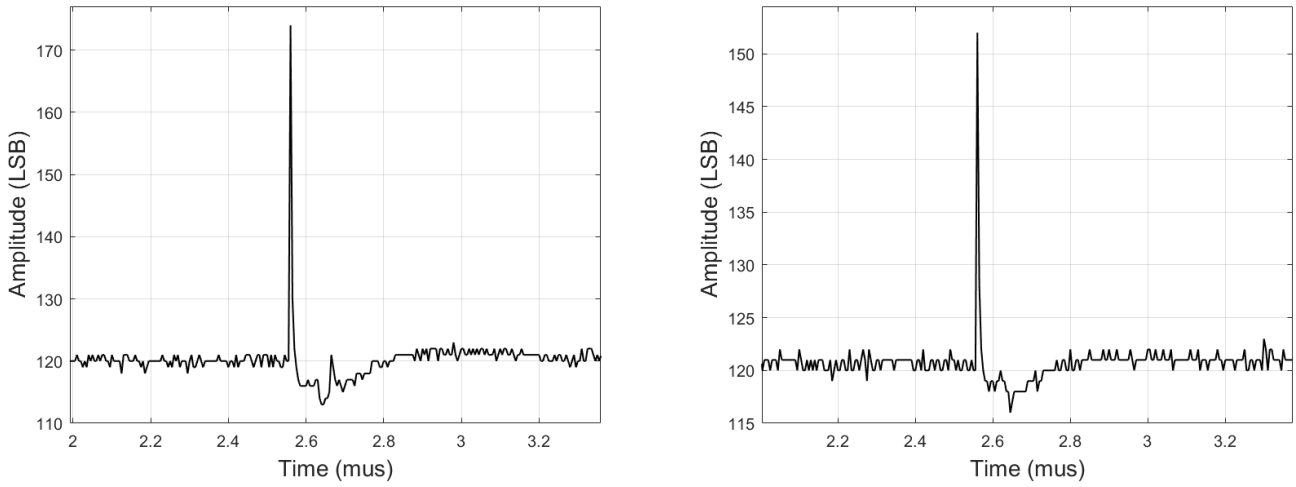

Figure 5.13: *Pulses recorded simultaneously on A106 and A108 during a PairDifference time calibration run. Voltages are given here in ADC units of Least Significant Bit.*

5.5.1.2 Direction reconstruction

The quality of the time delays determination can be assessed by evaluating the precision of the reconstruction for sources of known position. We first detail the reconstruction procedure before presenting the results achieved.

5.5.1.2.1 Method The reconstruction procedure applied in the offline analysis first consists in ordering the trigger times and performing a coincidence search, where the coincidence condition is defined in equation 5.2. If $L \geq 4$ consecutive triggers from L different antennas are in coincidence, we consider that they form an event of multiplicity L which can be associated to one single source. In order to determine with optimal accuracy the antenna trigger time, we then apply to the corresponding waveforms a cross-correlation treatment. Its principle is to determine, for the $L(L\text{-}1)/2$ pairs of signals S_i and S_j present in the event, the delay τ_{ij} which maximizes the cross-correlation coefficient Γ_{ij}:

$$\Gamma_{ij}(\tau_{ij}) = \frac{1}{\sqrt{\int {S_i}^2 \times \int {S_j}^2}} \int S_i(t) S_j(t - \tau_{ij}) dt, \tag{5.4}$$

where S_i and S_j correspond here to a subset of 200 samples around t_i and t_j respectively. In practice, treatment speed optimization led us to perform the cross-correlation treatment on the absolute values of the signals rather than the envelopes, the performances of the former being only slightly worse. The treatment yields a system of $L(L-1)/2$ equations :

$$\mathcal{D} = \mathcal{A}\mathcal{T} \tag{5.5}$$

where $\mathcal{D}$ is the vector containing the values τ_{ij}, $\mathcal{T}$ the vector of corrected trigger times t_i^* and $\mathcal{A}$ is the $(L(L-1)/2 \times L)$ matrix with values 1,-1,0 at appropriate positions. The system can be solved by a simple inversion :

$$\mathcal{T}^\dagger = \mathcal{A}^\dagger \mathcal{D} \tag{5.6}$$

where $\mathcal{A}^\dagger$ is the Moore-Penrose pseudo-inverse of $\mathcal{A}$, chosen such that the residuals of $\mathcal{A}\mathcal{T}^\dagger - \mathcal{D} = (\mathcal{A}\mathcal{A}^\dagger - 1)\mathcal{D}$ are minimal. This yields the corrected values t_i^* for antenna trigger times relative to an arbitrary reference t_{i0}^*=0.

The following step in the analysis chain consists in reconstructing the direction of origin of the events formed by coincident triggers. Given the extension of the TREND array and its timing resolution, the wavefront of an air shower can safely be approximated by a plane wave hypothesis. We may for example note from the plot shown in the left panel of figure 4.1 that the EAS wavefront departs from a plane by delays larger than 10 ns only for distances to the shower axis larger than 300 m. The plane wave reconstruction is performed through the minimization of the following quantity:

$$F_{plane} = \sum_{i=1}^{L-1} \sum_{j>i}^{L} \left[(\vec{x_i} - \vec{x_j}) \cdot \vec{k} - (t_i^* - t_j^*) \right]^2, \tag{5.7}$$

where L is the total number of antennas composing the event, t_i^* and t_j^* are the trigger times for antennas i and j corrected through the cross-correlation treatment, and $\vec{x_i}$, $\vec{x_j}$ their respective positions. The vector $\vec{k}$ can be written as $\vec{k} = \vec{n}/v$ where $\vec{n}$ is a vector of norm unity, orthogonal to the wavefront, and v is the wave propagation velocity, fixed at the value of the velocity of light c. The angular coordinates (zenith angle θ and azimuth angle ϕ) of $\vec{n}$ are the free parameters of the minimization of F_{plane}. We may note at this stage that angles are measured in TREND with respect to the direction of origin of the signal, with North taken as the reference for azimuth. The direction $(\theta, \phi) = (60°,90°)$ thus corresponds to a shower coming from West and 30° above the horizon.

A signal emitted by a point-like background source is however likely to exhibit a curved wavefront, —spherical under an isotropic hypothesis— if it is not too far from the antenna array. In the context of a self-triggering antenna array, it is therefore worth of interest to perform the reconstruction of the direction of the signal assuming a spherical wavefront. The source location and time of emission of a spherical wave can be estimated by minimizing the following function:

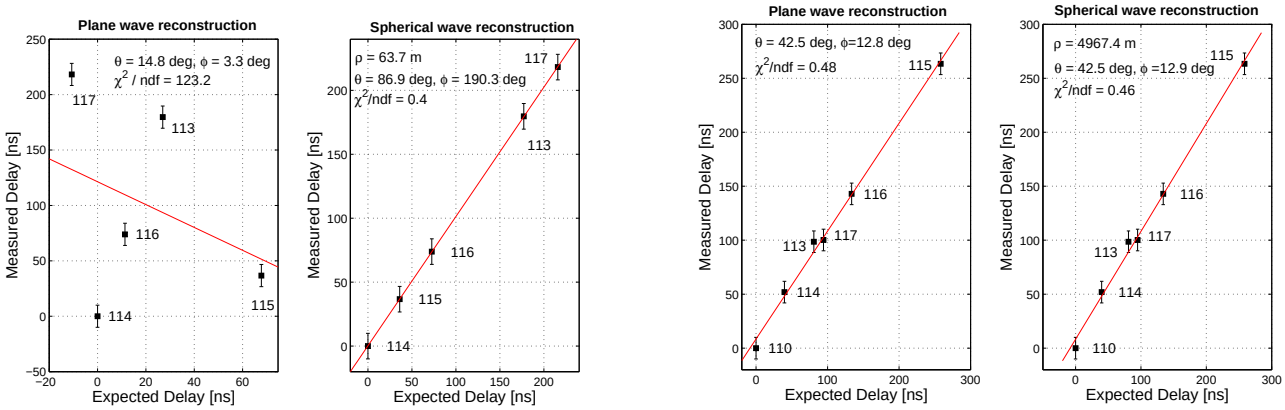

Figure 5.14: *Delay plots for 2 TRENDproto events for plane (left) and spherical (right) reconstructions. Delay plots are defined as the measured trigger times versus the values inferred from reconstruction. In the case of the spherical reconstruction, the parameter ρ corresponds to the distance to the center of pod 114. Antennas are referred by a number (110, 113 to 117) corresponding to their associated pod number. A resolution of 10 ns is assumed for the trigger time (see section 5.5.1). The first triggering antenna is used as the time reference. A linear fit of the points is performed. The event represented in the two left plots was recorded during the calibration run performed with a static source placed in the middle of the TRENDproto array (yellow star in Fig. 5.15). Obviously for sources so close to the antennas, the plane reconstruction fails. Taken from [207].*

$$F_{sph} = \sum_{i=1}^{L} (t_i^* - t_i^{exp})^2, \tag{5.8}$$

where L is here again the event multiplicity, t_i^* is the corrected trigger time for antenna i and t_i^{exp} its expected value, which can be written as :

$$t_i^{exp} = t_0 + \frac{||\vec{x_i} - \vec{x_0}||}{v}, \tag{5.9}$$

$\vec{x_i}$ being the antenna positions. The source position $\vec{x_0}$ and signal emission time t_0 are free parameters of the fit. As for the plane wavefront case, the wave velocity v is taken to be equal to the velocity of light. The **radius of curvature** of the wavefront, defined here as the minimal distance to the source $R = \min(||\vec{x_i} - \vec{x_0}||)$, is a parameter of the spherical reconstruction often used in the offline analysis.

The DMNGB routine from the PORT library [209] is used for the minimization of the F_{plane} and F_{sph} functions. A visual indication of the quality of the direction reconstruction can be obtained by plotting the measured trigger times versus the values calculated with the reconstruction results (see Fig. 5.14). Points deviating significantly from the first bisector are an indication of a bad reconstruction of the signal direction of origin. A linear fit of this distribution provides a qualitative evaluation of the reconstruction.

5.5.1.2.2 Results The quality of the reconstruction was verified in TRENDproto with data acquired while a car was placed at a determined position inside the array. Its gasoline engine sparks plugs would generate electromagnetic pulses which could easily trigger the close-by antennas. The car position could be reconstructed following the procedure above detailed with meter-scale resolution, as can be seen in Fig. 5.15. It was also noticed that the cross-correlation treatment presented in Eqs. 5.4 to 5.6 significantly improved the precision of the reconstructed source position, compared to using the raw trigger times. An explanation could be that the L trigger times are deduced from an over-constrained system of $L(L\text{-}1)/2$ equations. It can also be pointed out that the complete waveform information is taken into account in the cross-correlation treatment, while only one sample (the one with maximum amplitude) is used in the determination of the raw trigger time. Note nevertheless that the time difference between the two treatments is smaller than 3 samples (15 ns) for most signals and that the waveforms associated with these sources are usually characterized by rather long time extensions (several hundreds of nanoseconds). The effect of the cross-correlation treatment may therefore be not as significant in the case of prompt signals such as the ones expected for the electromagnetic emissions associated with EAS.

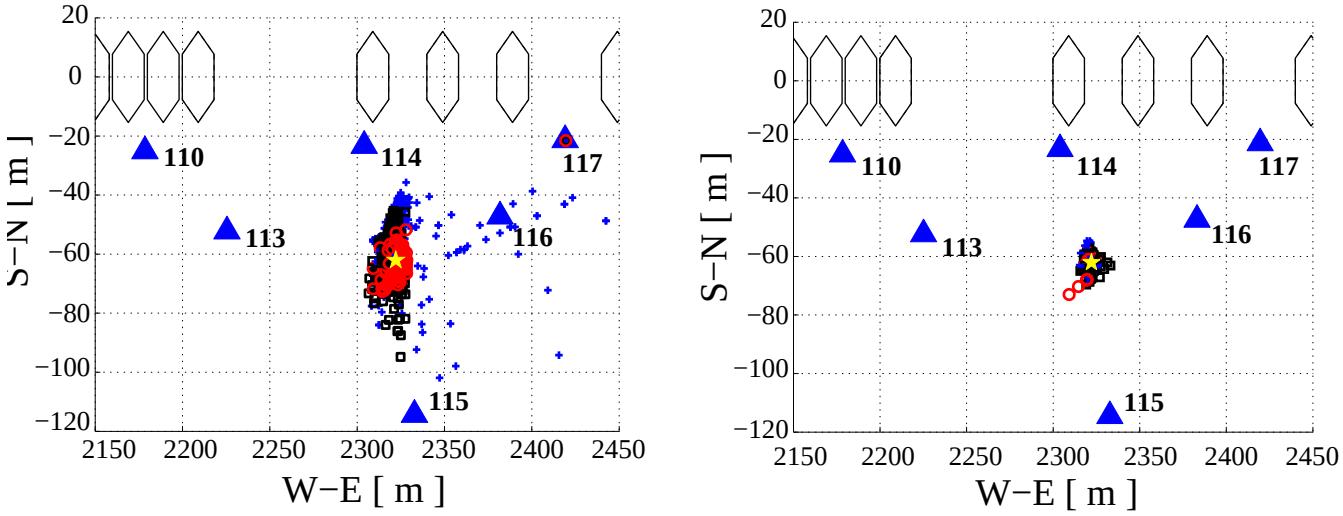

Figure 5.15: *Left: Reconstructed position of a static source for 1642 events recorded during a calibration run on the TRENDproto setup. They are shown as blue crosses, black squares and red circles for events triggering 4, 5 and 6 antennas respectively. The true source position is indicated with a yellow star. Antennas of are indicated by blue triangles, and are labeled by their pod number. Right: reconstructed positions of the source for the same data, after the cross-correlation treatment related to equation 5.4 was applied. Taken from [207].*

In TREND15 or TREND50, transient signals of unclear origin [210] could also be detected while planes were flying above the array. The reconstructed trajectories were then used to check the quality of the reconstruction, as illustrated in Fig. 5.16. The resolution achieved highly depends on the multiplicity of the event and the zenith angle, but values are typically 2-3° for 4 or 5-fold events, and down to 1° or better when multiplicity is above 10 detection units.

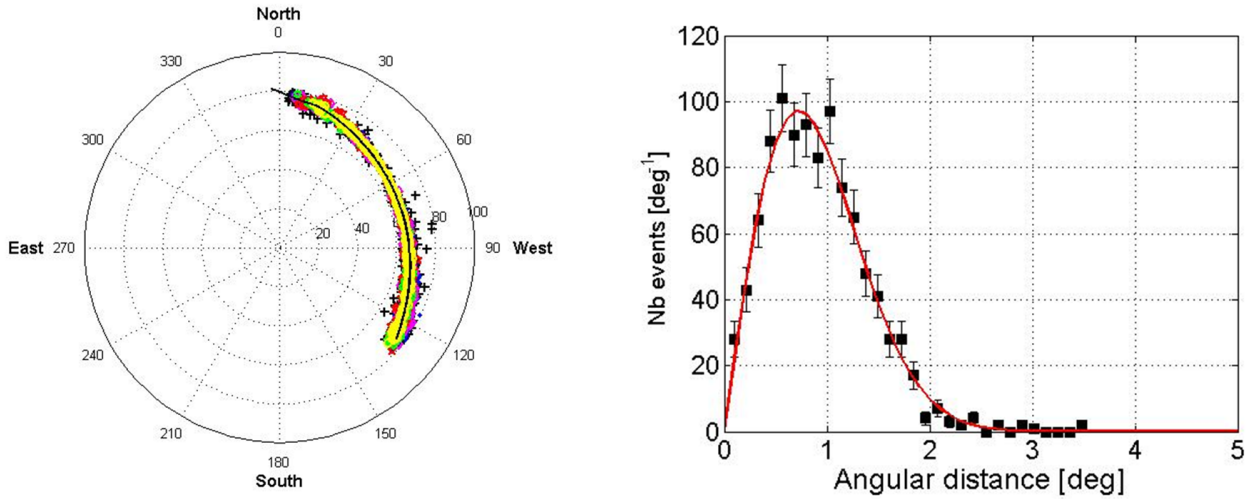

Figure 5.16: *Left: skyplot of 3037 events detected within 4 minutes by the TREND50 array and reconstructed under a plane wave hypothesis. These signals were most likely emitted by a plane flying above the detector. The black line is the mean reconstructed direction of the events, assumed to correspond to the trajectory of the plane. Yellow markers stand for events with multiplicity $L \geq 22$. Right: angular distance $\Delta\psi = \sqrt{(\phi - \phi_{track})^2 + (\theta - \theta_{track})^2}$ between reconstructed source directions (θ,ϕ) and the plane track (θ_{track},ϕ_{track}) for events with multiplicity $L \geq 22$. The ψ distribution is fitted by the function $f(\psi) = A \exp\left(\frac{-\Delta\psi^2}{2\sigma^2}\right) \sin\Delta\psi$, yielding an angular resolution $\sigma = 0.7°$ for this airplane. Taken from [206].*

5.5.1.3 Phase Difference Time Calculation

Despite satisfying results on the reconstruction of sources of known position, it was noted that the χ^2 values obtained through plane or spherical reconstructions were on average larger than the number of degrees of freedom, thus indicating possible systematic errors in delay computation.

Propagation delay in the fibers determined through optical measurements for the 21CMA experiment were also found to differ significantly from values deduced from the **PairDifference** measurements presented in section 5.5.1.1 (see Fig. 5.17). This discrepancy is hard to interpret: one could think that the difference increasing with distance from DAQ room points for example towards an incorrect value for propagation speed, but the opposite trends observed between East and West arms —PairDifference delays larger when moving towards antenna 120, but smaller towards antenna 140— discard this option.

To investigate this disturbing discrepancy in more details, it was decided to test a third independent method, proposed by Gu Junhua, researcher at NAOC, involved mainly in 21CMA and SKA, but also a precious contributor to the latest phase of TREND, and latter to GRANDProto35 (see chapter 6).

5.5.1.3.1 Method The protocol of the method, called Phase Difference Time Calculation (PDTC), is as follows :

(i) First, an antenna is set at position $\vec{x_0}$ in emitting mode by connecting it to a generator emitting at a sine wave of frequency ν_0. A bi-conical antenna (see Fig. 5.19) was used because of its large frequency response and isotropic gain pattern.

(ii) The emitted signal propagates —supposedly isotropically— and eventually reaches an antenna at positions $\vec{x_i}$, which therefore detects a signal of phase $\phi_i = 2\pi\nu_0(t - \|\vec{x_i} - \vec{x_0}\|/c)$ where c is the speed of light. The phase of the signal at DAQ level is then $\phi_i = 2\pi\nu_0(t - \|\vec{x_i} - \vec{x_0}\|/c - \tau_i)$, where τ_i corresponds to the propagation delay for antenna i.

(iii) The phase of the signal is then measured through a FFT performed on the background data (see section 5.4.3.3) recorded on the antennas. An example is shown on figure 5.18.

(iv) The process is then looped over a large number of frequencies ν_0. The propagation delay between any pair (i,j) of antennas can eventually be determined through:

$$\Delta\tau_{i,j} = -\frac{1}{2\pi}\frac{\partial(\Delta\phi_{i,j})}{\partial f} + \frac{\Delta x_{i,j}}{c} \tag{5.10}$$

(v) This treatment leads to a set of $L(L-1)/2$ equations where L is the number of antennas receiving the sine signal. Solving them following the same method as the one applied for the cross-correlation treatment (see Eq. 5.6) allows to determine τ_i.

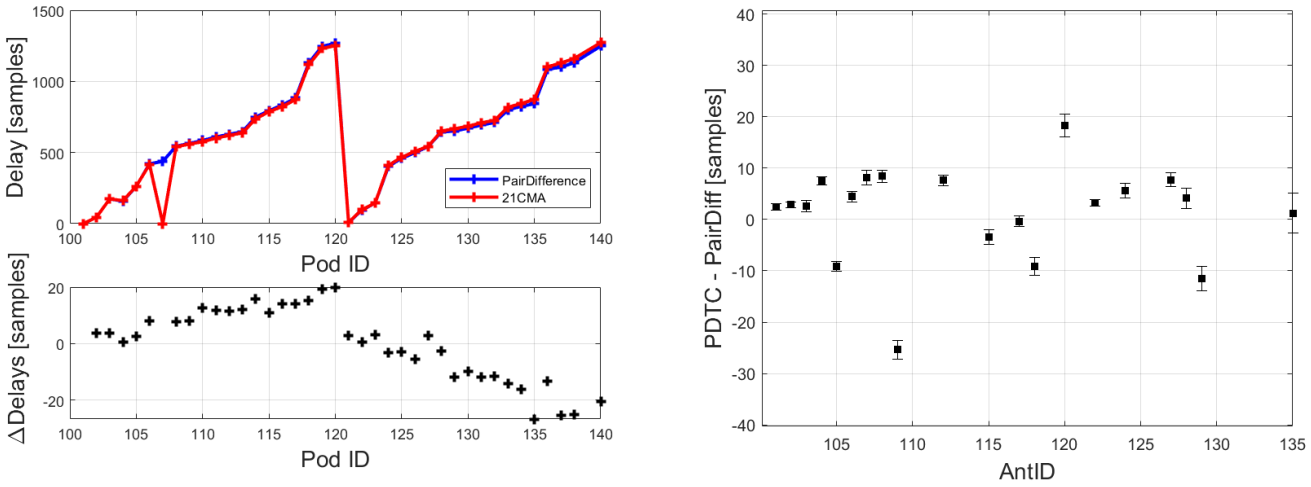

Figure 5.17: *Left: Signal propagation delays for fibers of the East-West arm with respect to the fiber of pod 101 in units of ADC samples (1 ADC sample = 5 ns). Results from optical measurements for 21CMA (red) and through the PairDifference method (blue) are displayed. We recall that the fibers run from pods 101 to 120 (121 to 140) for the East (West) arm. 21CMA measurements are not available for pod 107. Bottom: differences between the two measurements. Right: difference between the delays obtained with the PairDifference and PDTC methods.*

5.5.1.3.2 Results The PDTC method was implemented in August 2013 together with Gu Junhua, Zhang Jianli and Pierre Chauveau, a Master student from the Ecole Centrale de Lyon who worked on TREND at NAOC from April to August 2013 under my supervision. The best results were obtained for a frequency range 75-76 MHz with steps of 10 kHz.

The measurement was impeded by the limited power of the emitter, which produced a usable signal on 22 antennas only. The second issue was the limited duration of the recorded signal: the 5 ms-long traces of the background runs translate in a Fourier spectrum of frequency step $\Delta f = 200$ Hz. This sampling is probably too coarse to ensure that the phase is indeed computed at the exact frequency of the emitted sine wave. This causes, for some measurements, a sizable error in the phase determination.

The PDTC method resulted in delay values in most cases not compatible with the ones obtained from the PairDifference or 21CMA measurements (see Fig 5.17), thus pointing to possible systematic errors. Attempts to perform alternative measurements (e.g. using plane tracks or point sources of known position) did not allow to clarify the situation either, because of their too large statistical errors.

Results of source reconstructions were however considered as acceptable in regards to our (modest) needs for cosmic ray search. We eventually decided not to pursue our efforts on delay measurements, and chose to use the time delays obtained with the PairDifference method.

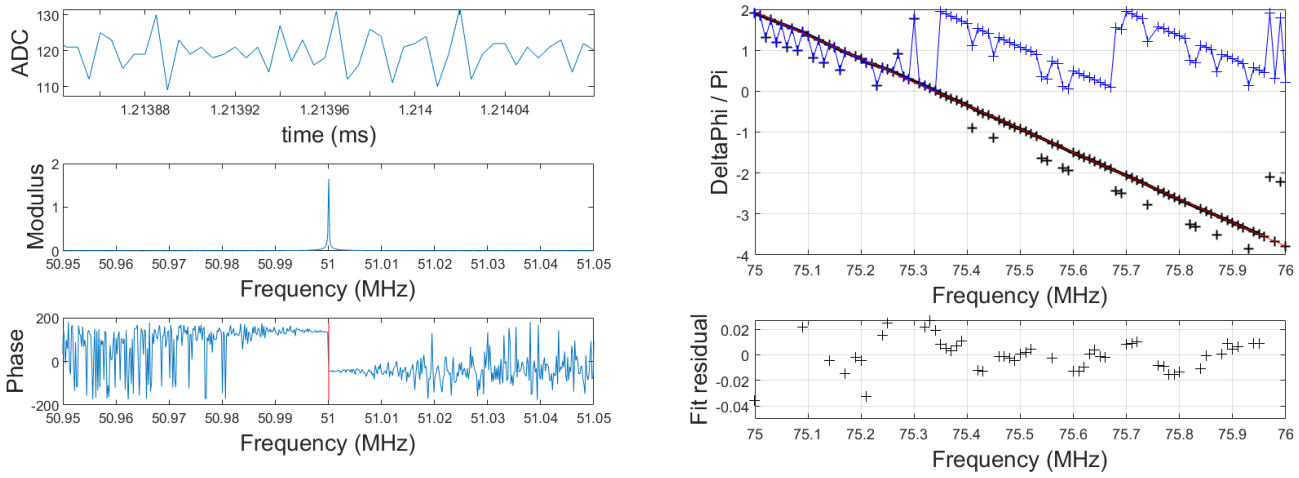

Figure 5.18: *Left: subset of the time-trace recorded on A102 (top) while a 51 MHz sine wave was emitted during PDTC measurements, together with modulus (middle) and phase (bottom) of its Fourier transform. Note how the Fourier analysis allows to recover the sine information, barely visible in the time domain. Right: Fit (red) of* $\Delta\phi_{102,105}$ *values after they were unfolded (black) from their original [0,2π] range (blue). The outliers in the unfolded distribution correspond to errors in the phase measurements and are excluded from the fit.*

5.5.2 Amplitude calibration

Figure 5.19: *Left: Pierre Chauveau, intern on TREND in 2013, checking the quality of the sinus wave fed into the emitting antenna placed behind him during a PDTC measurement. Right: setup used for the TREND absolute calibration: the same bi-conical antenna as for PDTC is flown by a balloon filled with Helium gas and fed by a sine wave. The emitter position is steered with four ropes handled at ground and measured with a theodolite visible in the foreground. The TREND50 antenna being calibrated can be seen in the left of the picture.*

5.5.2.1 Motivation & method

The goal of the TREND experiment was to demonstrate that extensive air showers could be detected with an autonomous radio array. As will be detailed in section 5.7, this requires a detailed and precise simulation of the TREND

detector's response to air showers. A key ingredient to this is a careful amplitude calibration of the detection units, i.e. determining the voltage induced at ADC output for a given electromagnetic radiation at antenna position.

This is a very complex measurement, in particular because calibrating sources can hardly achieve a precision much better than 10% on the amplitude of the emitted electromagnetic field [190], and also because ground reflections induce additional uncertainties on the received signal for open-field calibration procedures. End-to-end absolute calibration was therefore probably too challenging for TREND's modest human resources, and our attempts in this direction (see Fig. 5.19) are not worth being detailed in this document.

Several radio experiments however managed to perform successful absolute calibration of radio antennas at the ∼20% precision level, or slightly better [190, 211, 212, 213, 214], also demonstrating good agreement between experimental results and modelisation of their antenna response. We therefore decided to rely on NEC simulations to determine the response of the detection unit to incoming radio waves and to restrict our calibration procedure to the DAQ chain.

An additional difficulty however arises from the fact that the behavior of TREND setup is unstable, with significant variations of the gain with time (see section 5.6.2). This implies that a continuous calibration has to be performed, allowing to determine the exact status of each unit in the detector at any instant of data taking.

Fortunately, a continuous monitoring of the detector status can be performed thanks to a stable, periodic and well-understood calibration source: the diffuse radiation from our Galaxy. This represents the dominant source of stationary radiation in the TREND frequency range, as already mentioned in section 2.3.1.3, and has been extensively studied and modeled (see [165] and references therein for instance). When folded in the antenna response, it thus provides a signal at the output of the detection unit which amplitude can be estimated with excellent precision [215]. Ratio of the signal measured at the output of the DAQ chain to this expected value at input hence directly provides a measurement of the full DAQ chain gain. This method, used to calibrate the TREND DAQ chain, is detailed in the following. It was implemented by Sandra Le Coz and Valentin Niess for TREND50, but I was heavily involved in the definition, design and validation of the corresponding code.

5.5.2.2 The Galactic Transit Method

5.5.2.2.1 Expected signal at DAQ input As discussed already in section 2.3.2.3, an unpolarized radiation of spectral radiance B_ν induces a power spectral density $\mathcal{P}$ at the output of a detection unit given, in units of V^2/Hz, by:

$$\mathcal{P}(\nu) = \frac{R_L}{2} \int_{4\pi} B_\nu(\theta, \phi, \nu) A_{eff}(\theta, \phi, \nu) \sin\theta d\theta d\phi \tag{5.11}$$

where $R_L = 75\,\Omega$ is the input impedance of the electronic circuit loading the detection unit (see section 5.4) and $A_{eff}(\theta, \phi, \nu)$ its effective area, as defined in equation 2.18.

The diffuse radiation from our Galaxy can be modeled with codes such as GSM [165], which generates maps of sky temperature $T_{sky}(\theta, \phi)$ (see Fig. 5.20) through a wide range of frequencies with an accuracy better than 1%. Spectral radiance can be derived from sky temperature through the Rayleigh-Jeans approximation :

$$B_{sky} = \frac{2k_B\nu^2 T_{sky}}{c^2} \tag{5.12}$$

thus allowing to compute $\mathcal{P}_{sky}$, the corresponding power spectral density at DAQ input through Eq. 5.11.

As the Earth rotates, the Galactic Plane transits through the antenna field of view (see Fig. 5.20), inducing a characteristic variation of $\mathcal{P}_{sky}$ with time. At the latitude of Ulastai and for antennas oriented along the West-East direction, a minimum is expected around 11 h in local sideral time (LST) before the power increases to roughly twice this value around 18 h LST (see Fig. 5.21). This periodic time variation incidentally provides an efficient way to identify malfunctioning antennas.

Black-body radiation from the atmosphere can be neglected in the TREND frequency range (see Fig. 2.10) while other sources were not considered, hence the noise level expected at the output of the TREND detection unit is simply taken equal to the sky contribution: $\mathcal{P}_{ant} = \mathcal{P}_{sky}$. The rms values for the voltage at antenna output —square-root of $\mathcal{P}_{ant}$ integrated over all frequencies— range between 7.5 and 10 μV, depending on the position of the Galactic Plane in the antenna field of view.

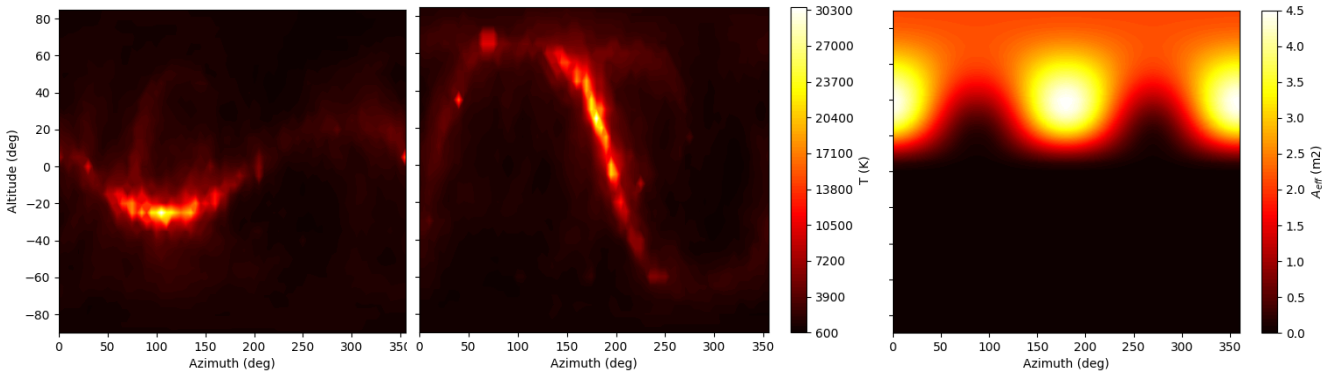

Figure 5.20: *Left: Sky temperature at 75 MHz in Horizontal coordinates, at 11h Local Sideral Time in Ulastai. Altitude (azimuth) is counted positively when moving up (East) from horizon (North). The sky radiation is dominated by the Galactic plane, mostly below horizon at that moment. This map was generated with the LFmap code (`www.astro.umd.edu/~emilp/LFmap`), an alternative to GSM. Middle: same at 18h LST. The Galactic Center, hottest point in the sky, is then above the horizon. Right: effective area of a TREND50 detection unit in the same coordinate system, when the antenna arms are oriented along the East-West axis. The effective area is then maximal for North (azimuth = 0°) and South (azimuth = 180°) incoming directions.*

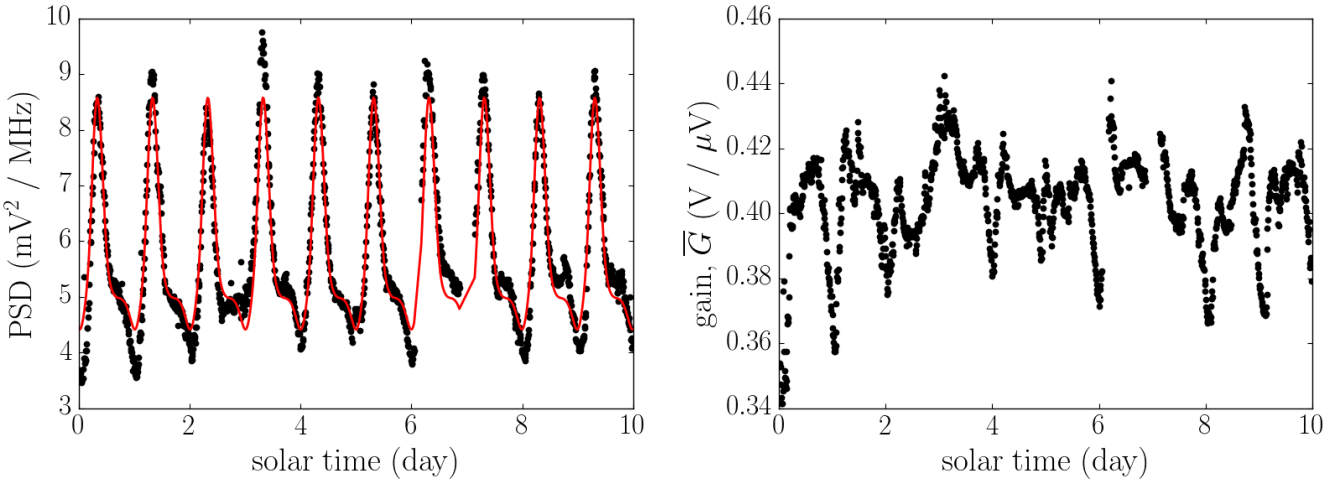

Figure 5.21: *Left: power density measured at antenna output at a frequency $\nu_i = 75$ MHz as a function of local solar time for antenna 113 during runs R3036 to R3049 (August 25$^{\text{th}}$ to September 4$^{\text{th}}$, 2011). Superimposed (red line) is the expected power density $\mathcal{P}_{ant}(\nu_i = 75\,\text{MHz})$ at output of the detection unit, adjusted by a scalar value $G_{75\,MHz}$, following equation 5.13. Right: estimated gain for A113 $\overline{G}$ for the same period of time. Taken from [206].*

5.5.2.2.2 Gain computation The gain of the DAQ chain at any given moment is then computed as the ratio of the measured PSD (see Eq. 5.3) to the noise level at antenna output estimated with equation 5.11. In practice:

(i) First, we estimate the frequency dependent voltage gain, G_{ν_i}, for a set of discrete frequency values $\nu_i \in [55, 95]$ MHz in steps of 5 MHz, as:

$$G_{\nu_i} = \sqrt{\frac{PSD(\nu_i)}{\mathcal{P}_{ant}(\nu_i)}} \tag{5.13}$$

(ii) Then, in order to filter out sharp band emitters, we remove outliers whose gain values depart more than $3\,\sigma$ from the mean value of the set, where σ is the estimated standard deviation from the set.

(iii) Finally, the average gain $\overline{G}$ is estimated as the mean of the subset values, as:

$$\overline{G} = \frac{1}{N_I} \sum_{i \in I} G_{\nu_i} \tag{5.14}$$

where I is the subset of valid values and N_I its cardinality.

An illustration of the whole procedure is given in Fig. 5.21 for the detection unit A113 over a period of 10 days, corresponding to 720 PSD measurements. Note however that our calibration procedure does not allow to distinguish a noisy period affecting all frequencies in the 50-100 MHz range from a variation of the gain. Nevertheless, such noisy periods can be partially vetoed during the analysis, as will be explained in section 5.7.1.

5.5.2.3 Systematic effects

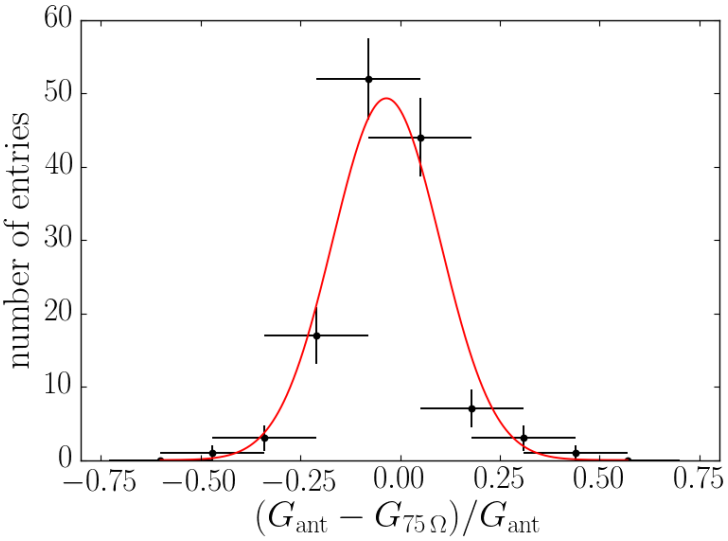

Figure 5.22: *Distribution of the relative difference* $R_G = \frac{G_{ant} - G_{75\Omega}}{G_{ant}}$ *between gains computed with antenna and* $75\,\Omega$ *plug at DAQ input for the 128 valid measurements performed. We find* $< R_G >= -3.6 \pm 1.2$ *%. This validates the DAQ chain calibration method and in particular the hypothesis that background sources beyond the sky emission have a minor contribution to the stationary noise level at the output of TREND detection units. A 13% precision on the DAQ calibration can also be inferred from the standard deviation of the* R_G *distribution. Taken from [206].*

Several effects may affect the calibration method above detailed: the electromagnetic background could be larger than the minimal level given by the sky, the actual antenna response could differ from the modeled A_{eff} value, or the NEC ground model (see Fig. 5.8 for details) considered in our treatment may not represent the true conditions. These effects may bias the actual value of $\mathcal{P}_{ant}$ and consequently the gain.

In order to quantify these effects and the validity of the TREND50 gain computation, the detection units were occasionally replaced by resistive end plugs ($R_0 = 75\,\Omega$). Since the end plug impedance matches the DAQ input impedance, the noise level at the DAQ input can be reliably estimated by its Johnson-Nyquist noise:

$$\mathcal{P}_{75\Omega} = k_B T R_0 \tag{5.15}$$

in units of V^2/Hz, where $T = T_{amb} + T_{\mathrm{LNA}}$, with T_{amb} the physical temperature of the end plug, taken equal to 290 K, and $T_{\mathrm{LNA}} = 28\,\mathrm{K}$ the nominal value of the noise equivalent temperature of the low noise amplifier. Amplifier noise indeed has a non-negligible contribution here, whereas sky temperature of several hundreds Kelvin justify that it was neglected in the computation of $\mathcal{P}_{ant}$. Noise contributions from later stages of the DAQ chain are considered negligible after the LNA 24 dB amplification of the signal.

A PSD measurement for this setup then directly allows to compute the DAQ chain voltage gain through equation 5.13, after substituting $\mathcal{P}_{ant}$ with $\mathcal{P}_{75\Omega}$.

Given the burden of this calibration procedure — plugging end plugs into electronic chain inputs instead of detection units and back —, the gain values were computed with this method for a total of 128 measurements only, recorded on different antennas and at different moments of the TREND50 operation period. They were then compared to gain values determined through the standard procedure, performed right after the detection units were reconnected. The relative difference between the two gain values is displayed in figure 5.22. The relative difference between the gains computed through these two independent methods has a mean value of 3.6%, thus validating the calibration procedure of the TREND50 detection units above detailed.

5.6 The TREND data

5.6.1 Datasets

5.6.1.1 TRENDproto & TREND15

The TRENDproto data selected for the air showers search were recorded between January 13 and May 8, 2009, for a total live time just below 10 days (584.7 hours). These data were the base of the work presented in reference [207].

The TREND15 radio array was put in operation on January 15, 2010, completed with the scintillator array on March 27, 2010. The initial software developed to process TRENDproto data was however not optimized for the much larger data volume of TREND15, making its full analysis hardly possible with these initial tools. After coincidences were found between the scintillator and radio arrays (see section 5.8.1), the main objective of TREND15 was fulfilled and priority was given to TREND50, TREND15 data being left aside.

5.6.1.2 TREND50

Two datasets were used for the search of cosmic rays with TREND50: the first one was recorded between January 13, 2011 and December 6, 2012, while antenna arms were oriented along the East-West axis. This dataset corresponds to a total of 314.3 live days, during which $8.6 \cdot 10^{10}$ T0 and $7.3 \cdot 10^{8}$ T1 triggers were processed and $9.7 \cdot 10^{9}$ time-traces recorded.

Antennas were then rotated towards the North-South axis — except for antennas 148 to 155, which were shut down — and the system ran in this configuration between December 11, 2012 and January 10, 2014 for a total of 120.6 live days, during which $9.6 \cdot 10^{9}$ T0 and $4.9 \cdot 10^{8}$ T1 triggers were processed, and $4.1 \cdot 10^{9}$ time-traces recorded. The live time of each individual antenna is represented in figure 5.23 for these two periods. Detailed information is also available in annex A.

During both East-West and North-South periods, data acquisition was also stopped for various periods of time for maintenance, upgrades or during the one-month annual closure of the site. Data were therefore split during the analysis procedure in 10 different periods, each corresponding to homogeneous run conditions (see annex A for details). In addition, failure of the DAQ room cooling system and a car accident severely damaging the optical fibers network caused several additional weeks of interruption of data acquisition in 2013.

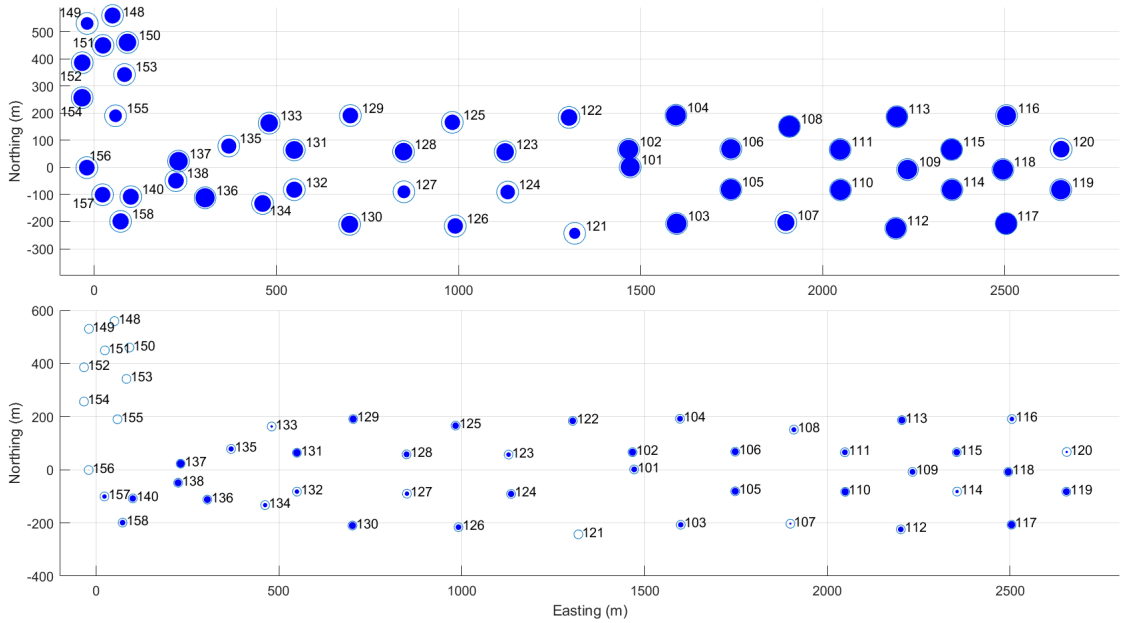

Figure 5.23: *Live-times of the TREND antennas represented by disks with a radius proportional to their values. Top: East-West period, bottom: North-South period. Live-time is defined here as the periods when antennas were part of the DAQ and in a state allowing to trigger on transient radio pulses. For both plots, the outer circle represents the total live-time of each period (314.3 and 120.6 days respectively). The average live time fraction of the detection units is 66 and 46% for each of the two periods.*

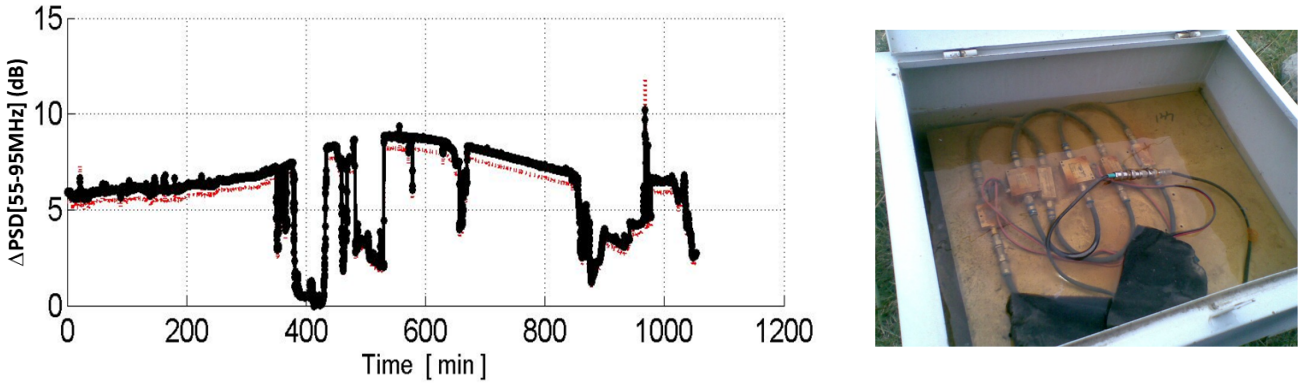

Figure 5.24: *Left: variation of the PSD value —averaged over the 55-95MHz frequency band— as a function of time for data recorded on antenna A101 over 18 hours. The gain exhibits sharp jumps atop the smooth fluctuation due to the transit of the Galactic Plane in the antenna field of view (see section 5.5.2 for details). No significant correlation with time or detection unit could be found for these jumps and their cause was never clearly identified, even though instability of the power supply is strongly suspected. Note the sharp rise of the PSD value is observed around $t = 950$ min because of a transitory source. Right: an electronic box full of water after a heavy storm.*

5.6.2 Data quality

5.6.2.1 Detector status

The status of the detector could be assessed with monitoring information acquired in standard acquisition mode: the number of T0 and T1 triggers logged for every unit and every 1.3 s time frame, and the periodic PSD measurements taken of all detection units carried out automatically on a 20 minutes-period basis after a DAQ upgrade performed in February 2012.

The analysis of the corresponding data shows that detector reliability was a major issue for TREND. As seen in section 5.4, the acquisition chain was composed of elements taken from the 21CMA experiment. The electronic elements were certainly fit for the very stable response of the 127 antennas forming a 21CMA pod, but turned out not to be adapted to the large dynamic range of TREND signals. Radio glitches of high intensity detected by TREND units could occasionally significantly damage amplifiers or optical transmitters, while monitoring data clearly showed that voltage supply or quality of the fibers connections —critical for the optical transfer of analog signals— varied over time, sometimes very abruptly (see Fig. 5.24). Finally, the harsh weather conditions in Ulastai —winter nights regularly below -30°C, heavy winds, snow and rain storms— were challenging for the material: cables degraded quickly, water could fill the electronic boxes or humidity could get inside the box holding the RF transformer at the antenna feed point (see Fig. 5.8) and eventually break the soldering bound of the transformer when freezing. These various issues required a constant and significant effort to identify, fix or replace the faulty parts of the setup. It was also the main motivation for the continuous calibration procedure implemented in TREND50 and described in section 5.5.2.

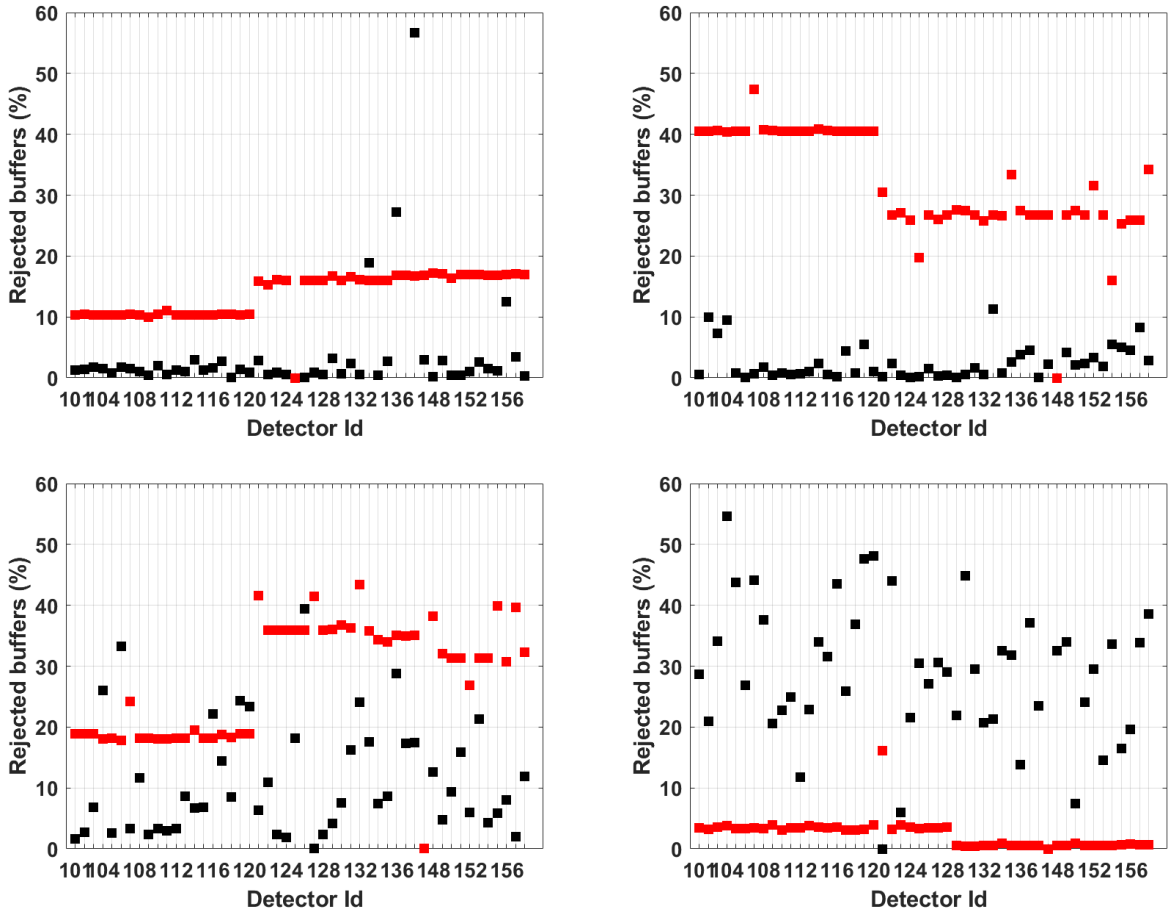

Figure 5.25: *Red: fraction of rejected time frames for each TREND50 detection unit. Black: fraction of time frames reaching the maximal T0 rate. Plots from top-left to bottom right corresponds to periods 2-3 (March 31 to Oct. 10, 2011), 4-5 (Nov. 3, 2011 to Feb. 11, 2012), 6-8 (Feb. 23 to Dec. 6, 2012) and 9-10 (Dec. 11, 2012 to Jan. 10, 2014).*

5.6.2.2 DAQ status

In standard acquisition mode, the index of each time frame successfully processed, the T0 and T1 rates were logged into the system for each and every time frame of a TREND50 acquisition. This allowed for a reliable offline monitoring of the DAQ live-time, presented in figure 5.25. This plot shows that the fraction of time frames rejected because not processed in the required 1.342 s time interval (see section 5.4.3) was around 10% at the start of TREND50 data taking. This however degraded with time, reaching ∼40% on average in February 2012. A major software upgrade, combined with a refurbishment of the hardware —the slowest processing units then being replaced with back-up ones— allowed to maintain the fraction of rejected time frames to workable levels in the last periods of TREND data taking. The fraction of time frames reaching the 190 Hz limit of for T0 (see section 5.4.3) increased steadily with time, clearly indicating a degrading radio environment, as discussed in the next section.

5.6.3 The TREND electromagnetic environment

As a self-triggered detector, TREND acquired a very large quantity of radio pulses. These were eventually rejected in the cosmic-ray candidates identification process. Before detailing this selection in section 5.7 and its results in section 5.8, we will show here how this data was used to study the radio environment of the TREND setup, again restricting our study to TREND50 data.

The first striking feature of the TREND50 data is the very irregular rate of triggers: while T1 rates average 30 Hz over the three years of data taking, they could shoot up to much larger values for short period of times as illustrated in Fig. 5.26 for a typical example. On longer timescales, the data acquisition conditions can be divided in two distinct periods: until September 2012, the total TREND50 T1 rate for a given run was 20 Hz on average, before rising up to 95 Hz after that date (see Fig. 5.27). This evolution was particularly significant for antennas A101-A120 located in the Eastern part of the array.

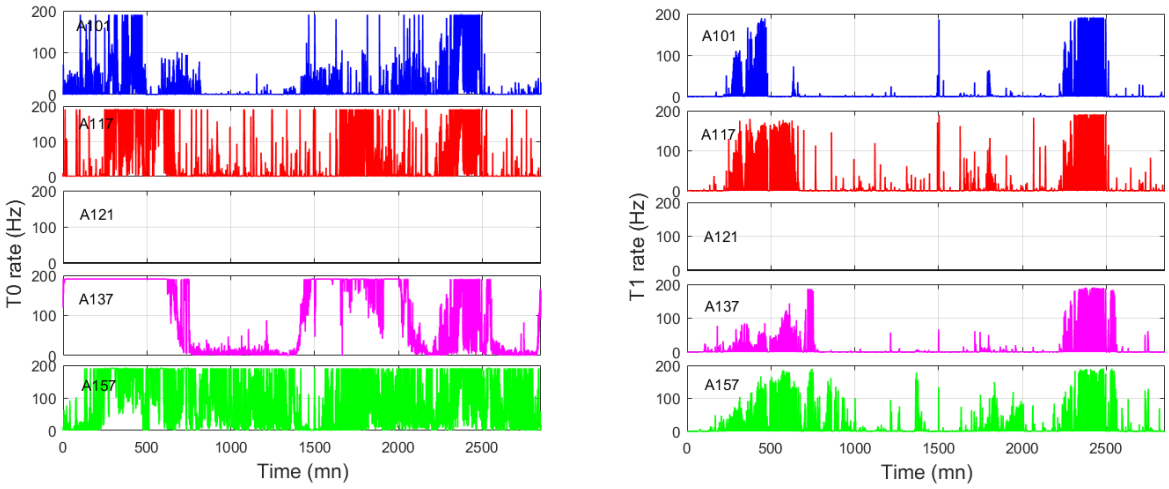

Figure 5.26: *Left: rate of T0 triggers as a function of time for some TREND50 detection units during run R3589 started on March 10, 2012. Right: same for T1 triggers. Note that A121 is not working in this run, despite being part of the DAQ. Taken from [206].*

Another interesting feature is the distribution of time delays Δt between consecutive events. As illustrated in figure 5.28 for one run, a clear periodic structure can be observed, with Δt values clustering around multiples of 10 ms. This indicates that these events most likely originate from the power grid elements surrounding the TREND50 detector, for which discharges may occur — on HV transformers or power line insulators — when the current reaches its extreme value, thus generating 10 ms-periodic electromagnetic bursts triggering the TREND50 array.

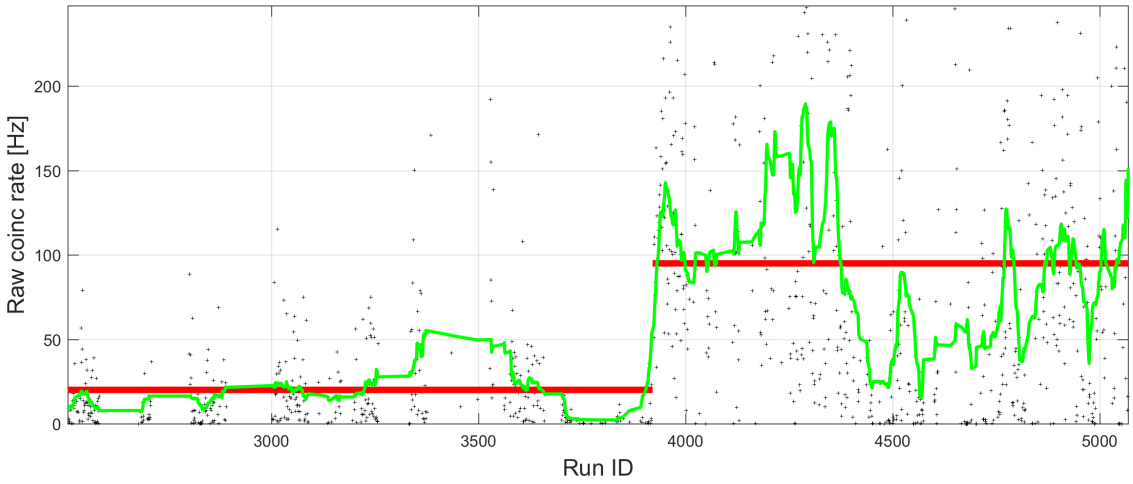

Figure 5.27: *Run-averaged T1 rate over the whole TREND50 array versus run ID (black dots). In green is displayed the curve smoothed over 30 consecutive runs for the purpose of clarity, and in red the average of the T1 rates over the periods 1-7 (January 13, 2011 - September 16, 2012) 8-10 (September 17, 2012 - January 10, 2014). Average T1 values are 20 and 95 Hz respectively. Taken from [206].*

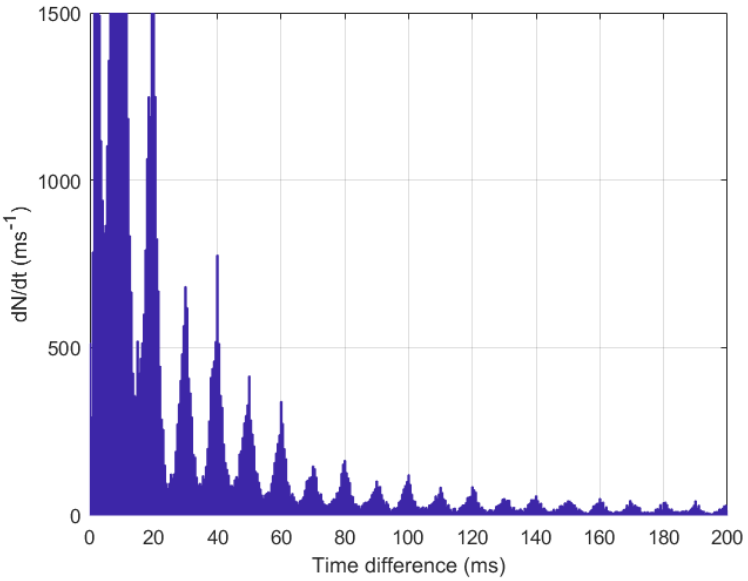

Figure 5.28: *Distribution of the time delays between two consecutive events for data recorded during run R3589. A periodic structure with T=10 ms clearly appears, signing the fact that many events in these data can be associated with 50 Hz power lines. Taken from [206].*

Reconstruction of the event sources provides a deeper insight in the TREND50 electromagnetic environment. Because of early selection cuts (see sections 5.7.1.1 to 5.7.1.3 for details), source reconstruction was performed for a small fraction of the total dataset only, following the method presented in section 5.5.1.2.1. Besides, the limited extension of the TREND50 array does not allow for a good handle on the actual distance to sources located outside the array. Yet, it can clearly be observed in Fig. 5.29 that events often cluster around — or in a direction compatible with — some specific elements in the TREND50 surroundings. Figure 5.29 also shows that the increased T1 rate observed after

September 2012 coincides with a larger number of sources reconstructed in the direction of three electrical transformers located around x=3300 m.

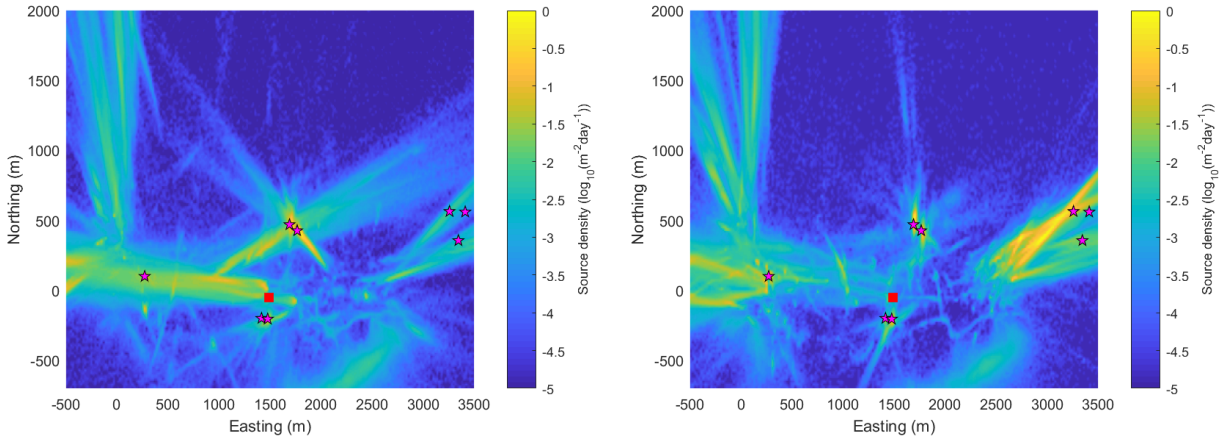

Figure 5.29: *Positions of reconstructed point-sources of TREND50 events for the period until September 2012 (left) and after that date (right). Superimposed are the locations of the TREND50 DAQ room (red square) and some HV transformers or power line insulators (stars) located in the vincinity of the TREND50 array. Many reconstructed source positions cluster around these positions, confirming that local power system elements constitute sources of background events. The finite extension of the TREND array implies a poor handle on the actual distance to sources, hence generating the long tails observed in the distribution of the reconstructed positions. Taken from [206].*

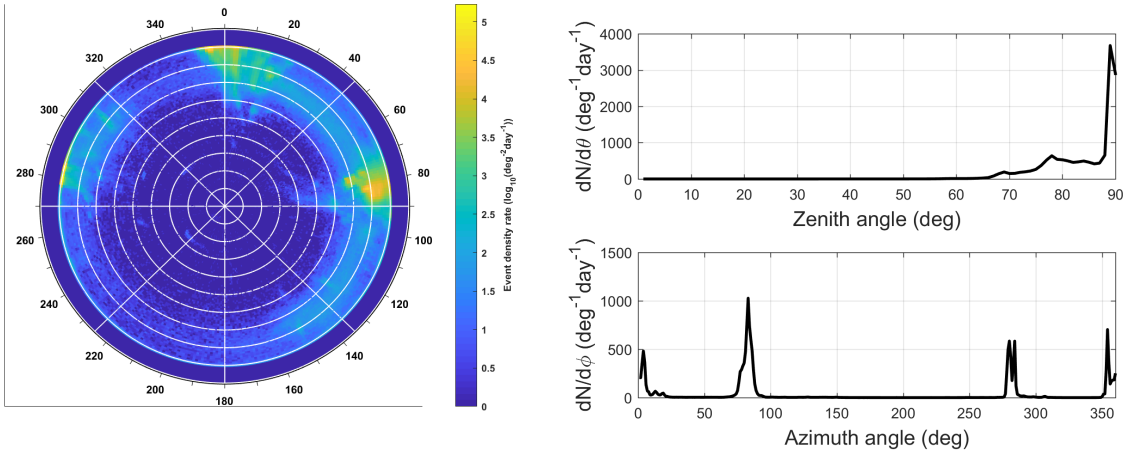

Figure 5.30: *Left: sky distribution of the TREND50 events direction of arrivals. Only events from the East-West period with valid spherical reconstruction and radius of curvature $R \geq 3000$ m are shown in this plot. Right: zenith (top) and azimuth (bottom) distribution for the same events. Taken from [206].*

For events reconstructed with a radius of curvature $R \geq 500$ m, a plane wavefront hypothesis is considered as valid, and the direction of origin of the wave can then be described by its zenith and azimuth angles (θ,ϕ). The distribution of these parameters is displayed in Fig. 5.30 for events with $R \geq$3000 m. Here again, a large majority of events cluster in specific directions mostly located along the horizon, even though reconstruction errors result in a leakage of this population to smaller zenith angles.

As a conclusion to this section, it clearly appears that, even in a remote location like the TREND site, background sources exist and trigger the antenna array at rates of several tens of Hz, much larger than what is expected for air showers. Yet, a large fraction of these events cluster in time and location, thus giving a good handle for their rejection through a dedicated offline treatment detailed in the next section.

5.7 Cosmic ray selection

More than 10^9 events triggered the TREND50 setup over its 434.9 live days of run, while simulations presented in section 5.7.2 point to a few thousands cosmic rays only detectable with this array. This means that a huge majority of the events detected by TREND50 are generated by background sources, an observation consistent with the results of the previous section. This statement of course applies as well to the TRENDproto and TREND15 data.

Fortunately, the features typical of background signals and those of air shower radio signals differ significantly. We therefore developed in the TRENDproto offline data treatment a series of **environment** and **candidate cuts** —respectively based on the typical characteristics of background and air shower events— in order to select air shower candidates. We then adapted and refined the treatment with TREND50. These cuts are detailed below.

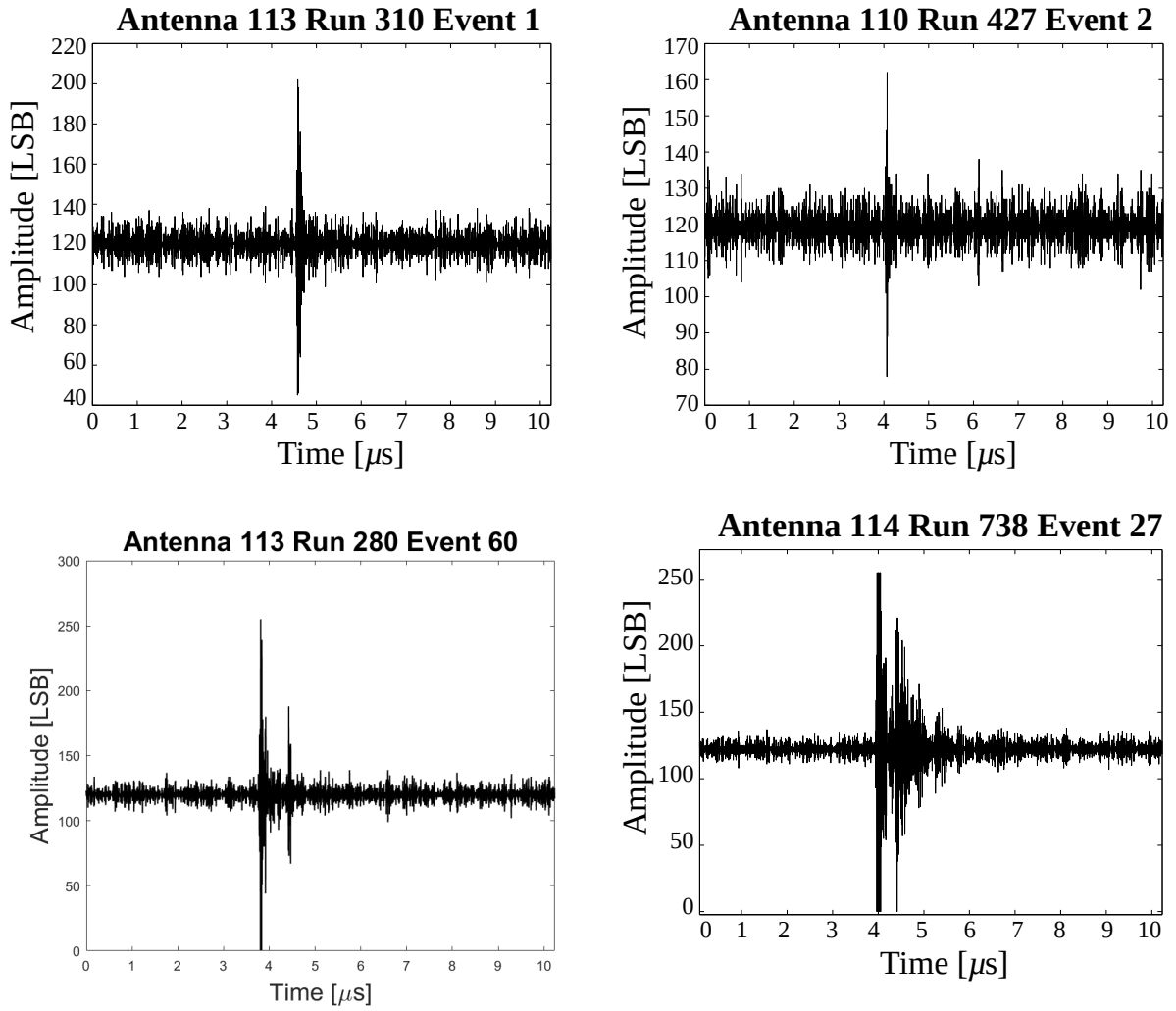

Figure 5.31: *Top: two waveforms passing rejection criterion based on pulse shape. Bottom: 2 waveforms rejected with this cut. Adapted from [207].*

5.7.1 Selection cuts

5.7.1.1 Noise bursts

As illustrated in figure 5.26, the antenna trigger rate is very irregular, with large bursts followed by quieter periods. These burst periods represent large volumes of data, but a minor fraction of the acquisition time. Excluding them from the air-shower search sample thus allows removing a large fraction of background events at a moderate cost for air-shower detection efficiency.

The following cut was therefore implemented in TRENDproto: any period of three minutes during which at least three events were detected with multiplicity $L \geq 4$ was rejected. In TREND50, the corresponding cut consisted in rejecting an event if another one occurred within a time period of ± 200 ms with at least one detection unit in common.

5.7.1.2 Pulse shape

As mentioned already in section 2.3.1.2, signals induced at antenna output by an air shower are expected to be brief (pulse width <300 ns at DAQ level) . On the other hand, signals from background sources are often significantly longer ($\sim 1\,\mu$s), and followed or preceded by other transient pulses within a few μs at most (see Fig. 5.31).

An offline treatment was therefore implemented to scan the time-traces and identify the periods when the signal exceeds the noise level by more than 4σ. If there is more than one such period in a given time-trace, or if the central period extends beyond 350 ns, then this time-trace is rejected and the corresponding antenna removed from the event.

5.7.1.3 Reconstruction

Events failing reconstruction —performed following the method described in section 5.5.1.2.1— are rejected. The quality of the reconstruction can be quantified by the χ^2/ndf value of the linear fit of the **delay plot** which represents the expected trigger times versus measured values, as illustrated in figure 5.14.

This was studied in TRENDproto with Monte-Carlo simulations of events associated with plane and spherical wave-fronts. The simulation of events associated with plane wave-fronts was done by first generating random values for the wave direction of propagation. Then the antennas trigger times were computed for each of these directions, and smeared afterward assuming a Gaussian time resolution with $\sigma = 10$ ns. The simulation of events associated with spherical wave-fronts proceeds as follows : a source position is randomly chosen within 500 m from the center of the TRENDproto array. The antennas trigger times were then computed assuming a spherical propagation of the signal from the point source and —as for the plane wavefront case— the computed trigger times are then randomly smeared, assuming a Gaussian distribution with $\sigma = 10$ ns for the timing resolution.

10000 plane wavefront events and 10000 spherical wavefront events were simulated with this procedure as triggering the six antennas of the prototype. The plane and spherical wave-fronts reconstruction procedures described in section 5.5.1.2.1 were then applied to these simulated events. A linear fit was then performed on their delay plots similarly to the case illustrated in figure 5.14).

The χ^2/ndf distributions resulting from this treatment are shown in figure 5.32. As expected, distributions are similar for plane and spherical wave-fronts for the spherical reconstruction, while the plane reconstruction for spherical wavefront events is, on the average, worse than for plane wavefront events. It seems reasonable from this result to exclude all events associated with a χ^2/ndf value above 2 for the plane reconstruction. However, data tend to exhibit larger χ^2/ndf values than what is observed with simulations, as already mentioned in section 5.5.1.3. The cut set to the plane waveform reconstruction of the direction of origin in our cosmic ray search procedure in TRENDproto was therefore $\chi^2/ndf < 5$.

In TREND50, the cut was loosened to $\chi^2/ndf < 30$ in both plane and spherical cases —allowing to keep a large number of events in the following steps of the analysis— and the slope of the linear fit of the delay plot was requested to be in the range [0.9, 1.1]. As direction reconstruction is significantly less precise for 4-fold events, and since some of the other selection cuts have proved to be less efficient with this minimal multiplicity, only events with at least five participating antennas are selected for the subsequent stages of the air-shower search.

Two more cuts associated with source reconstruction are applied in the air shower selection procedure:

- in TREND50 only events with a radius of curvature $R \geq 3000$ m are selected. The motivation for this cut is that TREND50 is expected to detect air showers with zenith angles larger than 40° in the vast majority of cases (see

Fig. 5.37). For such showers, the X_{max} position —considered in first approximation as the source of the radio emission, see section 4.1— is further than 3000 m from the shower core position. On the contrary, a majority of background sources are close enough from the array so that they can be associated with a radius of curvature smaller than this value. The corresponding cut in TRENDproto requests that spherical and plane reconstruction would yield an angular distance below 10, 7 and 4° for event with multiplicities of 4, 5 and 6 events respectively.

- only events with zenith angle $\theta \leq 80°$ in TREND50 (65° in TRENDproto) were selected. The signal/noise ratio is very unfavorable beyond this value, as background events cluster along the horizon (see Fig. 5.30), while very few air-showers are expected in this zenith range. This is probably due to the reduced sensitivity of the TREND antenna for waves with large zenith values (see Figs. 5.7 and 5.8).

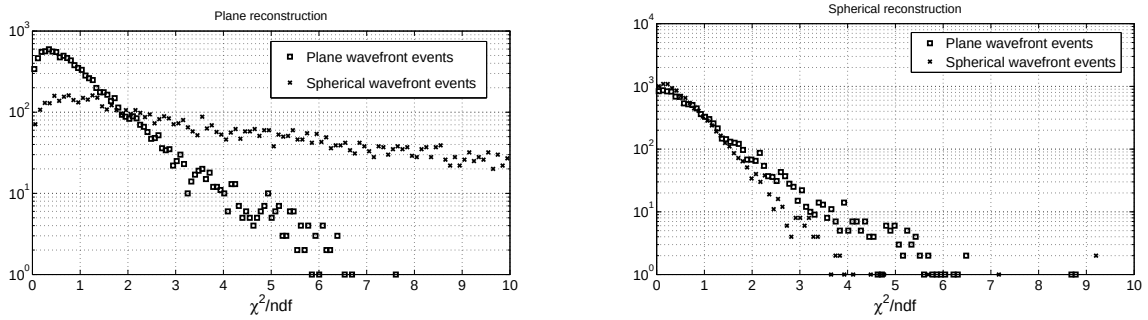

Figure 5.32: *Left : histogram of the χ^2/ndf values obtained from the linear fit of the delay plots (see Fig. 5.14) for the plane wave reconstruction of 10000 simulated plane wavefront events (squares) and 10000 simulated spherical wavefront events (crosses). In the case of spherical waves, the wave source position is randomly chosen on the ground within a distance of 500 m from the center of the antenna array. Right : χ^2/ndf distribution for the spherical wave reconstruction of the same events. Taken from [207].*

5.7.1.4 Trigger pattern at ground

Because of relativistic beaming effects already mentioned in section 2.3.1.2, cosmic ray air showers induce a radio footprint of modest size at ground. Besides, the dominant geomagnetic origin of the radio emission inducing a linear polarization of the EAS radio signal (see section 2.3.1.1), it is expected that, for most showers, all mono-polar TREND50 antennas within this footprint receive a comparable signal. Waves with elliptical polarization may instead induce strong differences of the induced signals, depending on the antenna orientation with respect to the electric field vector at that position. The corresponding events could therefore be characterized by extended illuminated area and/or "holes" in the trigger pattern. Two corresponding cuts are implemented in the TREND offline air shower selection procedure:

- it is first required that the mean distance of the antennas participating in the event to its barycenter position is smaller than 500 m.
- an event is also rejected if more than one hole in the trigger pattern exists (i.e. at least two non-triggered antennas surrounded by triggered antennas). It must be pointed out here that the polarization and amplitude patterns at ground could certainly be a great tool for background rejection, as detailed in section 4.3. The peculiar layout of the TREND50 setup (see Fig. 5.4.2), combined with the fact that antennas are mono-polar, however prevents this selection cut from being optimal for the analysis presented here.

Due to the limited extension of TRENDproto, this cut could be applied on TREND50 data only.

5.7.1.5 Neighboring events

As mentioned already, background events cluster in time (burst periods, see Fig.5.26) and space (fixed background sources location, see Fig. 5.30). It is natural to exclude these periods or locations from the air shower search, as they are characterized by disastrous signal/noise ratios. Two corresponding cuts were implemented in the TREND50 air shower search procedure:

- an event is rejected if at least another one is found within ± 30 s of the candidate's trigger time with a valid reconstruction (as defined in section 5.7.1.3) and at least 66% of its antennas in common with the candidate.
- an event is rejected if at least another one is found within ±10 minutes with a valid reconstruction yielding a radius of curvature $R \geq 500$ m an azimuthal difference $|\Delta\phi| < 10°$, and at least 33% of its antennas in common with the candidate.

5.7.2 TREND50 air showers simulations

In order to evaluate the air shower detection efficiency of the whole TREND50 data taking and processing chain, air shower events have been simulated in the most realistic way and processed through the standard TREND50 data analysis chain. The production of these run-wise simulated events, carried out by Sandra Le Coz, was as follows:

(i) First, the parameters of the air showers are defined: a fixed value is chosen for the primary particle energy E_i taken in the following set: [$5{\cdot}10^{16}$, $7{\cdot}10^{16}$, $8{\cdot}10^{16}$, $1{\cdot}10^{17}$, $2{\cdot}10^{17}$, $3{\cdot}10^{17}$, $5{\cdot}10^{17}$, $7{\cdot}10^{17}$, $1{\cdot}10^{18}$, $2{\cdot}10^{18}$, $3{\cdot}10^{18}$], where energies are given in eV. The direction of origin of the shower (θ, ϕ) is then drawn randomly from a uniform sky distribution, and the core of the shower $\vec{x}_{core}$ is also a random position in an area S_{draw} surrounding the array, where S_{draw} is defined as a function of θ and ϕ, and large enough so that all showers likely to trigger the TREND array fall into S_{draw}. The process is repeated N_{draw} times, until N_{sim} trajectories are produced with a minimum of five antennas falling within a distance $d \leq d_{min}$ from the shower axis. Here d_{min} ranges between 500 and 1000 m depending on E_i, and $N_{sim} = 10\,000$ for energies $E_i \leq 1 \cdot 10^{17}$ eV and $N_{sim} = 3\,000$ for $E_i > 1 \cdot 10^{17}$ eV.

(ii) Then the ZHAireS code [154] is used to simulate each shower $(E_i, \theta, \phi, \vec{x}_{core})$ and to compute the E-field transient signals induced by the shower at the TREND50 antenna locations. Simulations are carried out assuming a proton or an iron primary with equal proportions. The value of the Earth's magnetic field at the TREND site is taken into account and the standard US atmosphere is assumed.

(iii) The next step consists in simulating the antenna response to these electromagnetic waves using the NEC2 numeric code. At the end of this stage, each air-shower from the simulation set is associated with simulated voltage waveforms at the antenna output and form a so-called **simulated event**.

(iv) Then a random time t^* is drawn for each of these simulated events in a time window restricted to TREND50 acquisition periods when calibration data is also available. We then determine from the DAQ monitoring information (see section 5.6.2) which detection units participating in the simulated event were active and functioning at this instant, with corresponding processing units also ready to acquire data. Antennas failing this test are discarded from the event. For each remaining antenna, a 50-100 MHz filtering of the simulated signal is performed and a 200 MSamples/s digitization applied. The experimental gain value is then determined from the closest PSD measurement for this specific antenna through the method presented in section 5.5.2.2 and applied to the simulated waveform. The pretrigger signal of the experimental time-trace recorded at the instant closest in time to t^* is considered as a fair estimate of the noise conditions experienced on the antenna at this instant. It is duplicated to the time-trace length and added to the calibrated waveform, thus forming a simulated time-trace in the standard TREND50 format. If the maximum amplitude of at least five time-traces from the event exceed the experimental threshold values used in this specific run, then the event is finally inserted in the experimental dataset and blinded for the following steps of the analysis. This whole process guarantees that this simulated event corresponds at best to the set of time-traces that would have been recorded on disk in reality, should a shower of energy E_i and direction (θ, ϕ) have struck the TREND50 array at location $\vec{x}_{core}$ and instant t^*. The process is iterated for each simulated event.

(v) Finally the TREND50 offline data processing is applied to the dataset where the simulated events have been inserted. The processing consists in an implementation of the selection cuts defined in the previous section. At the very end of the chain remains a list of surviving simulated events N_{sel}. The results of the offline data processing on the simulated dataset are presented in table 5.1.

It appears from table 5.1 that the two periods of data acquisition with TREND50 result in very contrasted performances. While the East-West period exhibits satisfying values for the efficiency —about 40% of the initial air shower sample pass all implemented cuts—, it drops below 15% for the North-South period. Environment cuts are the

	EW		NS	
Cut	Nb	Survival %	Nb	Survival %
Raw	406	-	209	-
Bursts	309	76 ± 4	82	39 ± 6
Bad pulses	279	90 ± 4	77	94 ± 6
Valid recons	272	97 ± 2	73	95 ± 7
Mult≥5	272	100 ± 0	73	100 ± 0
Radius≤ 3000 m	263	97 ± 2	68	93 ± 7
$\theta \leq 80°$	246	94 ± 3	64	94 ± 7
Barycenter	241	98 ± 2	60	94 ± 6
Pattern	218	90 ± 4	38	63± 12
Direction neighbourgs	180	82 ± 5	31	81 ± 13
Time neighbors	169	94 ± 4	30	95 ± 8
Total	169	41 ± 4	30	14 ± 4

Table 5.1: *Results of the air-shower selection process for simulated data. See section 5.7.1 for cut definitions. Figures are computed for events with multiplicity 5 or more and initiated by a proton and iron primaries in equal proportions with* $E_i = 5 \cdot 10^{17}$ *eV. Similar (but often slightly degraded) results are obtained at other energies. Error bars are estimated following a binomial distribution:* $\delta f = 2\sqrt{\frac{f(1-f)}{n}}$*, with* f *the event survival fraction and* n *the number of events before the cut is applied. Taken from [206].*

most penalizing ones for the East-West periods (*bursts* or *direction neighbors* cuts in particular). Degradation of the electromagnetic environment during the North-South period (see Fig. 5.27) translates into much worse performance for the *bursts* cut, while this dataset efficiency is also affected by *signal cuts*, like the *pattern* cut, because of a significant degradation of the detector array status over time, with many more noisy or malfunctioning antennas compared to the East-West period.

5.7.3 Air-shower detection efficiency

The simulation of the TREND50 response to air showers presented in the previous section allows for a straightforward computation of the detector aperture for each energy value E_i:

$$\mathcal{A}_i = \int_{2\pi} S_{eff}(E_i, \theta, \phi) \cos\theta \sin\theta d\theta d\phi, \tag{5.16}$$

where the effective area $S_{eff}(E_i, \theta, \phi)$ is given by:

$$S_{eff}(E_i, \theta, \phi) = S_{draw}(E_i, \theta, \phi) \frac{N_{sel}(E_i, \theta, \phi)}{N_{draw}(E_i, \theta, \phi)}. \tag{5.17}$$

The set of $\mathcal{A}_i$ values is then fitted by the analytical function $f(E)$:

$$f(E) = a\left(1 + \mathrm{erf}\left(\frac{E-b}{c}\right)\right), \tag{5.18}$$

where a, b and c are adjustable parameters. The result is shown in figure 5.33, as well as the simulated differential spectrum of detected events, resulting from the product of $f(E)$ with the differential flux of cosmic-rays $\frac{d^4N}{dEdSd\Omega dt}$ is taken from [216]. The number of air shower events expected in duration Δt is finally given by:

$$N = \Delta t \int f(E) \frac{d^4N}{dEdSd\Omega dt} dE. \tag{5.19}$$

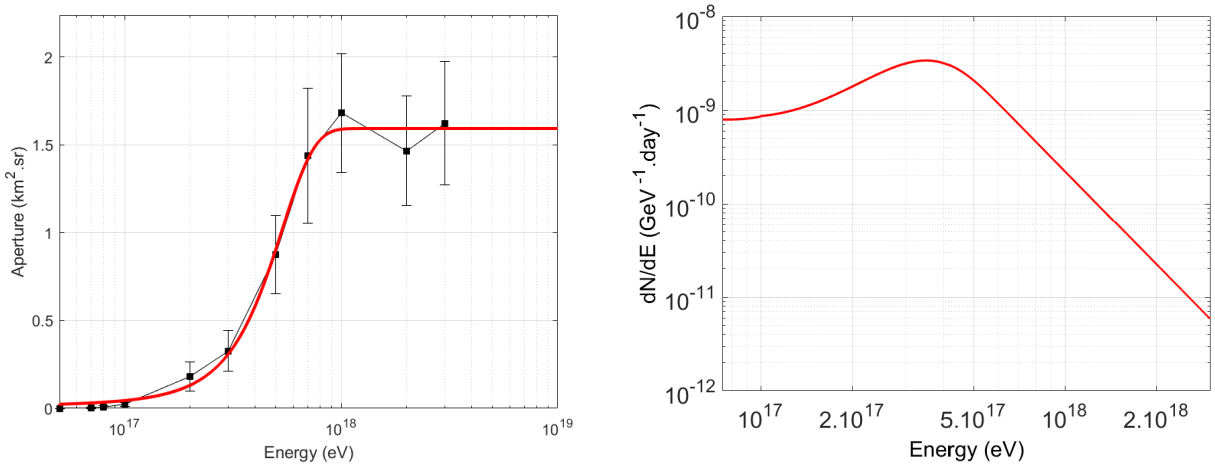

Figure 5.33: *Aperture of the TREND50 array as a function of energy for a fraction of the East-West period, computed from simulations assuming a shared p-Fe composition for the primaries. Right: differential cosmic ray spectrum expected for TREND50, derived from the aperture curve given in the left plot. Taken from [206].*

For the 251 live days of East-West data with valid calibration, we find an expected number of 340 ± 60 air showers detected, and 27 ± 8 air shower events for the 120.6 live days of the North-South period. The statistical errors are estimated by computing the number of events corresponding to a set of apertures $\mathcal{A}_i$ shifted by $\pm 1\sigma$ from the values obtained with equation 5.16.

5.7.4 Systematic effects

Several biases could affect the computation of the expected number of air showers above described. Below we list the major ones and evaluate their effect for the East-West dataset:

- **Gain:** the gain of the DAQ chain being computed as the ratio of the stationary noise rms at DAQ output to its value at antenna output (see section 5.5.2), underestimating the noise at antenna level would directly result in a systematical overestimate of the DAQ chain gain. However measurements of the electromagnetic background at the TREND site have shown that the sky noise level is extremely close to what is expected from the Galactic emission [207]. Besides, the independent calibration cross-check performed on a limited dataset results in a relative difference as low as 3.6% in average (see Fig. 5.22). The systematic overestimate of the DAQ chain gain is therefore of modest or null amplitude. For the purpose of completeness, we however calculated that a reduction of the gain by 5% — a conservative value— would lead to 304 air showers detected by the TREND array, instead of 340 determined for the standard DAQ gain values. We associate this value to the systematic uncertainty induced on the number of detected events by the gain computation.

- **Cosmic rays chemical composition:** experimental results converge towards a variation of the chemical composition of cosmic rays over the TREND energy range, from a heavy composition around 10^{17} eV to a lighter one at higher energies [217]. Yet, for the purpose of simplicity, a constant composition (50% proton - 50% iron) was assumed in our simulations over the energy range considered. The impact of this hypothesis was evaluated by computing the response of the TREND array to pure proton and pure iron fluxes. The number of air showers detected by the TREND array is 355 and 325 respectively.

- **Air shower radio-emission simulation code:** despite the fact that different simulation codes now converge to very similar results (see [153] for details), we evaluated the response of the TREND array to air showers simulated with CORSIKA+EVA [156] on a subset of 80 live days of data. The result was found to be statistically compatible with that of ZHAireS. This systematic effect can therefore be neglected.

We estimate the systematic error on the number of expected air showers detected by TREND to be the quadratic combination of these different components, thus resulting in $340 \pm 60(\text{stat})^{+15}_{-39}(\text{syst})$ air showers expected in the 251 live days of East-West period with valid calibration.

5.8 Results of the TREND experiment

We will present in this section the combined analysis of the TREND15 radio and scintillator data, and the TREND50 data selected through the identification procedure described in section 5.7.1. TRENDproto data was surely instrumental in defining the selection cuts but lacks the statistical power of TREND50. Hence the results presented in [207] are not detailed in the present document.

5.8.1 Scintillator coincidences in TREND15

The three-units scintillator array was operated in coincidence with the TREND15 radio array for 19 live days. During this period, 620 three-fold scintillator events were recorded, a number exceeding by far the ~ 0.06 random coincidences expected during that period of time (see Appendix B of [207] for computation details). The reconstruction of the direction of origin was possible for these three-fold events assuming a plane wavefront propagating at the speed of light. The resulting distribution, displayed on the left panel of figure 5.34 for the full statistics of events recorded with the scintillator array, confirms that these events were induced by air showers.

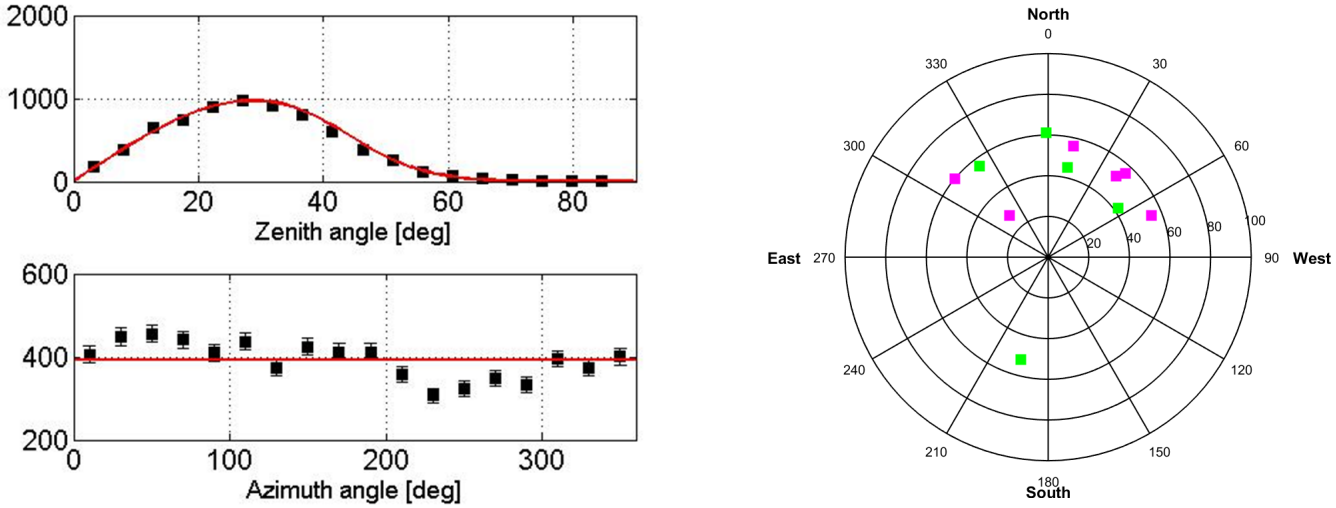

Figure 5.34: *Left: distribution of the direction of arrival for the 7060 3-fold events recorded with the TREND15 scintillator array over its full period of operation. The zenith angle distribution is fitted by a curve* $\frac{dN}{d\theta} = (a + b\theta)\sin\theta\cos\theta \times \frac{1}{1+e^{(\theta-\theta_0)/\theta_1}}$*, following [218]. Right: Distribution of the arrival direction for the 11 hybrid events detected with TREND reconstructed from the radio data. Events involving three (two) scintillators are shown in green (magenta).*

During this period of hybrid operation with the TREND15 radio array, three cosmic ray candidates —selected in the radio antenna data following the TRENDproto identification procedure described in 5.7.1— were recorded in coincidence with three scintillators and two others with two scintillators. One of these hybrid events is displayed in figure 5.35. We have carefully examined these coincidences and the various hypotheses for their origin. First, we can exclude the occurrence of random coincidences. The rate of random coincidences between two systems A and B, triggering on uncorrelated stationary noises, is computed in annex B of [207]. It writes as:

$$f_{rdm} = 2\frac{f_A f_B}{f_A + f_B}(1 - \exp(-(f_A + f_B)\Delta t)), \tag{5.20}$$

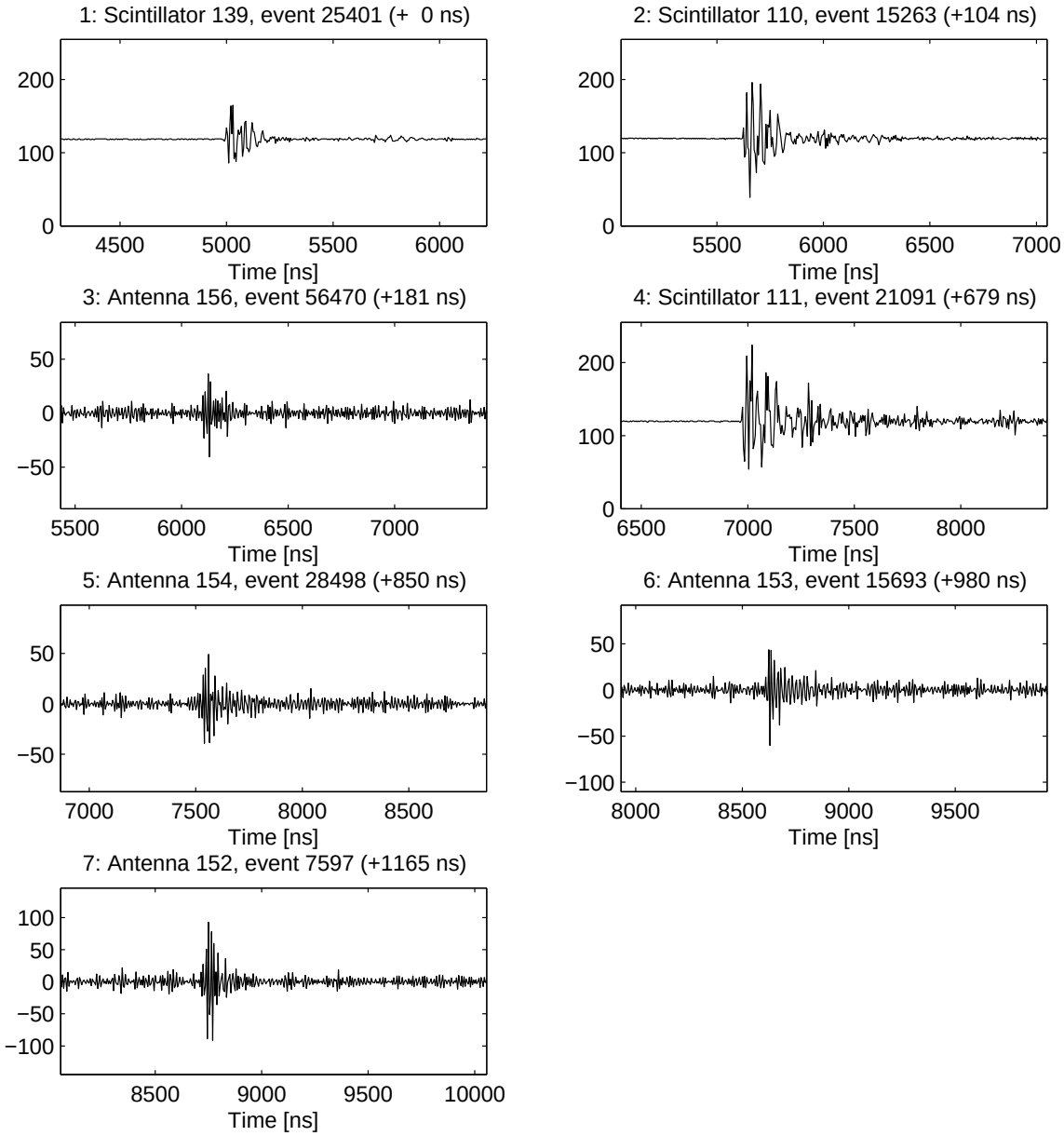

Figure 5.35: *Waveforms for the hybrid event A, involving 4 antennas and 3 scintillators in coincidence. Delays induced by signal propagation through the fiber and cables are not taken into account for in this display.*

Event	Radio antennas			Scintillators		
	Multiplicity	θ	ϕ	Multiplicity	θ	ϕ
A	4	52±1	195±2	3	49±3	191±4
B	4	61±3	359±2	3	67±5	3±4
C	5	42±1	36±3	3	36±3	56±5
D	4	45±1	12±2	3	49±3	10±5
E	7	56±2	323±2	3	56±4	331±5

Table 5.2: *Reconstructed zenith and azimuth angles (in degrees) for the 5 hybrid events detected with the TREND15 and TREND50 setups with 3-fold scintillator events (plane wave hypothesis). The direction reconstruction, performed independently for the antenna and ground array data, are statistically compatible with each other. The uncertainties are estimated using equation A.7 of [207], by assuming a time resolution of 10 and 20 ns for the antennas and scintillators respectively. Completed from [207].*

with f_A and f_B the trigger frequencies in A and B, and Δt the time window considered for a coincidence. The scintillators event rate is $f_A = 3.8{\times}10^{-4}$ Hz, while a value $f_B = 10$ Hz is a safe upper limit for the rate of radio events with multipicity 4 or more. Injecting these values in equation 5.20, it can be estimated that the rate of random coincidences between radio and scintillator events in the observed time window of $\sim 2\mu$s is less than one per year. The hybrid coincidences detected by TREND therefore have to be related to the same physical source. Second, the influence of PMT radiations on the antennas can also be excluded. For four out of these five coincidences indeed, antennas triggered before the scintillators. The time ordering of the triggers is also inconsistent with the transit time of an electromagnetic wave from the PMTs to the antennas in all five cases. Finally, direction reconstructions were performed separately for the radio and scintillator data for the three events with three scintillators. The results of these two independent reconstructions are in excellent agreement within uncertainties for the three events (see table 5.2). This agreement gives us strong confidence that these events have indeed been induced by EAS.

These five coincident events therefore constitute an unquestionable proof that autonomous radio-detection of cosmic rays has been performed by TREND15, and that the selection procedure defined in 5.7.1 has allowed to single them out from the background events. Data was taken with the scintillator array in 2011 after the radio array was extended to 50 units. Two additionnal hybrid events with 3-fold scintillator events (8 with two-folds) were detected during that period of time.

This work established for the first time that air shower events could be detected and identified with a fully independent radio setup outside of Antarctica. However this setup, because of the difference in the layouts of the scintillator and radio arrays, and indeterminacy of their respective effective areas, did not allow for an estimate of the radio detection efficiency. This was however possible with TREND50, as will be detailed in the next section.

5.8.2 Cosmic ray detection with TREND50

5.8.2.1 East-West period

Out of the $7.3 \cdot 10^8$ events recorded during the 314.3 live days of the TREND50 East-West period, a total of 564 air shower candidates survive the selection procedure described in section 5.7.1 (see table 5.3 for details). The distribution of their reconstructed directions of origin is displayed in figure 5.36. It shows a clear excess towards North, as expected for a dominant geomagnetic origin of the radio emission by air showers. One of the candidates is displayed in annex B for the purpose of illustration.

Among these 564 candidates, 408 were recorded during the 251 live days with valid calibration, a figure larger than — but compatible with — the $340{\pm}60^{+15}_{-39}$ air shower events expected during the same period of time according to simulations (see section 5.7.3). The experimental distribution of reconstructed directions, shown in figure 5.37, is also statistically compatible with the simulated set for most directions. An excess of events is however observed in the experimental set for directions closest to horizon and azimuth in the range $60° \leq \phi \leq 140°$, a direction —towards West— where background events are numerous for the East-West period (see Fig. 5.30). This excess is thus understood

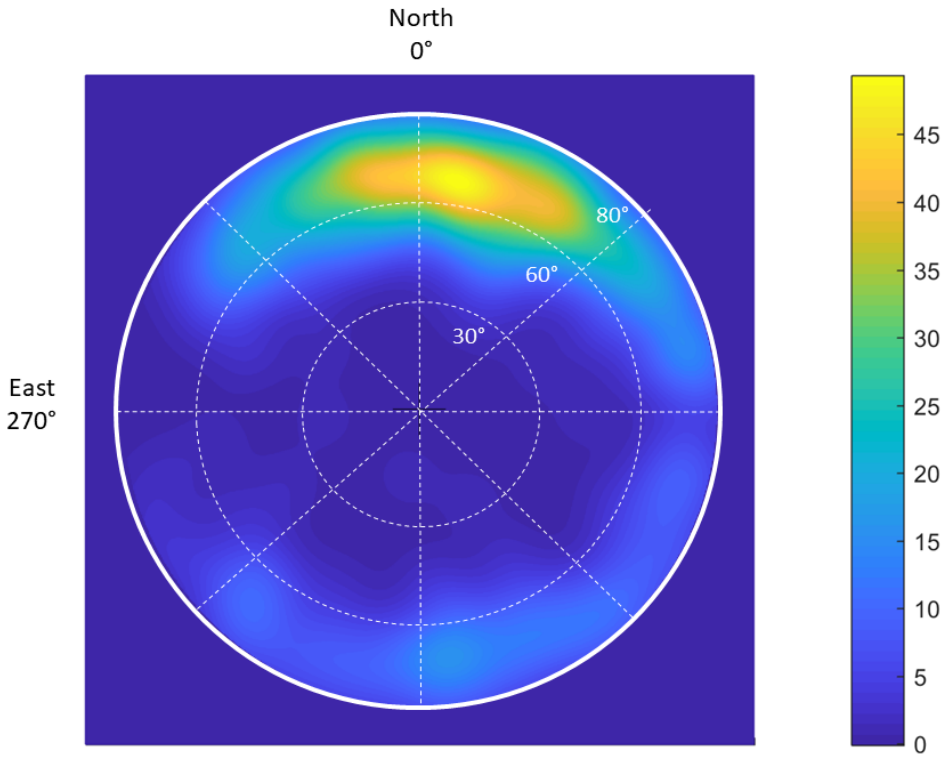

Figure 5.36: *Distribution of the arrival direction for the 564 air shower candidates selected in the East-West experimental data. The distribution is smoothed by the experimental angular resolution. Taken from [206].*

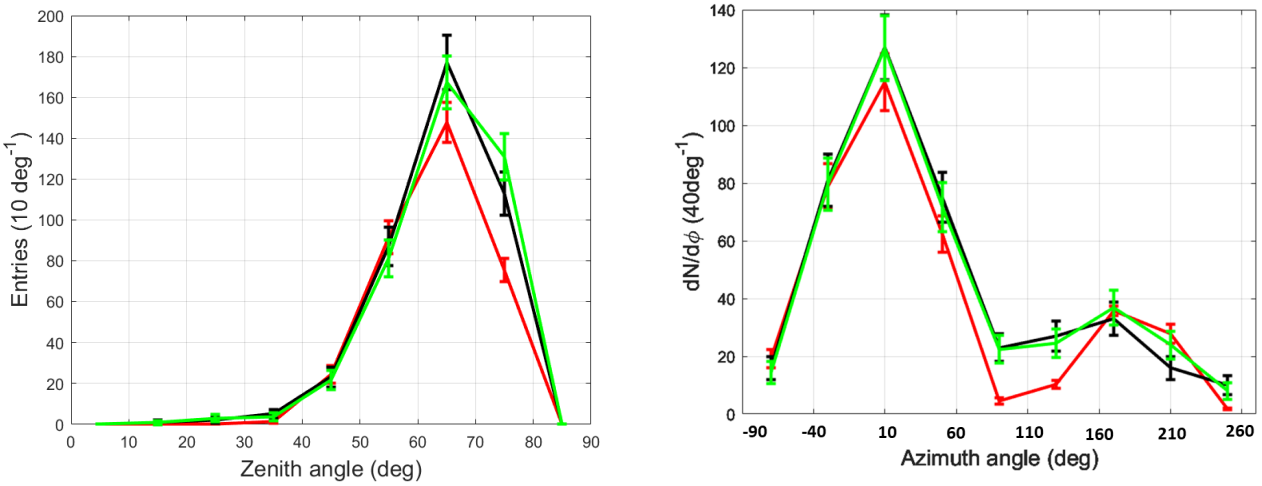

Figure 5.37: *Zenith (left) and azimuth (right) distributions for the 408 air shower candidates selected in the East-West experimental dataset with valid calibration (Periods 3 to 8), in black, and for the 340 events in the final selection from the simulated dataset in red. Also plotted in green are the distributions for the total experimental East-West dataset (Periods 1 to 8), after normalization. Adapted from [206].*

	EW		NS	
Cut	Stat	Surv. %	Stat	Surv. %
Raw	$7.3 \cdot 10^8$	-	$4.9 \cdot 10^8$	-
Bursts	$6.2 \cdot 10^7$	8.5	$1.5 \cdot 10^7$	3.1
Bad pulses	$2.9 \cdot 10^7$	46.3	$7.5 \cdot 10^6$	48.8
Valid recons	$1.9 \cdot 10^7$	67.0	$3.9 \cdot 10^6$	53.0
Mult≥5	$9.8 \cdot 10^6$	51.2	$2.8 \cdot 10^6$	70.9
Radius≤ 3000 m	$3.4 \cdot 10^6$	35.2	$1.1 \cdot 10^6$	37.5
$\theta \leq 80°$	$1.0 \cdot 10^6$	30.5	$3.0 \cdot 10^5$	27.9
Barycenter	$9.3 \cdot 10^5$	93.4	$2.9 \cdot 10^5$	97.6
Pattern	$3.4 \cdot 10^5$	37.2	$2.4 \cdot 10^5$	84.5
Direction neighbors	1400	0.4	557	0.2
Time neighbors	564	41.2	118	21.2
Veto	-	-	25	22.1
Total	564	$8.2 \cdot 10^{-5}$	25	$4.6 \cdot 10^{-6}$

Table 5.3: *Results of the air-shower selection process for the TREND50 East-West and North-South datasets. See sections 5.7.1 for cuts definition, and 5.8.2 for the "veto" cut. Taken from [206].*

as a contamination of the final sample of air shower candidates by background events at the ∼20% level. The small deficit of events observed towards South-East ($\phi = 220°$) is most likely a statistical fluctuation. This hypothesis is strengthened by the fact that this experimental point is closer to the simulated one when all data (i.e. including those without calibration) are included. The corresponding azimuthal distribution is shown in green in figure 5.37, after a coefficient K=408/564 —corresponding to the ratio of the respective number of candidates— is applied to it to renormalize for the different statistics. This demonstrates that the selection procedure defined for the TREND50 data and detailed in section 5.7.1 was overall successful in discriminating air showers from the ultra-dominant background.

5.8.2.2 North-South period

The results differ significantly for the North-South dataset, with 118 air shower candidates selected, while 27 were expected according to simulations. The most likely cause for this poor performance is the bad condition of the TREND50 array during most of the North-South period, with many antennas out of order during a large fraction of the data taking time (see Fig. 5.23), implying in particular a significant efficiency loss for the selection cut 5.7.1.4 based on the trigger pattern. This, combined with an increased number of background events due to the degraded electromagnetic environment (see Fig. 5.27), probably resulted in a large contamination of the final sample by background events.

It however appears that detection units A135 to A138 participate in 93 of these 118 selected candidates, a significant excess over simulations where these detection units are involved in only 10 of the 27 simulated events. If we reject all events where any of detection units A135 to A138 is involved —a selection called *veto cut* in the following— only 25 air shower candidates survive. The angular distribution of this population significantly differs from the background one, and at the same time resembles the one obtained for the 17 events of the final selection from simulations (see Fig. 5.38), even though limited statistics do not allow for firmer statement.

We can conclude from this paragraph that TREND50 was again able to discriminate air showers from background in this configuration where antennas are oriented along the North-South axis, but with a much reduced efficiency. This also points to the fact that the status and electromagnetic background conditions of the TREND50 array significantly affect the air shower selection procedure.

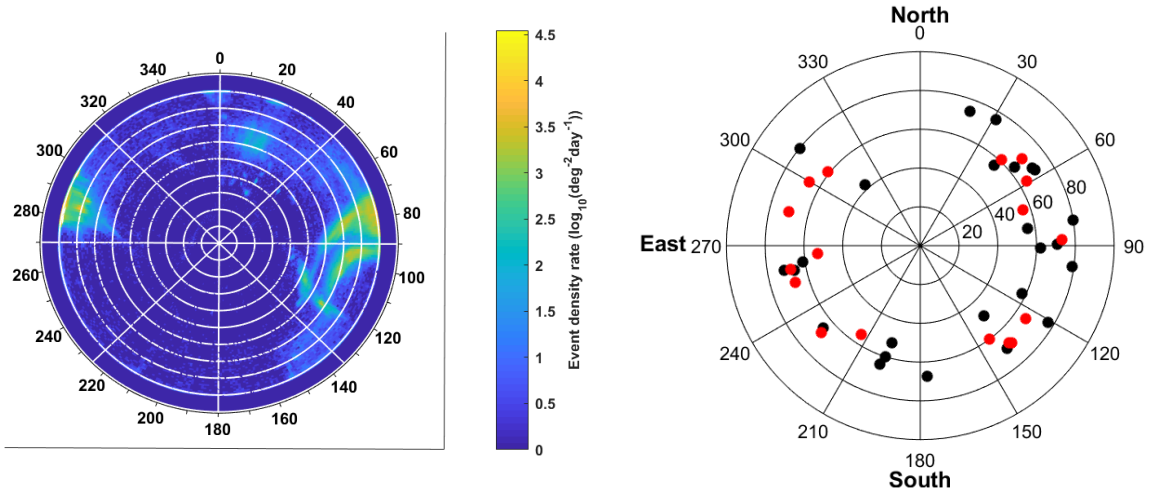

Figure 5.38: *Left: sky distribution of all events from the North-South period with successful point-source reconstruction and radius of curvature $R \geq 3000\,m$. Right: sky distribution of the 25 experimental (black) and 17 simulated (red) air shower candidates from the North-South dataset. Taken from [206].*

5.8.3 TREND50 detection efficiency

Besides computing the efficiency of the offline cuts detailed in table 5.1, simulations were also instrumental in evaluating TREND50's air shower detection efficiency. To do that, we first evaluated the response of an **ideal detector**, where all detection units of the TREND50 array are constantly in a running state, and the DAQ system achieves 100% live-time. This was carried out with a pure proton primary sample, and the corresponding simulated datasets were produced using the same mechanism as detailed in section 5.7.2, except that instant t^* in step (iv) is replaced by a set of instants $\{t_i\}$, where each t_i corresponds to optimal conditions for detection unit i (i.e. valid gain, DAQ system up and ready, etc).

This simulation results in a total of 10768 air showers detected by this ideal detector during the 251 live days with valid calibration of the East-West period, while the treatment developed in section 5.7.4 showed that 355 air shower events are expected to be detected by the setup in real conditions for proton primaries . The overall detection efficiency of the TREND50 detector can be estimated to 355/10768=3.3% for this period.

This is obviously a poor overall performance, but simulations allow for a deeper insight in this result. In particular, when performing the simulation following the standard procedure described in section 5.7.2 —i.e. taking into account the real, instantaneous status of the TREND detector— it is found that 1110 simulated events would have actually triggered data acquisition and been recorded to disk. Then 355 out of these 1110 events finally pass the offline air shower selection cuts detailed in section 5.7.1. The total 3.3% efficiency may thus be split in two independent parts: a **hardware efficiency** of value 1110/10768$\simeq$10%, and an offline **selection efficiency** equal to 355/1110$\simeq$32%.

The 10% hardware efficiency is mostly caused by the limited reliability of the TREND detector, already detailed in section 5.6.2. At any given instant, $\sim$40% of the detection units could for example exhibit degraded performances or would simply be non-functional (as A121 in Fig. 5.26, see also Fig. 5.23) while the DAQ dead-time was also far from negligible, with a significant degradation with time (see Fig. 5.25).

The 32% selection efficiency, for its part, is limited by two factors: the peculiar antenna layout, imposed by the necessity to stay at limited distance from the 21CMA baselines and their optical fibers, does not allow for an efficient mapping of the amplitude pattern at ground, an information that would otherwise be an efficient tool for background rejection. Consequently as much as 35% of events (composed mostly of background at this stage) pass the *Barycenter + Pattern* cuts in the East-West dataset (see table 5.3), while amplitude pattern at ground is potentially a very strong signature for air showers (see e.g. the right panel of figure 4.4). Likewise, measuring only one component of the electric field affects TREND's potential for air shower identification, as polarization information —yet a potentially powerful signature for EAS, see e.g. Fig. 4.6— cannot be used in that case.

Achieving such results with a detector as basic and perfectible as TREND is a strong indication that the paradigm presented in the introductory comments of part II of this document is true: autonomous radio detection of air showers should be achievable outside of polar areas, thanks to the very distinct signatures of air showers with respect to other transient radio signals, hence limiting the challenge of autonomous radio-detection to a technical one. By opening this possibility for stand-alone radio arrays, TREND was the seed for the GRAND project.

On a shorter time scale, TREND results triggered the GRANDProto35 proposal. This experiment aimed at improving both the selection and hardware efficiency of the TREND setup thanks to an upgraded detector deployed at the same site. This is presented in the next chapter.

Figure 5.39: *Left: Emilie Martineau-Huynh at the TREND site in 2011. Right: Elias Martineau-Huynh in Dunhang (Gansu) in 2013.*

Chapter 6

The GRANDProto35 project

Figure 6.1: *Setting up a GRANDProto35 prototype unit in August 2016.*

The GRANDProto35 project took shape in 2013, as an upgrade of the TREND experiment once the limitations of this pioneering setup, detailed in section 5.8.3, were clear to us. The expertise acquired with TREND allowed for rather precise ideas about how GRANDProto35 should be designed (see section 6.1), while the financial resources obtained by Wu XiangPing made it possible to implement them. The excitement of being able to design and bring to life an experiment were surely very positive aspects of the GRANDProto35 project, but there were downsides as well: during the 4 years —from 2014 to 2017— when the experiment was developed, I was the only physicist at the core of the project, while sharing my time with the TREND final analysis detailed in chapter 5, GRAND simulations (see chapter 3), management of the GRAND collaboration at birth and teaching duties which had resumed after I came back to Paris in September 2013. The lack of time and resources to carry out with the required care and rigor the necessary steps of detector design and validation (see section 6.2) generated significant frustration and stress, and it nearly seemed to me like a miracle that the system eventually worked when tested on site. This made the eventual negative outcome of the whole project (see section 6.3) even more cruel. I therefore have a slight feeling of bitterness thinking back to the amount of effort put in this project for such a limited output, but I am confident that the success of GRANDproto300, presented in the following chapter, will wash it out.

6.1 Objective and design

The GRANDProto35 (GP35) project aims at tackling the main issues encountered during the pioneering TREND experiment in order to demonstrate that a clean and efficient detection of air showers can be achieved with an autonomous radio array. It is hard to put precise figures behind these terms, but in the perspective of neutrino search with GRAND, a detection can probably be qualified as efficient if 80% of showers above threshold are indeed detected and identified. It is harder to be quantitative for detection cleanliness, as the background rejection performances of an autonomous radio array highly depends on the quality of its electromagnetic environment or the way its trigger is defined and events formed. In the specific case of GP35, the percent-range contamination of the final EAS candidates by background events —a factor 10 improvement compared to TREND— can probably be seen as satisfying. In order to reach these goals, the main improvements of the GP35 design with respect to TREND are the following:
• better data reliability, achieved thanks to a robust antenna design and an integrated electronic system based on a digitization of the signal at the foot of the antenna.
• an online data processing and acquisition allowing for a ∼100% duty cycle, even in the noisiest background conditions.
• an improved identification of the EAS signal, thanks in particular to a measurement of the polarization information of the electromagnetic wave.

In addition, the GP35 radio array is complemented by a network of 24 scintillators deployed at the same location as the radio setup, but running fully independently from it. The purpose of this particle array is to perform an independent and background-free detection of air showers hitting the detector, thus allowing for a qualitative, event-by-event evaluation of the EAS detection efficiency of the radio detector. This is detailed in section 6.2.5.

6.2 The GRANDproto35 detector

6.2.1 The GRANDProto35 layout

GRANDProto35 is deployed within the Ulastai Observatory, the site of the 21CMA (see section 5.3), therefore benefiting from its infrastructure, and in particular power supply and data transfer, just like TREND. Following an upgrade in 2016, four optical fibers connect each 21CMA pod of the South-North arm to the Observatory DAQ room. Further, the fibers of 22 of these pods were prolonged in summer 2017 to the locations of the GP35 detection units. This gave significantly more flexibility to define the detector layout, thus tackling one of the issue identified in TREND (see Fig. 5.6).

The 35 radio detection units and 24 scintillators composing the GP35 detector are deployed following a rectangular pattern along the North-South arm of 21CMA, with 7 rows of 5 units and 6 rows of 4 units respectively. The distance between antennas in a same row was set to ∼200 m, while two rows are separated by 400 m = 200 m / cos(60°). The local topography and the road bordering the array (see Fig. 6.2) imposed a denser deployment in the Southern part (a35 and below), with an antenna spacing of 100 m.

Only an approximate and incomplete simulation of the detector response was carried out by Zhang Jianli and Gu Junhua, my two colleagues from NAOC who also contributed to GP35. It was however enough to show that this layout

would efficiently detect inclined showers ($50° < \theta < 70°$) coming within $\pm 20°$ from North with energies above 10^{17} eV and a core position inside the instrumented area. The corresponding event rate was estimated to a few EAS events per day, a statistics sufficient to fulfill within 2 or 3 years the GP35 goals presented in the previous section.

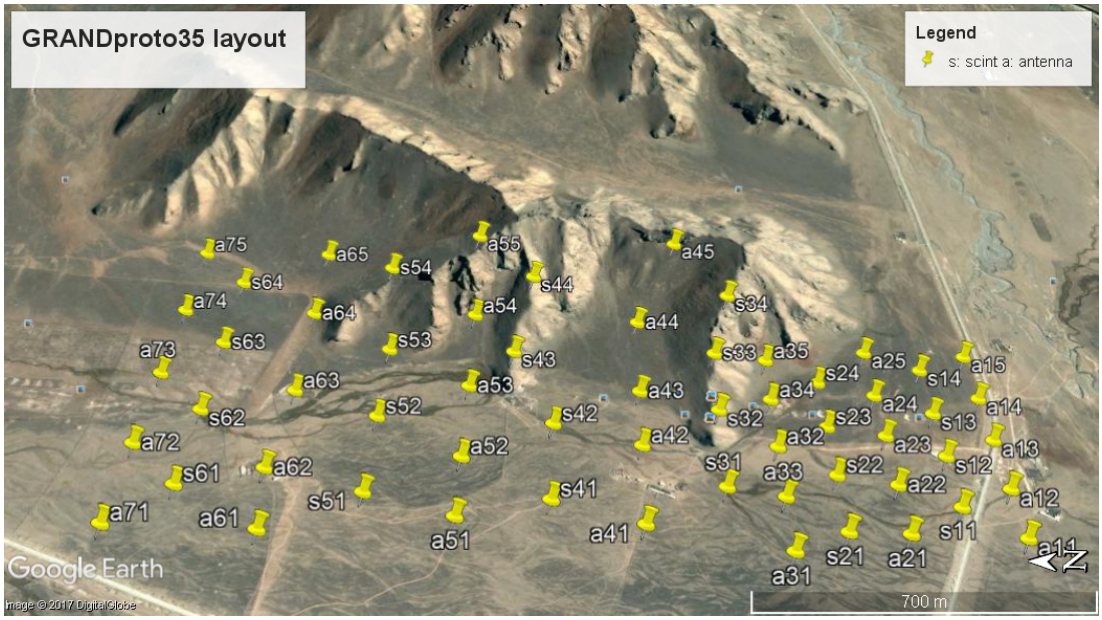

Figure 6.2: *The proposed GP35 layout. North is indicated with an arrow at the bottom right corner. Radio and particle detection units are identified by labels "aXY" and "sXY" respectively, X standing for the row index, and Y for the column index.*

6.2.2 The GRANDProto35 antenna

The antennas of the GRANDproto35 radio units are active bow-tie antennas that follow a design very similar to the CODALEMA antennas [168], later used by the Pierre Auger Observatory in the Auger Engineering Radio Array [169]. The main difference with the AERA detection unit is the vertical arm that was developed for GRANDproto35 antennas in addition to the two horizontal ones. The combined information of all three arms allows a full determination of the polarization of the signal (see section 6.2.3.2). The length of each arm is 1.07 m and the width 66 cm.

Each of the three arms is equipped with a custom ASIC low-noise amplifier (LNA) placed at the feed-point of the antenna. This design has the advantage that there is no intermediate transmission line between the radiator and the LNA, which input impedance can thus be adjusted to maximize the Signal/Noise transmission, thanks in particular to a 1 μH shunt inductance in parallel. This is illustrated in the right panel of figure 2.11 for the CODALEMA Butterfly antenna, which design closely resembles that of GP35. The ASIC design allows for a very modest 52 mA consumption for a 20 dB amplification, combined with a high linearity (1 dB compression point for a 7 dBm input power, which corresponds to a voltage amplitude of 0.6 V). This chip was designed by Didier Charrier specifically for EAS radio-detection applications. It was bought by NAOC through a contract established with SUBATECH in 2013 following my initiative.

The mechanics of the antenna (see Fig. 6.3) was designed by Zhang FuShun, a long-term collaborator of Wu XiangPing from Xi'An Electronic University, also involved in 21CMA and TREND. Specific care was taken to ensure the long term viability of the whole system, with three series of prototypes, initiated in 2013 and validated in 2016 only, after 6 antennas could be operated on the field for one year without any problem or sign of aging.

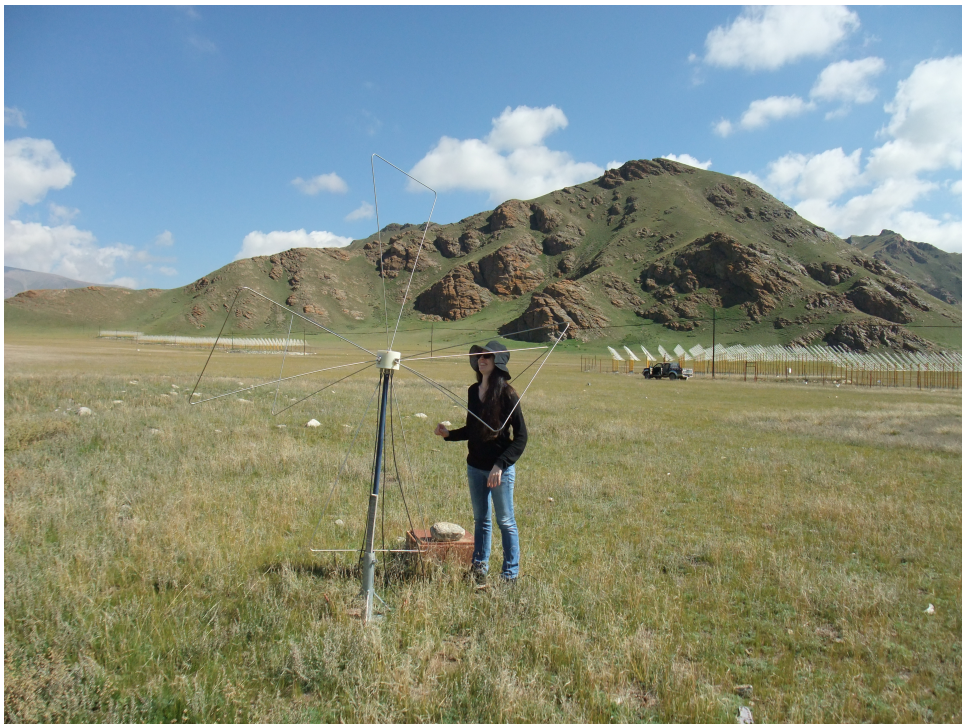

Figure 6.3: *Sandra Le Coz, post-doc on TREND and GRAND between 2014 and 2016, working on a GP35 prototype antenna in Summer 2016. The 6 antenna arms (2 for each direction) are connected to a nut —the white polyethylene cylinder visible on this picture— which holds the 3 Low-Noise Amplifiers. The 3 cables visible on this picture carry at the same time the DC voltage biases for the LNAs and the three antenna signals through a bias-Tee (see section 6.2.3.1).*

6.2.3 The GRANDProto35 front-end electronics

The results of the TREND experiment convinced me that a very fast treatment of the data —triggering, digitizing and recording— was a necessary condition for the success of autonomous radio-detection experiments. I knew there was world-class expertise on this topic at LPNHE, as the brilliant performances of the H.E.S.S. cameras demonstrated [204]. After I came back to LPNHE from China in September 2013, it was therefore a priority for me to convince these brilliant engineers to develop the GP35 electronics. I also hoped that reaching this goal would open the door for an institutional involvement of LPNHE in GRAND.

This plan was partly successful only: LPNHE indeed took in charge the prototyping of the GP35 Front-End electronics units, but only under the limited form of a service delivery, formalized through a contract signed in January 2015 between CNRS and NAOC. This was followed six months later by a contract between NAOC and the French company STAE for the production of the 35 units.

Turning the few initial ideas presented in section 6.1 up to an actual complex electronic equipment fulfilling its designed task was undoubtedly an edifying experience. The three years it took to reach this goal, in close collaboration with electronic engineers from LPNHE and STAE, dealing with administrative and financial constraints, taught me a lot on how to lead a project. In the following I present the design of this electronic system and the tests carried out before their shipping to site, in December 2017.

6.2.3.1 Design

A picture of the GP35 Front-End Unit electronic board is shown in figure 6.4 and its schematic in figure 6.5. The board can be divided in analog and a digital stages, and also includes timing and calibration units.

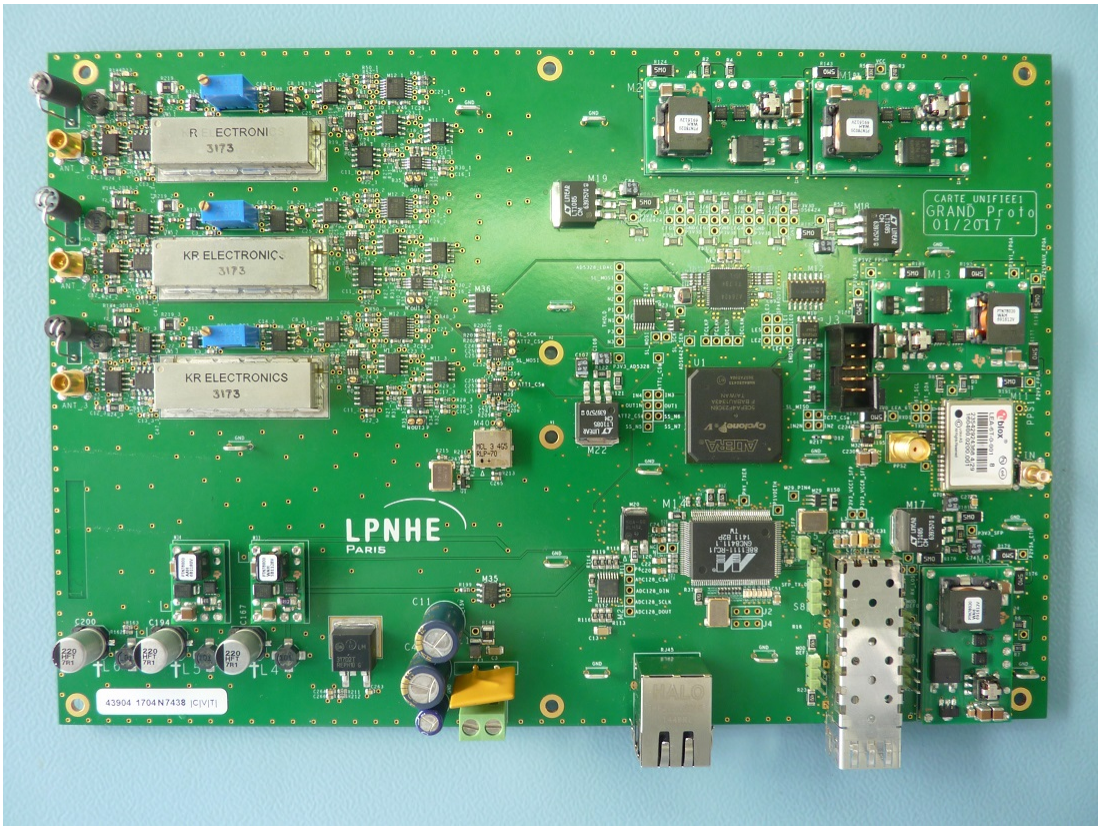

Figure 6.4: *A GP35 Front-End electronics board. The analog stage, with the three filters labeled "KR ELECTRONICS" in particular, lies in the top left corner of the board. The ALTERA FPGA (center right) can be seen just above the Marvell communication interface chip, as well as the uBlox GPS unit (right).*

6.2.3.1.1 Analog stage The signals coming from the three antenna arms X, Y, Z undergo three parallel and identical treatments. They first go through an amplifier of gain $G = 10$, which allows to raise the baseline noise slightly above 1 mV in normal conditions (corresponding to a power of -50 dBm). This is enough for a precise measurement of the noise fluctuation induced by the Galactic transit in the antenna field of view, a useful tool for calibration, as already detailed in section 5.5.2. This amplifier also performs an impedance adaptation between the 75 Ω impedance at LNA output and the 50 Ω impedance of the following stages of the electronic board. The signals are then filtered through sharp 30-100MHz band-pass filters, attenuating the signal by more than 50 dB at 20 and 125 MHz, with a group delay smaller than 15 ns in the nominal frequency range. Note here that the GP35 frequency range is slightly extended towards lower frequencies compared to TREND, thus allowing to capture more power from the EAS electromagnetic emission, as illustrated in figure 2.8. After filtering, the signal is split into two channels :

• in the trigger channel, the signals at the output of the filters are first amplified by an additional factor 10 and then compared to threshold values set by the user through the remote control program. A trigger flag is generated and sent to the FPGA (see below) if one channel exceeds the threshold level. Note that there are six independent trigger channels, corresponding to two polarities for each of the three channels. The user can activate/inhibit independently each of these trigger channels and set their respective threshold values, again through the remote control program.

• in the signal channel, the signals are processed through power detectors AD8310 which act as envelope detectors. The motivation for this treatment goes along the following argument. First, it can be noted signals at the output of antenna working in the tens of MHz frequency range undergo rapid oscillations (see Fig. 6.6), with a typical period of a few tens of nanoseconds. A proper recording of the antenna signal thus requires a sampling at a rate of 200 MSamples/s at least, which was at the limit of what was commercially affordable in the early 2010's for 12 bits sampling. Even more problematic, the typical 5 μs time-trace duration then corresponds to 1000 points, which turns into an event size of 2 kBytes for a single channel and a 16-bits sampling. Trigger rates above 1 kHz then quickly induce data transfer

rates which are very challenging to deal with in an extended radio array.

However, one should note that these rapid oscillations are simply the result of the incoming wave's processing by the antenna. Hence these fluctuations are characteristics of the antenna's response function and do not contain significant physical information on the incoming wave. Only the envelope does. Following the choice made by the EASIER project for the detection of Molecular Bremsstrahlung at GHz frequencies in Auger [219], we therefore chose to record only the envelope of the signal. We selected the AD8310 to perform this treatment because of its prompt 15 ns rise time. As illustrated in figure 6.6, a 60 MSamples/s sampling of the signal at the output of the power detector is then enough to guarantee that no information is lost in the time domain. This is also true for a 50 MS/s sampling, the rate eventually chosen for GP35. It however goes otherwise in the frequency domain, as all frequencies in the 30-100 MHz range are integrated in the detector's response. Given the 15 ns rise time of the power detector, any constant wave emitter in this band would for example generate a high constant level at the output of the envelop detector, with no way to treat it *a posteriori*. This makes the designed electronic system very vulnerable to environment noise. The good conditions measured at Ulastai (see section 5.3) convinced us that this risk was limited.

The other interesting feature of the AD8310 power detector is its logarithmic response with a typical slope of +20 mV/dB (see Fig. 6.10). Given the ±1 V input range of the ADC —the following element of the electronics chain, detailed in the *Digital stage* section— this in principle allows for a comfortable ∼100 dB dynamic range. A differential amplifier placed in between these two components allows to adjust the bias level of the signal to fit at best the ADC input range.

The analog stage also hosts a *Bias Tee*, a simple but ingenious system composed of capacitors and inductors which allows to carry on a single cable the AC radio signal and at the same time the 15 V DC bias voltage needed to power the LNA installed at the GP35 antenna feed-point (see section 6.2.2).

Jacques David, electronic engineer at LPNHE, who gained significant expertise on topics relevant for GP35 through his work on the EASIER project, led the development of the Front-End unit analog stage.

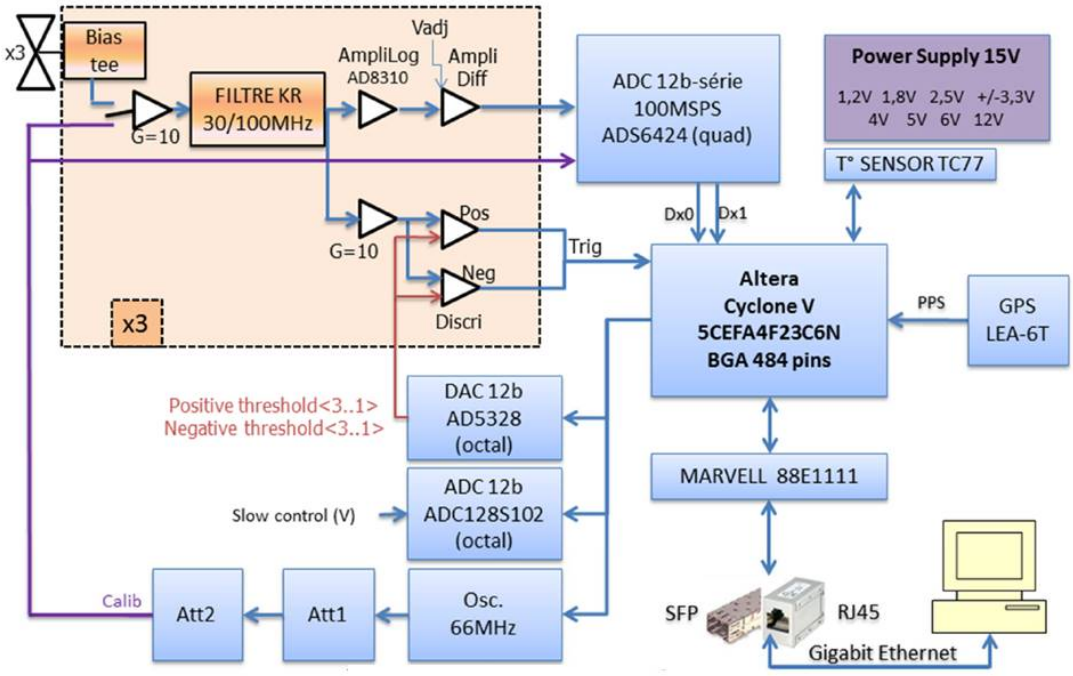

Figure 6.5: *Schematic of the GP35 electronics.*

6.2.3.1.2 Digital stage The three signals produced by the power detectors AD8310 are fed into an ADS6424 ADC, which continuously encodes these analog signals on 12 bits at a 50 MSamples/s pace. An ALTERA Cyclone V FPGA, then stores the digitized data in an internal ring buffer of adjustable size. When a trigger is produced (see above), a subset of data centered on the trigger instant is then copied to a FIFO memory buffer after being organized together with a trigger time stamp (see *Timing* paragraph) to form a so-called **GP35 event**. The event is eventually sent to a Marvell interface chip, which manages the communication with the central DAQ system *via* socket communication following the UDP protocol, using an optical fiber as the physical layer for this downstream data flow.

A second fiber is used for upstream communication, allowing the end user to control the Front-End unit through the FPGA: acquisition channels can be switched on and off, trigger thresholds can be adjusted, calibrations performed (see below) or slow control data collected. The FPGA for instance collects information on the voltage bias applied to the three LNAs, the temperature on the board or the trigger rate for each channel at a pace defined by the user.

This DAQ architecture was designed by Patrick Nayman, who applied many ideas he initially implemented in the H.E.S.S. camera. After Patrick retired in June 2016, David Martin took over responsibility of the digital part.

6.2.3.1.3 Timing The instant when an electromagnetic waves hits the detector has to be determined with a relative precision around (or better than) 10 ns for the purpose of direction reconstruction (see section 5.5.1). The front-end digitization of the antenna signal makes the use of a distributed clock to all units —as was done in TREND, see section 5.4.3— very complicated. The solution chosen for GP35 therefore relies on the use of a uBlox GPS receiver unit, which allows to build a timestamp with an absolute accuracy as good as 3 ns [220] in ideal conditions. The GPS unit in deed outputs to the FPGA a Pulse-Per-Second (PPS) signal with a 10 ns nominal period accuracy. A counter synchronized on the 125 MHz FPGA master clock and reset at every PPS signal, then builds a time stamp of the trigger instant with a 8 ns granularity, further improved down to 1 ns through a subtle mechanism which will not be detailed here.

6.2.3.1.4 Amplitude calibration As discussed in the case of TREND in section 5.5.2, a reliable, time-dependent calibration of the signal amplitude is key for EAS analysis. The use of a power detector, which performs a non-linear treatment of the incoming pulse, makes the calibration issue even more critical in GP35. It was therefore decided to integrate a calibration system to the Front-End unit. This took the form of a Quartz oscillator implanted on the DAQ board. This component generated a sine wave of 66.666 MHz frequency and amplitude adjustable thanks to two programmable attenuators. The three unit inputs could be switched to this signal by the end user, thus allowing to determine the actual chain response to this known input at any given instant.

6.2.3.2 Prototype validation

Here we detail the validation steps performed during the prototyping of the GP35 Front-End Unit.

6.2.3.2.1 Front-end unit design During its design phase, the circuit composing the analog stage was simulated by Jacques David with the MultiSim [221] software from National Instruments. I then ran this simulation to confirm that the envisioned treatment would fulfill the experiment requests. I used as an input for the simulation time-traces mimicking noise transients and EAS signals (see Fig. 6.6). The former corresponded to ∼100 events recorded at Ulastai in March 2013 with a custom system developed at IHEP to digitize signals from a TREND antenna at a 1GHz frequency [222]. The later were simulated responses of GP35 antenna to EAS radio signals. The EVA code [223] was used to perform these simulations for ∼1000 air showers of energies E=10^{17} eV and $5 \cdot 10^{17}$ eV, $50° < \theta < 70°$ and an azimuth within ±20° from North. The CODALEMA butterfly antenna model was used to compute the antenna response and a Gaussian noise corresponding to the Galactic emission in the 30-100 MHz range was added to the time-trace. I then performed an analysis on this limited dataset, defining a basic selection cut based on the pulse duration. More than 90% of simulated EAS signals passed this cut and more than 90% of background signals failed. This indicates that a 50MS/s sampling at the output of the power detector preserves information with sufficient precision for background rejection and further stages of analysis.

Moreover, simulations also showed that the recorded data allowed to retrieve polarization information with satisfying accuracy. It was in particular observed (see Fig. 6.7) that the parameter $\eta_V = \arctan \frac{V_Y}{V_X}$ computed with the EAS dataset —where $V_{X,Y}$ are the maximal values of the digitized data— showed a deviation from a similar quantity $\eta_E = \arctan \frac{E_Y}{E_X}$ computed from the electric pulse simulated at antenna position, while the value of η_E was nearly identical at all antenna location, in a direction perpendicular to Earth magnetic field and shower direction of propagation, a result in agreement with the study detailed in section 4.6.

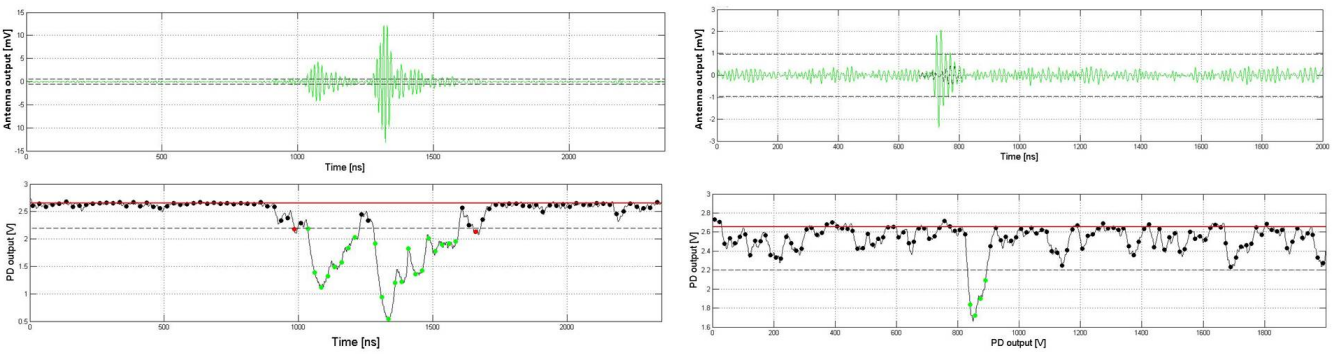

Figure 6.6: *Left: signal mimicking a background event for GP35 at antenna output (top) built from a TREND antenna signal recorded with a 1 GS/s digital system, and simulated response of the GP35 analog chain to this signal (bottom). See text for details. 60MS/s samples are shown as black dots. Right: same for a simulated EAS signal. The noise level is computed from Galactic emission, following the treatment presented in section 5.5.2.2.*

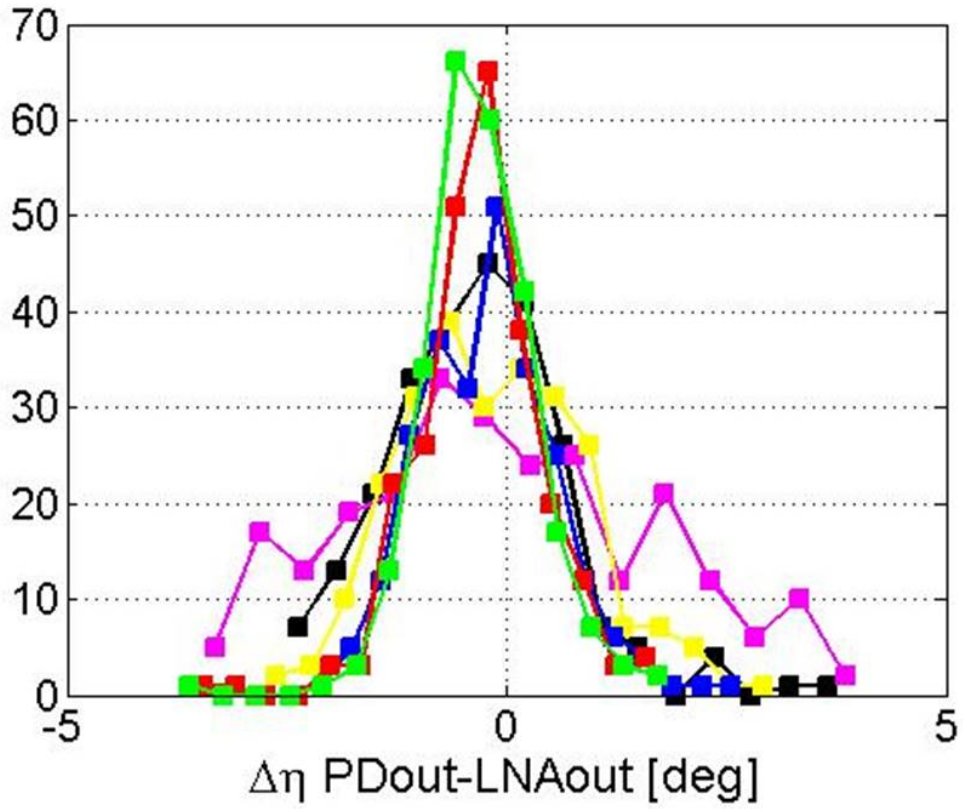

Figure 6.7: *Distribution of $\Delta\eta$ for a subset of ∼200 EAS simulated events. $\Delta\eta$ corresponds to the angular difference between the quantities $\eta_V = \arctan\frac{V_Y}{V_X}$ computed at the output of the Power Detector and LNA outputs. The distribution is shown for different ADC sampling frequencies ranging from 40 MS/s (purple) to 1 MS/s (red). We have $<\Delta\eta>= -0.3^\circ$ and $\sigma_{\Delta\eta} = 1.3^\circ$ at 60 MS/s. Also shown in black is the distribution for the angular offset between η_V, computed from the voltage at antenna output, and η_E, computed from the electric field at antenna position. Then $<\Delta\eta>= 0.0^\circ$ and $\sigma_{\Delta\eta} = 0.9^\circ$.*

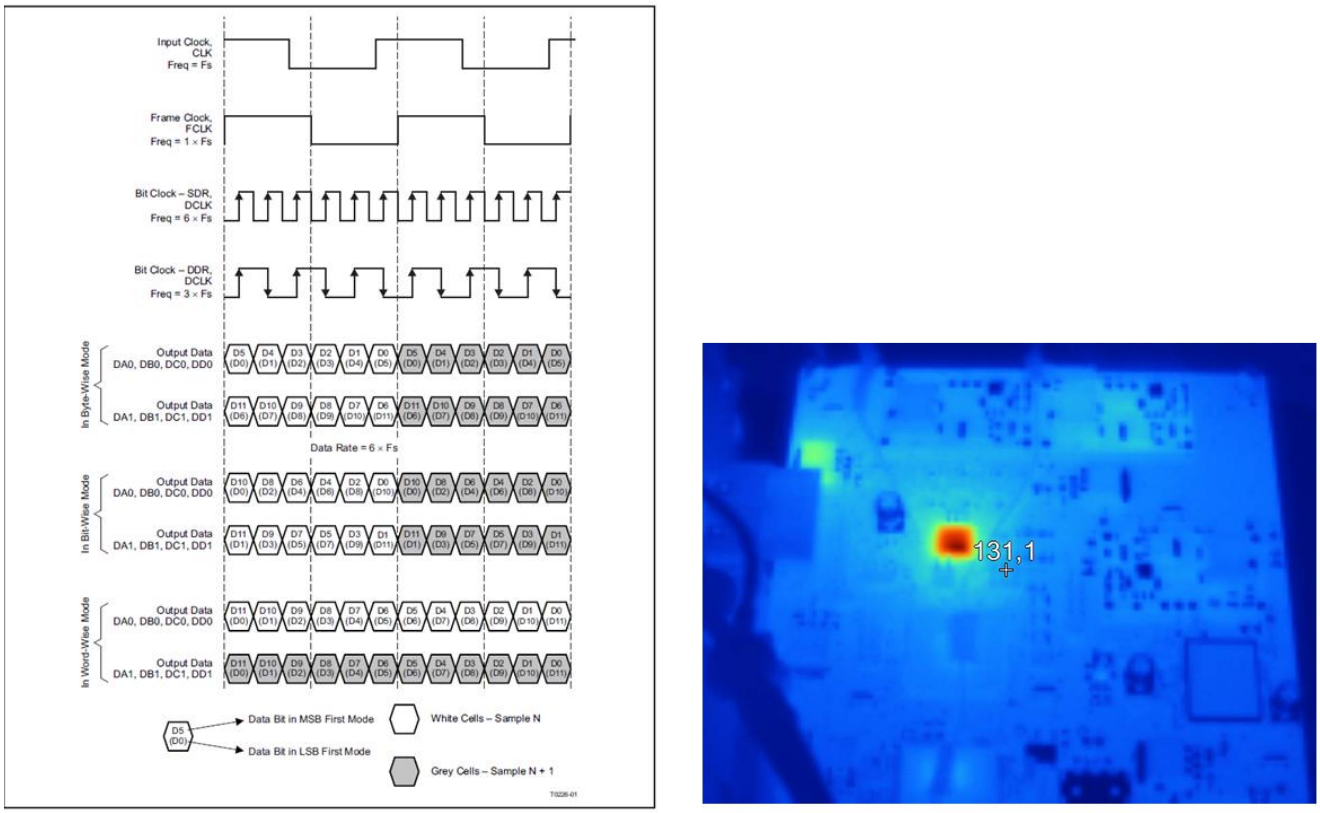

Figure 6.8: *Left: Scheme of ADC 2-wires serialization. In the original GP35 plan, the Frame Clock runs at a frequency F_s = 100 MHz (later slowed down to 50 MHz), In-Bit Wise Mode and Double Data Rate reading were chosen for data transfer. Taken from [224]. Right: picture of the GP35 prototype board taken with a thermal camera in June 2016, showing a temperature of 131.1° C close to the ADC.*

Of course, this analysis is incomplete and a more rigorous treatment would have been needed to evaluate various systematic effects (calibration, other sources of noise, etc) and optimize polarization reconstruction. Still, it clearly indicates that the GP35 detector could in principle provide a reliable measurement of the wave polarization.

6.2.3.2.2 Prototype functionality The first two complete prototype boards were available in November 2015, one year after the study officially started. Initial tests confirmed that power supply, analog stage or communication with the FPGA and GPS worked correctly, but inconsistencies were then found in the digitized data retrieved by the FPGA. To better explain the encountered issue, I will first describe in more details the basic principles of ADC reading.

For ADCs with multiple channels —4 in the case of ADS6424—, a serialized output (i.e. one bit after the other) is often preferred in order to minimize the number of output wires. The bits —binary voltage levels following the LVDS (Low Voltage Differential Signaling) standard— are then output from the ADC in synchronization with the front edges of a so-called Bit Clock square signal, derived from the master sampling clock (also called Frame Clock) distributed by the FPGA.

In the case of GP35, the Frame and Bit Clocks were initially chosen to be 100 and 300 MHz respectively, while the 12 bits of each sample are output on two wires. Each bit signal therefore lasts for 1.66 ns. These are then captured in the FPGA by a Double Data Rate (DDR) logic block which reads the input voltage at each rising and falling edge of the square Bit Clock, and eventually stores them in a serial-to-parallel shift register called a Deserializer inside the FPGA. The whole process is presented in figure 6.8.

Problems may however arise from the fact that the bit signal has to be read during the very short —1.6 ns in our case — time window when it is received, while various effects could affect the synchronization between ADC output and FPGA reading: the Bit Clock has for instance a nominal jitter of 350 ps [224], and delays of the signal propagation on

the PCB board or routing inside the FPGA can also amount to hundreds of ps. Various mechanisms exist to correct for these [225], but none were foreseen in the design. We therefore eventually faced the situation where FPGA reading was not properly synchronized, resulting in incoherent digitized data. The situation became critical when Patrick Nayman, the designer of the system, retired in June 2016. Fortunately, Olivier Le Dortz, electronics engineer at LPNHE, gave a decisive help to solve the issue. Within a few weeks, he introduced various delays in the FPGA firmware to account for the signal propagation time offset, proposed to bring the sampling frequency down to 50 MHz —thus doubling the time window for bit reading— and finally spotted a temperature issue with the ADC (see Fig. 6.8.) He finally figured out that the mask used for the implantation of the ADC on the PCB board was not the right one. This impeded the heat flow from the ADC to the PCB board, and the resulting high temperature of the ADC was causing malfunction. After the corresponding modifications were done, ADC data were finally found to be consistent, and the board qualification process could start, 8 months after the prototype boards were delivered.

6.2.3.2.3 Transient signals The first test was to confirm that transient pulses could be detected, i.e. their envelope properly recorded. This was done through a qualitative test in the lab, using an arbitrary signal generator, and then through tests at the Ulastai Observatory in August and December 2016 (see Fig. 6.9). As for (too) many topics of the GP35 project, limited resources did not allow for a dedicated quantitative analysis of the complete system response to transient signals (noise level, sensitivity, etc).

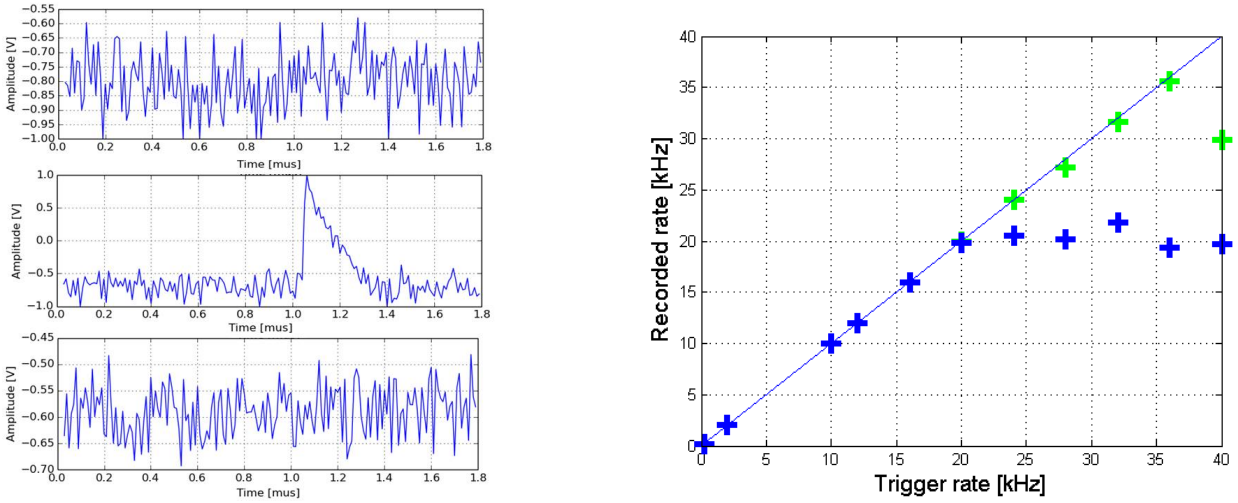

Figure 6.9: *Left: an event recorded at the Ulastai Observatory in December 2016 with a GP35 antenna plugged in a prototype GP35 Front-End unit. Time-traces are 1.8 µs long, corresponding to 90 samples. A transient pulse is observed on the Y channel (middle) , but not on X (top) and Z (bottom), which probably points to a detected wave polarized along the North-South axis. Right: measured rate of recorded events with the GP35 electronics as a function of the rate of impulses generated at the electronics input with a wave generator, for recorded pulse duration of 3.6 (blue) and 1.8 µs (green). Note here that the signal polarity is reversed compared to the simulated signal from figure 6.6 after a modification in the design. Taken from [226].*

6.2.3.2.4 Trigger rate In order to test the maximal detection rate of the GP35 unit —a key parameter, as pointed in section 6.1— a square signal was plugged into the prototype unit, with amplitude high enough to trigger the acquisition at each front edge. The comparison of the recorded events rate to the signal frequency, shown in figure 6.9, proved that the system was 100% efficient up to frequencies of 20 kHz for a time-trace of 3.6 μs, thus exceeding by far the specifications.

6.2.3.2.5 Amplitude calibration The calibration system presented in section 6.2.3.1 could be tested by taking dedicated data acquisition in a random trigger mode, after the inputs were switched to the calibration sine wave. The mean value of the output level is then plotted as a function of the input sine amplitude (see Fig. 6.10), which is controlled through the attenuation level set by the end user (see section 6.2.3). Repeating the operation for different

attenuation values allows to determine the calibration function, relating a signal amplitude level at input to the signal level at output. The output signal level was found to depend linearly on the signal attenuation level expressed in decibels over a range larger than 50 dB, as expected from the logarithmic response of the AD8310 component. This measurement is performed at the oscillator frequency only, but the flat frequency response of the system (see Fig. 6.12) allows to extend these calibration results over the whole 30-100 MHz frequency range.

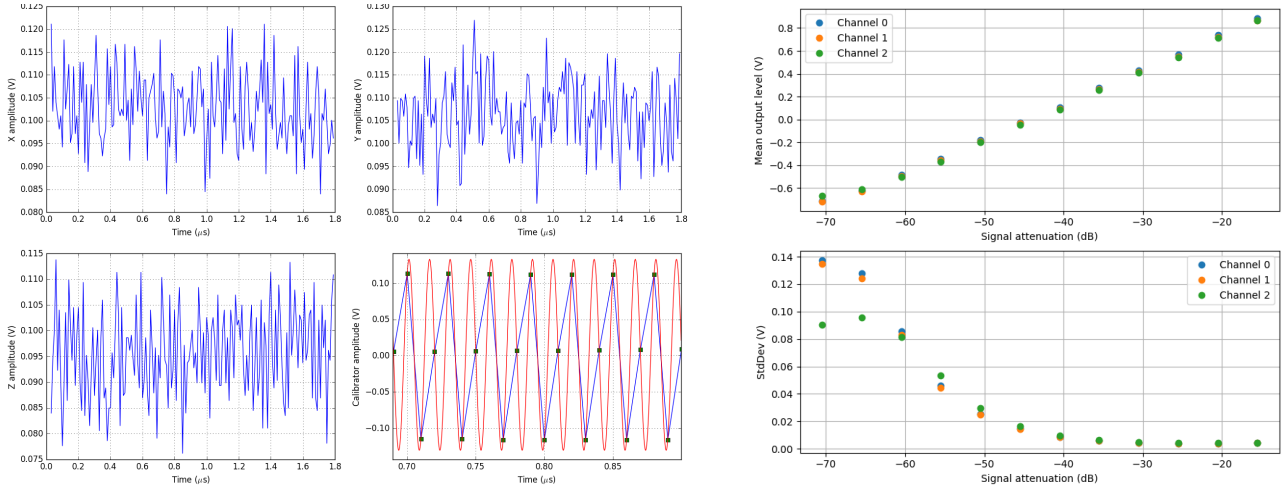

Figure 6.10: *Left: an event recorded with the GP35 Front-End unit in calibration mode (see section 6.2.4). The Quartz sine calibration signal is sampled with the 4^{th} channel of the ADC (green squares, bottom right panel). A sine fit with a fixed 66.666 MHz frequency (red) allows to monitor the amplitude of the input signal. A signal at this frequency necessarily induces a constant level at the output of the AD8310 power detector, given the 15 ns time response of this component. This can be seen on the three other plots corresponding to X, Y and Z antenna channels. Right: mean level (top) and mean standard deviation (bottom) of the recorded signals in calibration mode as a function of calibration signal attenuation. Each point corresponds to an average of 100 time-traces recorded in identical conditions. The larger RMS at low attenuation coefficient is explained by the higher gain of the power detector for small signals.*

6.2.3.2.6 Timing The relative accuracy of the trigger timing is measured by using a square signal fed into one channel of the two prototype boards through two cables of identical length. The two systems trigger on each edge of the square signal, and the time stamp values of each paired event are compared. Finally the standard deviation of the time difference distribution gives a direct measurement of the timing accuracy. A first test was performed in Ulastai in December 2016 over a few minutes only. The distribution of the time stamps differences Δt exhibited a standard deviation $\sigma_{\Delta t} = 8$ ns, which could be associated with a timing accuracy of $8/\sqrt{2} \sim 5$ ns, a performance well within the initial specifications.

Further tests carried out with the same setup in August 2017 at LPNHE however indicated that Δt could derive to significantly larger values over period of times of tens of minutes or more (see Fig. 6.11). A dedicated study on GP35 timing was therefore carried out by Enya Van den Abeele, 3rd year student at Sorbonne University, during a 2-months internship she carried out in Summer 2018 in LPNHE under my supervision, with significant help of Vincent Voisin, electronic engineer at LPNHE. Enya's work consisted in determining how the **Time mode** of the GPS — when the GPS assumes a fixed position to solely perform a time measurement [227]— would improve these results. Of course, the GPS has to lock its position to its true value to work correctly in this mode. One difficulty arised from the fact that the Front-End unit design did not allow communication of its position to the GPS, nor did it allow to retrieve the value computed by the GPS, as the PPS is the only signal output from the GPS unit (see section 6.2.3.1). Hence Enya, with the help of Vincent, established an independent communication with the GPS through its serial port, and interpreted the retrieved data using a dedicated software [228] from uBlox. The protocol of her tests consisted in switching the GPS to Time mode through a dedicated command sent to the FPGA once the GPS-computed position was within 10 m of its true value and then compare the timing precision to the ones obtained in **Survey-in Mode**, the alternative to Time Mode, in which the GPS computes its position from the GPS satellite constellation. Unfortunately this study

did not allow to reach a firm conclusion, mostly because of the poor GPS reception at LPNHE. Still, the results of the on-site tests detailed in section 6.3.1 tend to show that the Front-End units timing accuracy was within specifications.

Timing precision is certainly a topic where LPNHE could significantly contribute for the future stages of the GRAND project. In this perspective, LPNHE joined the T-REFIMEVE proposal led by the *Observatoire de Paris* and submitted in June 2019 to the *Programme d'Investissement d'Avenir*. LPNHE will benefit in this framework from an absolute time reference with a precision better than 1 ns, a great asset to carry out this task.

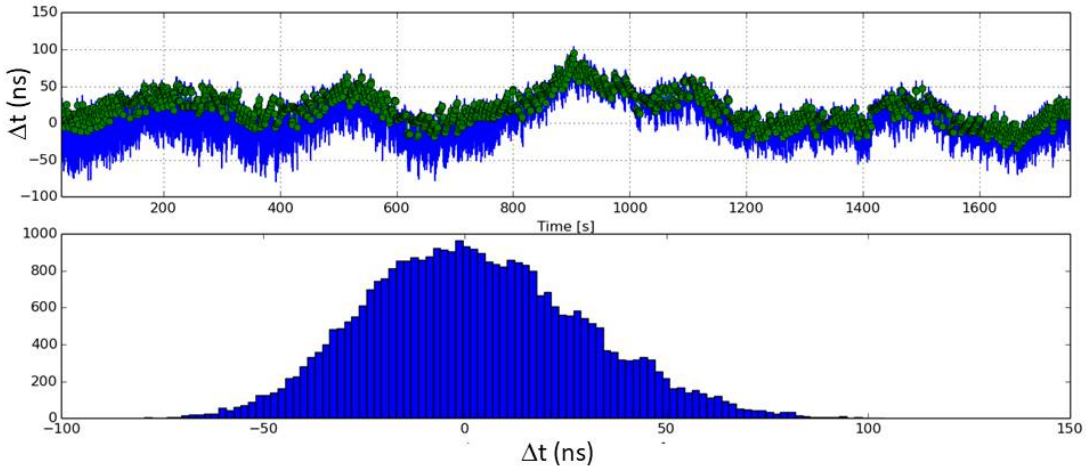

Figure 6.11: *Top: time difference Δt between time stamps from two GP35 boards triggering simultaneously on the same signal, issued by a square wave of period $T = 50$ ms, as a function of time. The green dots correspond to the first events triggered after a PPS signal is received by the two units. Bottom: the standard deviation of the Δt distribution for this specific test is 27 ns.*

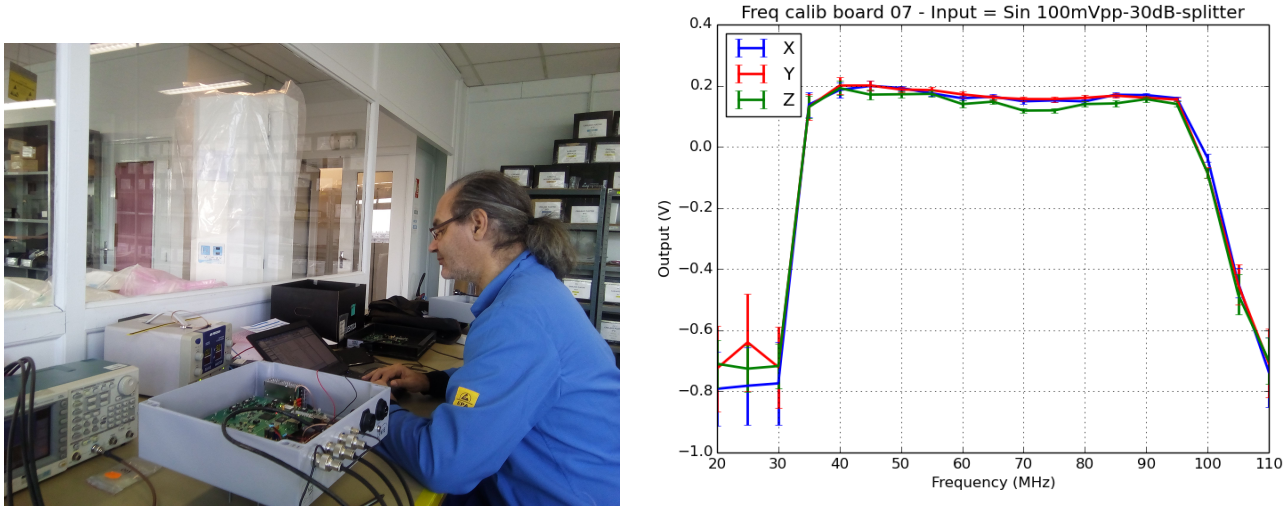

Figure 6.12: *Left: David Martin testing one of the 35 Front-End unit produced at STAE in November 2017. Right: average signal levels measured at the outputs of the unit b07 for a sine wave of fixed amplitude and variable frequency. A relative variation smaller than 10% was found in the range 35-95 MHz for a majority of units.*

6.2.3.3 Production validation

After the successful on-site tests carried out with the two prototype Front-End units in December 2016, STAE launched a pre-production of two additional units in January 2017, and the production of the 33 remaining pieces in July 2017. Production was completed in November 2017, and I carried out together with David Martin the final validation tests in the premises of STAE in December 2017 (see Fig. 6.12). These consisted in an automatized procedure I designed, evaluating the various functionalities of the boards: communication with the FPGA and the GPS, slow control information, trigger performance on square pulses of various amplitudes and frequencies. The system response was also calibrated using the internal oscillator (see paragraph *Calibration*) and an external sine wave. The latter also allowed to check the constant system response as a function of frequency (see Fig. 6.12).

All units but one passed the tests and could be shipped to China before the end of year 2017, which was a hard limit set by the buyer (NAOC) for administrative reasons. Still, the one year delay with respect to the initial planning was quite damageable to the whole GRAND project. Because of internal NAOC regulations, we were given a penalty preventing us from applying to laboratory funding for GRAND for the following three years.

6.2.4 The GRANDProto35 DAQ system

As for the Front-End electronics, I initiated the work on the GP35 DAQ system by defining its general concept and specifications, and then participated in its development by running extensive tests and reporting issues or requests for upgrades. However Gu JunHua is the author of the DAQ code, for which his expertise exceeds mine by far. I will therefore give only a very brief overview here.

The GP35 DAQ system has a multi-layer structure. At its core is a very basic system of formatted words exchanged between the Front-End Unit FPGA and the DAQ PC, embedded in a second layer of code constituting the actual DAQ software. This code is composed of two programs running on the DAQ PC. These were originally written in C, then translated in RUST [229] in 2018 following JunHua's initiative. `trend_server` is the "ear" of the DAQ: it collects data from the Front-End units on a given port of the PC. `send_msg` is its "mouth": it issues commands to the Front-End units on another one. These two programs do not communicate with each other. This is a built-in feature of the DAQ system, deriving directly from UDP protocol chosen for the socket communication in GP35. However in the RUST version of the program, an inner process makes sure that the acknowledge statement —expected from the Front-End unit in response to a message sent from the DAQ PC— is indeed received, and warns the user otherwise.

I developed an outer layer of code, which consists mostly of shell scripts, in charge of properly starting relevant processes and sending appropriate commands in a timely manner so that all runs smoothly. The standard user only accesses this layer in principle. Various acquisition modes were defined:
• in the **standard acquisition mode**, acquisition triggers when any of the selected channels (up to 6, corresponding to 2 polarities for 3 arms) exceeds the threshold defined by the user.
• in the **background acquisition mode**, an adjustable number of time-traces are recorded on random triggers. This is in particular useful to monitoring antenna status and electromagnetic environment.
• in the **calibration mode**, the three channels inputs are switched to the Quartz calibrator (see section 6.2.3.1) and acquisition is performed on random triggers.

6.2.5 The GRANDProto35 scintillator array

As mentioned in section 6.1, the GP35 radio detector was complemented by a a particle detection array. The project was led by IHEP mainly, thanks to a dedicated funding obtained from the Chinese National Science Foundation in 2013 by Gou QuanBu, who was in charge of the hardware until 2018 when Qian Xiangli —associated professor at Shandong Management University and former PhD student of Hu HongBo, my host at IHEP— took over. Zhang Yi, also a researcher at IHEP at that time, was in charge of the system's calibration, and two students from Hu HongBo's group carried out the simulation study. I also actively participated in this project, being involved in the definition of its goals and design. I also led the deployment of a 6-units prototype in Summer 2015 and its subsequent data analysis.

6.2.5.1 Detector efficiency

The purpose of the ground array was to validate the EAS nature of the candidates identified with the radio array. Unlike for radio arrays, events detected with a scintillator array are expected to be induced by air showers with a very

high probability. Indeed, random coincidences between scintillator units in time coincidence are extremely rare for three units or more and individual trigger rates in the hundreds of Hz range (see for instance Annex A of [207]). But high purity is not enough for the purpose of GP35 : excellent efficiency also has to be achieved inside the parameter space targeted for the radio array: E$\geq 10^{17}$ eV, $50° < \theta < 70°$, azimuth within $\pm 20°$ from North and core positions inside the instrumented area.

A dedicated simulation study was therefore carried out by Feng ZhaoYang and Wang Zhen, two PhD students of Hu HongBo. They used CORSIKA air showers covering this parameter space and a detector simulation from AS-Gamma [230], an IHEP-led experiment, using very similar scintillators, to come to the conclusion that the array of 24 units presented in figure 6.2 could reach sensitivities better for 90% for energies E$> 2 \cdot 10^{17}$ eV (see Fig. 6.13), provided that the scintillators are tilted by 50°from the horizontal towards North.

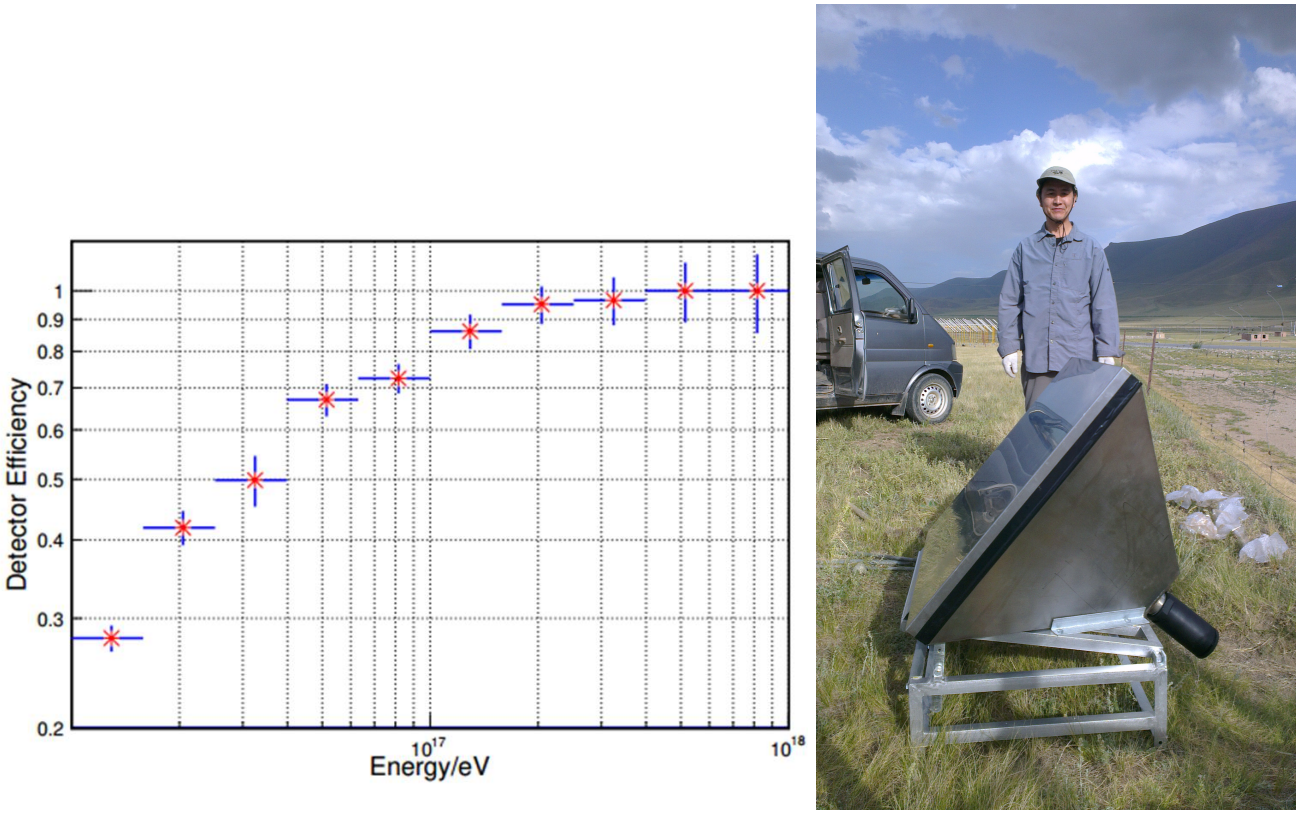

Figure 6.13: *Left: efficiency of the GP35 scintillator array for the detection of air showers. Here only showers with* $40° < \theta < 70°$*, azimuth within* $\pm 20°$ *from North and core positions inside the instrumented area are considered, and a multiplicity of three triggering units is sufficient for detection. Taken from [226]. Right: Gou QuanBou standing behind a GP35 scintillator during the deployment of the 6-units prototype detector in Summer 2015.*

6.2.5.2 Detector design

EJ-200 plastic scintillator tiles of $70.7 \times 70.7 \times 2$ cm^3 were selected as our detection target material. Plastic scintillator has the advantage of combining a fairly high light output with a fast signal that has a decay time of about 2 ns. Moreover, such a detector is easy to operate and maintain. An air light-guide connects the scintillator to a Hamamatsu R7725 phototube. In order to increase the light output, the outside faces of the scintillator and the inside of the light-guide are covered with reflective Tyvek 1082D. The detectors are mounted on a support tilted by 50° from the horizontal towards North (see Fig. 6.13).

High voltage supply for the PMT is built at the foot of the scintillator unit from the 12V voltage bias distributed from the pod. The PMT signal is also directly transduced at the foot of the antenna using the optical transducers from TREND (see section 5.4.2.2) and sent to the DAQ room on one of the four fibers available at the foot of the detection

unit. The DAQ system is identical to the one used for the TREND scintillator array presented in section 5.4.3.4.

More details on this setup and its characterization can be found in [226, 231]

6.2.5.3 Scintillator array prototype

A 6-units prototype was deployed on site in Summer 2015, forming a 200 m-side square, following the experimental design presented in the previous paragraph, except that the optical transducers were then placed inside the 21CMA pods, as the fibers had not been extended yet to the detection units position at that time.

An analysis I led allowed to reconstruct the direction of origin of the events detected over a few weeks with this setup. The resulting distribution, shown on the left panel of figure 6.14 is compatible with what is expected for air showers. Besides, the typical bump expected for Single Particle Peak (mostly muons) could be extracted from the amplitude distribution of individual units shown in right panel, thus allowing for an absolute calibration of the signal amplitude and subsequent energy reconstruction.

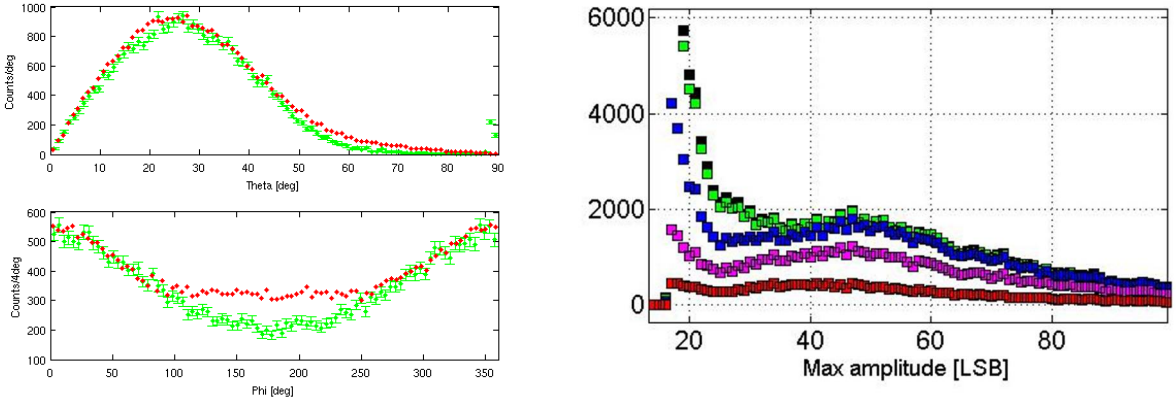

Figure 6.14: *Left: zenith (top) and azimuth (bottom) distributions of events reconstructed with the 6-scintillators prototype array deployed in Summer 2015. 3-fold coincidences are shown in red, larger multiplicities in green. The titled support of the scintillators explains the different rates measured towards North ($\phi = 0°$) and South ($\phi = 180°$) directions. Right: distribution of the signal integral for events measured with one scintillator for various integration windows. The Single Particle Peak is visible for optimal integration parameters. It corresponds to a 5 MeV deposited energy according to simulations.*

6.3 GRANDProto35 at the Ulastai Observatory

6.3.1 Detector commissioning

The commissioning of the GRANDProto35 experiment was initiated in Spring 2017, when two GP35 antennas were connected to the prototype Front-End electronics units. This setup allowed demonstration of the long-term stability of the system's response over periods of weeks, as illustrated on figure 6.15). DAQ live-time was also extensively studied during that period: the comparison of the trigger rate (an information available from the slow-control data) to the rate of events actually recorded to disk allowed to confirm that a 100% value could be achieved for Ulastai electromagnetic conditions (see Fig. 6.16). These tests allowed us to conclude that two of the most important specifications of the GRANDProto35 setup (see section 6.1) could be met in practice.

After these encouraging preliminary tests, it was foreseen that the radio units would be deployed in summer 2017 and that the Front-End units would be added upon reception, early 2018, allowing for the detector commissioning to start. I was naturally expecting to spend a significant time on site to participate in these key phases However, site access had become hazardous for foreigners by then. The first alert came on July 9, 2016, exactly 7 years after the Urumqi riots where 197 people were killed in the capital city of XinJiang. A police control placed on the road

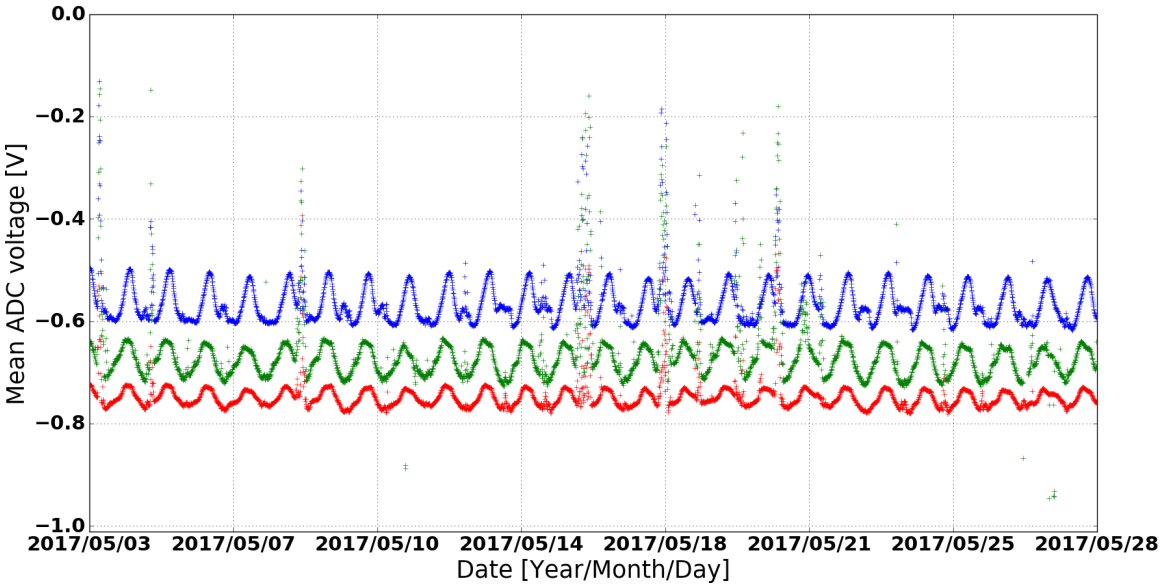

Figure 6.15: *Monitoring measurement of the signal mean voltage for a period of 28 days at the GRANDproto35 experimental site for channels X (blue), Y (green) and Z (red) of a test detection unit. The daily-periodic fluctuations correspond to the crossing of the antenna field of view by the Galactic plane. In this plot X and Y curves are shifted by constant offsets of +200 and +100 mV respectively for better readability. Taken from [226].*

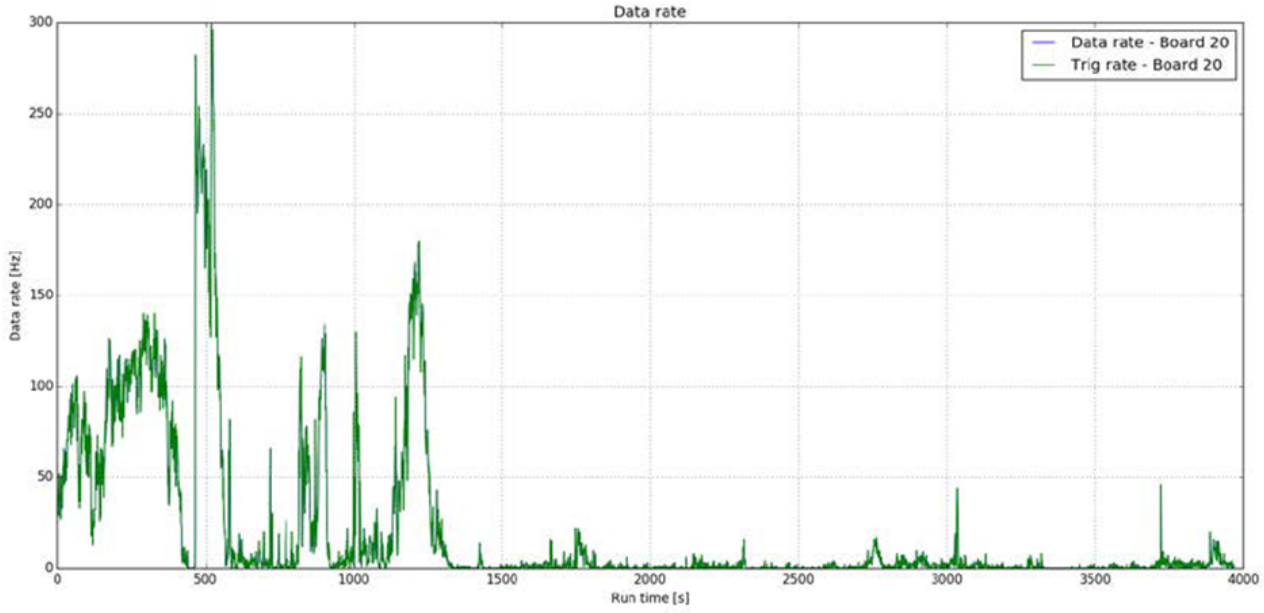

Figure 6.16: *Trigger rate (green) as a function of time for a ∼1 h acquisition taken in Ulastai in December 2016. The rate of recorded events is also plotted in blue, but following the trigger rate curve, it is not visible. This shows that a 100% live time was achieved for this acquisition, a performance routinely repeated during commissioning.*

to Ulastai that anniversary day denied access to Sandra Le Coz, Charles Timmermans, René Habraken[1] and myself. The policeman argued that we did not have the appropriate authorization, a request I never heard in my 30+ visits to Ulastai in the preceding 8 years. I could reach the site again in August and December 2016, but systematic police checks were then established routinely, enforcing a regulation which actually existed since long, but had never been applied so far.

The official procedure to obtain the required permit was complex, and had to be renewed at each visit. Despite obstinate efforts by Wu XiangPing over the following months, no waiver could be obtained for scientists. Failure on this effort, and more general considerations on XinJiang which will be detailed in section 6.3.2, led us to the conclusion that foreigners would not be able to go to Ulastai anymore. I therefore proposed in Summer 2018 to Chinese colleagues to take the lead for the GRANDProto35 project, as it seemed impossible for me to organize the commissioning and running of a setup I could not visit. Qian Xiangli, associate professor at the Shandong Management University, took over the lead for the scintillator array, and completed its deployment in Summer 2019. Unfortunately no proper candidate could be identified for the radio part, Gu Junhua being in particular already too busy with 21CMA and SKA to devote enough time for GP35. The lack of long term perspective for the project thus made the deployment of the radio array extremely slow. In April 2019, only fifteen antennas had been deployed, and only eleven of them were actually operating.

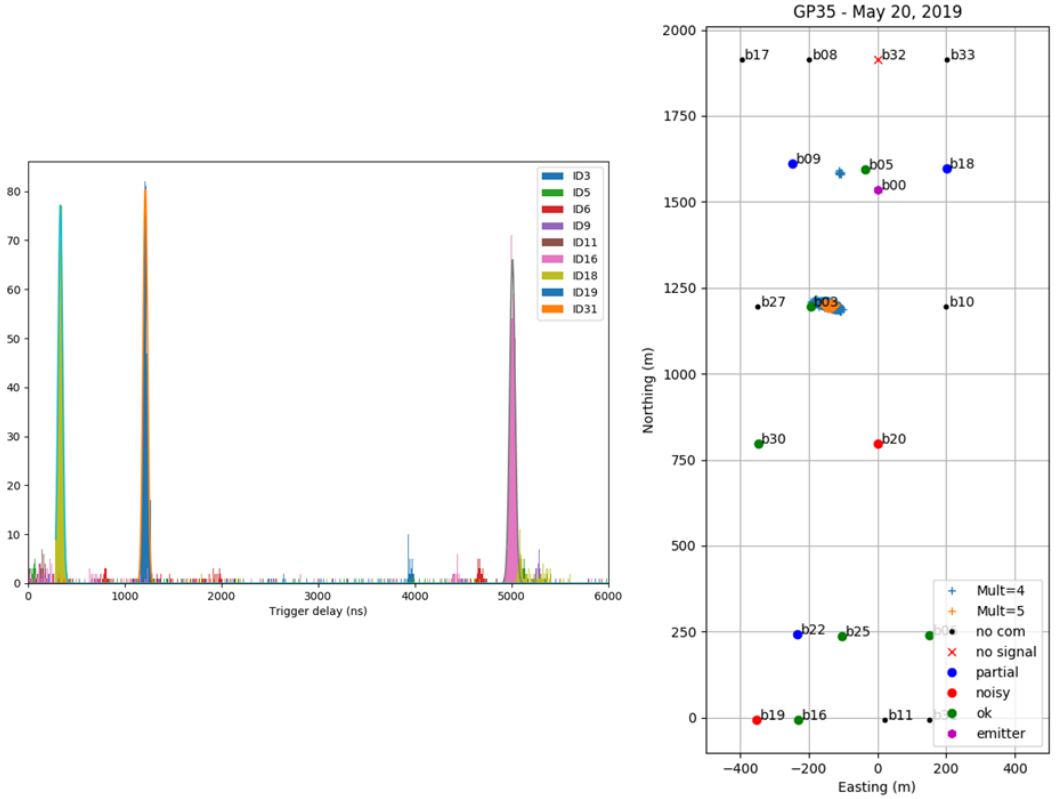

Figure 6.17: *Left: trigger times for events recorded during a time calibration run in May 2019. The time reference for each event is the first triggered antenna. The distributions are fitted with Gaussian, which standard deviation is 20 ns on average, corresponding to an intrinsic timing accuracy of ∼15 ns. Right: reconstructed source position for a calibration run performed at the same period, with events of multiplicity 4 in blue and 5 in orange. The source is reconstructed at position (WE = -160 m; SN = 1200 m) with a precision around 10 m for events of multiplicity 5. Also displayed are the positions of deployed antennas, with markers corresponding to their state and given in the legend.*

[1] Charles and René are two colleagues from the Radboud University in Nijmegen, and this was their very first visit to China in the framework of the GRAND project. Happily this calamitous start did not prevent our collaboration to flourish after that, as we will see in chapter 7

Timing performance and direction reconstruction were however tested in Spring 2019. The analysis I carried out on the recorded data showed a timing precision around 15 ns, allowing to reconstruct the source position with a precision around 10 m for events with five triggered antennas or more (see Fig. 6.17).

Since then, no further radio units were deployed. The stalled situation for the GP35 radio array for the last two years, combined with the progress of the GRANDProto300 project, presented in the next chapter, now make GRANDProto35 goals obsolete. I believe that GP35 would have been an ideal sandbox for Chinese students and researchers interested in EAS radio detection in order to develop an expertise and confidence allowing them to contribute significantly to the next stages of the GRAND project, but I failed to convince Chinese colleagues, sadly.

6.3.2 Scientific collaboration in China

The unfortunate situation we face on GP35 is a side effect of the Chinese government's policy. I will therefore now take the liberty to step aside from the presentation of my scientific activities for a moment, and discuss a bit more the issues related to scientific collaboration with Chinese researchers on projects based in China. These are, in any case, deeply linked to my work on TREND and GRAND, and are therefore relevant to this document.

A lot of criticisms can be heard in Western medias concerning the People's Republic of China and its government. Even if the five years I spent in China led me to significantly mitigate my judgment, I agree with the usual statement that the Chinese government sees freedom of speech and of information as threats to social stability, and fiercely fights against them by deploying its own propaganda. I also believe that the Chinese government follows an aggressive agenda to strengthen its influence in the world, science being one of its weapons in this respect. As long as this does not alter my own freedom of speech, this second point does not bother me so much, because politics is never absent from a country's research policy[2]. Lack of freedom is surely more problematic, but our options seem limited to me: China is too big, too powerful and the world too divided for pro-democracy movements to generate efficient pressure against PRC government. On the other hand, simply looking away always seemed to me like a hypocrite posture without any positive effect on the lives of Chinese people.

When the opportunity to work in China opened for me, I therefore hoped a third, empirical option was possible, allowing to establish a collaboration which my Chinese colleagues based on equity, respect and honesty. This meant talking openly with them about any topics beyond science —including politics— and when doing so, being honest about what I like —and do not like— in Western democratic systems, being clear about what I can and cannot accept in our scientific collaboration while always being respectful of my colleagues point of views. I hoped that this position would help for a better common understanding. I went and worked in China propelled by this idealistic vision, and I think I managed to stick to it: I did develop strong brotherhood feelings with technicians in Ulastai and other co-workers through labor in common —communication was often too limited and respective backgrounds too different to call this friendship—; I had passionate discussions with many fellow researchers about politics, culture, freedom or society. I am lucid enough to know that my personal actions did not have any impact on a large scale, and I am not even sure it influenced the people I worked with, but I felt at peace with my own consciousness while developing the TREND and GRAND projects in China.

Working in XinJiang could also be a source of concerns, as Han people, the dominant ethnic group in China, are sometimes accused of stealing this land from Uighurs, Muslims of Turkish origin who settled down in large parts of the province between the 5^{th} and 7^{th} centuries. However, even if tensions were often palpable between Han people and Uighurs —culminating in the Urumqi riots in Summer 2009– I could see through my numerous stays, encounters and travels in the XinJiang province that the culture of minorities —Uighurs, but also Mongols or Kazakhs present in the Ulastai area— was still vivid, more than 2000 years after the Han established control over XinJiang. In that respect, I found the regular critics of Westerners about minority oppression and cultural genocide by the Chinese government simply wrong[3], and inappropriate when officially formulated by countries —like France or the United States— who repeatedly and purposely destroyed local cultures in their countries or abroad throughout their history.

This position became extremely uncomfortable after 2016, when the freshly appointed Governor of the XinJiang Province implemented an extremely severe campaign against Uighurs, which only seems to reinforce in time. This

[2] In the specific case of France for instance, the development of high energy physics after World War II is clearly linked to the government's decision at that time to develop nuclear science for civil and military applications.

[3] The best example for this being the fact that Uighurs, like all other minorities in China, were exempted from the one-child policy imposed to Han people.

change was triggered by a wave of terrorist attacks in China. Three events in particular stroke the public opinion in China: a car driven by suicide terrorists crashed in the iconic Tian An Men Square on October 28, 2013; 31 people were slaughtered by five to ten people armed with knives at the Kunming Train Station in the Yunnan Province on March 1st, 2014; and a suicide bombing killed 39 people at the Urumqi market on May 22, 2014. The Chinese government accused Islamic terrorists to be responsible for these attacks and several others in the country during the same period of time. The Turkestan Islamic Party, a jihadist group with claimed ties to Al-Quaida, claimed in particular responsibility for the Tian an Men and Urumqi attacks.

In the beginning, the reaction of the authorities seemed moderate, a larger presence of police in the streets of Urumqi being the most obvious changes in the province after the May 2014 bombing. Soon however, Chinese colleagues in XinJiang started mentioning numerous arrests and death sentences pronounced against Uighur separatists, but reliable information was very hard to find. The tension raised with time, and the overall atmosphere eventually seemed completely paranoid and oppressive to me during what turned out to be my last visit to the XinJiang Province in April 2018 (see section 7.4). One month after that, an article published in *the Economist [232]* was the first piece of evidence shedding disturbing light on the situation in XinJiang. It claimed, with robust evidence, that a significant fraction of Uighur population —"upwards of a million" out of the eleven living in the province— were sent to "re-education camps". Several concurring news, including a UN report[233] in August 2018, confirmed that mass-scale internment was taking place in XinJiang. In the light of these information, it became impossible for what had then become the GRAND collaboration to keep on working in the XinJiang province. In agreement with our Chinese colleagues, decision was made in Summer 2018 that the GRAND collaboration would not be involved in the XinJiang province and by extension, would not participate in the GRANDProto35 experiment. I remained the only foreigner with ties to the project, offering backup and expertise to those willing to get involved in the project.

In a broader perspective, and to conclude this topic and chapter, I would state that the increasingly aggressive attitude of the Chinese government towards foreign powers represent for me a major concern and a threat to the development of international scientific collaboration based in China, and in particular GRAND.

Chapter 7

The GRANDProto300 project

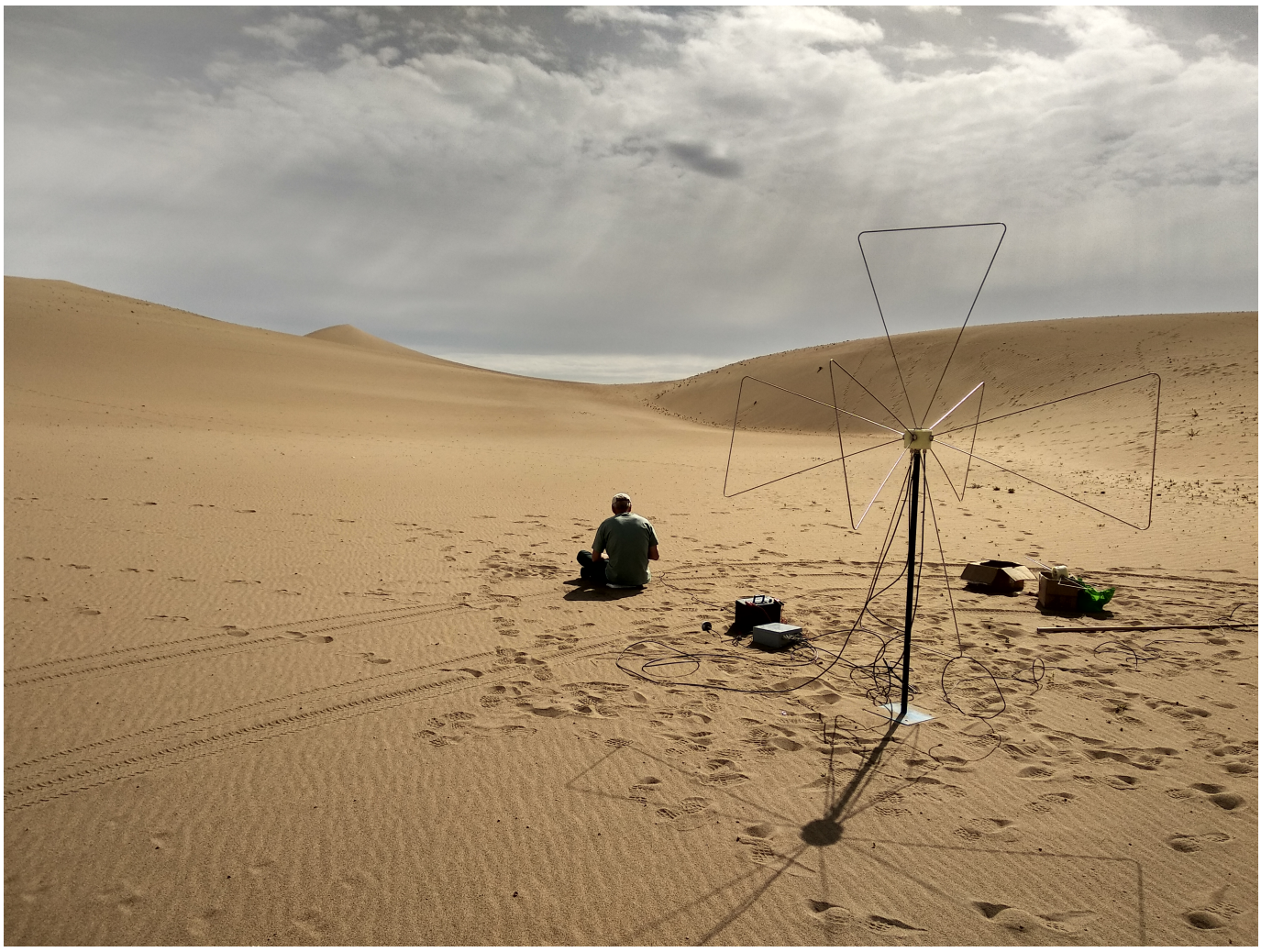

Figure 7.1: *Charles Timmermans running measurements during a site survey for the GRANDProto300 experiment in Summer 2018.*

The concept of GRANDproto300 was born in the seminal GRAND meeting held in LPNHE in February 2015 (see section 3.1.4). It was then refined through contributions by several members of the GRAND collaboration, with a prominent role played by Charles Timmermans, researcher at the Radboud University in Nijmegen and GRAND-Proto300 project leader. I was involved in the definition of GRANDProto300 objectives and detector design, briefly presented in sections 7.1 and 7.2, and took an active role in the computation of the detector effective area (section 7.3) and in the site survey (section 7.4). These initial sections are partly taken from [234].I will also discuss in section 7.5 the steps following GRANDProto300 in order to realize the full GRAND detector envisioned in chapter 3.

7.1 GRANDProto300 objectives

7.1.1 GRAND pathfinder

GRANDProto300 (GP300) primarily aims at validating the GRAND experimental principle by achieving the autonomous radio-detection of near-horizontal extensive air showers with high efficiency and a rejection of background transient events close to 100%. GP300 objectives are somewhat close to GRANDProto35 ones (see section 6.1) except that there is a specific focus here on very inclined showers ($\theta > 80^{\circ}$). This will allow to derive conclusions on the radio-detection of neutrino-induced showers, despite the fact that GP300 only targets cosmic-ray-induced EAS because of its limited size. Similarly to GRANDProto35 also, the efficiency of EAS detection would be evaluated quantitatively thanks to an independent array of particle detectors deployed at the same site as the radio detector. The GRAND group led by Miguel Mostafa at Pennsylvania State University is presently studying the design of this ground detector, a work I am not involved in and which will therefore not be detailed here.

In addition, GP300 will provide ideal material to evaluate the performances of the procedures presented in chapter 4 for the reconstruction of the direction of origin, energy and nature of the primary particles. Comparison to the numerous existing results (see [235] for an extensive review) will allow evaluating GP300 performances for GP300 reconstruction of energy and composition. The angular reconstruction may for its part be evaluated by studying the angular distribution of the reconstructed directions around the horizon line. No cosmic-ray event is expected to originate below the horizon which varies over a significant angular range for the GP300 site, because of its mountainous environment (see section 7.4.3). Studying the angular distribution of reconstructed events around the horizon should therefore provide valuable input on the angular resolution achievable in the few degrees angular range around $\theta = 90°$, the region of interest for neutrino search.

When these initial steps are achieved, GP300 will be used to test technological solutions for arrays of larger scales, in view of the full GRAND array. This is discussed in section 7.5.

7.1.2 GRANProto300 science case

GP300 is not only an engineering prototype, but also an instrument studying the physics of air showers and cosmic rays, and an observatory of astrophysical phenomena. This is presented in the following sections.

7.1.2.1 Air-shower physics

For air showers inclined by more than 70°, the only particles reaching ground are muons (see Fig. 7.2). The muon and electromagnetic contents of each individual shower will therefore be independently detected by the GP300 ground and radio arrays respectively. In addition, the radio array could provide a measurement of the shower energy at a 5% precision level [236]. These combined and independent information will be extremely valuable to better study the hadronic processes in air showers [139].

7.1.2.2 Ultra high energy gamma rays

As seen in section 2.2.1.3, UHE γ-rays induce nearly pure electromagnetic showers, a component fully absorbed by the atmosphere before reaching the ground for zenith angle larger than 65° (see Fig.7.2). The particle detector can therefore be used as a veto with an excellent rejection power in order to discriminate showers induced by UHE γ-rays from those associated to UHECRs. If no γ-rays are identified among a sample of 10 000 showers detected in 2 years, the limit on the fraction of UHE gamma rays will be 0.03% at 95% C.L. instead of 0.1% for the current best limit [238].

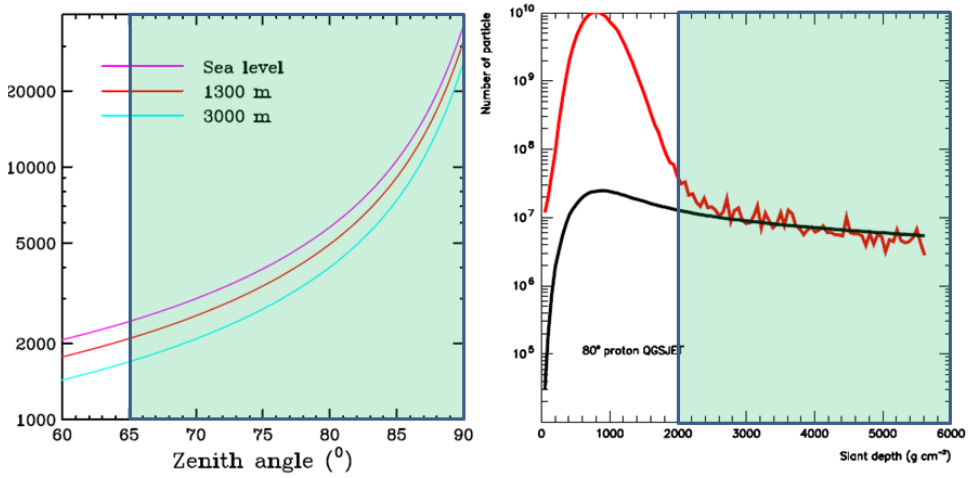

Figure 7.2: *Left: atmosphere column density as a function of zenith angle for various ground altitudes. Right: depth development of electromagnetic (red) and muonic (black) components of a typical shower induced by a proton (qualitatively identical to that induced by a nucleus), as simulated with ZHAireS, using the QJSJET model for hadronic interaction. Zenith angles larger than 65° (green shaded areas) correspond to slant depths above 2000 g.cm−2, for which electrons and positrons from the shower are fully absorbed in the atmosphere. The electromagnetic component corresponds here to an halo of electrons generated by hard muons interactions in the atmosphere. Taken from [237].*

The science case for γ-rays an the potential for their detection in GP300 will be studied by Simon Chiche during his PhD thesis at IAP, under the joint supervision of Kumiko Kotera and myself.

7.1.2.3 Galactic/extra-galactic transition

In the energy range between 10^{17} and 10^{18} eV, a transition between galactic and extra-galactic cosmic ray sources is expected [240], thus making this energy range particularly interesting for observations. A lot of work is still needed to provide robust and quantitative arguments evaluating the additional value brought by GP300 on this specific issue, but accurate measurements of the energy, composition and distribution of the arrival directions with the large event statistics (see section 7.3) should be great assets to distinguish between the different astrophysical source models.

7.1.2.4 Radio Astronomy

We discussed in section 1.7 the potential of GRAND for the study of Fast Radio Bursts. Valentin Decoene and Philippe Zarka extended the study they carried out for a 200 000 km^2 array to the specific case of GP300, and concluded that the detector's sensitivity would allow the detection of galactic events such as the Giant Pulses emitted by the Crab Pulsar [241, 242] or Fast Radio Bursts [243, 244] with energies above 750 Jy. Observations over the large field of view permitted by the unphased GP300 array would be an excellent complement to dedicated instrument with much better sensitivity but limited field of view.

GP300 could also allow to study the 21-cm line from the epoch of reionization (EoR), imprinted onto the Cosmic Microwave Background (CMB) as a line-like absorption feature, redshifted today to frequencies between 10 − 200 MHz [245]. By measuring the temperature of the sky with mK precision, as a function of frequency, the global EoR signature can be identified as well as the absorption feature due to reionisation below 100 MHz. A recent experiment has found a 500 mK-deep absorption feature at 78 MHz, differing from the theoretical predictions [109]. If antennas can be calibrated with sufficient precision, GP300 could achieve 1 mK sensitivity using only 30 antennas at 80 MHz thus will substantially improve the determination of the characteristics of this feature. No effort was carried out yet to evaluate how this performance could be achieved in GP300.

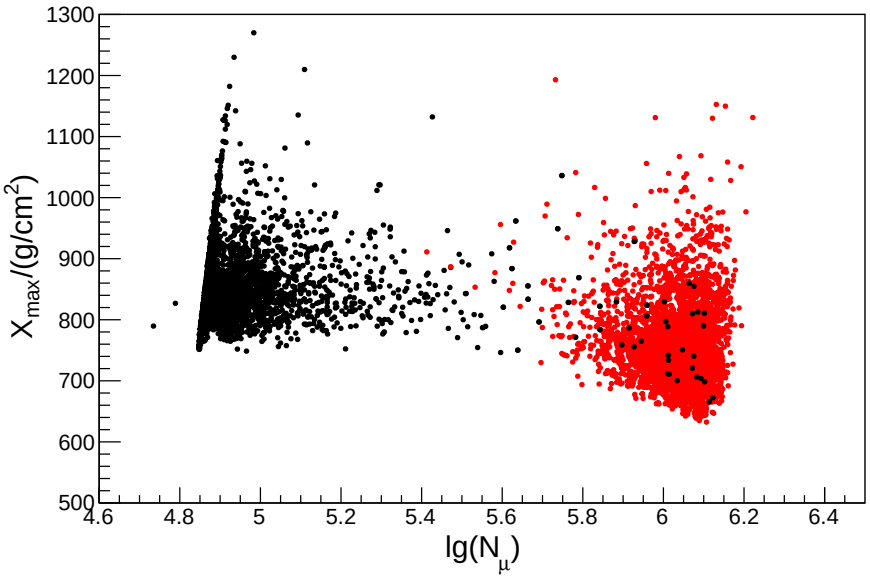

Figure 7.3: *Conex[239] simulations showing the position of the maximum of development of showers initiated by γ-rays (black) and protons (red) of same energies as a function of their number of muons. γ-rays showers induce a much smaller number of muons, their measurement thus allowing for an efficient discrimination between the two primaries. Plot presented by Foteini Oikonomou at the GRAND collaboration meeting in Karlsruhe, Feb. 2020.*

7.2 Detector design

7.2.1 Layout

The layout foreseen for the GP300 detector consists in 215 antennas disposed following an hexagonal grid with 1 km step size, while 72 additional antennas allow to form an infill of 250 or 500 m step size (see Fig. 7.4). The infill will allow to evaluate experimentally how detector density affects detection and reconstruction performances, while it will also allow to extend the GP300 energy range to lower energies (see section 7.3).

7.2.2 Antennas

The design of the GP300 antenna is very close on the HorizonAntenna presented in section 3.2.1.4. It was developed and built under the lead of Zhang PengFei, researched at the Xi'An Xidian University, following initial ideas by Didier Charrier. The two horizontal arms are bow-tie antennas with 45 cm arm extension. Simulations showed that a monopole is better suited for the vertical arm because of the ground influence. Commercial Low-Noise Amplifiers of 18 dB gain are installed at at the antennas' feed-points behind impedance-matching networks. In its present version, the antenna system is mounted atop a 3.5 m pole (see Fig. 7.4). 100 such units have been produced.

7.2.3 Front-End electronics

An electronic treatment of the antenna signal is performed at the antenna level with a system developed in Nijmegen by Charles Timmermans and his group, relying on the expertise acquired in the AERA experiment in particular. The analog signal is first filtered in the $30 - 230$ MHz frequency band, with a difference in group delays limited to 10 ns. It is then digitized using a 14-bit ADC (AD9694) running at a sampling rate of 500 MSamples/s. The total power consumption of the digitization process for all channels is slightly more than 2 W.

Digitized data is then processed inside a Zync FPGA with hardcore CPU (Xilinx XCZU5CG). The programmable logic will be used to remove narrow band sources and create a fast trigger. Furthermore, it will create a real-time

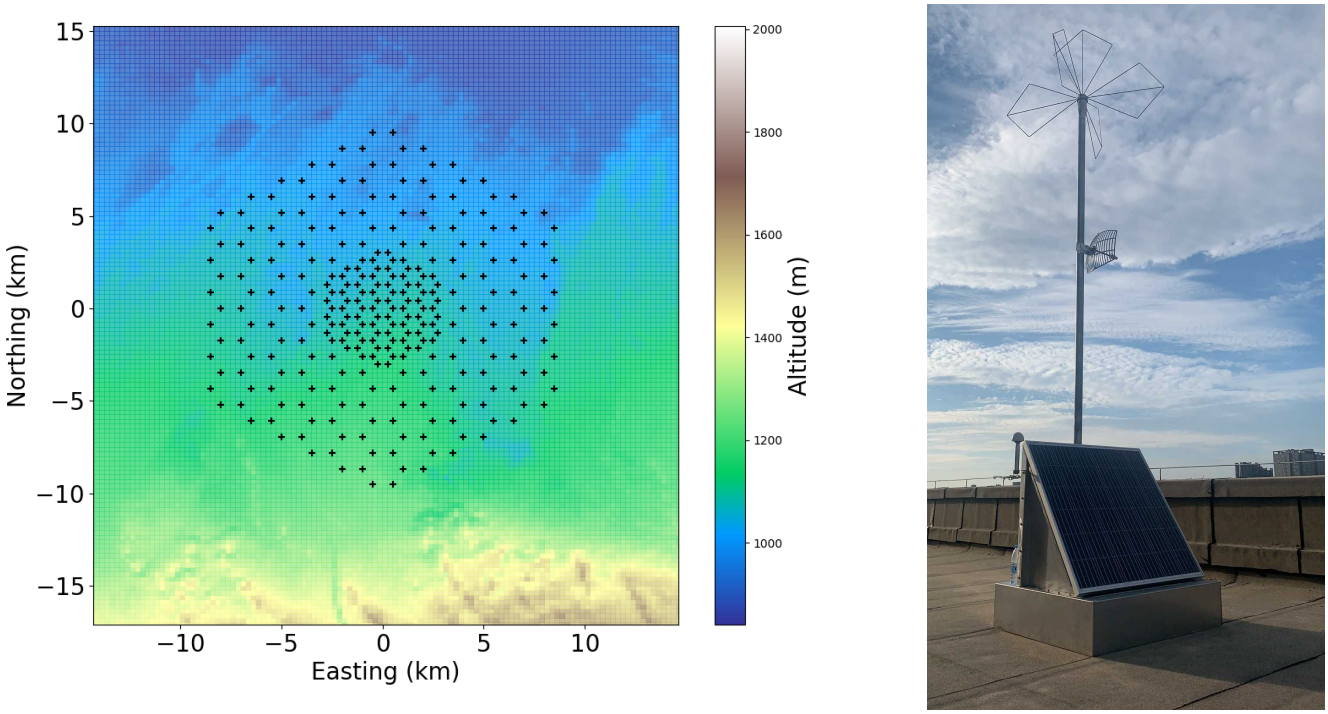

Figure 7.4: *Left: GP300 array layout (black crosses) displayed over one candidate site topography. Right: the GP300 prototype detection unit deployed at Xi'An Xidian University Campus in June 2019. The 3-arms antenna is mounted atop a 3.5 m antenna. A solar panel mounted atop the box placed at its foot will provide power to the front-end electronics (see section 7.2.3) installed in the box. On this plot the WiFi communication antenna (see section 7.2.3) is also visible.*

Fourier transform of the data that can be used for environmental monitoring and searches for astronomical phenomena (see section 7.1.2.4). A timestamp with a precision better than 10 ns is added to the triggered ADC data. The data is then read by the CPU where time-traces and frequency data are further analyzed, stored and transmitted to the central Central Data Acquisition (DAQ). The total consumption for this chip is estimated to be below 4 W.

Communication and data transmission will use WiFi technology. The *Ubiquity airMAX-AC* system fulfills our needs of reliability and transmission bandwidth (see section 7.2.3.1). At the antenna side, a *BULLET-AC* is used. The maximal power consumption of these units is 8 W, however the average power consumption has been measured to be about 3 W on AERA.

150 W-solar panels will allow for battery recharge even during the short winter days, thus securing a $\geq 80\%$ duty cycle of the units.

A first batch of 100 Front-End electronics boards was produced, and validation tests were succesfully completed by the GRAND teams at Purple Mountain Observatory and Xi'An Xidian University in June 2021.

7.2.3.1 Data acquisition

7.2.3.1.1 Trigger The trigger strategy is split in three stages. A first trigger level T0 is generated when the signal amplitude of one antenna channel exceeds a threshold of $5\,\sigma$, where σ is the mean stationary noise at the antenna output. The second level T1 is performed in the FPGA at the Front-End level. It consists, at least in the beginning, in a pulse shape analysis combined with a veto during noise bursts, as the TREND experiment in particular has shown that such treatments allow to reject 95% of the background events (see Table 5.3).

For each T1,a 4-byte GPS timestamp is sent to the DAQ. Assuming a maximal 1 kHz rate at the T1 trigger level

would lead to a data rate of 4 kB/s per detection unit. The DAQ analyzes the T1 timestamps, and issues a T2 trigger when time coincidences are found among a minimum of five detection units. Then 3 μs-long time-traces are transferred from the detection units participating in the T2 trigger to the DAQ. At this stage, the DAQ is designed to be able to manage a 10 Hz rate per detection unit, but direct extrapolations from TREND results lead to an estimated T2 rate of 10 mHz [246] providing a safe margin. The nominal data rate per detection unit is ∼80 kB/s accounting for ADC samples and header information (7.5 kB per event).

In parallel to this search for transient radio waves, it is expected that each station will calculate the Fast Fourier Transform (FFT) over 4096 samples in the $100 - 200$ MHz frequency range (i.e. 25 kHz frequency resolution) and will sum them over periods of 10 ms. The FFT data will be coded in 1 byte only, after the spectrum has been corrected for the constant slope induced by the Galactic emission. These data will be used both for status monitoring and search for transient radio events (see section 7.1.2.4). This results in a ~ 400 kB/s data transferred for each station for rge FFT data.

In a point to multi-point configuration such as the one designed for GP300, this corresponds to a total (i.e. 300 units) data throughput requirement of ~ 150 MB/s to the central DAQ. This will be the main bottleneck for the communication system and drives the final setup.

7.2.3.1.2 Communication The *Ubiquity airMAX-AC* system [247] relies on the WiFi communication of *BULLET-AC* devices to a single *ROCKET* base station. The *ROCKET* is abble to handle 62.5 MB/s at 100% capacity, while each detection unit produces a nominal data rate of ~ 500 kB/s when taking into account FFT and EAS data into account. Requiring that the *ROCKET* device works only at 60% of its capacity to ensure an efficient working network, up to 75 detection units can be connected to the same *ROCKET* base station. Therefore the GP300 array will be divided in 5 (overlapping) sectors.

The five *ROCKET* stations will be installed atop the DAQ room, located at one corner of the radio array. Finally *Ubiquity AirFiber*, with a nominal range of 100 km, will connect the DAQ room to the closest access point to the outside Ethernet, at a speed of 2 Gbps.

7.3 Exposure

The exposure of the GP300 detector was computed in a study carried out with Matias Tueros and Valentin Decoene.

An initial set of 5665525 trajectories were sampled on a 110 by 120 km area centered on the YiWu candidate site (see table 7.6). All azimuths, zenith angles between 45 and 89.9°and energies between 10^{16} and 10^{18} eV were considered. A geometric pre-selection, based on a conical parametrization of the radio-emission by the associated showers presented in section 3.6, allowed to select among those 12 000 showers likely to trigger the array.

The electromagnetic radiation of these selected showers were then simulated using ZHAireS. The shadowing effects due to the topography was also taken into account in the simulation. The antenna response to the electromagnetic signals was then computed using the GRAND HorizonAntenna specifications (see section 3.2.1.4) and a Butterworth numerical filtering was applied on the output signal in the $50 - 200$ MHz range. No noise was added in this study. It was considered that the shower would be detected if a voltage signal peak-to-peak above $5\,\sigma = 75\,\mu$V per event was observed on a minimal number of 5 antennas, with $\sigma = 15\,\mu$V the mean stationary noise expected at the output of the HorizonAntenna in the range $50 - 200$ MHz (see section 3.2.1.5). A simulated event is displayed in Figure 7.5.

The GP300 exposure was then computed following the method detailed in section 3.1.1 and the differential number of events per day was derived , using the spectrum obtained from the TALE measurements [18] . It can be seen from figure 7.3) that the infill allows detection down to $4 \cdot 10^{16}$ eV, while the 200 km^2 detector area makes it possible to collect significant statistics close to 10^{16} eV (see table 7.1). Additional simulations are being performed to adjust the GP300 layout by Zhang Kewen, Master2 intern with me from April to June 2021. This will allow to define the layout optimizing the exposure at low energies as well as reconstruction performances.

E (PeV)	30	42	74	100	133	177	237	316	562	1000
Rate (day^{-1})	4.1	93.2	1124.8	1531.7	1412.7	957.7	589.3	391.5	154.2	92.3
Contained rate (day^{-1})	4.1	93.2	989.7	1071.3	850.7	451.8	284.2	190.5	53.6	29.9

Table 7.1: *Detected event rates per day integrated over the energy range given by the values of columns i and $i+1$. The contained rates correspond to detected events with a shower core contained in the array. Taken from [234].*

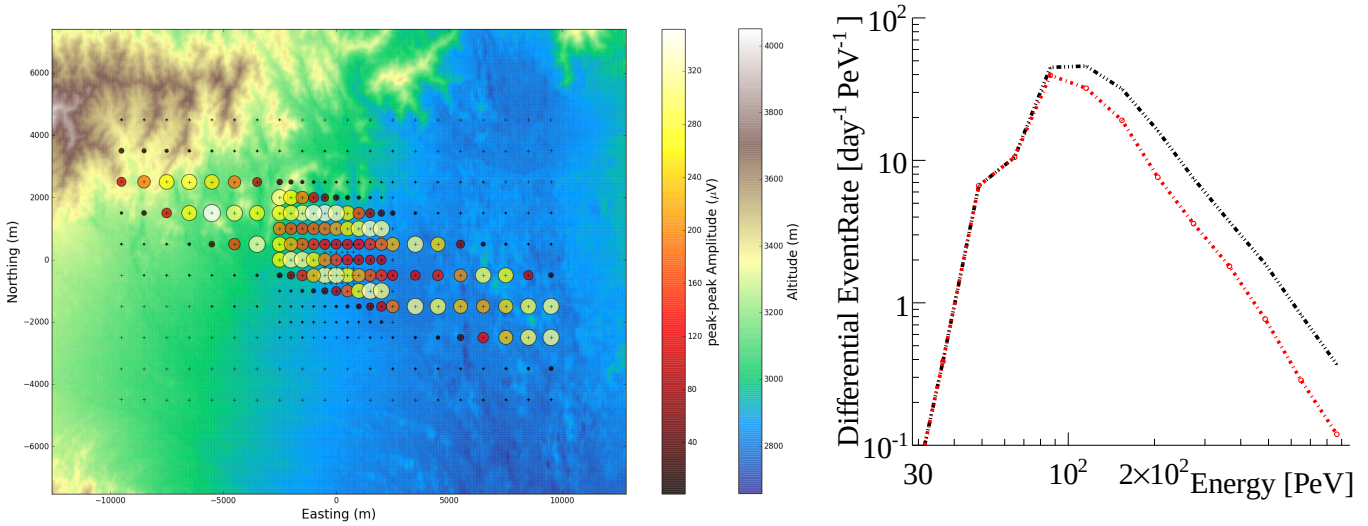

Figure 7.5: *Left: A simulated air shower (E=4.2 · 1017 eV, $\theta = 83°$) displayed atop the GP300 array layout in YiWu Valley (black crosses). Simulated antennas are represented by circles of radius proportional to the signal peak-to-peak amplitude at antenna output. The enhancement of signal amplitude along the Cerenkov ring is clearly visible. A square layout was used for this study, but results for an hexagonal layout are similar, and site location has a negligible effect on the event rate. Right: GP300 differential event rate as a function of the primary energy for the preliminary layout. In black (small-dotted line) the total detected event rate and in red (big-dotted line) the rate of detected events with a shower core contained inside the array, which should allow for better reconstruction performances. Taken from [234]*

7.4 Site selection

7.4.1 Selection process

Based on the past experience of TREND and AERA, it was clear to all members of the GRAND collaboration that the site selection was critical for the success of the GP300 experiment. Significant effort was therefore put in this process, which started with the definition of the following selection criteria, ranked by order of importance:

(i) Radio environment quality: the TREND experiment, and in particular the contrast in the results obtained during the quiet period up to September 2012 and those from the noisy one after that, as well as the self-trigger attempts in AERA [248, 249] clearly show how important the radio background environment is for self radio-detection of air showers. It is critical that this environment is well characterized and understood, and that the DAQ system matches its characteristics to ensure a 100% live time of the experiment. In the specific case of GP300, this means that only a limited number of constant wave (CW) emitters should be present (as these can be removed through digital filtering, prior to the trigger stage), while a threshold level corresponding to few standard deviation of stationary noise should induce a trigger rate below 1kHz.

(ii) Site access & infrastructure: a town must be easily reachable from site (less than 100 km and 2 hours drive) to host a life base for scientists working on the experiment, provide local staff and allow to transfer data to the rest of the world. Time needed to reach this town from international cities, and difficulty to bring materials to site are also important parameters.

(iii) Local support: active support to the project by local authorities is necessary, possibility to hire local staff for technical support is important and scientific support from close-by universities is welcome.

(iv) Environmental aspects: ground quality, vegetation or animals can affect array deployment, Wi-Fi data transmission and detector maintenance. Similarly weather and altitude have a strong impact on the working conditions

on site. These matter very much for a prospective experiment like GP300, which will require a lot of time working in the field.

(v) Topography: surrounding mountains allow better screening of background sources and improved reconstruction resolution [1].

(vi) Extension beyond GP300: the possibility to use the site of GP300 as a base for a further extension to the 10 000-antennas phase is an additional positive point.

Together with Charles Timmermans and Wu XiangPing, we then defined the process for site selection:

(i) Potential sites were first suggested by colleagues in China. As we will see in the next section, these proposals were often triggered by the presence of other scientific infrastructures.

(ii) Then a first selection is performed through a detailed study of the targeted areas using Google Maps. This allowed to discard sites in direct view of possible background sources (towns, villages, plants, etc) and also led to the discovery of other interesting candidate sites.

(iii) The following step consists in organizing a survey to evaluate the radio environment on site. This is a task not to be underestimated: radio environment site qualification are usually performed in the frequency domain, while for self triggering the time domain matters most. Besides, TREND showed that environment noise fluctuates significantly in time (see Fig. 5.26 for an illustration). Ideally, one would therefore like to make a survey measurement over periods of times of several weeks, in the exact same frequency range as the one defined for the experiment and using the same acquisition system. This is impossible in practice: such duration are not realistic and the GP300 acquisition system did not exist at the time the survey was performed. We therefore converged to a protocol where measurements are performed with a GRANDProto35 antenna connected to a digital oscilloscope through a 50-200 MHz filter, measuring the trigger rate for different threshold values. A spectrum analyzer is also used to evaluate the environment quality in the frequency domain. As possible FM emitters or constant-wave emitters could affect this measurement, it was associated with acquisition from an AERA Front-End unit.This setup allows for a reproducible and quantitative measurement in the 30-80 MHz frequency band usually free from constant wave emitters, which however overlaps with the GP300 frequency domain only in a limited range. The survey protocol consists in series of 10 to 20 measurements at various locations and different times within the targeted area, thus providing a reliable picture of the site's radio environment.

(iv) Once a possible deployment site is precisely identified, contact is made with local authorities to discuss legal and logistics aspects. Two critical points to be granted by authorities are access to site by GRAND collaborators, and a stable remote access to the GP300 DAQ and data.

(v) Eventually a temporary setup has to be installed on selected sites to monitor long term variations of the radio environment before the site is finally validated.

7.4.2 Survey results

The selection procedure was carried out by Charles Timmermans and myself, with excellent support by Feng Yang, who drove us around China, and help from Gu Junhua and Wang LiFei, technician at the Ulastai Observatory. Zhai NanNan and Shen DongXiang, students at the Urumqi University also participated in some of these campaigns. Five distinct survey campaigns (see Fig. 7.6) were carried out between August 2017 and December 2018, totaling more than 120 measurements. The results are summarized in Table 7.2.

Two sites were found to comply with all criteria defined in the previous section: the so-called *"Zone 2"* in Gansu, and LengHu in QingHai. LengHu was eventually selected in March 2019 as the priority candidate site, because of its larger potential for extension, excellent support of local authorities (see more details in section 7.4.3.2) and the large distance of Zone 2 to the closest city.

Figure 7.6: *Left: map of the sites surveyed for GP300. Right: reception organized in LengHu by the county official for a GRAND meeting in April 2019. In the middle of the picture stands the Governor of the HaiXi State, the administrative division which LengHu county belongs to.*

Besides this positive conclusion, the survey procedure taught us a lot on various aspects. First, for most sites surveyed (6 out of 8), environment conditions were considered compatible with GP300 requests (see Fig. 7.7 for an illustration). Besides, while scanning through satellite views of Western China, and driving through Gansu, QingHai and XinJiang, it clearly appeared that vast portions of land are probably valid for the deployment of autonomous radio arrays in these remote, void areas. This is an encouraging observation in the perspective of the GRAND full array. Then as we had anticipated, support of local authorities is in many cases excellent in Gansu and QingHai. These rural and remote communities see the possibility to host a project like GP300 —and beyond that, a GRAND HotSpot— as an excellent opportunity to develop local activities and enhance their visibility. However, plans for industrial development (oil, wind-mill farms, solar plants), military or administrative restrictions to land access (nature-protected areas in particular) turned out to be a major obstacle for site selection. In Gansu, such limitations forbid the access to Zone 1 and significantly restricted the allowed area for GP300 in Zone 2.This shows that it would be more efficient to first contact local authorities and agree on possible sites before performing surveys, contrary to the protocol defined. Even if the possibility to set up a world-leading experiment may allow to build a political support strong enough to use up such administrative restrictions, this is a point not to be underestimated in the perspective of GRAND.

7.4.3 The LengHu site

LengHu was selected by the GRAND collaboration as the priority candidate site for GP300 in March 2019. Besides the site's excellent radio environment and a ground topography favorable for deployment (see Fig. 7.8), the very strong support of the local authorities to the GP300 project explains why LengHu was selected. This support is part of LengHu city's ambition to host a scientific observatory, as shows the on-going construction of an optical telescope on a close-by mountain, in collaboration with astronomers from NAOC.

This support promptly materialized under the form of a caravan —in practice a former mobile police station— installed on the LengHu site to become the so-called Field-Termination Point (FTP), where the DAQ PC is installed (see Fig. 7.8). This was a necessary element for the long-term measurement, the following step in the selection protocol, which we chose to start in parallel to the discussions with the local authorities.

Inner Mongolia, August 23 - 28, 2017

Site	Radio	Infrastructures	Support	Environment	Topography	Extension
Mingantu heliograph [251] (42.2°N, 115.3°E, alt ∼ 1300 m)	C: very noisy spectrum. Transient rate $6-10\times R_0$ *	A: benefits from heliograph infrastructures	Not evaluated	A	B: gentle slopes but no mountains	A

Yunnan, December 19 - 21, 2017

Site	Radio	Infrastructures	Support	Environment	Topography	Extension
AiLao National Reserve (24.5°N, 101.0°E, alt ∼ 2000 m)	B: some FM emission. Transient rate $2-3\times R_0$ *	A: benefits from AiLao weather station infrastructures	Not evaluated, but strong support from Yunnan Observatory	C: vegetation and monkeys	A: strong slope + surrounding mountains	C

XinJiang, March 30 - April 3, 2018

Site	Radio	Infrastructures	Support	Environment	Topography	Extension
YiWu valley (43.5°N, 93.9°E, alt ∼ 2600 m)	B: some FM emission. Transient rate $3-4\times R_0$	Not evaluated	C: local authorities reluctant to host GP300	B: mountain weather conditions	A: gentle slope + surrounding mountains	Not evaluated
TianLai experiment [252] (44.1°N, 91.8°E, alt ∼ 1600 m)	B: some FM emission. Transient rate $3-4\times R_0$	A: benefits from the TianLai infrastructures	Not evaluated	B: data transmission impacted by small hills	B: no large denivelation, no mountain	Not evaluated

Gansu, August 29 - September 3, 2018

Site	Radio	Infrastructures	Support	Environment	Topography	Extension
Zone 1 (39.3°N, 93.5°E, alt ∼ 2000 m)	A: clean spectrum. Transient rate $\sim 2\times R_0$	B: 2 h to Akesai city	C: oil extraction development plans forbid deployment	B: bumpy terrain + ditches	A: gentle slope + surrounding mountains	A
Zone 2 (38.3°N, 94.3°E, alt ∼ 3200 m)	A: clean spectrum. Transient rate $\sim 2\times R_0$	C: 3 h to Akesai city	A: Very strong	B: flat ground but mountain + desert weather conditions. Camels	A: gentle slope + surrounding mountains	C
Zone 3 (39.5°N, 95.1°E, alt ∼ 1800 m)	C: strong FM emission	A: 1 h to Subei city	Not evaluated	B: bumpy terrain, ditches	A: gentle slope + surrounding mountains	A

QingHai, December 1 - 4, 2018

Site	Radio	Infrastructures	Support	Environment	Topography	Extension
LengHu (38.5°N, 93.3°E, alt ∼ 2800 m)	A: clean spectrum. Transient rate $\sim 2\times R_0$	B: 2 h to LengHu city	A: Very strong. However no neighboring university	B: flat and easy ground conditions but harsh mountain + desert weather conditions	A: gentle slope + surrounding mountains	A

Table 7.2: *Results of GP300 site survey. For each site, criteria defined in section 7.4.1 are ranked A (excellent), B (average) and C (bad). Criteria in red discard associated sites. Transient trigger rates were measured with the AERA electronics (see text), and expressed with respect to R_0, the trigger rate measured at the Ulastai site. *: results of the Inner Mongolia and Yunnan campaigns are possibly affected by self-induced noise caused by an AC/DC converter used during the measurements. After this problem was identified, measurements were performed using passive power supplies.*

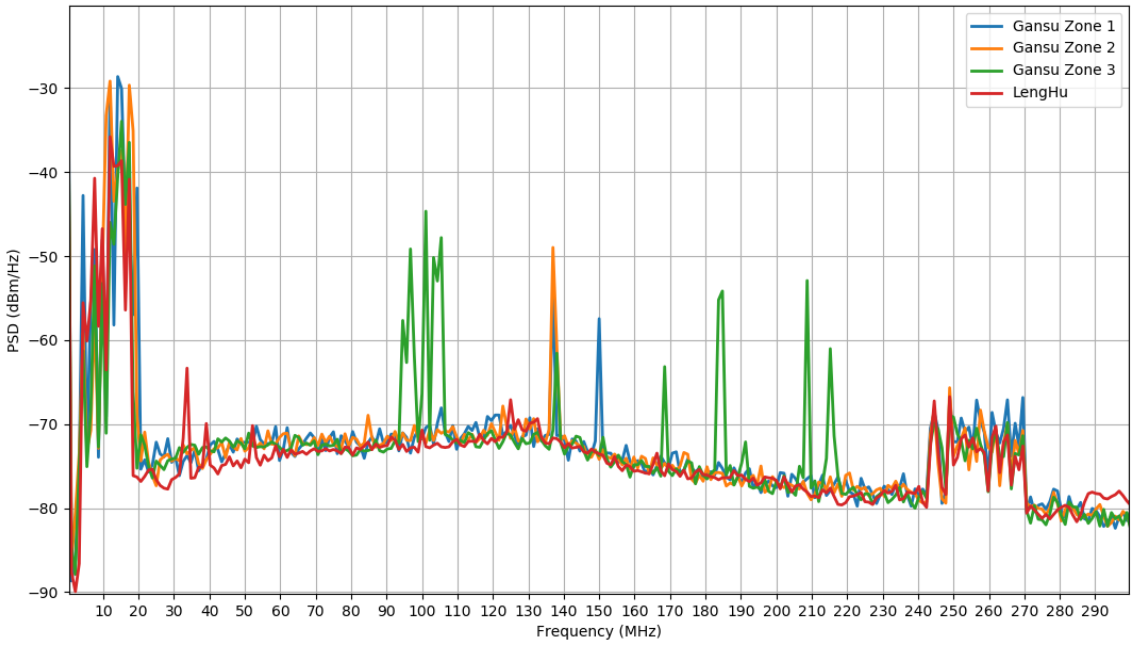

Figure 7.7: *Noise background measured at sites from the Gansu and QingHai campaigns with a GP35 antenna. On all sites, an emitter is visible at a narrow band around 137 MHz, a frequency used for satellite communication, as well as in the 240-270 MHz frequency range [250]. For Gansu Zone 3 additionally, strong FM emission is observed in the 90-107 MHz band, and CW emitters are detected at higher frequencies as well.*

7.4.3.1 Long-term measurement

The long term measurement was set up in August 2019, under the lead of Charles Timmermans, with participation of Feng Yang, Wang LiFei and myself.

Three GP300 antennas were deployed on site, forming a triangle of side 200 m at a distance of ∼2 km from the FTP. GP35 poles of 1.5 m height were used, as the mechanical structure of the GP300 unit was not ready by then (see Fig. 7.8). These three units were equipped with AERA Front-End units, with a modified analog stage: the filters frequency range was changed from 30-80 MHz to 50-200 MHz, and following a logic similar to GP35 (see section 6.2.3), power detectors were inserted behind them in order to match the 200 MHz ADC sampling frequency of the AERA units. As frequency information with power detectors, a fourth unit was installed in the center of the triangle and plugged into a spectrum analyzer.

All four units were equipped with Bullet antennas (see section 7.2.3.1), which could transfer the antenna data through WiFi to a Rocket receiver installed atop the FTP (see Fig 7.8).

The system could be successfully put in operation after a few days of work. However it appeared that measurements were strongly affected by noise emission from the charge controllers used to adjust the battery charging from the solar panels output. Data could not be exploited, but at least the setup could run for several days, thus validating the setup.

Figure 7.8: *Left: Charles Timmermans walking towards one of the stations deployed for the long term measurement. A second unit can be seen behind him, and the black dot further right is the FTP. The noisy charge controller is the small metallic box lying on the ground, connected to the battery and the solar panel. Right: setting up the Rocket antenna atop the Field Termination Point.*

7.4.3.2 Current situation

A trip to site was scheduled for January 2020 to replace the charge controller with quiet ones and deploy the prototype GP300 stations. However, once we reached DunHuang, the closest airport to LengHu, we learned that Charles and I were not allowed to access the site, because the permit required by foreigners to access LengHu county had not been delivered by the local military administration. The situation is now —supposedly— cleared, but then the Covid situation prevented any travel to site for the following year. Deployment of a first set of 100 units is now scheduled for summer 2021, pending an agreement can be signed with teh authorities concerning site access, logistics and absence of industrial deployments in a 20 km range around the detector.

7.5 Prospects: the path towards the GRAND instrument

The GRANDProto300 detector is primarily designed to fulfill the objectives defined in section 7.1. It is however hardly scalable to the 10 000 units of GRAND10k, not to mention GRAND200k. In particular, the Wi-Fi technology selected to comply with the trigger rates expected for GP300 —nominal values of 1 kHz for T1 and 10 Hz for T2— calls for 150 W solar panels (see section 7.2.3) to power the detection units. Their 1 m^2 surface represent a significant mechanical challenge to guarantee 100% working efficiency for long-term usage under windy conditions. The associated high-capacity batteries also impose a large maintenance burden. Second, the WiFi signal range does not extend much beyond 10 km in the rugged terrains optimal for neutrino detection [164]. These issues significantly impede the scalability of such a design. Atop of that, the price of Wi-Fi communication elements, solar panels and batteries affect the cost of GP300 detection units which reaches ∼4500€. Even if economies of scale will lower the unit price for GRAND200k, the 1000€ target price tag for a GRAND200k unit seems out of reach with the GP300 design.

Achieving a pure and efficient detection of air showers over a giant array (i.e. on the scale of several thousand km^2) at a reasonable cost thus remains a challenge to be addressed before considering building GRAND10k. Concrete work in this direction was initiated recently through a proposal called NUTRIG, which aims at building a data acquisition scheme applicable to a giant array. This proposal, jointly written with Tim Huege and Markus Roth from the Karlsruhe Institute of Technology, and Kumiko Kotera, was submitted to the joint call of the French *Agence Nationale de la*

Recherche and the German *Deutsche Forschungs Gemeinschaft* in April 2021. The general concept of the proposal is presented in the following section, mostly using text extracted from the proposal itself. A second step, presented in section 7.5.2, will consist at defining the hardware layer allowing to implement the DAQ defined with NUTRIG at the scale of GRAND10k.

7.5.1 The NUTRIG proposal

The NUTRIG proposal is summarized in figure 7.9. It aims at using the distinct signatures of background and EAS signals previously identified in the frame of TREND (see section 5.7) and AERA [248, 249] in order to significantly improve the trigger performances of GP300.

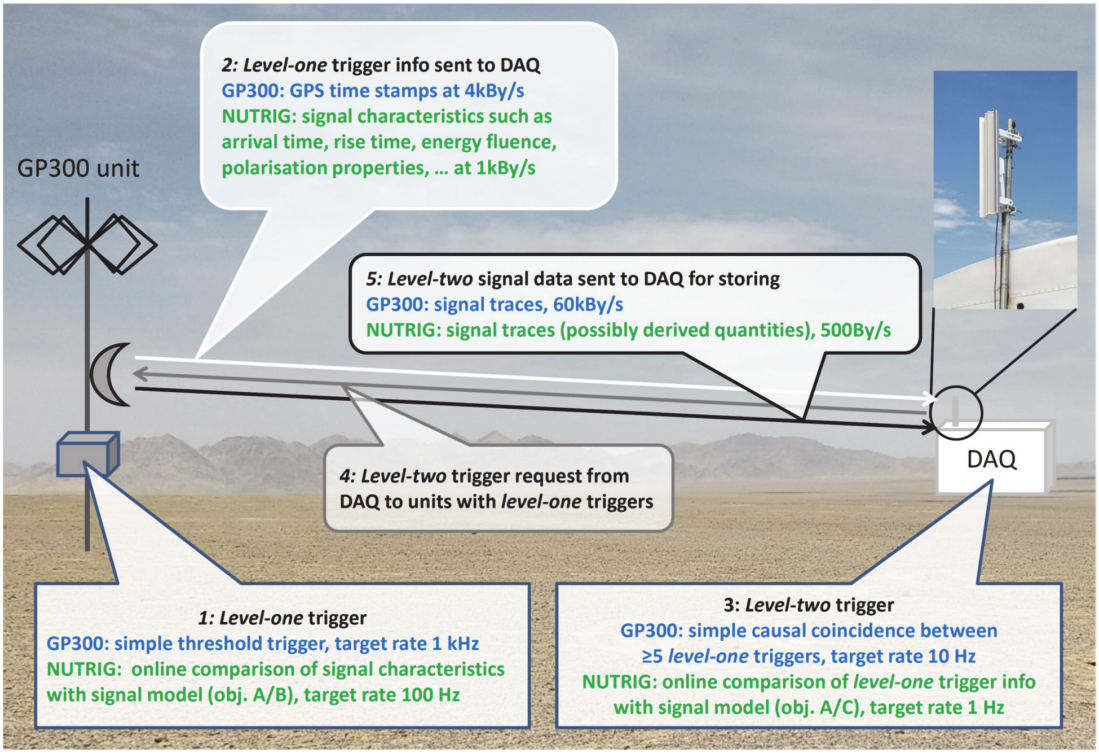

Figure 7.9: *Principle of trigger and data collection for GP300 and NUTRIG. Significant reduction of data rates will be achieved by exploiting advanced signal characteristics for the T1 and T2 trigger decisions, thereby facilitating high purity and efficiency. Objectives A, B, C refer respectively to the developments of a detailed signal model for GP300 data, T1 and T2 triggers. Taken from the NUTRIG proposal submitted to DFG-ANR.*

At the antenna level, various methods will be investigated to identify air shower pulses in the data: fit of template signals from a database of simulated air-shower pulses —a method successfully used in the Antarctica-based ARIANNA experiment [253]—, optimal filtering, matrix decomposition [254], wavelet analysis [255] or methods based on machine-learning, following here the work initiated at IAP on this topic [256]. All of these take advantage of the fact that EAS radio features are very well known and modeled (see section 2.3) while the background noise can be monitored on a continuous basis, a situation providing a powerful lever arm for signal identification. These methods will be implemented at the level of the FPGA or the embarked CPU in order to perform an on-the-fly treatment. We believe this could increase the signal purity by a factor 10 compared to the initial GP300 stage, while trigger performances for transient signals of low amplitudes could also be improved with these methods. This perspective is particularly appealing for neutrino detection, where a lower threshold would significantly increase the chance for large statistics, as most models predict that the flux falls steeply with increasing energy. Improved sensitivities around 10^{16} eV may even allow to bridge the gap with the IceCube[73] and KM3NeT [257] experiments, thus fostering interesting synergies with these two experiments.

While in the initial stage of GP300 the second level trigger is based on time coincidences between detection units (see section7.2.3.1), it is expected that a richer information transmitted from units with T1 triggers to the DAQ will allow to exploit the very unique signal characteristics imprinted by the superposition of the geomagnetic and charge-excess emission, the Cerenkov-like time compression (see Fig. 2.9) and the polarization pattern (see Fig. 4.6). In contrast, thermal emission or anthropogenic radio-frequency interference will exhibit very different signal characteristics and should thus be well-discernible. We therefore expect that a sophisticated T2 will bring the rate of recorded events down to 1 Hz on the GP300 layout thanks to a very high purity of the selected sample.

An important axis of work will consist of defining the actual information transferred to the DAQ by the units both for both trigger stages. An optimization trading off between a wealth of information being transmitted on every trigger on the one hand and the use of communication bandwidth on the other hand will be necessary, as the latter will be a key requirement for a later up-scaling. It should be noted in the particular case of T2 that all EAS radio detection experiments so far have recorded the full time traces of triggered detection units (i.e. a few microseconds of waveform data around the trigger time), which corresponds to event sizes of several kBytes typically. This will also be the case in the initial GP300 stage, but we will investigate whether recording reduced information only (e.g. envelope of the signal, standard-deviation of the noise at the trigger time, parametrization of the frequency spectrum) would still allow us to perform a precise offline reconstruction of the EAS. We estimate this work could bring the event size down to 500 Bytes, while the T1 information could amount to 10 bytes. The typical data rate would then be 10 By $\times$ 100 Hz = 1 kBy/s/triggered unit for T1, and 500By $\times$ 1 Hz = 500 By/s/triggered unit for T2, a gain of $\sim$50 compared to the initial GP300 phase.

The GP300 detector will be extensively used to test NUTRIG. Developments will indeed concern software mainly, and these will be uploaded to the detection units front-end FPGA and CPU for T1, and to the experiment's DAQ system for T2. It is not the purpose of the NUTRIG project to study the hardware layer of data transfer, which will be studied in a following step.

7.5.2 Further stages

Once the first NUTRIG results are available —hopefully in 2023—, it will become possible to define precisely the specifications and the strategy for the trigger and data transfer of GRAND10k, and determine which technology can be used to implement them. It is very difficult —and probably useless— to say more on this topic at the present stage, but we may note that the rapid progress in the field of communications in the last decade open exciting perspectives. The rise of the Internet of Things could be directly instrumental to GRAND, while systems such as wireless smart mesh networks [258] may be considered for data transfer. These cheap systems, with low power consumption, offer an elegant, robust and scalable solution for data transfer through data-hopping from one unit to the other down to central DAQ collectors.

Similarly, the design of GRAND10k detection units will be informed by GP300 around the same date, with further optimization of power consumption and mechanical design. Once GRAND10k has been built at a target date around 2026-7, the focus will shift to building the GRAND200k array, a tremendous task given the project size. I believe that the appropriate response to this challenge lies in the size of the project itself: the scale of the project forces us to adopt an industrial approach when building GRAND200k. This will probably mean freezing the detector design, and duplicate to the other hotspots forming the full GRAND200k instrument through mass production. For the electronics, developing a fully integrated application-specific integrated circuit (ASIC) board —an expensive solution when building only a few thousand boards— is likely the cheapest solution to build 200 000 units, while providing reduced power consumption a factor of 10 is typical— and increased reliability. For communication hardware and software infracstructure, solutions inspired by mobile network companies will be investigated. A precise and standardized procedure will have to be defined for detector transportation and installation, and factors linked to detector aging have to be carefully identified. For this purpose, the expertise acquired during previous construction stages will be crucial.

Conclusion

After a general introduction on the science case for ultra-high energy cosmic particles and the principle of their detection by antenna arrays in chapters 1 and 2, I presented in chapter 3 of this document the computation of the sensitivity of the GRAND array to UHE cosmic neutrinos. I first showed how a preliminary study I led up to 2015 initiated the GRAND proposal and triggered a more robust end-to-end simulation chain for this study. I then detailed my contributions to this work, focusing in particular on Radio Morphing, a semi-analytical tool which allows computing in a fraction of a second the electromagnetic emission by showers of particles initiated in the atmosphere by primary cosmic particles, while this calculation requires hours for standard Monte-Carlo programs. Radio Morphing thus became a key element for the simulation of neutrino-induced showers in GRAND. I also presented two distinct methods for the computation of antenna response to these transient electromagnetic signals and detailed how the ground topography plays a significant role in the detection of the very inclined showers induced by neutrinos. I finally derived in this chapter the sensitivity limit of the GRAND detector, which led to the conclusion that gigantic areas of $\mathcal{O}(200\,000)\,\mathrm{km}^2$ are required to reach the sensitivity allowing for the detection of neutrinos above $10^{17}\,\mathrm{eV}$, the goal of the GRAND project.

In chapter 4, I presented the study —carried out with Valentin Decoene and Simon Chiche, PhD students I supervize(d)— of radio signals induced by inclined air showers in the GRAND detector. I detailed in particular how simulations indicate that the specific features of very inclined showers should allow to reach an angular resolution as good as $0.1°$, thus opening the possibility for UHE neutrino astronomy in GRAND. I also explained how the polarization pattern of these inclined signal may for their part allow for a very effective identification of air showers over other types of radio transients through a method applicable online at the antenna level.

Identification of air showers from their radio signals is a key topic for autonomous radio arrays such as GRAND. I devote the second part of this document to the description of my work on this issue. I detailed in chapter 5 the TREND experiment, which I carried out in a remote valley of the Tianshan mountains with a few colleagues from France and China between 2009 and 2013. TREND was an autonomous array with distinct stages of 6, 15 and finally 50 mono-polar antennas. I presented the setup in details, and showed that despite its technical limitations, TREND successfully detected air showers from their sole radio emission, with a 10% efficiency due to hardware and a 32% efficiency for air shower selection. This discrimination is based on the distinct features of radio signals induced by air showers and background.

I presented in chapter 6 the GRANDProto35 project, designed as an upgrade of TREND aiming at an improved detection efficiency of cosmic rays. After detailing the successful validation steps of the GRANDProto35 detector, I explained how the dreadful situation in the XinJiang province prevented the start of the experiment.

I finally presented in chapter 7 the design and construction of the GRANDproto300 experiment, which should be very soon deployed in a desert area of Western China. I explained how this pathfinder of the GRAND experiment is expected to demonstrate the GRAND radio-detection principle of inclined showers, while being at the same time an appealing tool for the study of physics of cosmic particles in the $10^{16.5}$-$10^{18}\,\mathrm{eV}$ energy range.

As I come to the conclusion of this document, I think back to the amount of work and effort produced during these twelve years, the unique moments shared with my colleagues in these remote and beautiful areas of China and the vivid emotions experienced with them during the various steps of building the GRAND project. I realize we came a long way, but I am also fully aware that the path to achieve the detection of UHE neutrinos with GRAND is still very long and hazardous. Yet I always keep in mind that at the time I started my PhD in 1999, I heard at various occasions researchers making fun of colleagues fighting in the Virgo collaboration against sea tides, vibrations from distant highways or from growing tree roots, and other unexpected sources of noise degrading the performances of their detector, then orders of magnitude above the sensitivity needed for the detection of gravitational waves. We know how this ended, 20 years later. I am not saying that GRAND will be as successful as the Ligo or Virgo experiments (yet I

would not complain!), but I am extremely eager at giving it a shot, motivated by the success of our experimental work and the positive prospects of our simulation studies. I truly believe the GRAND effort is in line with the very essence of fundamental (experimental) research, which, in my opinion, consists —after a careful analysis of the scientific and experimental case, followed by the definition of the appropriate tools and plan to solve it— in facing such imposing experimental challenges in order to address fundamental questions in Science.

Appendix A

Summary of TREND data taking

Data compiled from /sps/hep/TREND/readSummaryProd.py

Period	RunInf	RunSup	Tot runs	DateInf	DateSup	DST duration (days)	NT0s	Nb timetraces	NT1s	Ncoincs dst	Nb cands	Cand rate (day-1)	Observations
1	2538	2585	44	13/01/2011	18/03/2011	22,86	7,10E+09	4,30E+08	2,90E+07	4,00E+06	43	1,8810149	No calibration data
2	2685	2890	76	31/03/2011	22/06/2011	40,4	1,50E+10	2,10E+09	4,81E+07	1,50E+06	93	2,3019802	
3	3000	3086	62	06/08/2011	10/10/2011	44,06	2,30E+10	1,90E+09	8,21E+07	3,20E+06	87	1,9745801	Upgraded DAQ
4	3157	3256	58	03/11/2011	09/01/2012	49,6	9,00E+09	1,00E+09	9,17E+07	8,20E+06	44	0,8870968	
5	3336	3371	31	13/01/2012	11/02/2012	23,19	1,70E+10	7,80E+08	8,30E+07	5,40E+06	54	2,3285899	Upgraded optical system
6	3562	3733	78	23/02/2012	19/06/2012	79,24	6,90E+09	9,00E+08	1,25E+08	5,20E+06	201	2,5365977	Upgraded DAQ
7	3835	3999	98	26/06/2012	09/10/2012	26,25	4,20E+09	8,80E+08	9,33E+07	3,60E+06	20	0,7619048	
8	4183	4389	139	18/10/2012	06/12/2012	28,73	3,80E+09	1,70E+09	1,77E+08	1,00E+07	22	0,7657501	
Total EW						**314,33**	8,6E+10	9690000000	7,30E+08	4,11E+07	564	**1,7942926**	
Mean rate (s-1)						27158112	63,3328267	7,13598942	**2,69E+01**	1,51E+00			
9	4444	5014	360	11/12/2012	21/04/2013	58,43	7,80E+09	1,60E+09	2,09E+08	6,00E+06	5	0,0855725	Antennas rotated to NS
10	5070	5913	305	24/04/2013	10/01/2014	62,2	1,80E+09	2,50E+09	2,79E+08	4,78E+06	20	0,3215434	
Total NS						**120,63**	9600000000	4,10E+09	4,87E+08	1,08E+07	25	**0,2072453**	
Mean rate (s-1)						10422432	18,421804	7,86764548	**4,68E+01**	1,03E+00		0	
Total all						3,76E+07			1,22E+09	5,19E+07			
Mean rate (s-1)									3,24E+01				

Figure A.1: *Summary of TREND data.*

Appendix B

EAS candidate

Below is displayed event 38605 from R3633, recorded by the TREND50 array on April 16, 2012. This is one of the selected EAS candidate.

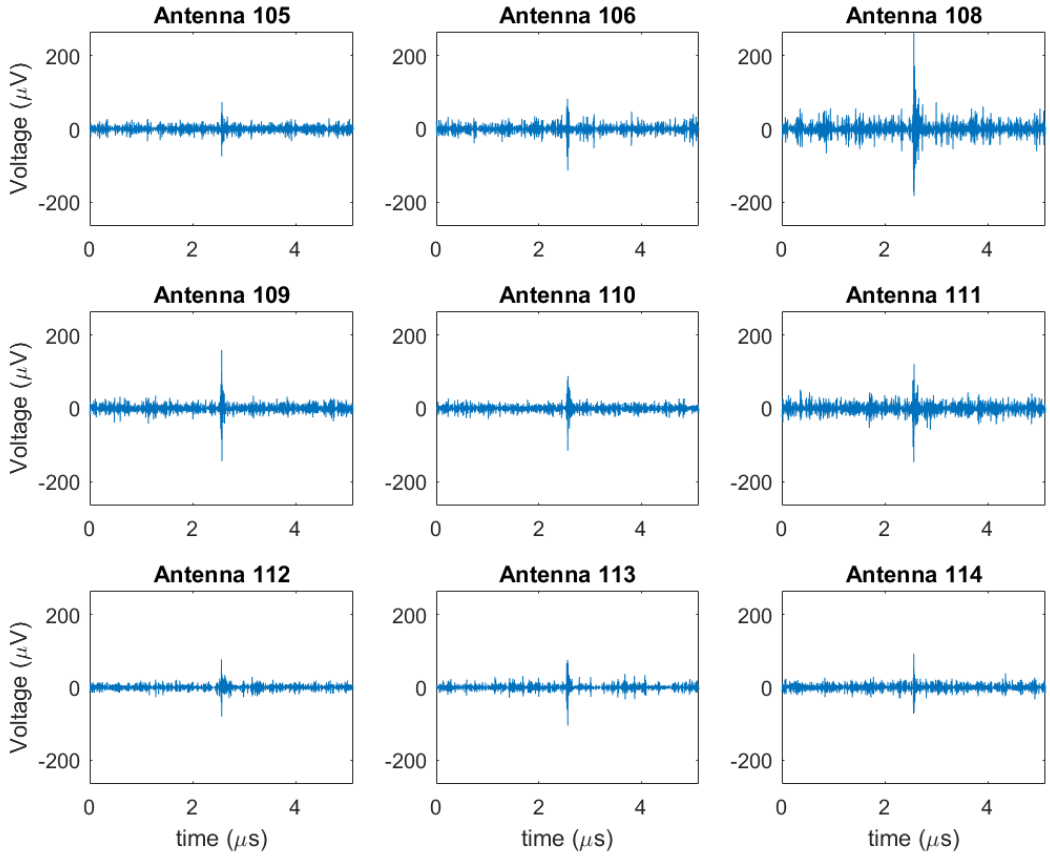

Figure B.1: *Timetraces of the detection units participating in the event 38605 from R3633. Taken from [206].*

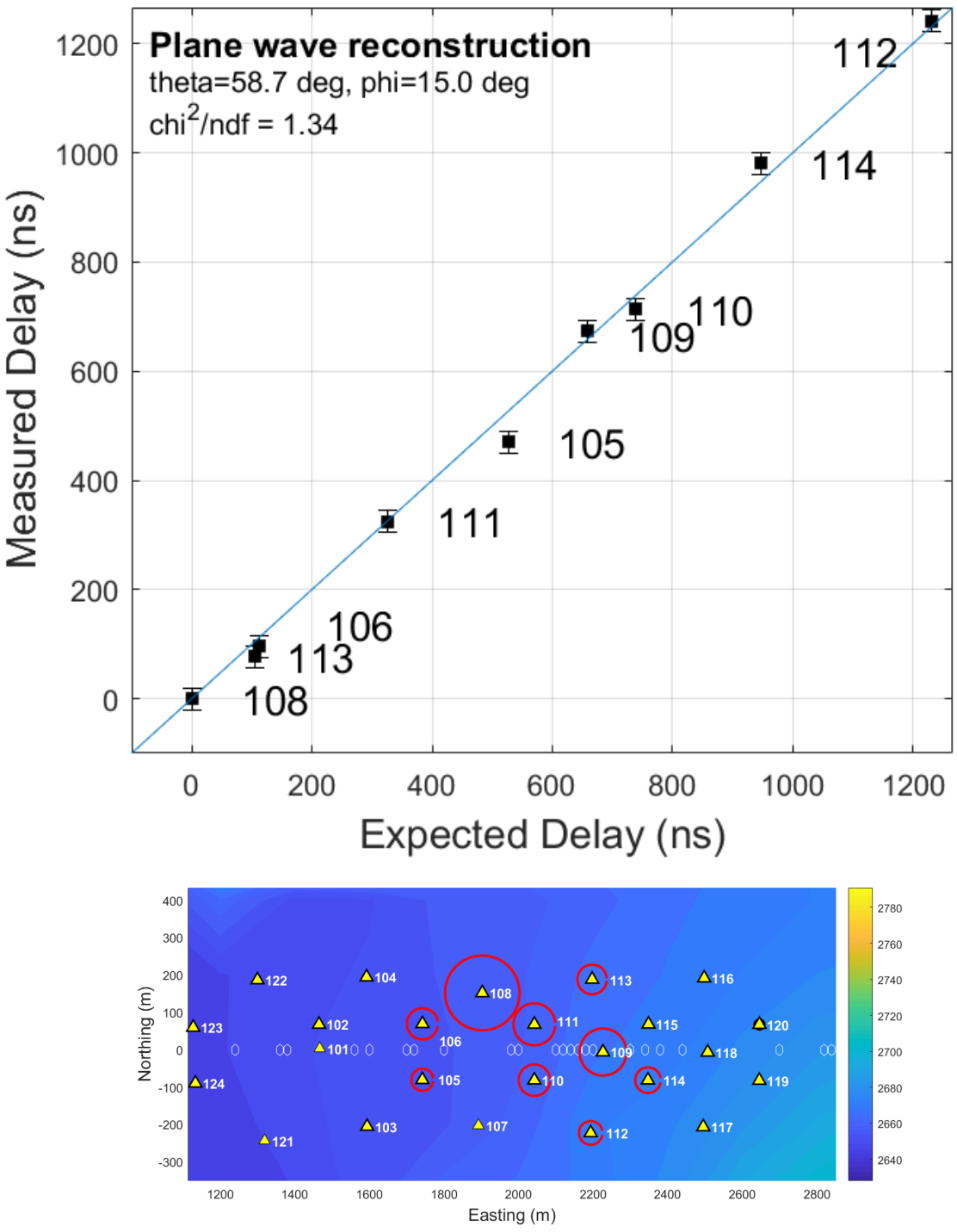

Figure B.2: *Top: experimental values of the trigger times for the detection units participating in the event 38605 from R3633 as a function of the values reconstructed for a plane wave with zenith and azimuth angles $\theta = 58.7°$ and $\phi = 15.0°$ respectively. Here the instant of trigger of detection unit 108 is taken as the time reference. Bottom: amplitude pattern of the same event. The radius of the circles are proportionnal to the maximum amplitude of the transient signal on the corresponding detection unit. Taken from [206].*

Bibliography

[1] J. Álvarez-Muñiz *et al.* (GRAND), Sci. China Phys. Mech. Astron. **63**, 219501 (2020), arXiv:1810.09994 [astro-ph.HE] .

[2] O. Martineau-Huynh, D. Allard, E. Parizot, V. Van Elewyck, J. Bolmont, J.-P. Lenain, K. Kotera, and V. Niess, "Observing the ultra-high energy universe with grand, contribution to gt04, prospectives 2020 in2p3," (2019).

[3] O. Martineau-Huynh, V. Van Elewyck, J. Bolmont, J.-P. Lenain, and V. Niess, "Neutrino physics with grand, contribution to gt06, prospectives 2020 in2p3," (2019).

[4] D. J. Bird, S. C. Corbato, H. Y. Dai, B. R. Dawson, J. W. Elbert, B. L. Emerson, K. D. Green, M. A. Huang, D. B. Kieda, M. Luo, S. Ko, C. G. Larsen, E. C. Loh, M. H. Salamon, J. D. Smith, P. Sokolsky, P. Sommers, J. K. K. Tang, and S. B. Thomas, App. Journal of Physics **424**, 491 (1994).

[5] P. Auger, P. Ehrenfest, R. Maze, J. Daudin, and R. A. Fréon, Rev. Mod. Phys. **11**, 288 (1939).

[6] J. Linsley, Phys. Rev. Lett. **10**, 146 (1963).

[7] M. Takeda *et al.*, Phys. Rev. Lett. **81**, 1163 (1998).

[8] M. Nagano and A. A. Watson, Rev. Mod. Phys. **72**, 689 (2000).

[9] R. Abbasi *et al.* (HiRes), Phys. Rev. Lett. **92**, 151101 (2004), arXiv:astro-ph/0208243 .

[10] M. Takeda *et al.*, Astropart. Phys. **19**, 447 (2003), arXiv:astro-ph/0209422 .

[11] O. Deligny (Pierre Auger, Telescope Array), PoS **ICRC2019**, 234 (2020), arXiv:2001.08811 [astro-ph.HE] .

[12] P. Homola, arXiv e-prints , arXiv:1804.05613 (2018), arXiv:1804.05613 [astro-ph.IM] .

[13] A. Aab *et al.* (Pierre Auger), JCAP **10**, 022 (2019), arXiv:1906.07422 [astro-ph.HE] .

[14] A. Aab *et al.* (Pierre Auger), Science **357**, 1266 (2017), arXiv:1709.07321 [astro-ph.HE] .

[15] A. Aab *et al.* (Pierre Auger), (2018), arXiv:1801.06160 [astro-ph.HE] .

[16] A. Aab *et al.* (Pierre Auger, Telescope Array) (2018) arXiv:1801.01018 [astro-ph.HE] .

[17] A. Yushkov *et al.*, "Report of the auger-ta working group on the composition of uhecrs, presentation at uhecr 2018." (2018).

[18] R. U. Abbasi, M. Abe, T. Abu-Zayyad, M. Allen, R. Azuma, E. Barcikowski, J. W. Belz, D. R. Bergman, S. A. Blake, R. Cady, and et al., The Astrophysical Journal **865**, 74 (2018).

[19] T. Bergmann, R. Engel, D. Heck, N. Kalmykov, S. Ostapchenko, T. Pierog, T. Thouw, and K. Werner, Astroparticle Physics **26**, 420 (2007).

[20] R. Alves Batista *et al.*, Front. Astron. Space Sci. **6**, 23 (2019), arXiv:1903.06714 [astro-ph.HE] .

[21] A. Aab *et al.* (Pierre Auger), Phys. Rev. D **96**, 122003 (2017), arXiv:1710.07249 [astro-ph.HE] .

[22] A. Castellina (Pierre Auger), EPJ Web Conf. **210**, 06002 (2019), arXiv:1905.04472 [astro-ph.HE] .

[23] N. R. Council, *Connecting Quarks with the Cosmos: Eleven Science Questions for the New Century* (The National Academies Press, Washington, DC, 2003).

[24] E. Kido, EPJ Web of Conferences **210**, 06001 (2019).

[25] B. Abbott *et al.* (LIGO Scientific, Virgo, Fermi-GBM, INTEGRAL), Astrophys. J. Lett. **848**, L13 (2017), arXiv:1710.05834 [astro-ph.HE] .

[26] S. S. Kimura, K. Murase, P. Meszaros, and K. Kiuchi, Astrophys. J. Lett. **848**, L4 (2017), arXiv:1708.07075 [astro-ph.HE] .

[27] K. Fang and B. D. Metzger, Astrophys. J. **849**, 153 (2017), arXiv:1707.04263 [astro-ph.HE] .

[28] A. Albert *et al.* (ANTARES, IceCube, Pierre Auger, LIGO Scientific, Virgo), Astrophys. J. Lett. **850**, L35 (2017), arXiv:1710.05839 [astro-ph.HE] .

[29] A. Bykov, N. Gehrels, H. Krawczynski, M. Lemoine, G. Pelletier, and M. Pohl, Space Science Reviews **173**, 309 (2012), arXiv:1205.2208 [astro-ph.HE] .

[30] M. L. Ahnen *et al.* (MAGIC), Mon. Not. Roy. Astron. Soc. **472**, 2956 (2017), [Erratum: Mon.Not.Roy.Astron.Soc. 476, 2874–2875 (2018)], arXiv:1707.01583 [astro-ph.HE] .

[31] J. Devin, F. Acero, J. Ballet, and J. Schmid, A&A **617**, A5 (2018), arXiv:1805.11168 [astro-ph.HE] .

[32] M. Aartsen *et al.* (IceCube), Science **342**, 1242856 (2013), arXiv:1311.5238 [astro-ph.HE] .

[33] B. P. Abbott, LIGO Scientific Collaboration, and Virgo Collaboration, Phys. Rev. Lett. **116**, 061102 (2016), arXiv:1602.03837 [gr-qc] .

[34] B. P. Abbott and others. (LIGO Scientific Collaboration and Virgo Collaboration), Phys. Rev. Lett. **119**, 161101 (2017).

[35] B. D. Metzger, Living Rev. Rel. **23**, 1 (2020), arXiv:1910.01617 [astro-ph.HE] .

[36] S. J. Smartt *et al.*, Nature **551**, 75 (2017), arXiv:1710.05841 [astro-ph.HE] .

[37] B. P. Abbott *et al.* (LIGO Scientific, Virgo, 1M2H, Dark Energy Camera GW-E, DES, DLT40, Las Cumbres Observatory, VINROUGE, MASTER), Nature **551**, 85 (2017), arXiv:1710.05835 [astro-ph.CO] .

[38] M. Ackermann *et al.* (Fermi-LAT), Astrophys. J. **799**, 86 (2015), arXiv:1410.3696 [astro-ph.HE] .

[39] M. Ackermann *et al.* (Fermi-LAT), Phys. Rev. Lett. **116**, 151105 (2016), arXiv:1511.00693 [astro-ph.CO] .

[40] M. G. Aartsen *et al.* (IceCube), (2017), arXiv:1710.01191 [astro-ph.HE] .

[41] M. G. Aartsen *et al.* (IceCube), Astrophys. J. **833**, 3 (2016), arXiv:1607.08006 [astro-ph.HE] .

[42] W. D. Apel *et al.*, Astropart. Phys. **47**, 54 (2013), arXiv:1306.6283 [astro-ph.HE] .

[43] *The Pierre Auger Observatory: Contributions to the 34th International Cosmic Ray Conference (ICRC 2015)* (2015) arXiv:1509.03732 [astro-ph.HE] .

[44] C. Jui (Telscope Array), in *34th International Cosmic Ray Conference (ICRC 2015) Den Haag, The Netehrlands, July 30-August 6, 2015* (2015).

[45] R. Alves Batista, R. M. de Almeida, B. Lago, and K. Kotera, (2018), arXiv:1806.10879 [astro-ph.HE] .

[46] D. Allard, Astroparticle Physics **39**, 33 (2012), arXiv:1111.3290 [astro-ph.HE] .

[47] K. Kotera, D. Allard, K. Murase, J. Aoi, Y. Dubois, T. Pierog, and S. Nagataki, Applied Journal of Physics **707**, 370 (2009), arXiv:0907.2433 [astro-ph.HE] .

[48] M. Bustamante, J. F. Beacom, and W. Winter, Phys. Rev. Lett. **115**, 161302 (2015), arXiv:1506.02645 [astro-ph.HE] .

[49] R. Alves Batista, A. Dundovic, M. Erdmann, K.-H. Kampert, D. Kuempel, G. Müller, G. Sigl, A. van Vliet, D. Walz, and T. Winchen, JCAP **1605**, 038 (2016), arXiv:1603.07142 [astro-ph.IM] .

[50] I. Valino (Pierre Auger), *Proceedings, 34th International Cosmic Ray Conference (ICRC 2015): The Hague, The Netherlands, July 30-August 6, 2015*, PoS **ICRC2015**, 271 (2016).

[51] A. Aab *et al.* (Pierre Auger), Phys. Rev. **D90**, 122005 (2014), arXiv:1409.4809 [astro-ph.HE] .

[52] A. M. Taylor, M. Ahlers, and D. Hooper, Phys. Rev. D **92**, 063011 (2015), arXiv:1505.06090 [astro-ph.HE] .

[53] J. Heinze, A. Fedynitch, D. Boncioli, and W. Winter, Astrophys. J. **873**, 88 (2019), arXiv:1901.03338 [astro-ph.HE] .

[54] K. Moller, P. B. Denton, and I. Tamborra, (2018), arXiv:1809.04866 [astro-ph.HE] .

[55] A. van Vliet, R. Alves Batista, and J. R. Horandel, PoS **ICRC2019**, 1025 (2020), arXiv:1909.01932 [astro-ph.HE] .

[56] K. Murase, (2015), arXiv:1511.01590 [astro-ph.HE] .

[57] K. Murase, Phys. Rev. D **76**, 123001 (2007), arXiv:0707.1140 [astro-ph] .

[58] K. Murase, S. Inoue, and S. Nagataki, Astrophys. J. **689**, L105 (2008), arXiv:0805.0104 [astro-ph] .

[59] K. Fang and K. Murase, (2017), arXiv:1704.00015 [astro-ph.HE] .

[60] K. Fang, K. Kotera, K. Murase, and A. V. Olinto, Physical Review D **90**, 103005 (2014), arXiv:1311.2044 [astro-ph.HE] .

[61] E. Waxman and J. N. Bahcall, Phys. Rev. **D59**, 023002 (1999), arXiv:hep-ph/9807282 .

[62] K. Mannheim, R. J. Protheroe, and J. P. Rachen, Phys. Rev. D **63**, 023003 (2001), arXiv:astro-ph/9812398 .

[63] J. N. Bahcall and E. Waxman, Phys. Rev. **D64**, 023002 (2001), hep-ph/9902383 .

[64] M. G. Aartsen *et al.* (IceCube), Astrophys. J. **809**, 98 (2015), arXiv:1507.03991 [astro-ph.HE] .

[65] M. Aartsen *et al.* (IceCube), Phys. Rev. D **98**, 062003 (2018), arXiv:1807.01820 [astro-ph.HE] .

[66] A. Aab *et al.* (Pierre Auger), Phys. Rev. D **91**, 092008 (2015), arXiv:1504.05397 [astro-ph.HE] .

[67] P. Gorham *et al.* (ANITA), Phys. Rev. D **98**, 022001 (2018), arXiv:1803.02719 [astro-ph.HE] .

[68] P. Allison *et al.* (ARA), Phys. Rev. D **102**, 043021 (2020), arXiv:1912.00987 [astro-ph.HE] .

[69] A. Anker *et al.*, JCAP **03**, 053 (2020), arXiv:1909.00840 [astro-ph.IM] .

[70] A. V. Olinto *et al.* (POEMMA), JCAP **06**, 007 (2021), arXiv:2012.07945 [astro-ph.IM] .

[71] J. Aguilar *et al.* (RNO-G), (2020), arXiv:2010.12279 [astro-ph.IM] .

[72] M. Aartsen *et al.* (IceCube Gen2), (2020), arXiv:2008.04323 [astro-ph.HE] .

[73] M. G. Aartsen *et al.* (IceCube), Phys. Rev. Lett. **117**, 241101 (2016), arXiv:1607.05886 [astro-ph.HE] .

[74] A. Aab *et al.* (Pierre Auger), Phys. Rev. D **102**, 062005 (2020), arXiv:2008.06486 [astro-ph.HE] .

[75] A. Aab *et al.* (Pierre Auger), Astrophys. J. **837**, L25 (2017), arXiv:1612.04155 [astro-ph.HE] .

[76] D. Fixsen, E. Dwek, J. C. Mather, C. Bennett, and R. Shafer, Astrophys. J. **508**, 123 (1998), arXiv:astro-ph/9803021 .

[77] M. G. Aartsen *et al.* (IceCube), Nature (2017), 10.1038/nature24459, arXiv:1711.08119 [hep-ex] .

[78] M. Bustamante and A. Connolly, (2017), arXiv:1711.11043 [astro-ph.HE] .

[79] D. Marfatia, D. W. McKay, and T. J. Weiler, Phys. Lett. B **748**, 113 (2015), arXiv:1502.06337 [hep-ph] .

[80] J. Stachurska (IceCube), in *36th International Cosmic Ray Conference (ICRC 2019) Madison, Wisconsin, USA, July 24-August 1, 2019* (2019) arXiv:1908.05506 [astro-ph.HE] .

[81] M. Ackermann *et al.*, Bull. Am. Astron. Soc. **51**, 215 (2019), arXiv:1903.04333 [astro-ph.HE] .

[82] K. Abe *et al.* (Super-Kamiokande), Phys. Rev. D **91**, 052003 (2015), arXiv:1410.4267 [hep-ex] .

[83] R. Abbasi *et al.* (IceCube), Phys. Rev. D **82**, 112003 (2010), arXiv:1010.4096 [astro-ph.HE] .

[84] A. De Angelis, M. Roncadelli, and O. Mansutti, Phys. Rev. D **76**, 121301 (2007), arXiv:0707.4312 [astro-ph] .

[85] J. Ellis, R. Konoplich, N. E. Mavromatos, L. Nguyen, A. S. Sakharov, and E. K. Sarkisyan-Grinbaum, Phys. Rev. D **99**, 083009 (2019), arXiv:1807.00189 [astro-ph.HE] .

[86] P. Baerwald, M. Bustamante, and W. Winter, JCAP **1210**, 020 (2012), arXiv:1208.4600 [astro-ph.CO] .

[87] K. Ioka and K. Murase, PTEP **2014**, 061E01 (2014), arXiv:1404.2279 [astro-ph.HE] .

[88] J. Kopp, J. Liu, and X.-P. Wang, JHEP **04**, 105 (2015), arXiv:1503.02669 [hep-ph] .

[89] J. H. Davis and J. Silk, (2015), arXiv:1505.01843 [hep-ph] .

[90] V. A. Fedorova and A. E. Rodin, Astronomy Reports **63**, 39 (2019), arXiv:1812.10716 [astro-ph.IM] .

[91] D. R. Lorimer, M. Bailes, M. A. McLaughlin, D. J. Narkevic, and F. Crawford, Science **318**, 777 (2007), arXiv:0709.4301 [astro-ph] .

[92] M. Amiri *et al.* (CHIME/FRB), (2018), 10.3847/1538-4357/aad188, arXiv:1803.11235 [astro-ph.IM] .

[93] L. G. Spitler *et al.*, Nature **531**, 202 (2016), arXiv:1603.00581 [astro-ph.HE] .

[94] B. Andersen *et al.* (CHIME/FRB), Astrophys. J. Lett. **885**, L24 (2019), arXiv:1908.03507 [astro-ph.HE] .

[95] F. Mottez and P. Zarka, Astron. Astrophys. **569**, A86 (2014), arXiv:1408.1333 [astro-ph.EP] .

[96] E. Platts, A. Weltman, A. Walters, S. Tendulkar, J. Gordin, and S. Kandhai, Phys. Rept. **821**, 1 (2019), arXiv:1810.05836 [astro-ph.HE] .

[97] V. Decoene, K. Kotera, and J. Silk, Astron. Astrophys. **645**, A122 (2021), arXiv:2012.00029 [astro-ph.HE] .

[98] E. Petroff, E. D. Barr, A. Jameson, E. F. Keane, M. Bailes, M. Kramer, V. Morello, D. Tabbara, and W. van Straten, Publications of the Astronomical Society of Australia **33** (2016), 10.1017/pasa.2016.35.

[99] V. Decoene, *Sources and detection of high energy cosmic events*, Ph.D. thesis, Sorbonne Universités (2020), `https://hal.archives-ouvertes.fr/tel-02991529`.

[100] V. Soglasnov, (2007), arXiv:astro-ph/0701190 [astro-ph] .

[101] S. A. Petrova, A&A **424**, 227 (2004).

[102] U.-L. Pen and L. Connor, Astrophys. J. **807**, 179 (2015), arXiv:1501.01341 [astro-ph.HE] .

[103] J. R. Pritchard and A. Loeb, Reports on Progress in Physics **75**, 086901 (2012), arXiv:1109.6012 .

[104] L. Koopmans *et al.*, Advancing Astrophysics with the Square Kilometre Array (AASKA14) , 1 (2015), arXiv:1505.07568 .

[105] D. C. Jacobs *et al.*, ApJ **734**, L34 (2011), arXiv:1105.1367 [astro-ph.CO] .

[106] Q. Zheng, X.-P. Wu, M. Johnston-Hollitt, J.-h. Gu, and H. Xu, Astrophys. J. **832**, 190 (2016), arXiv:1602.06624 .

[107] A. H. Patil *et al.*, Astrophys. J. **838**, 65 (2017), arXiv:1702.08679 [astro-ph.CO] .

[108] L. V. E. Koopmans *et al.*, PoS **AASKA14**, 001 (2015), arXiv:1505.07568 [astro-ph.CO] .

[109] J. D. Bowman, A. E. E. Rogers, R. A. Monsalve, T. J. Mozdzen, and N. Mahesh, Nature **555**, 67 (2018).

[110] S. Fraser *et al.*, Phys. Lett. **B785**, 159 (2018), arXiv:1803.03245 [hep-ph] .

[111] Halzen, Francis, "Interview to Jot Down news website," `https://www.jotdown.es/2014/05/francis-halzen-i-always-adv`

[112] F. Blanc *et al.* (ANTARES), (1997), arXiv:astro-ph/9707136 .

[113] S. Adrian-Martinez *et al.* (KM3Net), J. Phys. G **43**, 084001 (2016), arXiv:1601.07459 [astro-ph.IM] .

[114] The KM3NeT Collaboration *et al.*, arXiv e-prints , arXiv:2007.16090 (2020), arXiv:2007.16090 [astro-ph.IM] .

[115] J. Alvarez-Muniz, A. Romero-Wolf, and E. Zas, Phys. Rev. D **84**, 103003 (2011), arXiv:1106.6283 [astro-ph.HE] .

[116] D. Saltzberg, P. Gorham, D. Walz, C. Field, R. Iverson, A. Odian, G. Resch, P. Schoessow, and D. Williams, Phys. Rev. Lett. **86**, 2802 (2001), arXiv:hep-ex/0011001 .

[117] R. Abbasi *et al.* (IceCube), (2020), arXiv:2011.03545 [astro-ph.HE] .

[118] B. P. Abbott *et al.* (LIGO Scientific Collaboration and Virgo Collaboration), Phys. Rev. Lett. **116**, 061102 (2016).

[119] S. Yoshida and K. Murase, Phys. Rev. D **102**, 083023 (2020), arXiv:2007.09276 [astro-ph.HE] .

[120] M. Ahlers, M. Bustamante, and S. Mu, Phys. Rev. D **98**, 123023 (2018), arXiv:1810.00893 [astro-ph.HE] .

[121] I. Kravchenko *et al.*, Phys. Rev. D **73**, 082002 (2006), arXiv:astro-ph/0601148 .

[122] A. Nelles, in *European Physical Journal Web of Conferences*, European Physical Journal Web of Conferences, Vol. 216 (2019) p. 01008, arXiv:1811.10660 [astro-ph.IM] .

[123] I. M. Shoemaker, A. Kusenko, P. K. Munneke, A. Romero-Wolf, D. M. Schroeder, and M. J. Siegert, Annals Glaciol. **61**, 92 (2020), arXiv:1905.02846 [astro-ph.HE] .

[124] P. Gorham *et al.* (ANITA), Phys. Rev. Lett. **117**, 071101 (2016), arXiv:1603.05218 [astro-ph.HE] .

[125] P. Gorham *et al.* (ANITA), Phys. Rev. Lett. **121**, 161102 (2018), arXiv:1803.05088 [astro-ph.HE] .

[126] P. Allison *et al.* (ARA), Phys. Rev. D **93**, 082003 (2016), arXiv:1507.08991 [astro-ph.HE] .

[127] ARIANNA Collaboration, arXiv e-prints , arXiv:2006.03027 (2020), arXiv:2006.03027 [astro-ph.IM] .

[128] C. Kopper, in *Proceedings of 35th International Cosmic Ray Conference — PoS(ICRC2017)*, Vol. 301 (2017) p. 981.

[129] C. Haack and C. Wiebusch, in *Proceedings of 35th International Cosmic Ray Conference — PoS(ICRC2017)*, Vol. 301 (2017) p. 1005.

[130] D. Fargion, A. Aiello, and R. Conversano, in *Proceedings, 26th International Cosmic Ray Conference, August 17-25, 1999, Salt Lake City: Invited, Rapporteur, and Highlight Papers* (1999) p. 396, [2,396(1999)], arXiv:astro-ph/9906450 [astro-ph] .

[131] R. Gandhi, C. Quigg, M. H. Reno, and I. Sarcevic, Phys. Rev. D **58**, 093009 (1998), hep-ph/9807264 .

[132] R. Gandhi, C. Quigg, M. H. Reno, and I. Sarcevic, Astropart. Phys. **5**, 81 (1996), arXiv:hep-ph/9512364 .

[133] Y. S. Jeong, M. V. Luu, M. H. Reno, and I. Sarcevic, Phys. Rev. D **96**, 043003 (2017), arXiv:1704.00050 [hep-ph] .

[134] T. K. Gaisser, R. Engel, and E. Resconi, *Cosmic Rays and Particle Physics* (Cambridge University Press, 2016).

[135] R. Engel, D. Heck, and T. Pierog, Annual Review of Nuclear and Particle Science **61**, 467 (2011), https://doi.org/10.1146/annurev.nucl.012809.104544 .

[136] W. Heitler, *The quantum theory of radiation*, International Series of Monographs on Physics, Vol. 5 (Oxford University Press, Oxford, 1936).

[137] J. Blumer *et al.*, Journal of Physics G: Nuclear and Particle Physics **29**, 867 (2003).

[138] S. Jansen, *Radio for the masses: Cosmic ray mass composition measurements in the radio frequency domain*, Ph.D. thesis, Nijmegen U. (2016).

[139] D. d'Enterria, EPJ Web of Conferences **210**, 02005 (2019).

[140] G. Antchev *et al.* (TOTEM), Eur. Phys. J. C **79**, 103 (2019), arXiv:1712.06153 [hep-ex] .

[141] H. Dembinski *et al.* (EAS-MSU, IceCube, KASCADE-Grande, NEVOD-DECOR, Pierre Auger, SUGAR, Telescope Array, Yakutsk EAS Array), EPJ Web Conf. **210**, 02004 (2019), arXiv:1902.08124 [astro-ph.HE] .

[142] X. Bertou, P. Billoir, O. Deligny, C. Lachaud, and A. Letessier-Selvon, Astropart. Phys. **17**, 183 (2002), arXiv:astro-ph/0104452 .

[143] O. Martineau-Huynh and R. Engel, Proceedings, 21st International Conference, Neutrino 2004, Paris, France, June 14-19, 2004 **143** (2005).

[144] M. Sasaki and G. W.-S. Hou, (2014), arXiv:1408.6244 [astro-ph.IM] .

[145] A. Nepomuk Otte, A. M. Brown, A. D. Falcone, M. Mariotti, and I. Taboada, arXiv e-prints , arXiv:1907.08732 (2019), arXiv:1907.08732 [astro-ph.IM] .

[146] G. Vankova, S. Mladenov, M. Bogomilov, R. Tsenov, M. Bertaina, and A. Santangelo, (2015), arXiv:1509.05995 [astro-ph.IM] .

[147] T. M. Venters, M. H. Reno, J. F. Krizmanic, L. A. Anchordoqui, C. Guépin, and A. V. Olinto, (2019), arXiv:1906.07209 [astro-ph.HE] .

[148] S. Wissel *et al.*, JCAP **11**, 065 (2020), arXiv:2004.12718 [astro-ph.IM] .

[149] K. D. de Vries, O. Scholten, and K. Werner, Astropart. Phys. **45**, 23 (2013), arXiv:1304.1321 [astro-ph.HE] .

[150] O. Scholten, K. Werner, and F. Rusydi, Astropart. Phys. **29**, 94 (2008), arXiv:0709.2872 [astro-ph] .

[151] A. Aab *et al.* (Pierre Auger), Phys. Rev. D **89**, 052002 (2014), arXiv:1402.3677 [astro-ph.HE] .

[152] O. Scholten, T. Trinh, K. de Vries, and B. Hare, Phys. Rev. D **97**, 023005 (2018), arXiv:1711.10164 [astro-ph.HE] .

[153] Schröder, Frank G., Prog. Part. Nucl. Phys. **93**, 1 (2017), arXiv:1607.08781 [astro-ph.IM] .

[154] J. Alvarez-Muñiz, W. R. Carvalho, and E. Zas, Astroparticle Physics **35**, 325 (2012), arXiv:1107.1189 [astro-ph.HE] .

[155] J. Álvarez-Muñiz, W. R. Carvalho, A. Romero-Wolf, M. Tueros, and E. Zas, Phys. Rev. D **86**, 123007 (2012), arXiv:1208.0951 [astro-ph.HE] .

[156] K. Werner, K. D. de Vries, and O. Scholten, Astropart. Phys. **37**, 5 (2012), arXiv:1201.4471 [astro-ph.HE] .

[157] T. Huege, M. Ludwig, and C. W. James, AIP Conf. Proc. **1535**, 128 (2013), arXiv:1301.2132 [astro-ph.HE] .

[158] E. Zas, F. Halzen, and T. Stanev, Phys. Rev. D **45**, 362 (1992).

[159] C. W. James, H. Falcke, T. Huege, and M. Ludwig, Phys. Rev. E **84**, 056602 (2011).

[160] A. Zilles, O. Martineau-Huynh, K. Kotera, M. Tueros, K. de Vries, W. Carvalho Jr., V. Niess, N. Renault-Tinacci, and V. Decoene, Astropart. Phys. **114**, 10 (2020), arXiv:1811.01750 [astro-ph.IM] .

[161] K. Werner and O. Scholten, Astropart. Phys. **29**, 393 (2008), arXiv:0712.2517 [astro-ph] .

[162] T. Huege, M. Ludwig, O. Scholten, and K. D. de Vries, arXiv e-prints , arXiv:1009.0346 (2010), arXiv:1009.0346 [astro-ph.HE] .

[163] H. V. Cane, Monthly Notices of the Royal Astronomical Society **189**, 465 (1979), https://academic.oup.com/mnras/article-pdf/189/3/465/3216119/mnras189-0465.pdf .

[164] V. Decoene, N. Renault-Tinacci, O. Martineau-Huynh, D. Charrier, K. Kotera, S. Le Coz, V. Niess, M. Tueros, and A. Zilles, Nucl. Instrum. Meth. A **986**, 164803 (2021), arXiv:1903.10466 [astro-ph.IM] .

[165] H. Zheng, M. Tegmark, J. S. Dillon, A. Liu, A. Neben, J. Jonas, P. Reich, W. Reich, D. A. Kim, and A. R. Neben, Mon. Not. Roy. Astron. Soc. **464**, 3486 (2017), arXiv:1605.04920 [astro-ph.CO] .

[166] D. Ardouin, A. Bellétoile, D. Charrier, R. Dallier, L. Denis, P. Eschstruth, T. Gousset, F. Haddad, J. Lamblin, P. Lautridou, A. Lecacheux, D. Monnier-Ragaigne, A. Rahmani, and O. Ravel, Nuclear Instruments and Methods in Physics Research A **555**, 148 (2005), arXiv:astro-ph/0504297 [astro-ph] .

[167] C. Balanis, *Antenna theory : analysis and design* (Wiley, 2016).

[168] D. Charrier, in *4th International workshop on Acoustic and Radio EeV Neutrino detection Activities - ARENA 2010*, Vol. 662 (Nantes, France, 2010) pp. S142–S146.

[169] P. Abreu *et al.* (Pierre Auger), JINST **7**, P10011 (2012), arXiv:1209.3840 [astro-ph.IM] .

[170] G. Burke, "Numerical Electromagnetic Codes – User's Manual," (1992), `http://physics.princeton.edu/~mcdonald/examples/NEC_Manuals/NEC4UsersMan.pdf`.

[171] G. J. Feldman and R. D. Cousins, Phys. Rev. **D57**, 3873 (1998), arXiv:physics/9711021 [physics.data-an] .

[172] P. H. Barrett, L. M. Bollinger, G. Cocconi, Y. Eisenberg, and K. Greisen, Reviews of Modern Physics **24**, 133 (1952).

[173] A. Dziewonski and D. Anderson, Physics of the Earth and Planetary Interiors **25**, 297 (1981).

[174] S. Dutta and et al., European Physical Journal C **18**, 405 (2000), hep-ph/9905475 .

[175] N. Davidson, G. Nanava, T. Przedzinski, E. Richter-Was, and Z. Was, Comput. Phys. Commun. **183**, 821 (2012), arXiv:1002.0543 [hep-ph] .

[176] O. Martineau-Huynh *et al.* (GRAND), EPJ Web Conf. **116**, 03005 (2016), arXiv:1508.01919 [astro-ph.HE] .

[177] K. Fang *et al.*, *The Fluorescence detector Array of Single-pixel Telescopes: Contributions to the 35th International Cosmic Ray Conference (ICRC 2017)*, PoS **ICRC2017**, 996 (2018), arXiv:1708.05128 [astro-ph.IM] .

[178] A. Aab *et al.* (Pierre Auger), JCAP **1810**, 026 (2018), arXiv:1806.05386 [astro-ph.IM] .

[179] V. Niess and O. Martineau-Huynh, (2018), arXiv:1810.01978 [physics.comp-ph] .

[180] NASA LP DAAC, "ASTER Level 1 Precision Terrain Corrected Registered At-Sensor Radiance. Version 3. NASA EOSDIS Land Processes DAAC," (2015), `http://lpdaac.usgs.gov`.

[181] N. JPL, "Nasa shuttle radar topography mission global 1 arc second [data set]. nasa eosdis land processes daac," (2013).

[182] V. Niess, A. Barnoud, C. Cârloganu, and O. Martineau-Huynh, Comput. Phys. Commun. , 106952 (2019), arXiv:1904.03435 [physics.comp-ph] .

[183] J. Alvarez-Mu niz, W. R. Carvalho, K. Payet, A. Romero-Wolf, H. Schoorlemmer, and E. Zas, Phys. Rev. D **97**, 023021 (2018).

[184] M. Giller, A. Kacperczyk, J. Malinowski, W. Tkaczyk, and G. Wieczorek, **31**, 947 (2005).

[185] D. Gora, R. Engel, D. Heck, P. Homola, H. Klages, J. Pekala, M. Risse, B. Wilczynska, and H. Wilczynski, Astropart. Phys. **24**, 484 (2006), arXiv:astro-ph/0505371 .

[186] I. T. Union, "Propagation by diffraction - Recommandation ITU-R P.526-14," (2018), `https://www.itu.int/rec/R-REC-P.526/recommendation.asp?lang=en&parent=R-REC-P.526-14-201801-I`.

[187] J. Magliacane, "Splat!" (2014).

[188] A. B. V., A. Haungs, T. Huege, and F. G. Schroeder, (2017), arXiv:1712.09042 [astro-ph.IM] .

[189] M. Tueros and A. Zilles, arXiv e-prints , arXiv:2008.06454 (2020), arXiv:2008.06454 [astro-ph.IM] .

[190] A. Aab *et al.* (Pierre Auger), JINST **12**, T10005 (2017), arXiv:1702.01392 [astro-ph.IM] .

[191] Pieroni, Pablo, *Mediacion del flujo de neutrinos cosmicos ultra energeticos mediante detectores de superficie*, Ph.D. thesis, Buenos Aires (2015), `https://bibliotecadigital.exactas.uba.ar/download/tesis/tesis_n5927_Pieroni.pdf`.

[192] K. Fang, K. Kotera, M. C. Miller, K. Murase, and F. Oikonomou, JCAP **12**, 017 (2016), arXiv:1609.08027 [astro-ph.HE] .

[193] T. Huege, Phys. Rept. **620**, 1 (2016), arXiv:1601.07426 [astro-ph.IM] .

[194] A. Aab, P. Abreu, M. Aglietta, E. Ahn, I. Al Samarai, I. Albuquerque, I. Allekotte, P. Allison, A. Almela, J. Alvarez Castillo, and et al., Physical Review Letters **116** (2016), 10.1103/physrevlett.116.241101.

[195] S. Buitink *et al.*, Nature **531**, 70 (2016), arXiv:1603.01594 [astro-ph.HE] .

[196] P. A. Bezyazeekov *et al.* (Tunka-Rex), JCAP **1601**, 052 (2016), arXiv:1509.05652 [hep-ex] .

[197] V. Decoene, O. Martineau-Huynh, and M. Tueros, in preparation (2021).

[198] S. Chiche, K. Kotera, O. Martineau-Huynh, M. Tueros, and D. de Vries, Krijn, Submitted to Astropart. Phys (2021).

[199] W. D. Apel *et al.*, JCAP **1409**, 025 (2014), arXiv:1404.3283 [hep-ex] .

[200] A. Corstanje *et al.*, Astropart. Phys. **61**, 22 (2015), arXiv:1404.3907 [astro-ph.HE] .

[201] P. Schellart, S. Buitink, A. Corstanje, J. E. Enriquez, H. Falcke, J. R. Hörandel, M. Krause, A. Nelles, J. P. Rachen, O. Scholten, S. ter Veen, S. Thoudam, and T. N. G. Trinh, JCAP **2014**, 014 (2014), arXiv:1406.1355 [astro-ph.HE] .

[202] W. Galbraith and J. V. Jelley, Nature **171**, 349 (1953).

[203] T. C. Weekes, M. F. Cawley, D. J. Fegan, K. G. Gibbs, A. M. Hillas, P. W. Kowk, R. C. Lamb, D. A. Lewis, D. Macomb, N. A. Porter, P. T. Reynolds, and G. Vacanti, Astrophysical Journal **342**, 379 (1989).

[204] S. Funk, G. Hermann, J. Hinton, D. Berge, K. Bernlohr, W. Hofmann, P. Nayman, F. Toussenel, and P. Vincent, Astropart. Phys. **22**, 285 (2004), arXiv:astro-ph/0408375 .

[205] S. Zaroubi, in *The First Galaxies*, Astrophysics and Space Science Library, Vol. 396, edited by T. Wiklind, B. Mobasher, and V. Bromm (2013) p. 45, arXiv:1206.0267 .

[206] D. Charrier, K. de Vries, Q. Gou, J. Gu, H. Hu, Y. Huang, S. Le Coz, O. Martineau-Huynh, V. Niess, T. Saugrin, and et al., Astroparticle Physics **110**, 15ˇ01329 (2019).

[207] D. Ardouin *et al.*, Astropart. Phys. **34**, 717 (2011), arXiv:1007.4359 [astro-ph.IM] .

[208] Wikipedia, "Skywave," `https://en.wikipedia.org/wiki/Skywave`.

[209] PORT, "The port mathematical subroutine library," (1984).

[210] A. Aab *et al.* (Pierre Auger), JINST **11**, P01018 (2016), arXiv:1512.02216 [physics.ins-det] .

[211] P. A. Bezyazeekov *et al.*, Nuclear Instruments and Methods in Physics Research A **802**, 89 (2015), arXiv:1509.08624 [astro-ph.IM] .

[212] A. Nelles *et al.*, JINST **10**, P11005 (2015), arXiv:1507.08932 [astro-ph.IM] .

[213] W. D. Apel *et al.* (LOPES), Astropart. Phys. **75**, 72 (2016), arXiv:1507.07389 [astro-ph.HE] .

[214] P. Abreu *et al.*, Journal of Instrumentation **7**, P10011 (2012), arXiv:1209.3840 [astro-ph.IM] .

[215] J. Lamblin, International Cosmic Ray Conference **5**, 921 (2008).

[216] F. Fenu (Pierre Auger), in *The Pierre Auger Observatory: Contributions to the 35th International Cosmic Ray Conference (ICRC 2017)* (2017) pp. 9–16.

[217] T. Pierog, *The Fluorescence detector Array of Single-pixel Telescopes: Contributions to the 35th International Cosmic Ray Conference (ICRC 2017)*, PoS **ICRC2017**, 1100 (2018).

[218] D. Ardouin *et al.*, Astropart. Phys. **31**, 192 (2009), arXiv:0901.4502 [astro-ph.HE] .

[219] R. Gaior, *EASIER: Extensive Air Shower Identification using Electron Radiometer*, Ph.D. thesis (2013).

[220] u Blox, "u-blox gps-based timing," (2013).

[221] National Instruments, "MultiSim," `https://www.ni.com/fr-fr/shop/electronic-test-instrumentation/application-software-for-electronic-test-and-instrumentation-category/what-is-multisim/multisim-designers.html`.

[222] H. Lin, Z.-A. Liu, O. Martineau-Huynh, F. Guo, C. Wang, J. Zhao, and W. Lu, in *2013 IEEE Nuclear Science Symposium and Medical Imaging Conference and Workshop on Room-Temperature Semiconductor Detectors* (2013).

[223] K. D. de Vries, O. Scholten, and K. Werner, in *American Institute of Physics Conference Series*, American Institute of Physics Conference Series, Vol. 1535, edited by R. Lahmann, T. Eberl, K. Graf, C. James, T. Huege, T. Karg, and R. Nahnhauer (2013) pp. 138–142.

[224] Texas-Instrument, "Ads6424 data sheet," (2013).

[225] Texas-Instrument, "Understanding serial lvds capture in high-speed adcs," (2013).

[226] Q. Gou (GRANDproto35), in *Proceedings, 35th International Cosmic Ray Conference (ICRC 2017): Bexco, Busan, Korea, July 12-20, 2017* (2017).

[227] u-Blox, "GPS-based Timing Considerations with u-blox 6 GPS receivers: Application Note," `http://www.u-blox.com`.

[228] u Blox, "u-center for u-blox," (2018).

[229] J. Gu and O. Martineau-Huynh, "The grandproto35 daq system," (2018).

[230] M. Amenomori, S. Ayabe, S. W. Cui, Danzengluobu, L. K. Ding, X. H. Ding, C. F. Feng, Z. Y. Feng, X. Y. Gao, Q. X. Geng, and et al., The Astrophysical Journal **626**, L29ˇ2013L32 (2005).

[231] X. Wang, X. Qian, Y. Yu, C. Feng, O. Martineau-Huynh, Y. Zhang, Q. Gou, W. Liu, and Y. Feng, "Characterization of the photomultiplier tubes for the scintillation detectors of grandproto35 experiment," (2020), arXiv:2005.10515 [physics.ins-det] .

[232] the Economist, "China has turned xinjiang into a police state like no other," (2018).

[233] Committee on the Elimination of Racial Discrimination, United Nations, "Concluding observations on the combined fourteenth to seventeenth periodic reports of China," `https://tbinternet.ohchr.org/Treaties/CERD/SharedDocuments/CHN/CERD_C_CHN_CO_14-17_32237_E.pdf`.

[234] V. Decoene, in *36th International Cosmic Ray Conference (ICRC2019)*, International Cosmic Ray Conference, Vol. 36 (2019) p. 233, arXiv:1909.04893 [astro-ph.IM] .

[235] J. Becker Tjus and L. Merten, Phys. Rept. **872**, 1 (2020), arXiv:2002.00964 [astro-ph.HE] .

[236] E. M. Holt, F. G. Schröder, and A. Haung, The European Physical Journal C **79** (2019), 10.1140/epjc/s10052-019-6859-4.

[237] E. Zas, New Journal of Physics **7**, 130ŏ013130 (2005).

[238] M. Niechciol (Pierre Auger), in *The Pierre Auger Observatory: Contributions to the 35th International Cosmic Ray Conference (ICRC 2017)* (2017) pp. 56–63.

[239] T. Pierog, M. Alekseeva, T. Bergmann, V. Chernatkin, R. Engel, D. Heck, N. Kalmykov, J. Moyon, S. Ostapchenko, T. Thouw, and et al., Nuclear Physics B - Proceedings Supplements **151**, 159ŏ013162 (2006).

[240] B. R. Dawson, M. Fukushima, and P. Sokolsky, Progress of Theoretical and Experimental Physics **2017** (2017), 10.1093/ptep/ptx054, arXiv:1703.07897 [astro-ph.HE] .

[241] V. Soglasnov, in *WE-Heraeus Seminar on Neutron Stars and Pulsars 40 years after the Discovery*, edited by W. Becker and H. H. Huang (2007) p. 68, arXiv:astro-ph/0701190 [astro-ph] .

[242] T. Eftekhari, K. Stovall, J. Dowell, F. K. Schinzel, and G. B. Taylor, Astrophys. J. **829**, 62 (2016), arXiv:1607.08612 [astro-ph.SR] .

[243] D. R. Lorimer, M. Bailes, M. A. McLaughlin, D. J. Narkevic, and F. Crawford, Science **318**, 777ŏ013780 (2007).

[244] K. Masui, H.-H. Lin, J. Sievers, C. J. Anderson, T.-C. Chang, X. Chen, A. Ganguly, M. Jarvis, C.-Y. Kuo, Y.-C. Li, and et al., Nature **528**, 523ŏ013525 (2015).

[245] J. R. Pritchard and A. Loeb, Reports on Progress in Physics **75**, 086901 (2012).

[246] O. Martineau-Huynh *et al.*, (2016), 10.22323/1.236.1143.

[247] Ubiquity, "Air Max system," `https://airmax.ui.com/`.

[248] T. Asch, *Self-Triggering of Radio Signals from Cosmic Ray Air Showers*, Ph.D. thesis (2008).

[249] A. Schmidt, *Realization of a Self-triggered Detector for the Radio Emission of Cosmic Rays*, Ph.D. thesis (2011).

[250] I. T. Union, "Nomenclature of the frequency and wavelengths bands used in telecommunication," (2015), *https* : $//www.itu.int/dms_pubrec/itu-r/rec/v/R-REC-V.431-8-201508-I!!PDF-E.pdf$.

[251] W. Wang, Y. Yan, and D. Liu, Publications of the Astronomical Society of Japan **65**, S18 (2013).

[252] X. Chen, International Journal of Modern Physics: Conference Series **12**, 256ŏ013263 (2012).

[253] S. W. Barwick *et al.*, Astropart. Phys. **90**, 50 (2017), arXiv:1612.04473 [astro-ph.IM] .

[254] S. Prohira, arXiv e-prints , arXiv:1910.11314 (2019), arXiv:1910.11314 [astro-ph.IM] .

[255] M. T. Akhtar, W. Mitsuhashi, and C. J. James, Signal Processing **92**, 401 (2012).

[256] F. Fuhrer, T. Charnock, A. Zilles, and M. Tueros (2018) arXiv:1809.01934 [astro-ph.IM] .

[257] R. Coniglione (KM3NeT), in *25th European Cosmic Ray Symposium* (2017) arXiv:1701.05849 [astro-ph.IM] .

[258] AnalogDevices, "Smartmesh wirelesshart solutions," (2021).